Understanding the activation mechanisms of small molecules and developing new strategies for low-temperature pollution control using heterogeneous catalysis

Ibrahim Hatoum

CENTRALE LILLE

THÈSE

Présentée en vue d'obtenir le grade de

DOCTEUR

En

Spécialité : Chimie théorique, physique, analytique

Par

Ibrahim Hatoum

DOCTORAT DELIVRE PAR CENTRALE LILLE

Titre de la thèse :

Compréhension des mécanismes d'activation de petites molécules et développement de nouvelles stratégies de dépollution basse température en catalyse hétérogène

Understanding the activation mechanisms of small molecules and developing new strategies for low-temperature pollution control using heterogeneous catalysis

Soutenue le 15 décembre 2023 devant le jury d'examen :

Présidente	**Rose-Noelle VANNIER,** Professeure, UCCS, Centrale Lille
Rapporteur	**Nicolas BION,** DR CNRS, IC2MP, Université de Poitiers
Rapporteur	**Fréderic MEUNIER,** DR CNRS, IRCELYON, Université Claude Bernard Lyon 1
Membre	**Claude MIRODATOS,** DR CNRS Émérite, IRCELYON, Université Claude Bernard Lyon 1
Directeur de thèse	**Christophe DUJARDIN,** Professeur, UCCS, Centrale Lille
Co-encadrante	**Mélissandre RICHARD,** Maître de conférences, UCCS, Centrale Lille

Thèse préparée dans le laboratoire UCCS, Ecole Doctorale SMRE 104

Table of content

General Introduction

Air pollution presents a substantial challenge to public well-being, contributing to severe health issues. The world health organization (WHO) estimates the number of deaths due to pollution to be around 9 million per year, which corresponds to 20% of deaths worldwide. A significant source of this pollution is the transportation sector, primarily due to vehicle emissions. Among the various reactions occurring in exhaust emissions, the CO oxidation reaction has garnered considerable attention from researchers. Despite its apparent simplicity, the reaction mechanism has been the subject of extensive debate and discussion in the literature. While three-way catalysts have made significant strides in reducing emissions, the challenge of addressing cold start issues remains unresolved. Consequently, gaining a comprehensive understanding of the catalyst's behavior under reaction conditions at low temperatures is essential to improve catalyst formulations. At lower temperatures, the CO oxidation reaction on platinum group metal (PGM) catalysts exhibits distinct phenomena, including surface reconstruction and hysteresis. The hysteresis phenomenon, associated with activity variations within temperature cycles, is a subject of ongoing debate in the literature and various interpretations and explanations have been proposed over time to elucidate these intriguing phenomena. In-situ techniques provide valuable insights into the species formed on the catalyst's surface during a reaction. Among these techniques, the combination of SSITKA (Steady-State Isotopic Transient Kinetic Analysis) and IR (Infrared) spectroscopy emerges as the most suitable method for investigating reaction mechanism and identifying the diverse species formed on the catalyst surface. To our knowledge, there have been no prior studies that have employed the SSITKA-IR technique to investigate the mechanism of the CO oxidation reaction in the existing literature.

This manuscript is structured into five chapters. The **first chapter** provides an overview of the existing literature concerning air pollution, governmental regulations, with a particular focus on the three-way catalyst system and the challenges posed by the cold start problem. Additionally, it offers insights into the CO oxidation reaction mechanism, specifically the formation of surface adsorbed species, and discusses surface phenomena such as hysteresis and surface reconstruction. Furthermore, within this opening chapter, a comprehensive introduction to the SSITKA technique is presented. This encompasses an exploration of its fundamental parameters and principles, mechanistic models, and a consideration of its limitations. Additionally, it highlights advancements in the technique, notably the coupling of SSITKA with IR spectroscopy with some examples.

The chapter 2 of this manuscript delves into the materials and methods utilized throughout this thesis work. It provides a comprehensive account of the experimental conditions employed for the characterization and synthesis of various materials. Furthermore, the configuration of the setup used for the experiments is detailed. Lastly, the chapter offers an overview of the experimental conditions followed for the different catalytic tests.

Chapter three is dedicated to the application of the SSITKA-IR technique in the context of the CO oxidation reaction on Pt/Al_2O_3 and Pd/Al_2O_3 catalysts. The primary objective of this chapter is to identify the species generated during the reaction and to differentiate between active and inactive species. The findings reveal that linear and bridged carbonyls are active species in the CO oxidation reaction. Additionally, this chapter addresses the role of hydrogen-carbonate species, concluding that they do not actively participate in the reaction mechanism. Instead, they are formed through the interaction between the product CO_2 and hydroxyl groups present on the Al_2O_3 support.

The fourth chapter investigates the reactivity of the linear and bridged carbonyls that have been identified previously as active species in CO oxidation reaction. The research work explores the decomposition of the carbonyls IR signal into various bands, each with distinct site attributions and kinetic rate exchange characteristics. Furthermore, this chapter reveals an important insight—while certain bands within the linear and bridged carbonyl groups may exhibit fast exchange rates, not all of them play a role in product formation. In particular, some bands may have high reactivity but do not significantly influence the overall product formation process, adding depth to our understanding of the reaction mechanism.

Finally, in the **last chapter** the hysteresis phenomenon observed on Pt/Al_2O_3 and Pd/Al_2O_3 catalysts have been studied with the use of SSITKA-IR technique. This chapter focuses on unraveling the behavior of the linear and bridged bands during both light-off and light-out conditions, aiming to explain the observed differences in activity. It was shown that the hysteresis can be attributed to a substantial change in the kinetic behavior of the intermediate species, likely stemming from a reconstruction phenomenon occurring during the light-out phase. Furthermore, this chapter explores the effect of reductive pulses on the activity of the catalysts, revealing increases in activity, especially for Pd/Al_2O_3.

Résumé de thèse

Le contrôle de pollution de l'air représente un défi considérable à la fois en termes de santé publique et pour le maintien environnemental. L'Organisation Mondiale de la Santé (OMS) estime que le nombre de décès dus à la pollution s'élève à environ 9 millions par an, soit 20% des décès dans le monde. Une source importante de cette pollution est le secteur des transports, principalement en raison des émissions des véhicules à moteur thermique. La solution utilisée pour limiter l'émission de polluant se trouve dans l'instauration d'un pot catalytique (catalyse 3 voies et DeNOx) en sortie d'échappement. Diverses réactions d'oxydo-réduction se produisent ainsi dans la ligne d'échappement, et parmi-elles, la réaction d'oxydation du CO qui a suscité beaucoup d'attention de la part des chercheurs. Malgré sa simplicité apparente, le mécanisme de réaction a fait l'objet de nombreux débats et discussions dans la littérature. Bien que les catalyseurs trois voies aient fait d'importants progrès dans la réduction des émissions, la forte pollution observée lors des démarrages à froid, lorsque le catalyseur n'est pas encore actif, demeure un problème irrésolu. Par conséquent, acquérir une compréhension complète du comportement du catalyseur dans des conditions de réaction à basse température s'avère nécessaire pour résoudre ce défi. La réaction d'oxydation du CO réalisée sur des catalyseurs à base de métaux du groupe du platine (PGM) fait face à des comportements distincts, avec notamment l'apparition de phénomènes de reconstruction de surface et d'hystérésis. Le phénomène d'hystérésis, associé à des variations d'activité en montée et descente de température, fait l'objet de débats constants dans la littérature. Ainsi, plusieurs interprétations et explications ont été proposées au fil du temps pour élucider ce phénomène intrigant, mettant en avant l'utilisation de diverses techniques d'analyse.

Les techniques d'analyse *in situ* fournissent des informations précieuses sur les espèces formées à la surface du catalyseur pendant une réaction. Parmi celles-ci, la combinaison de la technique SSITKA (Analyse cinétique de l'échange isotopique transitoire en régime stationnaire) et de la spectroscopie infrarouge (IR) émerge comme la méthode la plus adaptée pour étudier les mécanismes de réaction. À notre connaissance, aucune étude antérieure n'a employé le couplage SSITKA-IR pour enquêter sur le mécanisme de la réaction d'oxydation du CO sur PGM dans la littérature existante.

L'objectif principal de ce travail de thèse a été de démêler les mécanismes sous-jacents de l'oxydation du CO sur les catalyseurs PGM déposé sur alumine (γ-Al_2O_3) à basse température,

avec pour but ultime d'améliorer la performance du catalyseur dans ces conditions difficiles. Pour atteindre cet objectif, notre principal axe de recherche s'est orienté vers l'investigation du phénomène d'hystérésis observé à basse température. Notre mission première a été d'éclaircir ce phénomène, non seulement pour le comprendre, mais aussi pour tirer parti de cette connaissance afin d'améliorer l'efficacité du catalyseur à basse température. Une approche en plusieurs étapes a été adoptée pour parvenir à une compréhension globale. La première étape a consisté à utiliser la technique SSITKA-IR afin de caractériser la surface du catalyseur et de distinguer les espèces actives et les espèces inactives lors de la réaction d'oxydation de CO.

Le troisième chapitre de cette thèse se penche spécifiquement sur les différentes espèces formées à la surface des catalyseurs Pt et Pd supportés sur alumine et impliquées dans la réaction d'oxydation du CO. La technique IR a identifié la formation d'espèces carbonyles linéaires et pontés, ainsi que d'espèces hydrogénocarbonates à la surface des deux catalyseurs. Selon la technique SSITKA, les espèces subissant un échange isotopique rapide, en phase avec la cinétique de formation du produit CO_2, sont considérées comme des contributeurs actifs au mécanisme de réaction. Dans ce contexte, les carbonyles linéaires et pontés ont été identifiés comme les principales espèces actives, tandis que les espèces hydrogénocarbonates se sont vues reléguées au rang d'espèces inactives. L'expérience impliquant l'échange direct $^{12}CO_2/^{13}CO_2$ sur le support d'alumine nu a fourni des preuves claires que les espèces hydrogénocarbonates sont en réalité formées par l'interaction du produit CO_2 avec un groupe hydroxyle de surface. Ce phénomène de ré-adsorption explique le décalage initial observé dans les profils de concentrations normalisées de ^{13}CO et $^{13}CO_2$ lors de l'expérience SSITKA. De plus, le comportement des espèces hydrogénocarbonates est remarquablement similaire sur les deux catalyseurs Pt/Al_2O_3 et Pd/Al_2O_3. Cette observation suggère que la ré-adsorption de CO_2 se produit principalement sur le support d'alumine lui-même, plutôt que par une diffusion de surface (spillover) à partir des particules métalliques. La non-nullité des valeurs de N_C (concentration d'espèces de surface contenant du carbone-13) obtenues sur les catalyseurs Pt et Pd, même après une pré-saturation en $^{12}CO_2$, suggère soit une saturation partielle du support d'alumine par des carbonates, soit la présence d'autres espèces intermédiaires contenant du carbone dans le mécanisme d'oxydation du CO. Cela nous amène donc à conclure prudemment sur la signification de ces résultats. En effet, le réservoir (*pool*) correspondant à N_C pourrait être divisé en deux catégories : 1/ les hydrogénocarbonates spectateurs et 2/ des espèces intermédiaires actives contenant du carbone, qui pourraient inclure par exemple des hydrogénocarbonates formés métalliques ou différents types d'espèces chimiques. En

conclusion il est également important de noter que, même si toutes les espèces supposées actives suivent un échange isotopique $^{12}CO/^{13}CO$ similaire, toutes ne participent pas nécessairement au mécanisme de réaction. En fait, l'une de ces espèces peut être spectatrice mais avec une conversion rapide en espèce réactive. Après avoir identifié les principaux intermédiaires actifs dans la réaction d'oxydation du CO sur Pt et Pd supportés sur alumine, notre attention s'est tournée vers la distinction de la réactivité de ces différentes espèces carbonyles au cours de la réaction.

Dans le chapitre quatre, nous avons utilisé la modélisation cinétique pour approfondir la réactivité des espèces carbonyles de surface. Dans le cas de Pt/Al_2O_3, quatre types d'espèces carbonyles linéaires ont été identifiés suite à une déconvolution du signal IR, basée sur la littérature existante, en 4 bandes distinctes. Les cinétiques d'évolution de ces bandes au cours de l'échange isotopique $^{12}CO/^{13}CO$ ont été analysées donnant ainsi des informations sur leur comportement intrinsèque. Chaque bande présente des caractéristiques uniques de site d'adsorption et de constante cinétique d'échange. Les constantes les plus grandes ont été attribuées aux bandes associées à l'adsorption de carbonyles sur les sites de Pt terrasse (2080 cm^{-1}) et Pt marche (2059 cm^{-1}). En revanche, notre étude a confirmé la nature non active des espèces carbonyles adsorbées sur des particules de plus petites taille (~ 1 nano et sub-nanométrique), en accord avec leurs constantes cinétiques d'échange plus faibles. Grâce à une analyse encore plus poussée, nous avons pu identifier le CO linéaire adsorbé sur les sites de Pt marche (*step*) comme l'intermédiaire principal dans la formation de CO_2, tandis que le CO linéaire adsorbé sur les sites de terrasse du Pt semble jouer un rôle plus mineur dans la formation du produit, malgré sa constante cinétique d'échange plus élevée. En utilisant la même méthode sur le cas de Pd/Al_2O_3, différents types de carbonyles linéaires et pontés ont été identifiés sur la surface du Pd avec l'aide de la littérature. 5 bandes distinctes ont cette fois-ci été déconvoluées pour évaluer leur comportement cinétique. L'analyse a mis en lumière les rôles de chaque espèce dans la réaction d'oxydation du CO. L'échange le plus rapide a été observé pour la bande à 1957 cm^{-1}, associée à l'adsorption de carbonyles pontés sur Pd(100), ainsi que pour la bande à 2059 cm^{-1}, liée à l'adsorption de carbonyles linéaires sur des sites faiblement coordonnés. Alors que les carbonyles pontés se sont révélés jouer un rôle majeur dans la production de CO_2, les bandes L1 et L2, correspondant au CO adsorbé linéairement sur Pd ne semblent jouer, quant à eux, que des rôles mineurs. De même, le CO adsorbé sur les sites « bridge-bound » et « 3 fold hollow » semblent être des espèces inactives dans la réaction d'oxydation du CO, en accord avec leurs plus faibles constantes cinétiques d'échange

isotopique. Une des conclusions essentielles de cette étude est qu'une espèce peut s'échanger rapidement (constante cinétique élevée) sans affecter significativement la formation des produits, comme observé dans le cas des CO linéaires dans le système Pd/Al_2O_3. La signification de cette étude réside dans la révélation que les carbonyles linéaires et pontés, autrefois considérés comme des espèces actives, sont en réalité composés de plusieurs sous-catégories d'espèces différenciées par leurs sites d'adsorption, dont toutes ne participent pas au mécanisme de réaction.

Les informations obtenues dans les chapitres précédents ont servi de base à l'analyse et la compréhension du phénomène d'hystérésis dans le chapitre cinq. Dans le cas du Pt/Al_2O_3, une comparaison des constantes cinétiques dérivées du modèle cinétique précédemment décrit révèle une diminution des valeurs pendant la phase de descente en température, ce qui est en corrélation avec la diminution de l'activité catalytique. De plus, une réduction de l'intensité des bandes de CO linéaire est observée pendant la phase de descente en température, en accord avec les calculs SSITKA. Cependant, la comparaison de la distribution des espèces carbonyles présentes sur Pt dans les deux conditions (montée et descente en température) n'offre pas une explication satisfaisante de la différence observée en termes d'activité catalytique. Il est à noter que, étant donné les conditions non isothermes d'analyse pour les deux conditions, fournir une explication est difficile la température ayant un impact sur les paramètres cinétiques. Dans le cas de Pd/Al_2O_3, où la température a été maintenue constante dans les deux conditions, le phénomène d'hystérésis a pu être attribué à des variations dans le comportement cinétique des différentes bandes IR lors de l'échange isotopique. Notamment, une légère modification de l'ordre de réactivité des espèces a été observée, associée à une réduction significative des constantes cinétiques pendant la descente en température ainsi qu'à une diminution de la quantité d'intermédiaires actifs déterminée par SSITKA. De plus, le comportement de la principale espèce intermédiaire lors de l'échange isotopique diffère entre les deux conditions. Par conséquent, il est raisonnable d'attribuer le phénomène d'hystérésis à un changement substantiel dans le comportement cinétique des espèces intermédiaires, probablement dû à un phénomène de reconstruction de surface se produisant lors de la montée en température. Un autre aspect exploré dans ce travail de thèse concerne l'application de pulses réducteur d'H_2 pour étudier leur impact sur la performance catalytique. L'objectif ultime est ici de trouver un moyen de maintenir un niveau élevé d'activité du catalyseur à l'aide de conditions transitoires. L'effet de ces pulses sur l'activité des deux catalyseurs se traduit par une augmentation significative de la conversion de CO observée pour Pd/Al_2O_3, tandis que l'effet sur Pt/Al_2O_3 est

plus mineur. Plus précisément, pour Pd/Al_2O_3, une nette diminution de l'intensité des bandes de carbonyles pontés et des bandes d'hydrogénocarbonates est observée après les pulses d'H_2. Il est important de noter que l'activité catalytique accrue n'est pas maintenue dans le temps. Par conséquent, il est crucial d'introduire les pulses d'H_2 de manière transitoire pour maintenir une activité importante. Pour cela des pulses brefs (1 s) peuvent être suffisants pour obtenir une augmentation substantielle de la conversion. Cependant, pour atteindre la conversion maximale, une exposition plus longue à H_2 est nécessaire.

Chapter I- Literature Overview

1- Air pollution: Challenges and Solutions

1.1- Air pollution

Air pollution is one of the world's largest health and environmental problems. Almost the entire world population (99%) breathes air that exceeds World Health Organization (WHO) air quality limits, and threatens their health [1]. The primary air pollutants are substances that are emitted directly into the environment mainly due to the combustion of biomass and fossil fuels. These pollutants include gases like sulfur dioxide (SO_2), nitrogen dioxide (NO_2), carbon monoxide (CO), Volatile Organic Compounds (VOCs), and particulate matter (PMs). Air quality monitoring carried out in more than 6000 cities across 117 countries shows, for example, that residents are still inhaling harmful levels of fine particulate matter and nitrogen dioxide. People residing in low and middle-income countries are particularly exposed to high levels of air pollution. The findings have led the WHO to highlight the significance of decreasing the use of fossil fuels and implementing other concrete measures to reduce air pollution. Meanwhile, more and more evidences are emerging regarding the negative impact of air pollution on human health, indicating that even small quantities of certain air pollutants can cause significant harm to the body. These health impacts have economic costs: they shorten lifespan, increase medical costs and reduce productivity through lost working days. In France, air quality has improved in the last two decades but there are still several regions where the limit values for pollutants are not being met. Atmospheric pollution is the number one issue of environmental concern for the French population today. Approximately 47 000 people die prematurely each year in France (~8% of total deaths) as result of fine particle and NO_2 pollution according to a recent study of *Santé Publique France* [2]. Moreover, the annual direct and indirect economic costs associated to air pollution is estimated to €100 billion.

The character of air pollution is undergoing a shift. Household air pollution has been decreasing globally since 1990 due to the replacement of biomass, such as wood and dung, with liquefied petroleum gas and renewable sources of energy for household heating and cooking [3]. However, the gains made in this area have been overpassed by the increase in ambient air pollution, propelled by the rapid expansion of megacities, industrial production globalization, the proliferation of toxic chemicals and pesticides, and the growing use of motor vehicles [4]. This increase is particularly significant in the most rapidly industrializing countries. While industrial pollution has decreased by 45 to 65 percent in 20 years, transportation pollution has increased by more than 30 percent due to the increase in car traffic. To solve this issue, the

passenger car market is undergoing a major transformation worldwide. For example, on June 8, 2022, the European Parliament voted to end the sale of new thermal cars in 2035, a major step towards achieving carbon neutrality by 2050 [5]. Consequently, the French car fleet is entering a phase of massive electrification. While the electrification of the vehicle fleet is an essential lever, it is not enough for the transition to be fully effective from an environmental, social and economic point of view. The deployment of electric vehicles must also be accessible to all, beneficial to the climate by using decarbonized electricity, and limit its impact on the electricity grid and earth resources. These limitations slow down the transition so that thermal vehicles still represent more than 90% of the fleet today.

Most engines use the combustion of fuels made from crude oil as a source of energy. Even if many efforts have been made to find solutions to reduce the emissions of harmful exhaust gases, any improvement in technology to reduce pollution from mobile sources is always justified [6]. Combustion exhaust gas is mostly composed of carbon dioxide (CO_2), water vapor (H_2O), and nitrogen (N_2). Despite the fact that carbon dioxide and water vapor are greenhouse gases contributing to global warming, they are not poisonous or harmful for Humans. Most importantly undesirable, noxious, or toxic substances such as carbon monoxide (CO), hydrocarbons (properly indicated as C_xH_y, but commonly shown simply as "HC"), nitrogen oxides (NO_x) are also released from incomplete combustion, unburnt fuel and excessive combustion temperatures, respectively, as well as particulate matter.

1.2- Regulations and current abatement technology

1.2.1- History: Euro 1 to Euro 6d

Recognizing the problem of atmospheric pollution has led to the introduction of regulations controlling and limiting harmful emissions from automobile exhaust. Since 1992, the Euro emission standards have been in place to control vehicle emissions in Europe for passenger cars (diesel and gasoline). The regulated pollutants CO, HC, NOx and particulate matter (PM) have all been targeted for significant reductions with the help of these successive standards (Euro 1 to 6). Euro 6d, currently applicable, was introduced in 2020 to further reduce harmful emissions from cars and other vehicles (Table I-1).

Table I-1- European emissions regulations limits.

Standard	Date of application	CO (mg/km)	HC (mg/km)	NO_x (mg/km)	PM (mg/km)	NH_3
Euro 6d	2020	1000	100	60	5	-
Euro 7	2025	500	100	60	4.5	20

1.2.2- The upcoming Euro 7

Euro 7 standards have been revealed recently and should be in place in 2025 (Table I-1). The proposal includes a number of changes, including updated limits for pollutant emissions, broadened boundary conditions for Real Driving Emission (RDE) testing, extended emission durability periods, as well as first-ever limits for particulate emissions from brakes. It will limit NOx emissions to 60 milligrams per kilometer for diesel engine (this is already the case for gasoline) [7]. The ultimate goal is to reduce nitrogen dioxide pollution from motor vehicles by 35% by 2035 and carbon monoxide emission standards (500 mg/km). In addition to these pollutants, the proposal introduces limits for ammonia for cars and vans to not exceed 20 mg/km. The proposal also lowers the cut point for PN measurement from the current 23 nm to 10 nm (PN_{10}) and regulates particles from brakes, as an upgrade for Euro 6 regulation. Moreover, until 2016, emissions have been measured in the laboratory using the Worldwide Harmonized Light Vehicles Test Cycles (WLTC) for Euro 6 certification and since 2017, the RDE tests have been applied to passenger cars that meet the Euro 6 emission norm [8].

In Euro 7, pollutant emissions will be assessed from the moment the engine is turned on, unlike the Euro 6d standard where emissions were measured after the coolant reached 70 °C [9]. Although the objectives of the future Euro 7 standard may seem unambitious due to the fact that the factual limits do not change much compared to Euro 6, the boundary conditions as seen in Figure I-1: emission measurements in real conditions and no longer in the laboratory, more representative driving scenarios, measurement during cold starts, hard accelerations or high altitudes, etc.

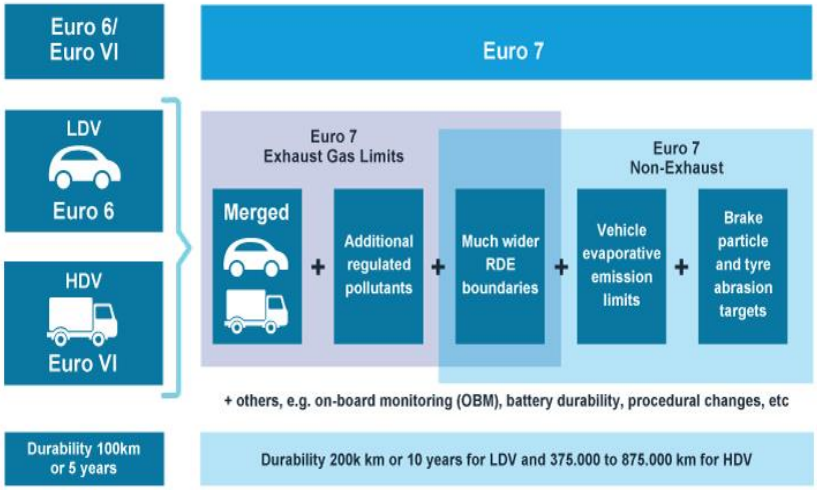

Figure I-1- Euro 7 prediction compared to Euro 6 regulation [10].

Thus, major developments in exhaust gas treatment will be necessary. One of the main challenges will be to accelerate the warming up of exhaust systems so that they reach their effective temperature as quickly as possible, with a focus on cold start, being the most critical phase in terms of pollutant gas emissions.

1.2.3- Three-Way catalysis for gasoline engines

Following these regulations, the automotive industry stepped up its efforts to develop technologies aimed at reducing pollutant emissions from diesel and gasoline engines. For diesel engines, selective catalytic reduction (SCR) systems such as DeNOx (or selective catalytic reduction of nitrogen oxide) have been widely adopted. Likewise, the Three-Way Catalysis (TWC) systems have been applied to gasoline engines in order to reduce harmful emissions. We will focus here on this new technology applied to gasoline engines, which will be discussed in the following section.

Since 1982, the TWC has been extensively applied to the post-treatment of exhaust gas from gasoline engines [11]. The effective control of emissions is accomplished on an active catalyst by oxidizing CO and HCs simultaneously, forming CO_2 and water, and reducing nitrogen oxides to nitrogen gas (N_2) according to equations I-1 to I-3. Other reactions can also occur in addition of these, such as the water-gas shift reaction [12].

$$2\,CO + O_2 \rightarrow 2\,CO_2 \qquad \text{(I-1)}$$

$$C_xH_y + O_2 \rightarrow CO_2 + H_2O \qquad \text{(I-2)}$$

$$2\,NO \rightarrow N_2 + O_2 \qquad \text{(I-3)}$$

The design of active solid material placed in the exhaust pipe (Figure I-2) includes several components such as: a substrate, the washcoat, an active phase, and several promoter elements [13].

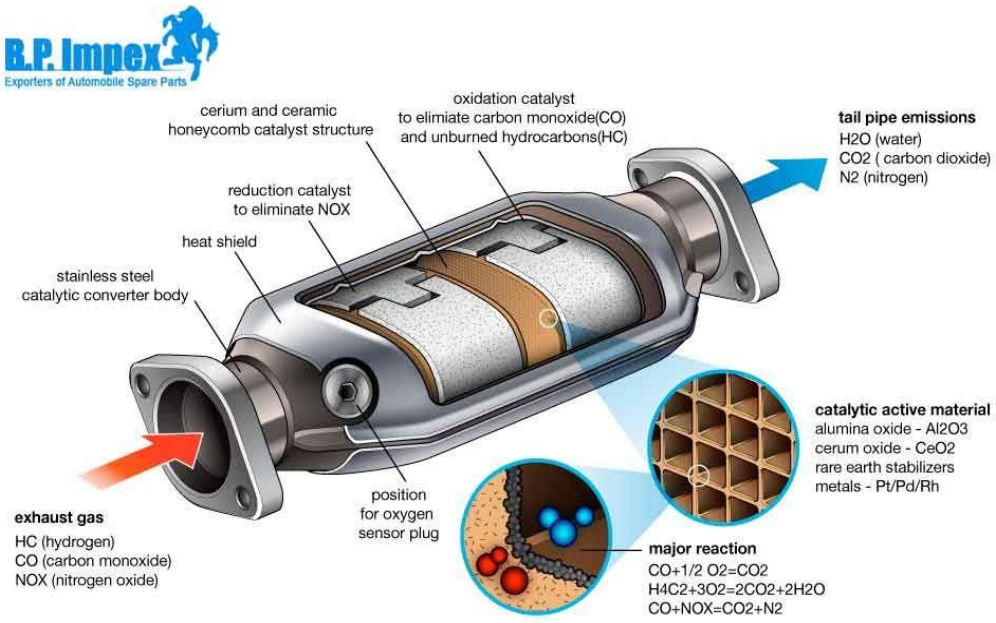

Figure I-2- Schematic image of a three-way catalytic converter [14].

The substrate has a honeycomb structure and is typically made of cordierite, but metallic foil substrates have also been developed. The advantage of a metal monolith lies in their high conductivity and low heat capacity but ceramic monolith as cordierite ($Al_3Mg_2AlSi_5O_{18}$) has been widely applied in most catalyst converter because of their low cost, excellent resistance to thermal shock and low coefficient of thermal expansion [15].

The washcoat is a high surface area material containing a doped alumina-based material (Al_2O_3) which is chosen for its thermal stability and resistance to sintering [16]. To maintain the air-to-fuel ratio close to the stoichiometry, the washcoat incorporates a component with a high oxygen storage capacity (OSC) such as CeO_2. Indeed, an important parameter in TWC is to maintain an air-to-fuel ratio close to the stoichiometry (14.7:1) in order to effectively convert the three main pollutants simultaneously as shown in Figure I-3 [12, 17]. Cerium ions can easily switch between III+ and IV+ oxidation states by creating and regenerating oxygen vacancies [15]. This

feature allows the ceria-containing catalyst material to store oxygen from the exhaust stream when there is an excess of oxygen, thereby promoting to conversion of NO_x. On the other hand, it releases oxygen to the exhaust stream when there is a deficiency, which promotes the conversion of CO and HCs to CO_2. The addition of promoter elements, such as alkaline earth metals or trivalent rare earth metals (Y, La, Pr, Nd) is also crucial for TWC materials to achieve thermal stability [18]. In the exhaust pipe, the catalysts are often subjected to high temperatures for prolonged periods, reaching up to 800-1000 °C. At these temperatures, the support can experience severe sintering leading to several issues that can negatively impact the catalytic performance as a reduction in surface area, loss of available reactive oxygen within the ceria lattice and sintering of the active metal catalyst [15].

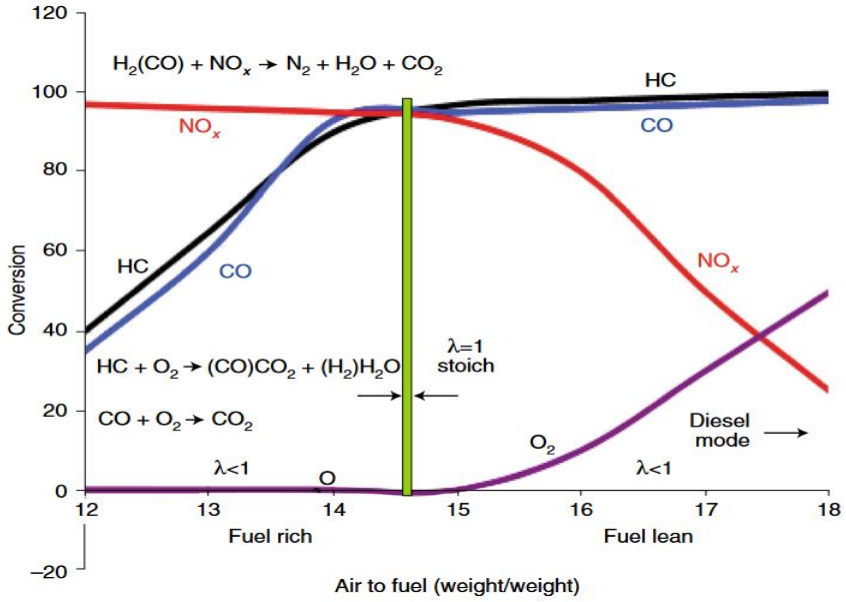

Figure I-3- Typical performance of a TWC as a function of A/F ratio [19].

Finally, the active phase is commonly made of elements from platinum group metals (PGMs) such as platinum, palladium and rhodium. Pt and Pd are used for the oxidative process of three-way catalysis, while Rh is necessary for reducing NO_x emissions. The use of precious metals in TWC poses several challenges due to their scarcity, high cost, and potential for deactivation (sintering or poisoning) [20]. As a result, the choice and loading of PGMs must balance the required efficiency of the converter with the market price of PGMs. Attempts to replace PGMs with more abundant base metal oxides such as Cr, Ni, Co, Cu and Mn were unsuccessful in meeting the requirements for catalytic converters in terms of activity and selectivity, despite efforts made by automobile and catalyst companies to find alternative options that could reduce costs [21]. The development of TWC performance has led to the introduction of a new system called Four-way conversion catalyst (FWC). This advanced system has the capacity to not only

remove the three primary pollutants (CO, HC, NO) from gasoline exhaust but also effectively tackle the issue of particulate matter.

In summary, the ideal catalyst should possess several key characteristics, such as high activity and selectivity, rapid light-off, excellent thermal stability and a large capacity of oxygen storage. Despite their efficiency, a significant limitation for modern three-way catalyst design is in terms of cold-start performance, particularly during the first few minutes of a vehicle journey. Indeed, high temperatures (>250-300 °C) are required from engine exhaust to achieve effective conversion rates [15]. For this reason, it is crucial to give special attention to the cold start problem in order to thoroughly understand and effectively address this issue.

1.3- Cold Start challenge

For a modern gasoline engine, about 90% of pollutants will be released during the first minutes of operation after a cold start due to the incomplete combustion of fuel [22]. Various factors, such as the composition of the exhaust gas, the volume and composition of the catalyst, affect the catalyst's performance during the cold-start period [23]. However, the main cold-start problem is caused by the fact that the temperature of the catalyst is the most crucial factor in achieving efficient conversion. During start-up, the engine exhaust is not hot enough to heat up the catalyst to the required threshold temperature, also known as the light-off temperature for the catalytic reactions to begin. The temperature ranges at which the light-off typically occurs is between 250 and 300 °C [24, 25]. Thus, the challenge is to get heat the catalyst as fast as possible to initiate the catalytic reaction. To address this challenge, researchers have been working on designing three-way catalyst with enhanced low-temperature catalytic performance and strategies to improve their light-off temperatures.

Several initiatives have been taken to improve the efficiency of catalytic converters at low temperatures, like catalytic solutions or new system approaches. The effectiveness of any of these ideas is assessed based on several criteria, including their ability to reduce emissions and light-off temperature, their thermal stability over extended periods and mileage and the complexity, durability and cost of the system. An actual strategy for lowering light-off temperatures in catalytic converters is to increase the precious metal loading, particularly palladium [26, 27]. However, this approach is limited by the high cost of these metals. Some researchers have also shown that increasing the amount of Pd in the catalyst does not enhance

catalytic performance beyond a certain level [28], as excessive concentrations of these precious metals can lead to significant CO and Pd interactions making the desorption of CO from Pd a rate-limiting step [29]. Another strategy consists of using HC traps which have been applied successfully in diesel applications. During the cold start-period, HC can be captured and held in a trap until the catalyst is heated and becomes active. Then HC are released and subsequently oxidized in the conventional TWC [30]. The trap is typically made of hydrophobic zeolite-based materials like ZSM-5, zeolite Y and zeolite beta [31]. One of the challenges associated with using a zeolite trap is that precious metal in the three-way catalyst can be poisoned by SiO_2 that migrates from the trap during hydrothermal aging at temperature above 750 °C. Moreover, zeolite materials have poor hydrothermal stability at temperatures above 850 °C [19]. Last approach was to use different methods to quickly heat the catalyst by minimizing the time after a cold-start for the catalyst to be sufficiently warm to enable high conversion of the harmful exhaust compounds [23]. This was achieved through the use of an electrically heated catalyst or close coupled catalyst. Typically, conventional three-way catalysts are installed in an underfloor position, which is quite far from the engine. However, close-coupled catalysts are situated much closer to the engine, often on the manifold [32, 33]. This position helps to minimize the duration required for the engine exhaust to heat up the catalyst. Successful experiments showed that the time needed to reach hydrocarbon light-off can be shortened to as little as 10 seconds [24, 34]. Using metal monolith with high thermal conductivity and low heat capacity is the preferred substrate for close-coupled catalysts allowing for rapid heating. Major challenges of using close-coupled catalysts is (i) to find materials that can resist deactivation after being exposed to high temperatures, typically around 1050 °C and (ii) the space requirements and heat management in under hood location [30]. Finally, another simple way to accelerate the heating of the catalyst was investigated by using electrically heated catalysts (EHC). The concept consists of electrically heating a pre-catalyst supported on a metal substrate, enabling it to rapidly reach the temperature required for efficient light-off [35]. The EHC technology uses sintered metals or metal foils to create a resistive element, which is coated with the catalyst material [23]. However, the use of EHC has been proven to be possible, but there are significant concerns about its long-term durability, power consumption and cost of the metal substrate and system [24].

As you have understood, the "cold start" issue remains relevant in catalysis, and studying catalytic mechanisms at low temperatures is important. This is precisely the objective of this thesis, which aims to investigate two specific aspects. Firstly, we will examine the CO oxidation

and its hysteresis phenomena, seeking to understand the factors that influence this process at lower temperatures. Secondly, we will use a particular technique called SSITKA-IR (Steady State Isotopic Transient Kinetic Analysis) coupled to InfraRed Spectroscopy to deepen our understanding of these low-temperature catalytic phenomena. Therefore, the following two paragraphs provide a comprehensive overview of the current state of research in these two specific areas.

2- CO oxidation reaction

2.1- Introduction

Carbon monoxide (CO) is a poisonous gas that is often referred to as the silent killer as it lacks any color, taste or smell. It is commonly produced due to incomplete combustion of fossil fuels and most of its emission occurs during the cold start of vehicles [25, 29]. Even a small exposure to CO can be fatal as it binds easily with hemoglobin in blood cells replacing by this way vital oxygen. In recent years, catalytic CO oxidation has gained significant attention due to its demand in various industrial processes, such as pollution reduction in industries, petrochemical waste abatement, fuel and hydrogen production for fuel cells [36, 37]. Furthermore, as seen previously, CO is a major source of air pollution from the automotive industry and its oxidation is a key reaction that takes place in the three-way catalytic converter [38].

This reaction is catalyzed commonly by the use of transition metals to activate surface reactions. Among transition metals, PGMs such as platinum (Pt), palladium (Pd) and rhodium (Rh)- are known to have the highest activity because of their ability to dissociate molecular oxygen at low temperatures and form strong bonds with atomic oxygen and CO. Despite many attempts to enhance their efficacy in CO oxidation, such as incorporating promoters or using reducible oxides as supports, the use of PGM catalysts for CO oxidation at room temperature remains a challenge [39]. In recent studies, it has been found that gold (Au) is highly effective in catalyzing the oxidation of CO close to the ambient temperature [40]. Gold's high activity is attributed to its selective binding to CO and non-selective loose binding to other reactants, resulting in sufficient concentration of CO on surfaces, thus lowering the activation energy to a negligible value making the reaction occur at room temperature. Despite the favorable characteristics of gold catalysts for CO oxidation at low temperatures, their limitations in terms of overall TWC performance and cost make Pt and Pd catalysts the preferred choices for addressing the multi-reaction requirements of TWC systems.

2.2- Mechanisms on PGMs

2.2.1- The Langmuir-Hinshelwood mechanism

Despite the simplicity of the CO oxidation reaction in the presence of O_2, researchers have proposed more than 20 different steps that may occur during the process [41]. Among these, the Langumir-Hinshelwood (LH) dual-site mechanism is considered to be one of the most plausible mechanisms for low temperature CO oxidation on PGMs. It proceeds via the conventional three-steps scheme [42]: adsorption of the gaseous species (CO and O_2), diffusion over the surface, then reaction between adsorbed species and production of gaseous carbon dioxide as illustrated in Figure I-4.

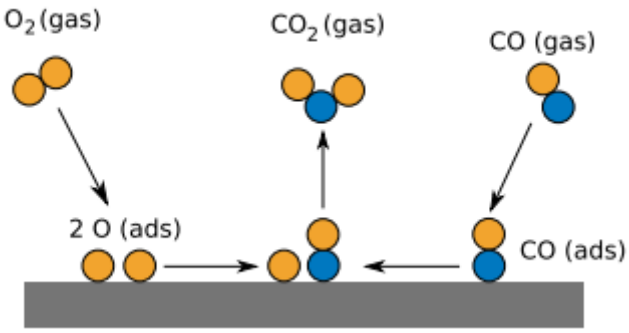

Figure I-4- Schematic of Langmuir-Hinshelwood mechanism [43].

An important aspect to consider is the availability of sites that can accommodate both reactants in close proximity where they can tend to strongly bind to reactive surfaces. This will lead to the formation of islands with reactive interfaces and pores in between [44].

The O_2 adsorption step in this mechanism is often considered to be the rate-limiting step [45]. Traditional PGM catalysts with inert supports such as SiO_2, Al_2O_3 and zeolites are inefficient at low temperature because of the significant competition between CO and O_2 adsorption and activation on the metal sites. CO is strongly adsorbed, which hinders O_2 adsorption and activation. By consequence high working temperatures (>100 °C) are required to weaken CO adsorption and facilitate O_2 adsorption [46, 47]. This makes CO oxidation less effective and is called CO poisoning.

2.2.2. The carbonate and alternative mechanisms

Particular attention has also been made on the adsorbed species formed on the catalyst surfaces during CO oxidation. Various adsorbed species, including linear and bridged carbonyls, as well

as carbonates, have been reported in the literature for PGMs based catalysts. However, the role and contribution of carbonates to the overall reaction mechanism are still subject of ongoing discussion and investigation.

Ackermann *et al.* [48] identified the presence of two active surface oxides on Pt(110) in their study. The first oxide, known as the incommensurate oxide, forms a hexagonal PtO_2 layer and has been observed during CO oxidation over Pt nanoparticles supported on Al_2O_3 [49]. The second reactive oxide, with a commensurate structure, has not yet been directly observed on high surface area nanosized catalysts. But the formation of this oxide requires the stabilization of an additional carbonate species according to their computational calculations. It is worth highlighting that this study marked the first instance where the presence of a carbonate species was specifically proposed as a potential reactive intermediate in the context of CO oxidation over platinum [50]. Later, Mose-Debusk *et al.* [51] proposed a catalytic cycle demonstrating the conversion of CO to CO_2 solely through isolated platinum (Pt) centers supported on θ-Al_2O_3 surfaces with participation of reactive carbonates formed at these atomically dispersed sites (Figure I-5).

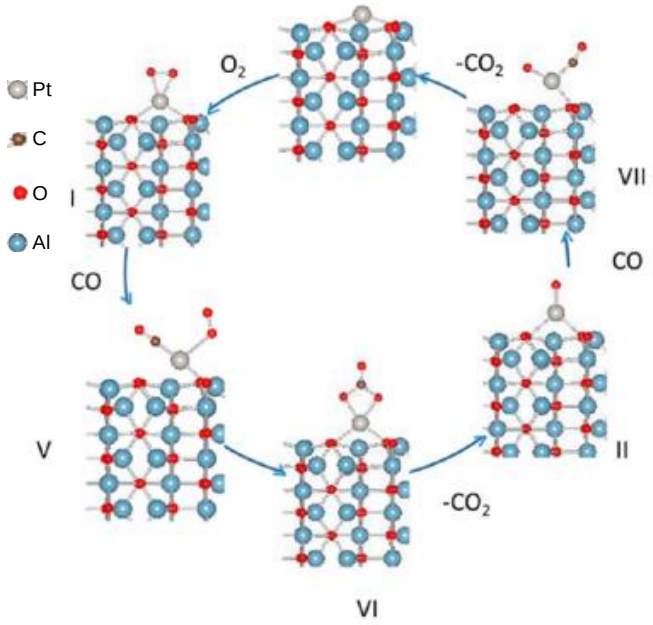

Figure I-5- Pathway for CO oxidation on single Pt Atoms supported on the (010) surface of θ-Al_2O_3 [51].

In Figure I-5, CO may add on the oxidized Pt atom supported on Al_2O_3 leading to the formation of an adsorbed bidentate carbonate. This carbonate species then undergoes decomposition, resulting in the release of CO_2 to form a new adsorbed PtO site. This latter can further react with a second CO molecule, leading to the release of a second CO_2 molecule and the regeneration of the initial atomic Pt species.

In complete contrast, recent research by Ding *et al.* [52] revealed that isolated platinum atoms present in zeolitic (H-ZSM5) and Al-doped SiO_2 supports acted as spectator sites in CO oxidation and water-gas shift catalysis at relatively low temperatures (373 K). Newton *et al.* have proposed in their study a room-temperature cyclic mechanism reaction, involving both carbonates and carbonyls (linear and bridged species) adsorbed on Pt for the CO oxidation (Figure I-6).

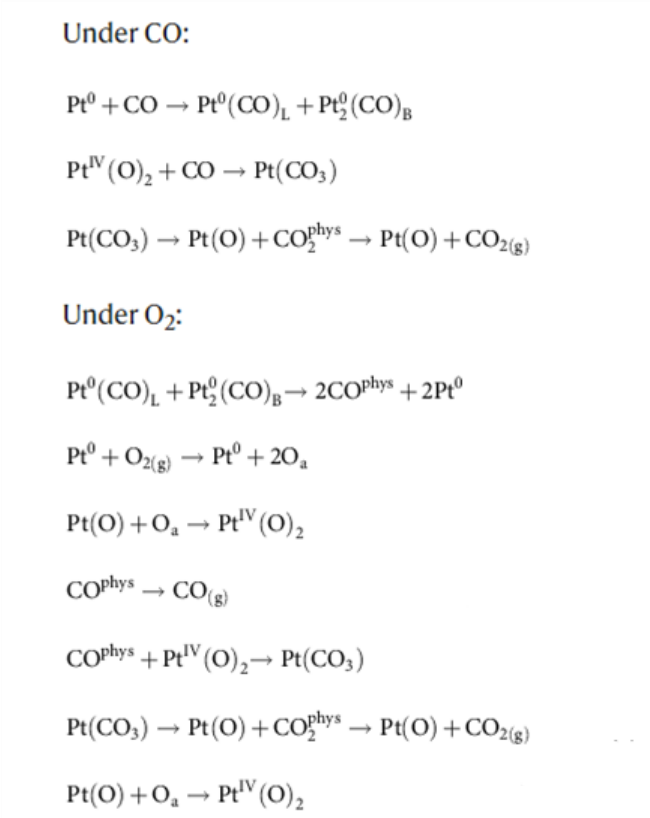

Figure I-6- Mechanism route proposed for the CO oxidation reaction with the involvement of linear and bridged carbonyls as well as carbonates [53].

The successful execution of the catalytic cycle relying on these Pt carbonates necessitates the active yet indirect involvement of the Pt nanoparticles, which constitute the majority of the Pt in the catalyst (estimated to be around 80%) [53]. In an another study from the same authors, they demonstrate using combined Mass spectrometry (MS), Diffuse reflectance infrared Fourier transform spectroscopy (DRIFTS) and X-ray absorption fine structure (XAFS) that the most active element for CO_2 production is a platinum carbonate characterized by a high wavenumber absorption band at 1690 cm^{-1} [50]. DRIFTS analysis confirmed the existence of Pt carbonates on Pt/Al_2O_3 catalysts with low loadings (0.18 and 1 wt%) but no specific investigations regarding the intrinsic activity of these Pt carbonates were conducted or discussed in the study.

Fottinger *et al*. have examined in their studies the formation mechanism of carbonates on Pd-alumina and Pd-zirconia catalysts using labelled $^{13}C^{18}O$ as reactant [54, 55]. They proposed, by examining the vibrational frequencies of carbonates and the stretching range of surface hydroxyl (OH) groups that carbonates are formed through the reaction of carbon monoxide (CO), adsorbed on support oxygen vacancy site, with surface OH species (Figure I-7) followed by immediate reaction of CO_2 with the oxide support.

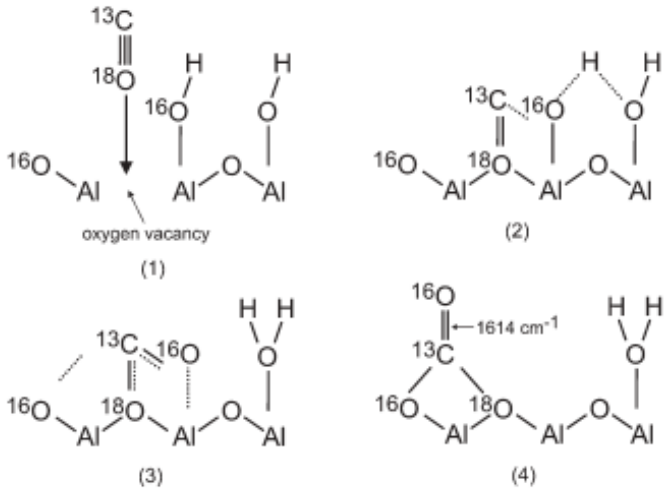

Figure I-7- Proposed reaction pathway for carbonate formation on Pd/Al_2O_3 [55].

Murata *et al.* have demonstrated the strong correlation between the fraction of Pd^0-CO_{linear} species and CO oxidation activity. They have thus shown that Pd corners and Pd(111) are highly active sites for this reaction [56]. The fraction of Pd^0-CO_{linear} species was found to be influenced by the shape and surface structure of the Pd particles supported on Al_2O_3. No information was mentioned about the observation and the role of carbonates.

Other pathways of carbonate formation were reported in literature. One mechanism involves the disproportionation of carbon monoxide (CO) on PGM noble metals leading to the formation of carbon dioxide (CO_2) and elemental carbon (Equation I-4).

$$2CO \rightarrow CO_2 + C \text{ (inverse Boudouard reaction)} \qquad \text{(I-4)}$$

The produced CO_2 can subsequently react with either O^{2-} ions or OH groups present on the alumina support to form adsorbed carbonates (CO_3^{2-}) or bicarbonates (HCO^{3-}), respectively [57, 58]. In the latter case, carbonates are not the source of CO_2 formation, but rather its consequence. However, numerous experimental and theoretical studies have indicated that the dissociation of CO on Pd is unlikely, even for CO pressures of up to 1 bar and elevated temperatures of approximately 500 K [59, 60].

Despite extensive discussions and debates in the literature regarding the formation of carbonates on the surface PGM/Al_2O_3 catalysts during the CO oxidation reaction, there is still a lack of clear information regarding the role of these species in the CO_2 formation. **Are they a source of CO_2 or the result of reabsorption? The question remains open.**

2.3- Hysteresis in CO oxidation reaction

Another interesting phenomena observed in CO oxidation reaction on PGM catalysts is its hysteresis behavior making it a fascinating subject of investigation [61]. Most experimental data on hysteresis reported in literature are limited and scattered, with a narrow range of catalysts and reactions being studied. Only a few studies have specifically focused on hysteresis during CO oxidation, linking it to the catalyst's structure and characteristics. This section aims to summarize the plausible interpretations of the hysteresis behavior during CO oxidation.

In heterogeneous catalysis, temperature hysteresis refers to a phenomenon where a reaction parameter, such as reaction rate or degree of conversion, does not match with increasing or decreasing temperature. This results in the creation of a **hysteresis loop**, where the ascending and descending branches of the conversion (%) vs. temperature plot do not align. In recent studies, a normal hysteresis behavior was observed during the heating-cooling cycles of CO oxidation reaction on Pt and Pd supported catalysts (Pt/Al_2O_3, Pd/Al_2O_3, Pt/CeO_2, Pd/$SiO_{2...}$) corresponding to higher conversions during extinction as illustrated in Figure I-8 [62–64]. Three distinct activity regions are reported during the hysteresis catalytic process: the first region exhibits low activity prior to the light-off temperature, characterized by CO adsorption on the catalyst surface. It’s followed by a region of high activity at higher temperatures after the light-off temperature. Finally, a region named as bi-stability is detected during the cooling phase before the light-out temperature.

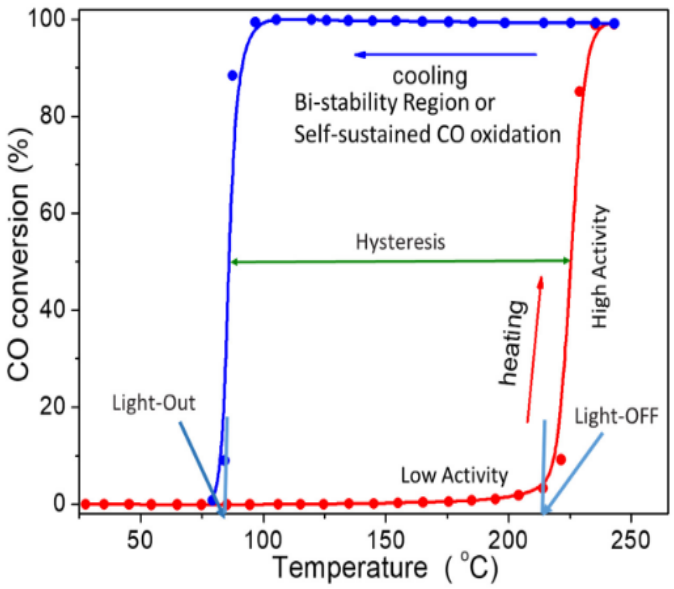

Figure I-8- Typical hysteresis during ignition (light-off) and extinction (light-out) of exothermic CO oxidation reaction [41].

As discussed before, Hauptmann *et al.* [65] proposed that the low activity of the ignition process could be attributed to CO poisoning and thus the blockage of active sites for dissociative oxygen adsorption at low temperatures. In contrast, the high activity of the catalyst during extinction could be explained by several factors reported in Table I-2 and described hereafter.

Table I-2- Origin of hysteresis hypotheses reported in literature.

Origin of hysteresis	References
Presence of multiple steady states	[66, 67]
Slow surface transition	[42]
Interaction between kinetics and intrapellet diffusion resistance	[68]
Isothermal multiplicity	[69–72]
Formation of CO islands	[73]
Thermal effect	[74, 75]

In literature, several hypotheses were discussed to understand the origin of hysteresis. It can be for example attributed to the presence of **multiple steady states** in a catalytic system where, during a gradual temperature change, one steady state is replaced by another state with different kinetic features. This will cause the reaction to proceed at a different rate even at constant reactor temperatures [66, 67]. Carlsson *et al.* have linked the occurrence of the hysteresis loop

on Pt based catalysts with the **slow transition** from an oxygen-enriched surface and platinum oxide formation, which is present during extinction, to a CO-covered surface including Pt reduction [42]. Another explanation was proposed by Hegedus *et al.* [68] involving the **interaction between CO oxidation kinetics and intrapellet diffusion resistance.** They discovered a widening of the hysteresis loop upon catalyst aging. This impact was linked to morphological variations caused by Pt particles sintering, which leads to different oxidation and reduction rates [42]. Chakrabarty *et al*. provided an explanation for hysteresis based on the **interference between surface reactions and sorption processes**. They proposed that the sorption of reactants on the catalyst surface plays a significant role in generating hysteresis behavior, leading to **isothermal multiplicity** [69]. Similar observations of multiplicity have been explained by (i) the competition of reactant sorption on Pt catalyst [70, 71] , (ii) the switching of CO complexation types on the catalytic surface, as well as (iii) the interaction between O_2 and chemisorbed CO [72]. The isothermal multiplicity can also be attributed to the alternation between active metallic Pt species and surface-oxidized Pt nanoparticles. Some authors have also suggested that the formation of hysteresis loops in CO oxidation can be attributed to the **formation of CO islands** on the catalyst surface [73]. More recently, Frank-Kamenetskii introduced the concept of temperature hysteresis in heterogeneous catalysis based on the macro-kinetic transition from **the kinetic mode to the diffusion mode** during hysteresis [76]. Finally, **thermal effects** are often associated to the hysteresis phenomenon in CO oxidation due to the highly exothermic nature of the reaction and the thermal inertia of the catalyst [41]. Subbotin and colleagues proposed that when the reaction rate reaches a certain level, the heat generated at the active reaction sites becomes too significant to be effectively dissipated into the surrounding environment [74]. Several factors can exacerbate this behavior such as poor heat conductivity of porous oxide supports or ineffective heat dissipation by inactive catalytic mass. As a result, the actual temperature at the active centers becomes higher than the average temperature of the catalyst bed, leading to local overheating and a higher conversion rate than expected at the measured temperature. When the heat source is turned off the excessive heat takes a longer time to dissipate maintaining a higher temperature at the active sites compared to the temperature measured by a thermocouple and by consequence a higher catalytic activity at lower temperatures during extinction [75].

Two types of hysteresis can be observed (i) the **normal** hysteresis as described above where the extinction activity is higher compared to the light-off step and (ii) the **inverse** hysteresis where the catalytic activity during ignition exceeded the activity during extinction. The latter

was observed in the case of CO, NO and C_3H_6 gas mixtures oxidation reaction on Pt supported catalyst (Figure I-9).

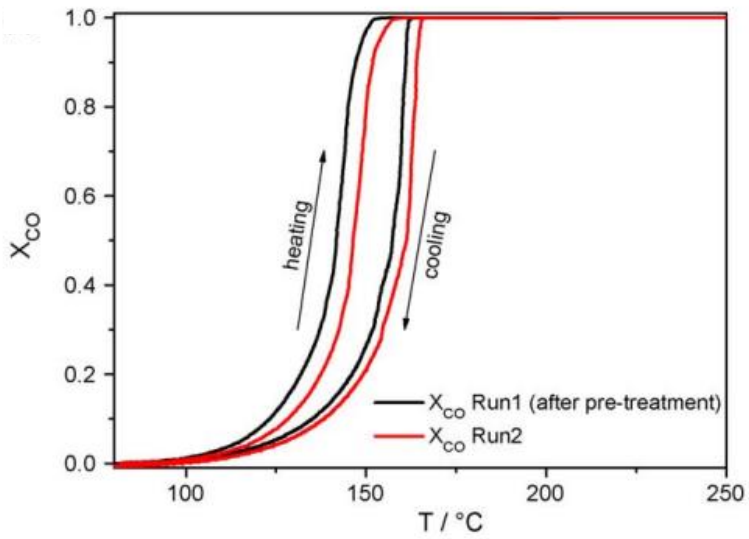

Figure I-9- CO conversion light-off and light-out cycles experiment in presence of NO gas mixture [77].

This inverse behavior was attributed to the high-temperature oxidation of Pt in the presence of NO or C_3H_6, leading to the formation of a less catalytically active oxide phase compared to metallic Pt. At low temperatures, the Pt oxide is then reduced back to metallic Pt [77]. In some cases, a switch from normal hysteresis to inverse hysteresis is even observed during the CO oxidation reaction, known as **reverse** hysteresis. Dubbe *et al* observed this trend using a $CO/NO/O_2$ mixture on Pd/Al_2O_3 catalysts attributing this result to the reversible oxidation of the Pd surface (Figure I-10) [78]. Other research has also reported reverse hysteresis of CO oxidation in case of unsupported catalysts, such as Pd/Ag alloys [79].

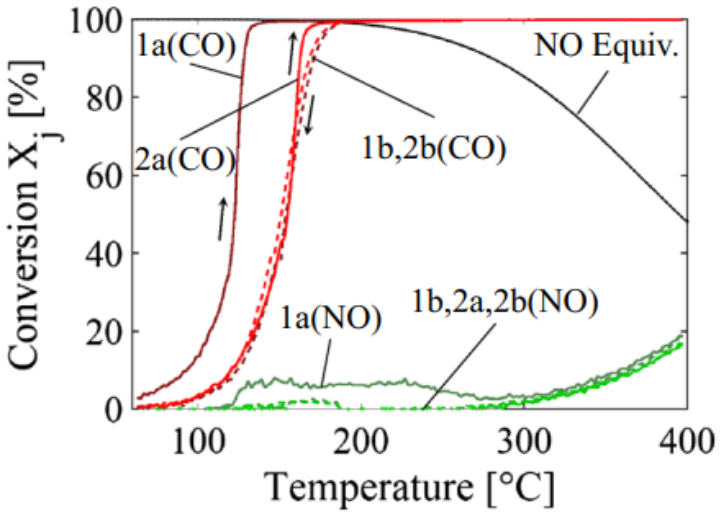

Figure I-10- Conversion curve in case of CO/NO/O_2 mixture on Pd/Al_2O_3 [78].

The hysteresis profile seems also very sensitive to different parameters as particle size, reactant concentrations inlet gas composition, pretreatment or support used. For example, Casapu *et al.* [80] conducted a study on the effect of Pt particle size distribution on hysteresis in CO oxidation over Pt/Al_2O_3 catalyst. Their findings revealed that the type of hysteresis strongly depends on the Pt particle size. Inverse hysteresis was observed for catalysts with very small Pt nanoparticles (<2 nm), while normal hysteresis appears for catalysts with larger Pt nanoparticles as illustrated in Figure I-11. This difference in hysteresis behavior was attributed to various factors, including different strengths of CO adsorption at the surface and bulk of the catalyst, oxidation of Pt nanoparticles, regeneration of the catalyst's active sites and the exothermic nature of the CO oxidation reaction.

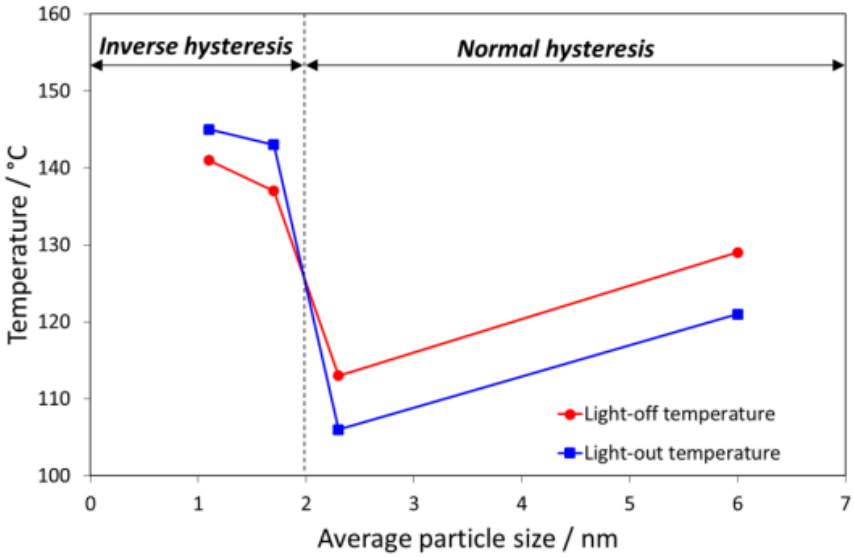

Figure I-11- Light-off and light-out temperatures vs. average Pt particle size during CO oxidation on Pt/Al_2O_3 catalysts [80].

The impact of the inlet gas stoichiometric ratio of CO and O_2 on catalyst behavior has been studied and recent findings suggest that it can influence both the conversion profile and the dynamic behavior of the catalyst. Newton's work highlighted the dependence of the hysteresis effect on the O_2/CO ratio during CO oxidation over Pt surfaces and supported catalysts like Pt/Al_2O_3. The optimal ratio was found to be between 1 and 5, indicating that hysteresis behavior is most pronounced within this range [50]. Other studies focused on investigating the influence of CO concentrations at various inlet temperatures on hysteresis behavior (see Figure I-12). It was found that higher CO concentrations resulted in wider hysteresis loops due to CO self-inhibition [64, 81].

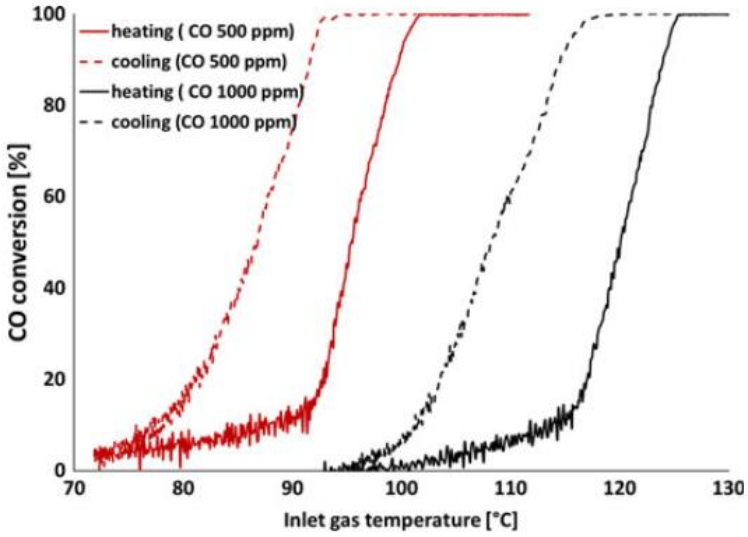

Figure I-12- Temperature-programmed CO oxidation with different concentration of CO [81].

In contrast, the width of hysteresis does not change upon varying the CO concentrations using Pt/CeO_2 monolith catalysts suggesting the effect of support on hysteresis profile [62]. The porosity of the catalyst support seems to influence the temperature hysteresis. For example , no hysteresis was observed in case of Pt supported on a non-porous titania catalyst (Pt/TiO_2) while Pt supported on porous silica (Pt/SiO_2) exhibits a hysteresis behavior for CO oxidation [82]. The pretreatment of catalyst samples can also affect the hysteresis loop as shown by Schalow *et al.* who observed a slow hysteresis effect and reduced activity during CO oxidation on preoxidized Pd nanoparticles vs. metallic ones [83]. Finally, the hysteresis profile is highly sensitive to the ambient atmosphere composition since a transition between normal and inverse hysteresis can be observed in more complex gas mixtures. For example, adding H_2O in a gas mixture containing CO increases the width of the typical hysteresis [64]. In contrast, when C_3H_6 is present, the normal hysteresis observed for Pt/Al_2O_3 catalyst in CO/O_2 mixture switches to inverse hysteresis. This behavior was attributed to the competition between the adsorption of C_3H_6 oxidation intermediates and CO on the active sites, particularly during the extinction phase of the reaction [81].

In conclusion, in the literature the phenomenon of hysteresis during CO oxidation has been the subject of a number of studies and different interpretations on its origin have been reported. Among possible explanations, some do not necessarily contradict each other but rather approach the problem from a macroscopic (e.g., mass and heat diffusion effects) or a microscopic (e.g., mechanistic and structural aspects) perspective. At this point it seems important to focus a little of our attention on PGM surface reconstruction phenomenon under

CO/O_2 atmosphere, which has been widely reported in the literature, in order to fully understand the plausible causes of hysteresis.

2.4- Surface reconstruction on PGM under CO/O_2 atmosphere

2.4.1- Reconstruction on Pt surface

Under certain conditions, the active phase of the catalyst can form during the reaction as a result of exposure to one of the reactants. For example, in the presence of an excess of O_2, a noble metal catalyst can form an oxide surface that can be consumed by CO to produce CO_2 and create an oxygen vacancy, O_v. After that, the active surface is regenerated by filling O_v with O_2 gas. This process is known as the Mars-van Krevelen (MvK) mechanism [84]. Same type of behavior can occur with platinum single crystal under CO/O_2 exposure in a different mechanism where volatile Pt(g) and CO_2 are created by the reaction between PtO_2 and CO. The oxide is restored by the reaction of Pt(g) with O_2, forming PtO_2(g) and then PtO_2(s) [85]. This proposed mechanism can account for the loss of metal and a surface retexturing effect in a catalyst, although it occurs at a very slow rate.

The different surfaces of Pt have been observed under CO/O_2 reaction conditions showing different behaviors [86, 87]. Ackermann *et al.*[48] have determined the structure evolution of **Pt (110) surface** under CO oxidation conditions (up to 0.5 bar and 625 K) using X-Ray diffraction (XRD). They observed 3 well defined structures according to the CO/O_2 ratios: (i) the bulk-terminated Pt(110) surface, (ii) the commensurate oxide, and (iii) the incommensurate oxide. According to their results, these two latter oxides, illustrated in Figure I-13 below, have much higher catalytic activity than the metallic surface. Interestingly, the commensurate oxide only appears at high temperature under CO/O_2 mixture, stabilized by carbonate ions as suggested by density functional theory (DFT) calculations.

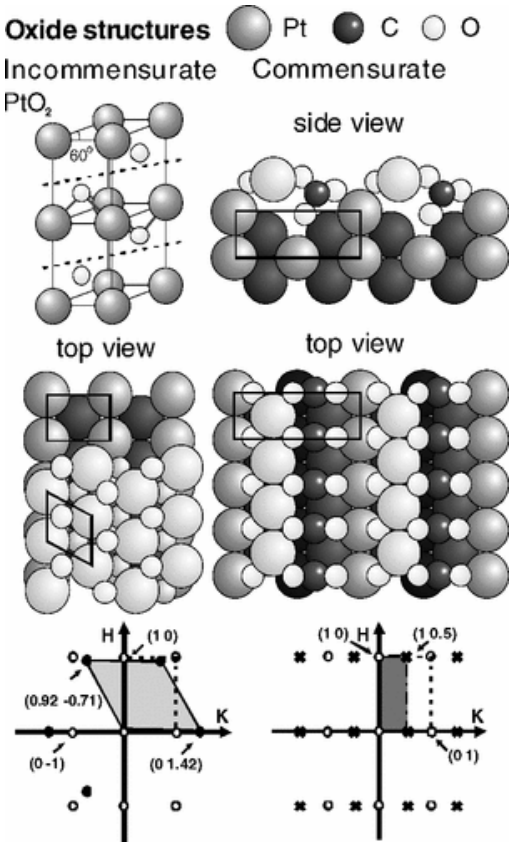

Figure I-13- Pt oxide structures formed under CO oxidation reaction condition from Pt (110) surface as observed by XRD [48].

Goodman *et al.* [88, 89] don't agree with previous conclusion regarding the superior activity of Pt oxide compared to the reduced metal. At relatively high pressures (8 Torr of CO) and with stoichiometric or oxidizing CO/O_2 conditions they evidenced 3 reaction regimes as represented in Figure I-14:

(i) T<575 K: a CO-inhibited metallic regime displaying a low CO_2 formation rate limited by CO desorption.

(ii) 575-600 K: an oxygen-rich metallic regime with a high CO_2 formation rate,

(iii) T> 600 K, a high-temperature regime where the CO_2 formation rate is either mass transfer limited (limitation of CO diffusion to the sample) on the metallic surface or limited by the reduced reactivity of the oxidized surface. To interrupt this regime and slow down the reaction rate, the sample must be cooled to 525 K or less to allow CO to repopulate the surface.

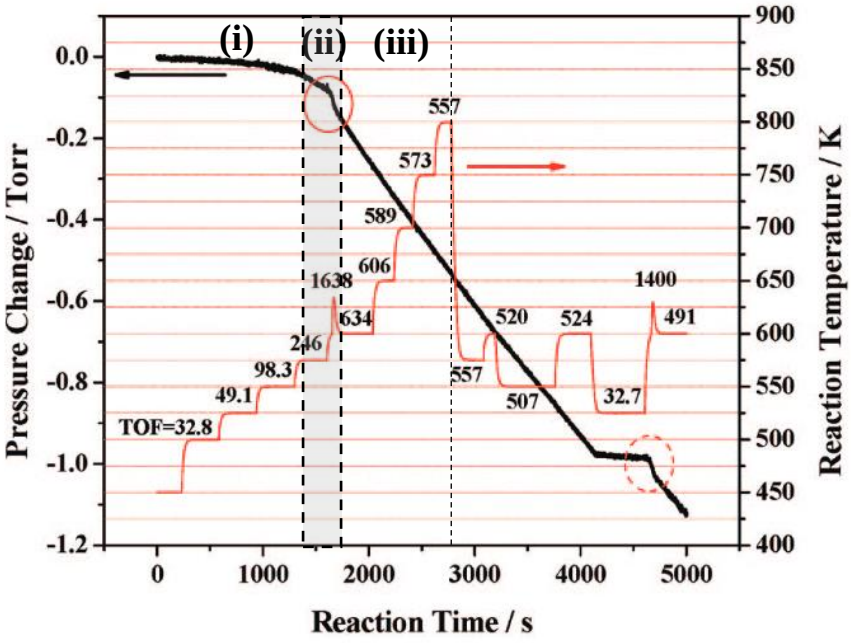

Figure I-14- Gas-phase pressure change (black line) as a function of time and reaction temperature (red line) associated with corresponding TOF values over PGM single crystals (O_2/CO=1/1 ; CO pressure =8 Torr). Adapted from [88].

Concerning the activity of the oxidized Pt(111) surface towards CO oxidation, the literature presents also conflicting results. Weaver *et al*. [90] suggest that the oxidized Pt(111) surface exhibits lower activity compared to the metallic phase consistent with conclusions drawn by Goodman *et al*. for Pt(110) surface. In contrast, other authors suggest that Pt-oxide on Pt(111) constitutes a highly active phase in the CO oxidation contrary to a low–active metallic phase [91, 92]. The authors argued that the low activity of the metallic phase is due to a partially CO-poisoned surface with islands of adsorbed O. The low-activity regime transitioned abruptly to a higher activity regime, in which Infrared of Reflexion-Absorption Spectroscopy (IRRAS) revealed the absence of CO on the surface, leading the authors to conclude that the surface was fully covered with O [92]. In another study, the Pt (111)-rich film have been oxidized with O_2 forming PtO_2 layer, where CO consumed immediately the oxide leaving the Pt surface in the metallic state. This experiment demonstrated that when most of the CO had reacted, the catalyst transitioned to a state of higher reactivity under more oxidizing conditions and simultaneously PtO_2 was formed. This indicates that PtO_2 is an active catalyst for the oxidation of CO [93].

The Pt(100) surface has not been extensively studied under realistic chemical conditions. In an *operando* scanning tunneling microscopy (STM) study, the surface was exposed to CO, O_2 and mixtures of both at pressures of 100-125 kPa at 365-423 K [94]. When starting with a pure CO atmosphere, the reaction kinetics revealed a peak in CO_2 production upon increasing the O_2

concentration. This was attributed to a surface transition from CO-poisoned to an optimally covered surface with a CO/O ratio. As the mixture became increasingly O_2-rich, the reactivity declined due to insufficient CO reaching the O-covered surface. However, small increases in reactivity were observed, similar to Pt(111) and Pt(110) surfaces, attributed to an oxidation of the surface of unknown structure. These jumps in reactivity were not consistently observed and could be affected by the surface's history, such as reaction-induced roughness or polishing-induced roughness via the formation of platinum carbonyls [95]. The behavior of Pt(100) surface toward CO/O_2 atmosphere appears complex but it is worth to note that it is also the most reactive surface for the Boudouard reaction (Equation I-4).

Finally, supported Pt catalysts also revealed two activity regimes: (i) low-activity due to CO poisoning at low temperature and (ii) high activity at low CO concentration and high temperature. On the basis of in-situ X-ray absorption spectroscopy (XAS), the high activity phase was ascribed to a defect-rich platinum oxide [96]. The depletion of carbon monoxide at high activity allows oxygen to interact with the surface and enhances the catalytic activity by changing the rate-limiting step.

In summary, both Pt(111) and Pt(110) surfaces switch to higher reactivity under O_2-rich conditions and at the same time, a new structure is formed on both surfaces. PtO_2 was also observed to form on both surfaces after depletion of CO but this oxide formation did not affect the reactivity which remained in the mass transport limitation regime. This suggests that PtO_2 could be active, either through defects in the oxide or at the boundary between the oxide and adsorbed CO islands on the reduced metallic Pt surface. Under reaction conditions, the behavior of the Pt(100) surface was found to be complex and dynamic patterns were observed. However, certain uncertainties still persist, such as the nature of the active phase under O_2-rich conditions if it is chemisorbed O on a metallic surface or on a surface oxide. While the STM study suggested that it might be a surface oxide, the atomic structure of this oxide is entirely unknown.

2.4.2- Reconstruction on Pd surface

Compared to Pt, palladium (Pd) has a higher tendency to undergo oxidation. The resulting palladium oxides are more stable at and below room temperature. Majority of the investigations have centered on Pd(100) surface as a model catalyst using various techniques including X-ray Diffraction (XRD) [97, 98], STM [99], X-ray Photoelectron Spectroscopy (XPS) [100] and IR spectroscopy [101].

Blomberg *et al.* [100] have conducted *in situ* XPS experiments to study the CO oxidation reaction over Pd(100) surface. They concluded that the catalytic activity of Pd at near-stoichiometric pressure ratios can be explained by the presence of two distinct states: (i) a CO-poisoned inactive state at low temperatures and (ii) a highly active state with a high coverage of chemisorbed O above the activation temperature. This result was consistent with the finding of Frenken *et al*. [99, 102, 103] that the oxide phases are reactive for CO oxidation reaction over Pd(100) surface, which obeys the MvK mechanism.

As for Pt, the IRRAS measurements made by Goodman *et al*. [89] provide the main foundation for the argument against the surface oxide as the active phase on the Pd(100) surface. Their measurements revealed the presence of three distinct phases. The first phase was characterized as a CO-poisoned surface with low reactivity at low temperatures. As the sample was heated a "hyperactive" transient phase appears, followed by a decrease in turnover frequency (TOF). In the third regime, the surface is thought to be deactivated due to the presence of an oxide. The "hyperactive" regime observed in the study was attributed to a metallic surface covered with adsorbed oxygen, although no specific evidence was provided to support this conclusion. Similar trends and behaviors were observed for the Pd(111) and Pd(110) surfaces in the study. Chen *et al*. [101] conducted further investigations using an IRRAS setup capable of reaching low wavenumbers, down to 450 cm^{-1}, to investigate the presence of metal oxide bonds in PdO. In their experiment, started with a reduced surface, they didn't observe the vibrational signatures of the oxide developing, even after the surface transitioned to a state of higher activity. These findings suggest that PdO may not be present on the active Pd(100) surface.

The oxidation process of the Pd(111) surface is similar to that of the Pd(100) surface, albeit with the formation of a distinct surface oxide. Toyoshima *et al*. investigated the oxidation of Pd(111) and the oxidation of CO using near-ambient pressure XPS combined with differential-pumping MS technique at three different temperatures [104]. Their results are resumed in Figure I-15 illustrating the formation of different species and their reactivity to form CO_2. They found that at a relatively low temperature (200 °C), the metallic Pd surface is present but poisoned by CO molecules leading to a low reaction rate. In the same study at 300 °C, they observed a significant increase of the reaction rate with formation of a surface oxide probably in the form of Pd_5O_4. Two oxygen species with different coordination numbers (3 and 4) exist in this surface oxide but the authors found that only the 3-coordinated species was reactive. A formation of cluster oxide also takes place during the reaction, but it is not reactive and instead

hinders the reaction on the surface oxide. At higher temperatures (400 °C), a PdO bulk oxide is formed which is less reactive compared to the surface oxide.

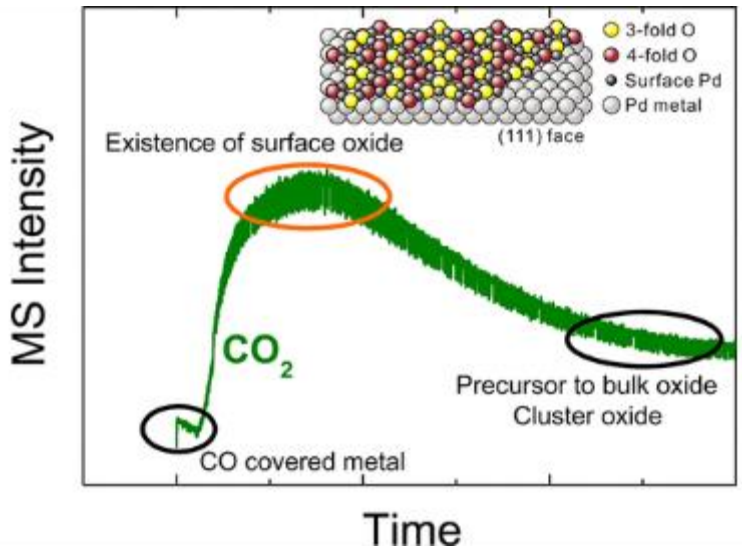

Figure I-15- Different species formed during CO oxidation on Pd(111) surface [104].

In contrast to the Pd(100) and Pd(111) surfaces, the Pd(110) surface has received far less interest. Berlowitz *et al.* performed a detailed kinetic analysis of CO oxidation on the Pd(110) surface in the pressure range of 0.1–800 hPa [105]. The comparison between the *in situ* deactivated samples and those deactivated by pre-oxidation led to the hypothesis that the formation of an oxide occurred, which blocked the active sites involved in the reaction. However, above 475 K, the oxide exhibited greater activity compared to the reduced surface covered with CO. Chen *et al*. have highlighted that the oxygen-covered (1 monolayer) Pd surface, called "hyperactive" surface, presents the highest activity in CO oxidation. In contrast, under stoichiometric CO/O_2 conditions and similar temperatures and pressures, Pd surface filled with chemisorbed CO exhibits much lower activity [106]. Toyoshima *et al*. conducted an investigation of the catalytic CO oxidation reaction on a Pd(110) surface under sub-Torr steady-state conditions using a near-ambient pressure XPS system and MS [107]. They found that below a critical temperature (<165 °C), the rate of CO_2 formation was relatively low. XPS spectra indicated that the metallic Pd surface was predominantly covered with CO molecules, resulting in CO poisoning at lower temperatures. Above the critical temperature, CO molecules completely disappeared, and the surface was dominated by chemisorbed oxygen species. A small amount of PdO bulk oxide was also observed on the surface. As temperatures increased further, the quantity of chemisorbed oxygen decreased, and the rate of CO_2 formation decreased as well. These findings suggest that the presence of chemisorbed oxygen is associated with the catalytic activity via a Langmuir-Hinshelwood mechanism.

The reactivity of PdO(101) toward CO oxidation was investigated by Zhang *et al.* through temperature-programmed reaction spectroscopy, IRRAS and DFT experiments [108]. Following CO(ads) saturation at 95 K, it was observed that 71% of the CO underwent a reaction when the temperature was increased to 650 K, resulting in the formation of CO_2, while the remaining CO desorbed from the surface. The authors showed that CO molecules initially adsorb on coordinatively unsaturated (cus) Pd sites of PdO(101) located next to O_{cus} atoms leading to a IR peak at 2135 cm^{-1}.

Graham *et al.* studied the surface evolution of a polycrystalline Pd film using spectroscopic ellipsometry during the transient CO oxidation reaction [109]. They observed the formation of dense PdO layers when using lean conditions while a stable metal surface is observed under rich conditions (Figure I-16). Moreover, a large hysteresis in the conditions for PdO formation was observed as well as spontaneous oscillations in catalytic activity and surface composition. Their results suggest that the PdO-terminated surface can exhibit enhanced activity compared to metallic surface. After undergoing multiple oxidation-reduction cycles the oxidized surface is even more stable. An oscillating activity was also observed for the metallic surface, transitioning between a state predominantly covered with chemisorbed O(ads) (high activity) and another state predominantly covered with CO(ads) (low activity).

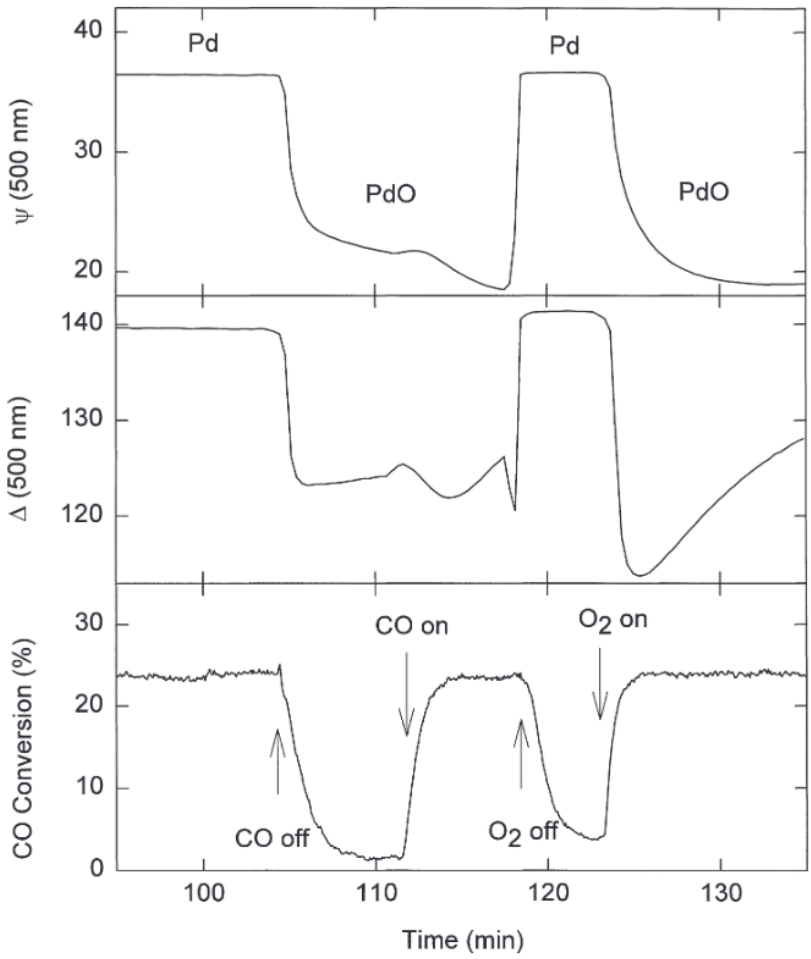

Figure I-16- Ellipsometric angles Δ and ψ (in degrees) and corresponding CO conversion over Pd surface at 440 °C (1% CO/2.5% O_2 in N_2) [109].

Based on IRRAS measurements performed on a Pd foil, it was further confirmed that an active surface covered with chemisorbed O(ads) may be present. The experimental results obtained on the foil were similar to those observed on single crystals. Under CO-rich reaction conditions at 500 K, CO(ads) was initially detected and the formation of CO_2 was limited. However, as the CO concentration decreased, the reactivity increased, and CO(ads) became undetectable. Interestingly, no vibrational signatures of Pd oxide were observed during this process [101]. These findings support the notion of an active surface primarily covered with O(ads).

To summarize on the reconstruction surface on Pd, various types of oxides have been identified under reaction conditions in the case of the Pd(100) surface and similarly on the Pd(111) surface. The reactivity increases significantly with the formation of these Pd oxides. In contrast, it has been observed that no surface oxide forms on the Pd(110) surface. Instead, layer of surface adsorbed oxygen with a comparable O coverage develops. The oxidation of Pd surfaces can occur as consequence of the active catalyst consuming CO from the gas phase, leading to a

highly oxidizing local environment. Furthermore, surface oxidation contributes to enhanced reactivity by providing additional reactive oxygen atoms. The enhanced reactivity of the oxides may be explained by intrinsic or MvK reaction-induced flaws in the oxide, which can bind CO considerably more easily under reaction conditions.

3- The SSITKA-IR technique to study CO oxidation mechanism

3.1- Introduction

Due to its critical significance in numerous catalytic processes and environmental applications, the CO oxidation reaction has been the focus of extensive debate and investigations. Many physical and/or chemical activities, such as diffusion, adsorption/desorption, surface reconstruction or hysteresis that take place at the interface between the catalyst surface and the reactants can have both positive and negative effects on the catalytic performance [110]. The origin of hysteresis remains a topic of great interest and contention in the literature, leading to diverse interpretations and theories regarding its underlying cause. Furthermore, the interplay of CO and O_2 on the catalytic surface adds another layer of complexity. The presence of CO can induce surface reconstructions, influencing the catalytic activity and altering the reaction pathways. This has led to contrasting perspectives among researchers, with some attributing the highest activity for CO oxidation to the presence of an oxide phase of the catalyst, while others emphasize the role of the metallic phase. Thus, understanding the mechanism occurring on the catalyst surface and the various pathways in which it is involved become critical. This requires the use of in-situ techniques to determine site reactivity and to characterize the chemical composition and structure of both the catalytic active surface sites and the accommodated adsorbed reaction intermediate species [111].

In this section, we will explore the principle, limitations and examples of Steady-State Isotopic Transient Kinetic Analysis coupled to IR Spectroscopy (SSITKA-IR). This advanced in situ technique offers a powerful approach to investigate surface kinetics and gain valuable information about reaction mechanisms, the nature of surface-adsorbed reaction intermediates formed, and their evolvement in reaction mechanism. By elucidating the principles and outlining the limitations, we can appreciate the potential of SSITKA-IR and its significance in overcoming challenges related to understanding the CO oxidation mechanism.

3.2- Principles and parameters of SSITKA

The Steady-State Isotopic Transient Kinetic Analysis (SSITKA) is one of the most powerful techniques to obtain valuable information on catalyzed heterogeneous reactions. This technique, firstly developed by Happel [112], Bennett [113], and Biloen [114], combines the advantages of both steady-state and transient techniques and has been applied in several research studies as a means of obtaining real-time information on both reaction mechanisms and the intermediate species involved in catalyst-surface reactions [115–118].

The SSITKA method involves the abrupt substitution of a reactant (R) with its isotope (*R) in a way that has minimal impact on the overall system [119]. Throughout the process, the partial pressures of reactant components, the temperature, and the space velocity are maintained at constant levels [120, 121]. Consequently, the overall reaction remains unchanged, while the isotope component is transferred from the reactant molecule to the various reaction products (P→*P) through multiple active reaction intermediates. Using stable isotopes in this process enables direct *in situ* evaluation of forward and reverse reaction rates of individual elementary reaction steps as well as the determination of surface concentrations of truly active reaction intermediates [122]. The reaction feed and the resulting products are usually analyzed and quantified by gas chromatography (GC) and mass spectrometry (MS).

Based on the normalized gas-phase transient isotopic response curves (Z(t)) obtained from MS, as illustrated in Figure I-17, various intrinsic kinetic parameters can be determined and enable us to understand the reaction mechanism at a near to molecular level under realistic, steady-state conditions.

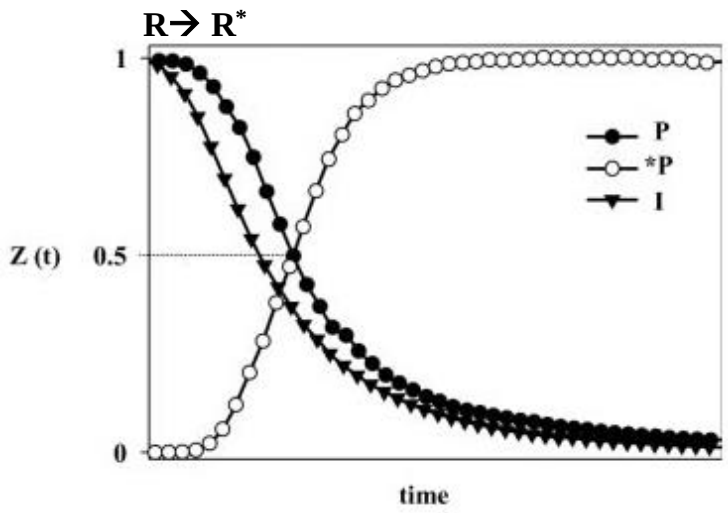

Figure I-17- Representation of normalized transient response curves of unlabeled product P, labeled product *P and inert tracer I during R→*R reactant isotopic switch à t=0. Adapted from ref[111].

If there are no disturbances in the reaction system, such as changes in flow rate, pressure or temperature, and no mass isotope effects, then the transient response curves of unlabeled product noted $Z_p(t)$ and of labeled product $Z_P^*(t)$ functions will be symmetrical and intersect each other at Z=0.5 as shown in Figure I-17. The Z_I (t) function reflects the transient response curve of an inert tracer introduced in the gas feed (e.g. He, Kr, Ar…). In SSITKA experiment, this inert tracer is introduced in a small amount to either of the isotopic-tracer feed streams during the step change allowing to estimate the gas-phase holdup in the reactor system [119]. The initiation of the inert-tracer transient response is typically considered as the start time of the transient experiment (t_0).

The SSITKA results allow precise quantification of the overall mean surface-residence time (τ_p) and the concentration (N_p) of all the adsorbed intermediates that are found in the reaction path from the reactant to the given final product. An advantage of SSITKA is that the latter parameters are accurately obtained without the need to make assumptions regarding the underlying kinetics or mechanism, such as the order of the reaction, the irreversibility of the reaction, or the composition of the reaction pathway [123].

The mean-surface residence time τ_p of intermediates is equivalent to the area between the product $Z_p(t)$ and the tracer $Z_I(t)$ transient response curves expressed by the integral formula of equation (I-5):

$$\tau_P(s) = \int_0^{t_{s.s}} [Z_I(t) - Z_P(t)]\, dt \qquad \text{(I-5)}$$

This statement suggests that the estimation of τ_p is not dependent on the micro-kinetic model or reaction path. It is based on the measured $Z_p(t)$ time response curve, which reflects the prevailing microkinetic and reaction mechanism being studied [111].

The concentration of all adsorbed reaction intermediates (N_p), leading to the formation of product P, is estimated based on the integral between the experimental response curves of the product and inert gaz ($Z_p(t)$ and $Z_I(t)$) and the material balance using equation (I-6):

$$N_P(mol\ g_{cat}^{-1}) = \frac{F_T\ Y_p^f}{W} \int_0^{t_{s.s}} [Z_I\ (t) - Z_P(t)]\ dt \qquad \text{(I-6)}$$

Where Y_p^f is the steady-state concentration (mole fraction) of product P measured experimentally under the non-isotopic reaction feed, W is the amount of catalyst used (in g) and F_T is the total molar flow rate (in mol s^{-1}). Otherwise, N_p can be expressed by equation (I-7) where r_p represents the steady-state rate of formation of P (mol g^{-1} s^{-1}).

$$N_p = \tau_p \,.\, r_p \qquad \text{(I-7)}$$

The corresponding **surface coverage of intermediates (θ)** over the exposed active phase can further be determined according to the following relationship:

$$\theta = N_p \,/\, N_{active\ sites} \qquad \text{(I-8)}$$

Finally, **the *SSITKA* turn over frequency (TOF_{ITK})**, which represents the number of product molecules produced per catalytic site per unit of time for a given temperature, can be determined. This TOF_{ITK}, also written k, has the particularity of being based on the number of *true* active sites determined by SSITKA according to equation (I-9), assuming a pseudo-first-order of reaction [119, 124]. Conversely, the TOF_{chem} calculation carried out on supported metal catalysts is typically based on a number of active sites ($N_{active\ sites}$) equivalent to the metal dispersion obtained by separate chemisorption measurement [124, 125]. While TOF_{chem} can provide valuable information about the catalytic activity of the metal, it may not accurately represent the true site activity.

$$TOF_{ITK}(s^{-1}) = \frac{r_p}{N_p} = \frac{1}{\tau_p} = k \qquad \textbf{vs.} \qquad TOF_{chem}(s^{-1}) = \frac{r_p}{N_{active\ sites}} = \frac{1}{\tau_p}\theta = k\theta \qquad \text{(I-9)}$$

It is worth noting that assumption is made which assumes that for each adsorbed reaction intermediate identified in the catalytic cycle, there is one corresponding active site [111]. However, this assumption does not discriminate between the different types of active sites, such as the number of surface metal atoms comprising the active site.

3.3- Mechanistic models of SSITKA

In SSITKA, the catalyst surface is viewed as collection of interconnected compartments or pools, with each pool representing a uniform or well-mixed subsystem within the reaction pathway that corresponds to a distinct adsorbed active reaction intermediate species [126]. It is also assumed that there is no mixing time associated with each pool except for the main residence time of surface adsorbed intermediates. Figure I-18 illustrates this SSITKA model with n pools in series where R, *R, P, *P, A and *A stand for the reactant, product and intermediates species or their labelled counterparts, respectively [119]. As previously described above, N_i^A and N_i^{*A} represent the concentration of unlabeled and labeled intermediates in each individual pool (i=1,2,…n), where the overbar "¯", if present, indicates a steady-state condition. Before the SSITKA switch (Figure I-18*a*), $\overline{r}_a^R/\overline{r}_{a-}^R$ and $\overline{r}_d^P/\overline{r}_{d-}^P$ are the respective steady-state rates of adsorption/desorption of reactants and desorption/re-adsorption of products while $\overline{r}_i^A/\overline{r}_{i-}^A$ are the steady-state transfer rates ("-" subscript indicates the reverse way) between pools of intermediate species. Then, in steady-state regime the following relationship holds:

$$\overline{r}_a^R - \overline{r}_{a-}^R = \overline{r}_i^A - \overline{r}_{i-}^A = \overline{r}_d^P - \overline{r}_{d-}^P \qquad \text{(I-10)}$$

Now considering at t=0 (Figure I-18*b*), the reactant R is suddenly replaced by its isotope *R. During the SSITKA switch, all intermediate A and product P species are progressively and ultimately totally replaced by their labelled counterpart *A and *P (Figure I-18*c* and Figure I-18*d*). During this process, the distribution of isotopes strictly depends on the intrinsic steady-state transfer rates $\overline{r}_i^A$ between pools and the intrinsic reactivity associated with each intermediate.

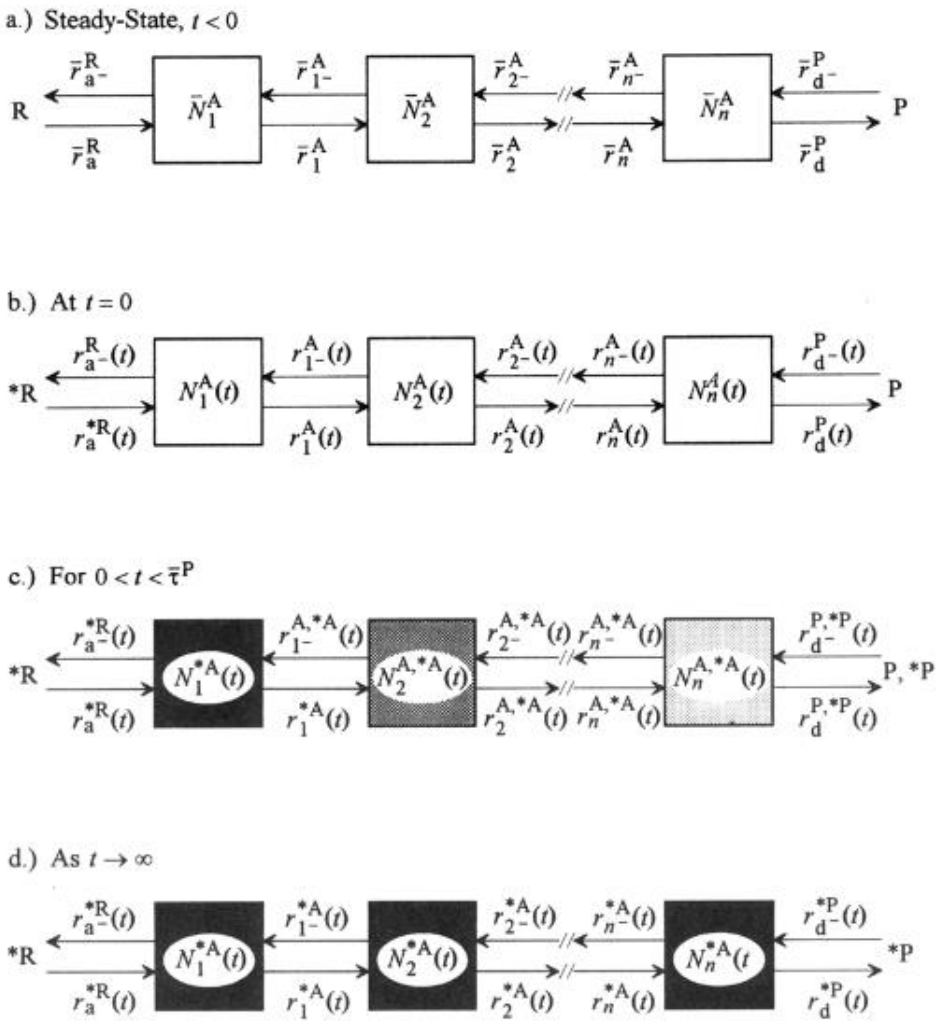

Figure I-18- SSITKA model of n pools in series showing the isotopic distribution of reactants R, intermediates A and products P: a) before and b-d) during R→*R switch [119].

As defined in previous section, the concentration N_P and the mean surface residence time τ_p of the overall intermediate species are the 2 general parameters that can be determined using the SSITKA model without the need to make any assumption about the underlying kinetics or mechanisms. However, additional specific kinetic parameters can be calculated from different mechanistic models based on assumptions on the nature of the reaction (reversible or irreversible), the type of adsorption (reversible or irreversible) and type of pools system (single/multiple in series/multiple in parallel). The development of several models based on transient isotopic tracing has enabled the determination of crucial kinetic parameters in heterogeneous catalysis, which includes reversible reaction paths [127]. Table I-3 shows six "simple" mechanistic catalyst-surface models, together with the formulae for the associated transient response (F(t)) and kinetic parameters.

Table I-3- SSITKA mechanistic models with associated transient responses and kinetic parameters [119].

Model	Transient Responses and Kinetic Parameters
1 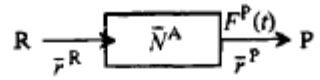	$F^{P}(t) = \exp(-t/\bar{\tau}^{A})$ $\bar{\tau}^{P} = \bar{\tau}^{A} = \left\{\frac{\bar{r}^{P}}{\bar{N}^{A}}\right\}^{-1} = \frac{1}{k}$ $\bar{r}^{P} = \bar{r}^{R}$
2 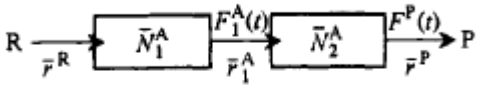	$F^{P}(t) = \frac{\bar{\tau}_1^{A}}{\bar{\tau}_1^{A}-\bar{\tau}_2^{A}}\exp(-t/\bar{\tau}_1^{A}) - \frac{\bar{\tau}_2^{A}}{\bar{\tau}_1^{A}-\bar{\tau}_2^{A}}\exp(-t/\bar{\tau}_2^{A})$ $\bar{\tau}_1^{A} = \left\{\frac{\bar{r}^{P}}{\bar{N}_1^{A}}\right\}^{-1}$ $\bar{\tau}_2^{A} = \left\{\frac{\bar{r}^{P}}{\bar{N}_2^{A}}\right\}^{-1}$ $\bar{\tau}^{P} = \bar{\tau}_1^{A} + \bar{\tau}_2^{A}$ $\bar{r}^{P} = \bar{r}^{R} = \bar{r}_1^{A}$
3 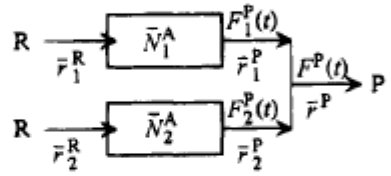	$F^{P}(t) = \bar{x}_1^{A}\exp(-t/\bar{\tau}_1^{A}) + \bar{x}_2^{A}\exp(-t/\bar{\tau}_2^{A})$ $\bar{x}_1^{A} = \frac{\bar{N}_1^{A}}{\bar{N}_1^{A}+\bar{N}_2^{A}}$ $\bar{\tau}^{P} = \bar{x}_1^{A}\bar{\tau}_1^{A} + \bar{x}_2^{A}\bar{\tau}_2^{A}$ $\bar{r}_1^{P} = \bar{r}_1^{R}$ $\bar{x}_2^{A} = 1 - \bar{x}_1^{A}$ $\bar{r}_2^{P} = \bar{r}_2^{R}$
4 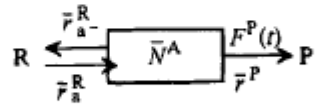	$F^{P}(t) = \exp(-t/\bar{\tau}^{P})$ $\bar{\tau}^{P} = \bar{\tau}^{A} = \left\{\frac{\bar{r}^{P}}{\bar{N}^{A}}\left(1 + \frac{\bar{r}_{a^-}^{R}}{\bar{r}^{P}}\right)\right\}^{-1}$ $\bar{r}^{P} = \bar{r}^{R} - \bar{r}_{a}^{R}$
5 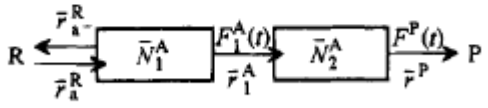	$F^{P}(t) = \frac{\bar{\tau}_1^{A}}{\bar{\tau}_1^{A}-\bar{\tau}_2^{A}}\exp(-t/\bar{\tau}_1^{A}) - \frac{\bar{\tau}_2^{A}}{\bar{\tau}_1^{A}-\bar{\tau}_2^{A}}\exp(-t/\bar{\tau}_2^{A})$ $\bar{\tau}_1^{A} = \left\{\frac{\bar{r}^{P}}{\bar{N}_1^{A}}\left(1 + \frac{\bar{r}_{a^-}^{R}}{\bar{r}_1^{A}}\right)\right\}^{-1}$ $\bar{\tau}_2^{A} = \left\{\frac{\bar{r}^{P}}{\bar{N}_2^{A}}\right\}^{-1}$ $\bar{\tau}^{P} = \bar{\tau}_1^{A} + \bar{\tau}_2^{A}$ $\bar{r}_1^{P} = \bar{r}_1^{R}$
6 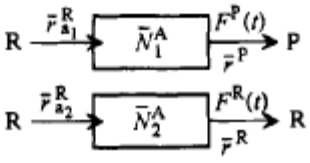	$F^{P}(t) = \exp(-t/\bar{\tau}_1^{A})$ $F^{R}(t) = \exp(-t/\bar{\tau}_2^{A})$ $\bar{\tau}^{P} = \bar{\tau}_1^{A} = \left\{\frac{\bar{r}^{P}}{\bar{N}_1^{A}}\right\}^{-1}$ $\bar{\tau}^{R} = \bar{\tau}_2^{A} = \left\{\frac{\bar{r}^{R}}{\bar{N}_2^{A}}\right\}^{-1}$ $\bar{r}^{P} = \bar{r}_{a_1}^{R}$ $\bar{r}^{R} = \bar{r}_{a_2}^{R}$

Briefly, the simplest and first model corresponds to an irreversible adsorption of the reactants occurring at a single type of catalytic site (single pool of adsorbed reaction intermediates). According to this model, the steady-state rate of reactant adsorption and product formation are equals: $\bar{r}^{R} = \bar{r}^{P}$ such that the surface residence time of the intermediate species ($\bar{\tau}^{A}$) can be expressed as equation (I-11):

$$\overline{\tau}^A = \frac{\overline{N}^A}{\overline{r}^R} = \frac{\overline{N}^A}{\overline{r}^P} \quad \text{(I-11)}$$

In model 4, an irreversible reaction proceeding by a single pool with reversible adsorption of the reactant is considered. In this case, the calculation of the steady-state reaction rate includes a term corresponding to the adsorption rate and the calculation of the surface residence time of the intermediates includes a term referred to the rate of desorption. Models 2 and 5 illustrate irreversible reactions that take place through multiple pools in series, where the output from the first intermediate pool serves as the input for the next one by taking into account reversible or irreversible adsorption of reactants, respectively. In such cases, the total surface residence time is determined by the summation of the residence time on each pool. Model 3 is relevant to catalytic surfaces that contain multiple sites with varying levels of activity, or multiple pathways leading to the same final product (multiple pools in parallel). Assuming all of these pathways are irreversible first-order reactions, the overall transient response is determined by the summation of an exponential function that is multiplied by the fractional number (x_i) of intermediates (N_i) in the i^{-th} pool at steady-state conditions. The overall surface residence time of the intermediates is calculated by summing up the residence time of each pool multiplied by the fractional number of intermediates present in that pool. Finally, model 6 represents the existence of two types of adsorption sites, one reactive and the other non-reactive, leading to 2 expressions similar to those in model 1.

By assuming that a reaction is pseudo-first order, the differences between the kinetic models can easily be distinguished by plotting the logarithmic behavior of the isotopic transient response of the product (Figure I-19).

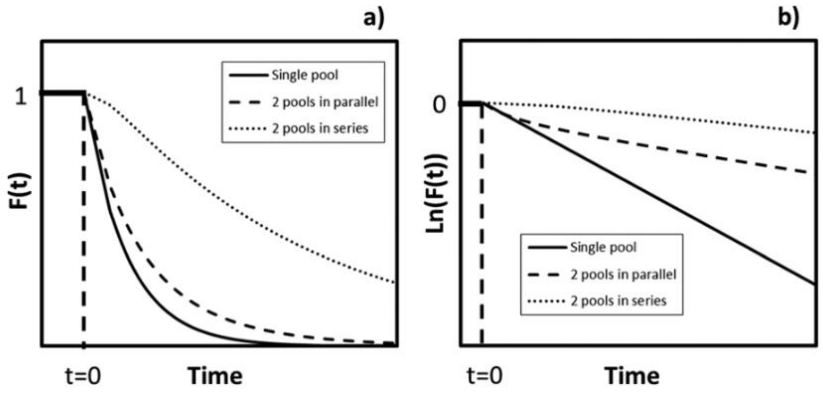

Figure I-19- Comparison of the transient response (a) and logarithmic transient response (b) of single pool, two pools in series and two pools in parallel models [110].

In contrast to the other two models, the series pool model does not show an immediate decrease after the isotopic switch at t=0. The variations between the multiple pools in parallel and single pool models are most easily observed in a logarithmic plot (Figure I-19b), where the single pool model is represented by a straight line, while the parallel pool model deviates from this line. This model derivation did not consider reversible reactions because interpretation of transient response became more challenging. In this case, numerical methods utilizing nonlinear least-squares regression have been created to obtain kinetic parameters for these reactions [127]. Otherwise, different limitations observed in SSITKA should be taken into consideration to have a good interpretation of the results and will be discussed in the next section.

3.4- Limitations and improvements

3.4.1- Reactant adsorption and product readsorption

Avoiding or interpreting the effects of re-adsorption in SSITKA can be challenging and problematic. Such effects can significantly impact the transient responses and interfere with determining the kinetics of the catalyst surface. When analyzing the composition change in the gas phase, it's essential to consider the adsorption of reactants, which can occur not only on the catalyst surface reservoir but also through the entire plug-flow reactor system. This adsorption will result in a chromatographic effect where the reactant will appear in parallel to the inert tracer but with a time delay. An alternative solution can help reduce this effect by increasing the space velocity of reactants but sometimes it cannot be completely avoided. The chromatographic effect can be considered negligible if the area between the response of the reactant and the inert is less than 20% of the area between the response of the product and inert [110]. In others cases, simplified corrections of chromatographic effect should be applied in the analysis of transient response [128].

If product re-adsorption occurs at the reactive sites, this can lead to a reduction in activity and reaction rate. In contrary, if the adsorption occurs at non-reactive sites, the activity remains unaffected. However, the abundance of surface intermediates leading to product will be the sum of both reactive and non-reactive adsorption sites. As a result, the mean surface-residence time attributed to the reaction will be overestimated, and the reactivity will be undervalued. Reducing the length of the catalyst bed or increasing the weight hourly space velocity (WHSV) can help to mitigate the effects of interparticle re-adsorption within the catalyst bed. Another solution is to add into the feed stream the unlabeled product which will annihilate the re-

adsorption sites for the labeled product formed during the reaction [119]. The latter approach has been applied by Goodwin and Ali who has introduced the unlabeled product into the methanol synthesis reaction feed on Pd/SiO_2 showing a halving of the τ(MeOH) value compared with usual reaction [129]. In another study, Calla *et al.* have cofeeded CO_2 in the CO oxidation reaction over Au based catalysts to introduce competitive adsorption and correct this effect [130].

3.4.2- Diffusion effect

Concentration gradients within the catalyst bed (interparticle) or within the catalyst particles (intra-particle) may arise due to diffusional effects, which can significantly impact the transient responses and cause interference with the determination of kinetic parameters associated with catalyst-surface reactions [119]. The presence of interparticle or external diffusional effects can be detected by varying the gas space velocity during experiment. However, intraparticle or pore diffusion can be more challenging to prevent. The latter is influenced by several factors such as gas diffusivity, reaction rate and stoichiometry, as well as catalyst properties like pore size, porosity and particle diameter. Small-sized catalyst particles or a nonporous support are preferred to eliminate intraparticle diffusional effect and obtain the true intrinsic reaction rate.

3.4.3- Isotopic effect

It is crucial to maintain steady-state conditions to obtain precise values of the kinetic parameters. Therefore, any isotopic effects on reaction conditions should be avoided. This is not the case for Hydrogen/Deuterium exchanges (H_2/D_2) due to the significant kinetic and thermodynamic differences resulting from the relatively large mass differences and bonding energies between hydrogen isotopes [119]. As a consequence, the kinetic rates and surface concentration may be significantly changed after this isotopic switch [131]. H_2/D_2 exchange can still be valuable for detecting bonds breakages within a particular molecular species during adsorption-desorption or reaction processes and gave better direct information about the number and activity of sites involved in the H_2/D_2 exchange process [132].

The isotopic effect is minimal when using $^{12}C/^{13}C$ or $^{14}N/^{15}N$ isotope couples in SSITKA experiments. However, the use of oxygen isotopic exchange ($^{16}O/^{18}O$) to determine kinetic parameters can be challenging for oxide catalysts or catalysts with oxide supports. This is because oxygen exchange can occur between the gas phase, the catalyst surface, and the catalyst bulk, which may cause the $^{16}O/^{18}O$ transient to not relax back to zero after this step change

[110]. The bulk oxide in the catalyst can serve as an oxygen source for exchange, complicating the analysis. In order to minimize oxygen exchange with the bulk, low temperatures need to be maintained during the SSITKA measurement [132]. Despite this challenge, Peil and co-workers were able to demonstrate that lattice oxygen diffusivity and total oxygen uptake can be quantified using SSITKA [133].

3.5- Coupling SSITKA with vibrational spectroscopic technique to study CO oxidation

3.5.1- Advantages of coupling SSITKA with Infrared spectroscopy

One drawback of the SSITKA technique is its inability to identify the nature of intermediate species. Thus, coupling SSITKA with a vibrational spectroscopic technique means that we can benefit from the advantage of both techniques to obtain kinetic information and identifying the structural properties of the surface-adsorbed active or inactive species at molecular level under the realistic steady-state conditions of the reaction. Moreover, a comparison between the isotopic exchange rate of the surface species measured by *operando* IR and the exchange rate of species in the gas phase measured by MS helps to distinguish active and spectator species (Figure I-20). If the exchange rate of surface species is as fast as the exchange of products in the reactor outlet, then the surface species can contribute to the main reaction pathway (I*/I = intermediate species). On the contrary, slower isotopic exchange or no exchange would indicate the detection of a spectator species (S*/S) [134].

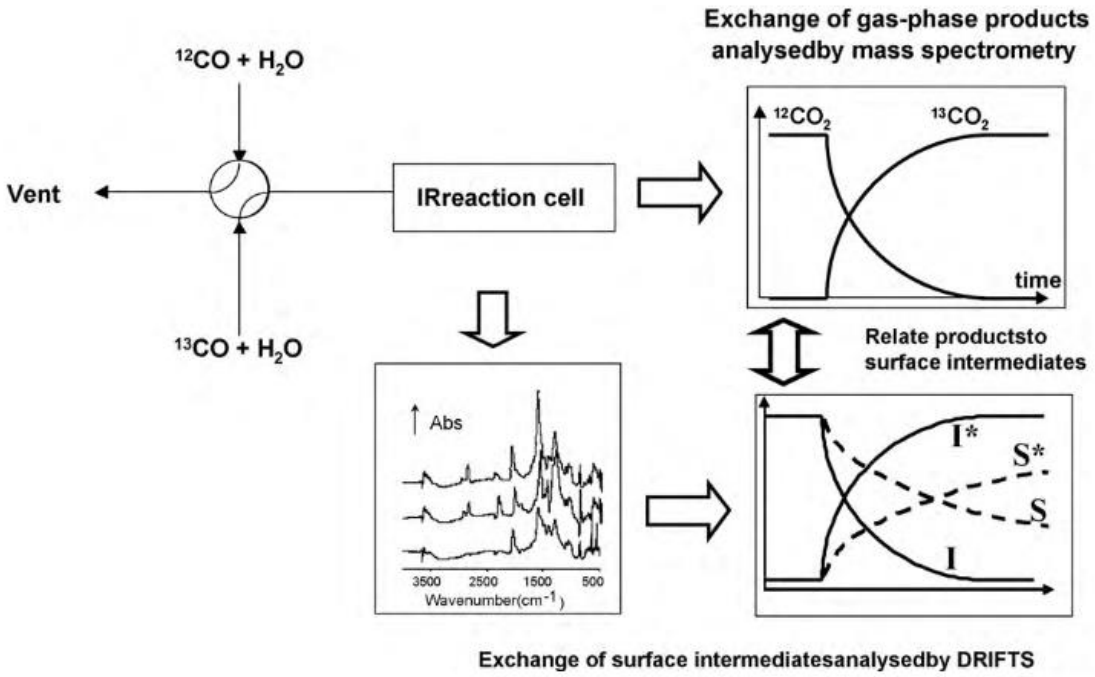

Figure I-20- Schematic representation of a SSITKA-IR) coupling for operando investigation of catalytic reactions [134].

SSITKA combination with *in situ/operando* IR spectroscopic techniques was firstly introduced by Dalziel *et al*. in 1957 [135] and Tamaru *et al*. in the late 1960s [122, 136]. The main challenge in this combination is the construction of the reactor cell that requires a specific design to carry out both measurements, SSITKA and IR, under the desired reaction conditions. Chuang and coworkers were the first to develop their own IR transmission cell during the 1990s to couple both techniques in order to study hydroformylation ($Ar/^{12}CO/H_2/C_2H_4$ to $^{13}CO/H_2/C_2H_4$) on $Rh\text{-}Ce/SiO_2$ catalyst [116, 118, 137].

The coupling has also been extended to other IR spectroscopic techniques, such as DRIFTS (Diffuse Reflectance Infrared Fourier Transform Spectroscopy) which was been tested for the first time by Goguet and co-workers in 2004 to study reverse water-gas-shift (WGS) reaction mechanism on Pt/CeO_2 material [138]. Since then, a flourishing number of SSITKA-DRIFTS studies on WGS and reverse WGS using Pt or Au-supported catalyst on oxide have appeared in the literature [117, 139–156]. For example, a lot of SSITKA-DRIFTS experiments were carried out on Pt/CeO_2 catalyst to compare formate and carbonyls reactivity during WGS reaction. The conclusions showed that the reaction occurs mainly via a redox mechanism where CO adsorbed linearly on Pt is oxidized to produce CO_2 using lattice oxygen from the CeO_2 support [144, 149].

DRIFTS can be a precise quantitative tool for operando studies if the band intensities are well calibrated. However, the technique presents some limitations such as lower resolutions, due to the large dead volume of the commercial DRIFTS cells or the fact that only small portion of the sample is analyzed, and the possibility of concentration and temperature gradients within the sample due to nonzero conversion over the packed bed. Concerning transmission IR mode coupled with SSITKA, the thickness of the wafers used can sometimes cause mass transport limitations. However, it allows the entire sample volume to be probed during the IR analysis, with the exception of boundary regions of the wafer and/or regions hidden by the sample holder [134]. Finally, it is important to note that in both transmission and DRIFTS modes, temperature probe and control can also be challenging, especially at high reaction temperatures.

3.5.2- CO oxidation evaluation using SSITKA and SSITKA-IR techniques

Historically, research has primarily focused on reactions such as CO hydrogenation (Fischer-Tropsch) [157–160], CH_4 oxidation [121, 161–164], selective NO reduction [165–169]. However, there have been relatively few studies on CO oxidation illustrated Table I-4, and there are also few research groups specifically working on SSITKA-IR.

Table I-4- Compilation of the studies carried out on the CO oxidation reaction using SSITKA technique.

CO Oxidation reaction	Reference
Over commercial three-way catalyst	[170]
Over Supported gold catalysts	[130, 171–174]
Over Doped CeO_2 catalytic material (M-Ce-O)	[175]
Over Pt/Al_2O_3	[176]

Oulaci *et al.* [170] utilized the SSITKA technique to investigate the CO oxidation reaction over a three-way catalyst formulation. They observed a bimodal distribution of active sites responsible for the formation of CO_2 (see Figure I-21).

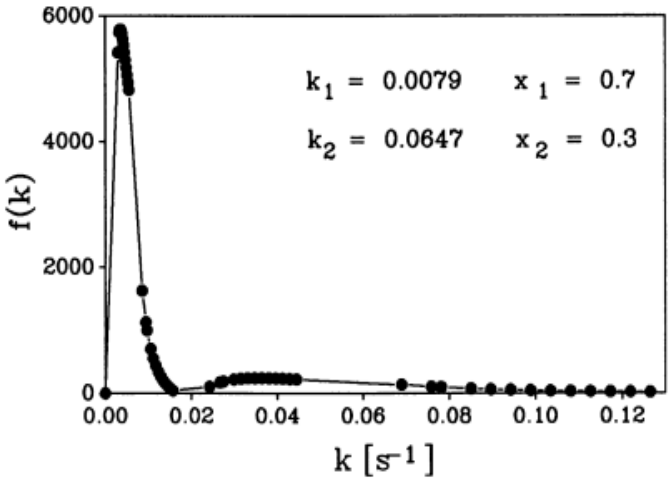

Figure I-21- Steady-State CO oxidation at 95 °C: Activity distribution of the catalytic sites (k_i= average site pool activity [s^{-1}], X_i= fraction of sites activity k_i) [170].

This bimodal activity distribution could not be solely attributed to the bimetallic nature of the three-way catalyst, as a similar bimodal activity distribution was also observed in mono-metallic catalysts. While the presence of two types of active metal sites on both catalysts could not be excluded, the low activity "sites" (with longer lifetimes) might be attributed to reactions with the rare earth oxides on the support or to multiple adsorption-desorption processes on metal sites.

Calla *et al.* conducted research on the CO oxidation reaction employing supported gold catalysts. In one study, they utilized the SSITKA technique to examine the impact of water presence on the reaction activity. Their findings from SSITKA revealed that the presence of water enhances both the intrinsic turnover frequency and the surface coverage of reactive intermediates [171]. In another study, they examined the influence of the support on the catalyst's activity for the CO oxidation reaction using SSITKA [130]. They found that the coverage of active carbon-containing intermediates (θco) was higher over Au/TiO_2 compared to Au/Al_2O_3. This elevated coverage of species-forming products on Au/TiO_2 is attributed to the greater availability of active surface oxygen on the titania catalyst compared to the alumina catalyst.

Polychronopoulou *et al.* conducted an investigation on the CO oxidation reaction over Cu-Ce-O and Zn-Ce-O solids using SSITKA coupled with DRIFTS to gain insights into the reaction mechanism over these catalysts [175]. They conducted firstly $^{12}CO/O_2 \rightarrow {}^{13}CO/O_2$ isotopic switch followed by $^{12}CO_2$ to $^{13}CO_2$ switch on these solids surface to examine the interaction of CO_2 with the catalyst surface and determine the formation of adsorbed carbonates. Figure I-22

presents SSITKA-DRIFT spectra recorded during the gas switching process over the Cu-Ce-O catalyst during $^{12}CO/^{13}CO$ and $^{12}CO_2/^{13}CO_2$ switch.

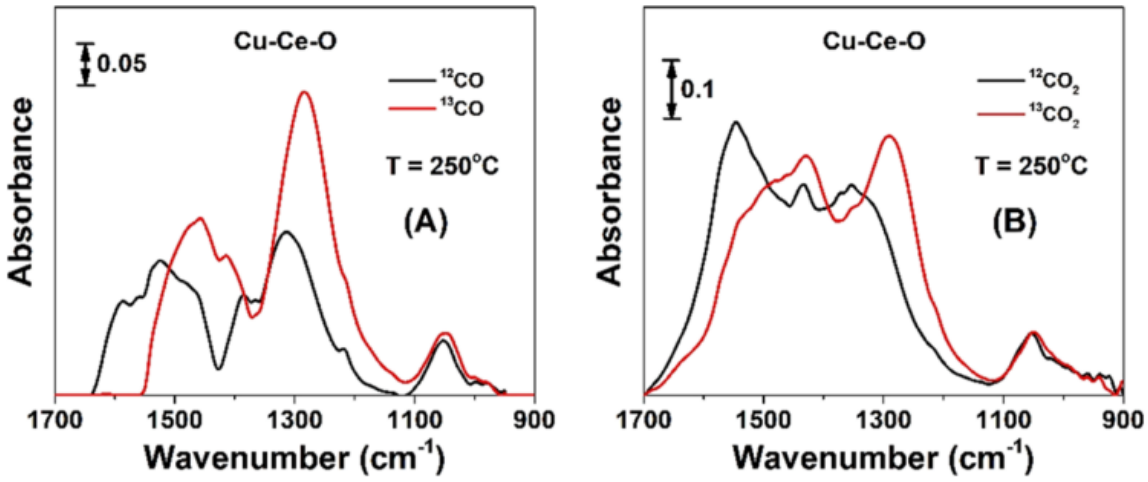

Figure I-22- SSITKA-DRIFTS spectra recorded in the 1700-1900 cm^{-1} IR region during the gas following switch (A) $^{12}CO/O_2$ –> $^{13}CO/O_2$ (B) $^{12}CO_2/O_2$ → $^{13}CO_2/O_2$ for the Cu-Ce-O solid [175].

Notably, they observed a red shift of the IR bands corresponding to the adsorbed carbonate species in both cases indicating that $^{12}CO_2$ adsorption on the Cu-Ce-O catalyst is a reversible step, as it can be exchanged with gaseous $^{13}CO_2$. In contrast, no isotopic shift was recorded on pure CeO_2 and Zn-Ce-O in the case of the $^{12}CO_2$ → $^{13}CO_2$ switch step. They concluded that such carbonate-type species should be considered as spectator (inactive) species, likely contributing to the catalyst's deactivation.

Pansare *et al.* [173] conducted an insightful study to investigate the deactivation of Au/Al_2O_3 and Pt/Al_2O_3 catalysts in the CO oxidation reaction. They employed SSITKA to analyze the contributions to the overall activity from the intrinsic site activity (k, s^{-1}) and the concentration of surface intermediates (N_{CO2}) to gain a deeper understanding of the catalyst deactivation.

They observed a significant reduction in k the intrinsic site activity for Au1 and Au2 catalysts, while the Pt catalyst showed a minimal decrease in k (see Figure I-23).

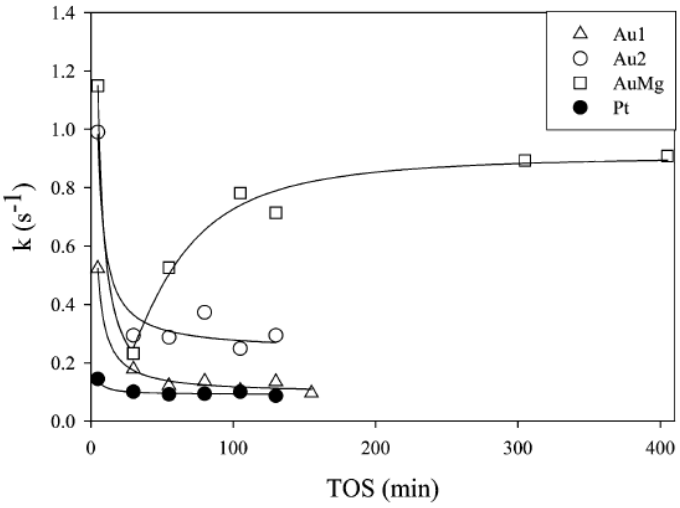

Figure I-23- Intrinsic SSITKA site activity variation with time-on-stream for Au1, Au2, Au(Mg) and Pt catalysts [173].

Concerning the concentration of surface intermediates, they observed a rapid decrease of these intermediates during the first 30 minutes of time of stream (see Figure I-24).

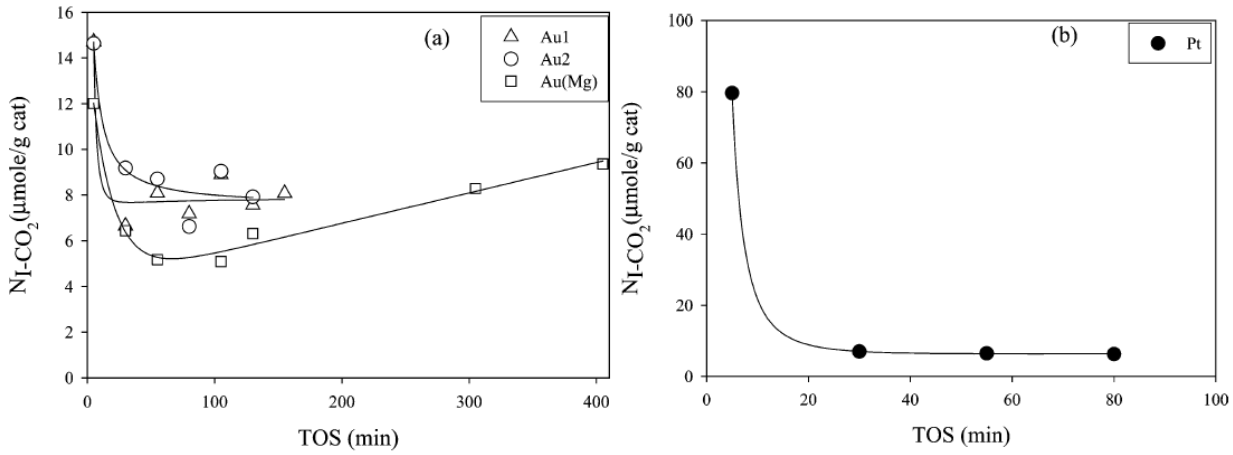

Figure I-24- Concentrations of reactive intermediates as a function of time-on-stream for (a) Au1, Au2 and Au(Mg) catalysts, (b) Pt catalyst [173].

However, the decrease in N_{CO2} for the Au catalysts (around 50%) was less significant compared to the Pt catalyst (around 90%). Based on the changes in k and N_{CO2}, they concluded that the deactivation of the Pt catalyst was mainly attributed to a decreased concentration of reactive surface intermediates. On the other hand, for Au1 and Au2 catalysts, both N_{CO2} and k decreased, but the primary cause of deactivation was the decrease in k (around 70%). The decrease in N_{CO2} in Au catalysts was likely due to carbon deposition from CO on the active sites, a phenomenon previously demonstrated for Pt [176]. This carbon deposition reduced the adsorption of reactants and subsequently increased the formation of reactive intermediates.

4- General Conclusion

Air pollution poses a significant challenge to the well-being of the population, contributing to severe health issues. Governments are actively seeking solutions to reduce pollution through various approaches. The transport sector is a major contributor to air pollution, primarily due to the emissions from vehicles. The CO oxidation reaction, one of the three reactions in exhaust emissions, has garnered considerable interest from researchers due to its simplicity. However, despite its simplicity, the reaction mechanism has been the subject of numerous discussions and debates in literature. Although three-way catalysts have significantly reduced emissions, the issue of cold start remains unresolved. Furthermore, increasingly stringent regulations are pushing researchers and industries to explore different approaches to address the problem of cold start while adhering to emissions limits. Consequently, gaining a comprehensive understanding of the catalyst's surface under reaction conditions at low temperature appears to be an ideal approach to tackle this issue.

At low temperatures, the CO oxidation reaction on PGM metals exhibits different phenomena, such as surface reconstruction and hysteresis. The reasons behind surface reconstruction have been contradictory, with some proposing that the transition from low to high activity is linked to the catalyst's transition from a metallic to an oxide phase, while others suggest the opposite. Similarly, the hysteresis phenomenon, which is related to variations in activity, has been a topic of debate in the literature concerning its origin. Over time, various interpretations and explanations have been proposed and discussed to shed light on these intriguing phenomena. The phenomena of reconstruction, changes in oxide vs. metallic phase, or changes in adsorbed species CO vs. O lead to remarkable oscillations in CO oxidation reactivity. The surface state of the catalyst strongly depends on the ambient conditions, whether they are rich or lean in oxygen, which can partially explain the hysteresis observed during the reaction. These surface changes play a crucial role in the dynamics of the CO reaction and are essential to understand in order to optimize catalytic performance and address issues related to cold start and emissions.

In situ techniques offer valuable insights into the species formed on the catalyst surface during a reaction. Among these techniques, the SSITKA technique coupled with IR spectroscopy stands out as the most suitable method to investigate the reaction mechanism and identify the various species formed on the catalyst surface. Indeed, to date, there has been a notable lack of studies investigating the CO oxidation reaction on supported PGM catalysts using the SSITKA technique combined with IR spectroscopy. Employing this approach is of utmost importance

as it will enable us to unravel the underlying mechanisms governing the CO oxidation reaction at low temperatures. More importantly, it will allow us to discern the structure and nature of the adsorbed species on the catalyst surface and distinguish between active and inactive species. By understanding the role of these key intermediates, we aim to shed light on the intriguing hysteresis phenomena observed during the CO oxidation reaction at low temperatures. This comprehensive study will pave the way for a more profound understanding of the reaction kinetics and surface interactions, which are crucial for designing highly efficient catalysts for various applications, including air pollution control and emissions reduction.

References

1. Almost everyone now breathing polluted air, warns WHO. In: UN News. https://news.un.org/en/story/2022/04/1115492. Accessed 18 Jul 2022

2. SPF Impact de pollution de l'air ambiant sur la mortalité en France métropolitaine. Réduction en lien avec le confinement du printemps 2020 et nouvelles données sur le poids total pour la période 2016-2019. https://www.santepubliquefrance.fr. Accessed 22 Jun 2023

3. Forouzanfar MH, Afshin A, Alexander LT, et al (2016) Global, regional, and national comparative risk assessment of 79 behavioural, environmental and occupational, and metabolic risks or clusters of risks, 1990–2015: a systematic analysis for the Global Burden of Disease Study 2015. The Lancet 388:1659–1724. https://doi.org/10.1016/S0140-6736(16)31679-8

4. Landrigan PJ (2017) Air pollution and health. The Lancet Public Health 2:e4–e5. https://doi.org/10.1016/S2468-2667(16)30023-8

5. Amendments adopted by the European Parliament on 8 June 2022 on the proposal for a regulation of the European Parliament and of the Council amending Regulation (EU) 2019/631 as regards strengthening the CO_2 emission performance standards for new passenger cars and new light commercial vehicles in line with the Union's increased climate ambition (2022) - Amendment P9_TA (2022)0234. https://www.europarl.europa.eu/doceo/document/TA-9-2022-0234_EN.html. Accessed 21 Jun 2023.

6. Kašpar J, Fornasiero P, Hickey N (2003) Automotive catalytic converters: current status and some perspectives. Catalysis Today 77:419–449. https://doi.org/10.1016/S0920-5861(02)00384-X

7. Commission proposes new Euro 7 standards. In: European Commission - European Commission. https://ec.europa.eu/commission/presscorner/detail/en/ip_22_6495. Accessed 22 Jun 2023

8. European Commission proposes Euro 7/VII emission standards. https://dieselnet.com/news/2022/11eu.php. Accessed 22 Jun 2023

9. Réglementation : future norme d'émissions Euro 7 (2022). In: Guillaume Darding. https://www.guillaumedarding.fr/reglementation-future-norme-d-emissions-euro-7-8904983.html. Accessed 3 Apr 2023

10. Euro 7 emission standards (2023). In: INSIGHT https://www.infineuminsight.com/engb/articles/euro-7-emission-standards. Accessed 22 Aug 2023

11. Wu J (2019) Development of novel catalytic materials with low content of precious metals for the after-treatment of automobile exhaust gas. Doctoral dissertation, Université de Lille, Sciences et Technologies

12. Wang J, Chen H, Hu Z, et al (2015) A Review on the Pd-Based Three-Way Catalyst. Catalysis Reviews 57:79–144. https://doi.org/10.1080/01614940.2014.977059

13. Twigg MV (2011) Catalytic control of emissions from cars. Catalysis Today 163:33–41. https://doi.org/10.1016/j.cattod.2010.12.044

14. India BAS (2018) Let's Understand How Catalytic Converters Work? https://www.bpautosparesindia.com/blog/lets-understand-how-catalytic-converters-work/. Accessed 23 Nov 2020

15. Rood S, Eslava S, Manigrasso A, Bannister C (2020) Recent advances in gasoline three-way catalyst formulation: A review. Proceedings of the Institution of Mechanical Engineers, Part D: Journal of Automobile Engineering 234:936–949. https://doi.org/10.1177/0954407019859822

16. Devaiah D, Reddy LH, Park S-E, Reddy BM (2018) Ceria–zirconia mixed oxides: Synthetic methods and applications. Catalysis Reviews 60:177–277. https://doi.org/10.1080/01614940.2017.1415058

17. Montini T, Melchionna M, Monai M, Fornasiero P (2016) Fundamentals and Catalytic Applications of CeO_2-Based Materials. Chem Rev 116:5987–6041. https://doi.org/10.1021/acs.chemrev.5b00603

18. Si R, Zhang Y-W, Wang L-M, et al (2007) Enhanced Thermal Stability and Oxygen Storage Capacity for $Ce_xZr_{1-x}O_2$ (x = 0.4−0.6) Solid Solutions by Hydrothermally Homogenous Doping of Trivalent Rare Earths. J Phys Chem C 111:787–794. https://doi.org/10.1021/jp0630875

19. Farrauto RJ, Deeba M, Alerasool S (2019) Gasoline automobile catalysis and its historical journey to cleaner air. Nat Catal 2:603–613. https://doi.org/10.1038/s41929-019-0312-9

20. Lox ESJ, Engler BH (1999) Environmental Catalysis — Mobile Sources. In: Environmental Catalysis. John Wiley & Sons, Ltd, pp 1–117

21. Heck RM, Farrauto RJ, Gulati ST (2016) Catalytic Air Pollution Control: Commercial Technology. John Wiley & Sons

22. Rehn LPP (2013) Caractérisation et impacts des émissions de polluants du transport routier : Apports méthodologiques et cas d'études en Rhône Alpes. Thèses, Université de Grenoble

23. Skoglundh M, Fridell E (2004) Strategies for Enhancing Low-Temperature Activity. Topics in Catalysis 28:79–87. https://doi.org/10.1023/B:TOCA.0000024336.98281.0e

24. Farrauto RJ, Heck RM (1999) Catalytic converters: state of the art and perspectives. Catalysis Today 51:351–360. https://doi.org/10.1016/S0920-5861(99)00024-3

25. Bosteels D, Searles RA (2002) Exhaust Emission Catalyst Technology. Platinum metals review 46:27–36

26. Shelef M, McCabe RW (2000) Twenty-five years after introduction of automotive catalysts: what next? Catalysis Today 62:35–50. https://doi.org/10.1016/S0920-5861(00)00407-7

27. Gandhi HS, Graham GW, McCabe RW (2003) Automotive exhaust catalysis. Journal of Catalysis 216:433–442. https://doi.org/10.1016/S0021-9517(02)00067-2

28. Kang SB, Han SJ, Nam SB, et al (2012) Activity function describing the effect of Pd loading on the catalytic performance of modern commercial TWC. Chemical Engineering Journal 207–208:117–121. https://doi.org/10.1016/j.cej.2012.06.003

29. Martínez-Arias A, Hungría AB, Fernández-García M, et al (2004) Light-off behaviour of PdO/γ-Al_2O_3 catalysts for stoichiometric CO–O_2 and CO–O_2–NO reactions: a combined catalytic activity–in situ DRIFTS study. Journal of Catalysis 221:85–92. https://doi.org/10.1016/S0021-9517(03)00277-X

30. Heck RM, Farrauto RJ (2001) Automobile exhaust catalysts. Applied Catalysis A: General 221:443–457. https://doi.org/10.1016/S0926-860X(01)00818-3

31. Lafyatis DS, Ansell GP, Bennett SC, et al (1998) Ambient temperature light-off for automobile emission control. Applied Catalysis B: Environmental 18:123–135. https://doi.org/10.1016/S0926-3373(98)00032-0

32. Pfalzgraf B, Rieger M, Ottowitz G (1996) Close-coupled Catalytic Converters for Compliance with LEV/ULEV and EG III Legislation - Influence of Support Material, Cell Density and Mass on Emission Results. SAE Transactions 105:123–130

33. Collins NR, Chandler GR, Brisley RJ, et al (1996) Catalyst Improvements to Meet European Stage III and ULEV Emissions Criteria. SAE Transactions 105:310–325

34. Heck RM, Hu Z, Smaling R, et al (1995) Close Coupled Catalyst System Design and ULEV Performance After 1050° C Aging. SAE Transactions 104:1217–1222

35. Shimasaki Y, Kato H, Abe F, et al (1997) Development of Extruded Electrically Heated Catalyst System for ULEV Standards. SAE Transactions 106:409–425

36. Grabow LC, Gokhale AA, Evans ST, et al (2008) Mechanism of the Water Gas Shift Reaction on Pt: First Principles, Experiments, and Microkinetic Modeling. J Phys Chem C 112:4608–4617. https://doi.org/10.1021/jp7099702

37. Wang L, Yang L, Zhang Y, et al (2010) Promoting effect of an aluminum emulsion on catalytic performance of Cu-based catalysts for methanol synthesis from syngas. Fuel Processing Technology 91:723–728. https://doi.org/10.1016/j.fuproc.2010.02.003

38. Henein NA, Tagomori MK (1999) Cold-start hydrocarbon emissions in port-injected gasoline engines. Progress in Energy and Combustion Science 25:563–593. https://doi.org/10.1016/S0360-1285(99)00003-9

39. Lin J, Wang X, Zhang T (2016) Recent progress in CO oxidation over Pt-group-metal catalysts at low temperatures. Chinese Journal of Catalysis 37:1805–1813. https://doi.org/10.1016/S1872-2067(16)62513-5

40. Pan F, Zhang W, Ye Y, et al (2018) Adsorption Synthesis of Iron Oxide-Supported Gold Catalyst under Self-Generated Alkaline Conditions for Efficient Elimination of Carbon Monoxide. Catalysts 8:357. https://doi.org/10.3390/catal8090357

41. Al Soubaihi R, Saoud K, Dutta J (2018) Critical Review of Low-Temperature CO Oxidation and Hysteresis Phenomenon on Heterogeneous Catalysts. Catalysts 8:660. https://doi.org/10.3390/catal8120660

42. Carlsson P-A, Österlund L, Thormählen P, et al (2004) A transient in situ FTIR and XANES study of CO oxidation over Pt/Al_2O_3 catalysts. Journal of Catalysis 226:422–434. https://doi.org/10.1016/j.jcat.2004.06.009

43. Cisternas J, Escaff D, Descalzi O, Wehner S (2010) Carbon Monoxide oxidation on Iridium(111) surfaces under colored noise. Int J Bifurcation Chaos 20:243–254. https://doi.org/10.1142/S0218127410025685

44. Akhter S, White JM (1986) The effect of oxygen islanding on CO and H_2 oxidation on Pt(111). Surface Science 171:527–542. https://doi.org/10.1016/0039-6028(86)91058-7

45. Widmann D, Behm RJ (2014) Activation of Molecular Oxygen and the Nature of the Active Oxygen Species for CO Oxidation on Oxide Supported Au Catalysts. Acc Chem Res 47:740–749. https://doi.org/10.1021/ar400203e

46. Allian AD, Takanabe K, Fujdala KL, et al (2011) Chemisorption of CO and Mechanism of CO Oxidation on Supported Platinum Nanoclusters. J Am Chem Soc 133:4498–4517. https://doi.org/10.1021/ja110073u

47. Michalak WD, Krier JM, Alayoglu S, et al (2014) CO oxidation on PtSn nanoparticle catalysts occurs at the interface of Pt and Sn oxide domains formed under reaction conditions. Journal of Catalysis 312:17–25. https://doi.org/10.1016/j.jcat.2014.01.005

48. Ackermann MD, Pedersen TM, Hendriksen BLM, et al (2005) Structure and Reactivity of Surface Oxides on Pt(110) during Catalytic CO Oxidation. Phys Rev Lett 95:255505. https://doi.org/10.1103/PhysRevLett.95.255505

49. Newton MA, Chapman KW, Thompsett D, Chupas PJ (2012) Chasing Changing Nanoparticles with Time-Resolved Pair Distribution Function Methods. J Am Chem Soc 134:5036–5039. https://doi.org/10.1021/ja2114163

50. Newton MA (2017) Time Resolved Operando X-ray Techniques in Catalysis, a Case Study: CO Oxidation by O_2 over Pt Surfaces and Alumina Supported Pt Catalysts. Catalysts 7:58. https://doi.org/10.3390/catal7020058

51. Moses-DeBusk M, Yoon M, Allard LF, et al (2013) CO Oxidation on Supported Single Pt Atoms: Experimental and ab Initio Density Functional Studies of CO Interaction with Pt Atom on θ-Al_2O_3(010) Surface. J Am Chem Soc 135:12634–12645. https://doi.org/10.1021/ja401847c

52. Ding K, Gulec A, Johnson AM, et al (2015) Identification of active sites in CO oxidation and water-gas shift over supported Pt catalysts. Science 350:189–192. https://doi.org/10.1126/science.aac6368

53. Newton MA, Ferri D, Smolentsev G, et al (2015) Room-temperature carbon monoxide oxidation by oxygen over Pt/Al_2O_3 mediated by reactive platinum carbonates. Nat Commun 6:8675. https://doi.org/10.1038/ncomms9675

54. Föttinger K, Emhofer W, Lennon D, Rupprechter G (2017) Adsorption and Reaction of CO on (Pd–)Al_2O_3 and (Pd–)ZrO_2: Vibrational Spectroscopy of Carbonate Formation. Top Catal 60:1722–1734. https://doi.org/10.1007/s11244-017-0852-7

55. Föttinger K, Schlögl R, Rupprechter G (2008) The mechanism of carbonate formation on Pd–Al_2O_3 catalysts. Chem Commun 320–322. https://doi.org/10.1039/B713161E

56. Murata K, Eleeda E, Ohyama J, et al (2019) Identification of active sites in CO oxidation over a Pd/Al_2O_3 catalyst. Phys Chem Chem Phys 21:18128–18137. https://doi.org/10.1039/C9CP03943K

57. Dropsch H, Baerns M (1997) CO adsorption on supported Pd catalysts studied by adsorption microcalorimetry and temperature programmed desorption. Applied Catalysis A: General 158:163–183. https://doi.org/10.1016/S0926-860X(96)00418-8

58. Bertarione S, Scarano D, Zecchina A, et al (2004) Surface reactivity of Pd nanoparticles supported on polycrystalline substrates as compared to thin film model catalysts: infrared study of CH_3OH adsorption. Journal of Catalysis 223:64–73. https://doi.org/10.1016/j.jcat.2004.01.005

59. Kaichev VV, Morkel M, Unterhalt H, et al (2004) C–O bond scission on "defect-rich and perfect" Pd(111)? Surface Science 566–568:1024–1029. https://doi.org/10.1016/j.susc.2004.06.100

60. Rupprechter G, Kaichev VV, Unterhalt H, et al (2004) CO dissociation and CO hydrogenation on smooth and ion-bombarded Pd(111): SFG and XPS spectroscopy at mbar pressures. Applied Surface Science 235:26–31. https://doi.org/10.1016/j.apsusc.2004.05.120

61. Imbihl R, Ertl G (1995) Oscillatory Kinetics in Heterogeneous Catalysis. Chem Rev 95:697–733. https://doi.org/10.1021/cr00035a012

62. Carlsson P-A, Skoglundh M (2011) Low-temperature oxidation of carbon monoxide and methane over alumina and ceria supported platinum catalysts. Applied Catalysis B: Environmental 101:669–675. https://doi.org/10.1016/j.apcatb.2010.11.008

63. Subbotin AN, Gudkov BS, Yakerson VI (2000) Temperature hysteresis phenomena in heterogeneous catalysis. Russian Chemical Bulletin 49:1373–1379. https://doi.org/10.1007/BF02495080

64. Salomons S, Hayes RE, Votsmeier M, et al (2007) On the use of mechanistic CO oxidation models with a platinum monolith catalyst. Applied Catalysis B: Environmental 70:305–313. https://doi.org/10.1016/j.apcatb.2006.01.022

65. Hauptmann W, Votsmeier M, Vogel H, Vlachos DG (2011) Modeling the simultaneous oxidation of CO and H_2 on Pt – Promoting effect of H_2 on the CO-light-off. Applied Catalysis A: General 397:174–182. https://doi.org/10.1016/j.apcata.2011.02.031

66. Kalinkin AV, Boreskov GK, Savchenko VI, Dadayan KA (1980) Study of CO oxidation on the (111) face of nickel during Ni−NiO phase transition. React Kinet Catal Lett 13:111–114. https://doi.org/10.1007/BF02074180

67. Orlik SN, Koval' GL, Fesenko AV, et al (1979) Kinetics of CO oxidation on a palladium-containing catalyst. Theor Exp Chem 15:59–61. https://doi.org/10.1007/BF00524911

68. Hegedus LL, Oh SH, Baron K (1977) Multiple steady states in an isothermal, integral reactor: The catalytic oxidation of carbon monoxide over platinum-alumina. AIChE Journal 23:632–642. https://doi.org/10.1002/aic.690230503

69. Chakrabarty T, Silveston PL, Hudgins RR (1984) Hysteresis phenomena in CO oxidation over platinum-alumina catalyst. The Canadian Journal of Chemical Engineering 62:651–660. https://doi.org/10.1002/cjce.5450620511

70. Dauchot JP, Cakenberghe JV (1973) Oscillations during Catalytic Oxidation of Carbon Monoxide on Platinum. Nature Physical Science 246:61–63. https://doi.org/10.1038/physci246061b0

71. Rathouský J, Kíra E, Hlaváček V (1981) Experimental observations of complex dynamic behavior in the catalytic oxidation of CO on Pt/alumina catalyst. Chemical Engineering Science 36:781–782. https://doi.org/10.1016/0009-2509(81)85095-6

72. Zahradnik J, McCarthy EF, Kuczynski GC, Carberry JJ (1975) Effect of Ambient Atmosphere on Sintering of α-$A1_2O_3$ Supported Pt Catalysts. In: Kuczynski GC (ed) Sintering and Catalysis. Springer US, Boston, MA, pp 199–209

73. Haaland DM, Williams FL (1982) Simultaneous measurement of CO oxidation rate and surface coverage on $PtAl_2O_3$ using infrared spectroscopy: Rate hysteresis and CO island formation. Journal of Catalysis 76:450–465. https://doi.org/10.1016/0021-9517(82)90274-3

74. Subbotin AN, Subbotina IR, Golosman EZ (2015) Hysteresis phenomena in heterogeneous exothermal catalytic reactions and methods for decreasing the overheating of catalyst nanoclusters. Mendeleev Communications 25:216–218. https://doi.org/10.1016/j.mencom.2015.05.020

75. Yuranov I, Kiwi-Minsker L, Slin'ko M, et al (2000) Oscillatory behavior during CO oxidation over Pd supported on glass fibers: experimental study and mathematical modeling. Chemical Engineering Science 55:2827–2833. https://doi.org/10.1016/S0009-2509(99)00557-6

76. Frank-Kamenetskii DA (2015) Diffusion and Heat Exchange in Chemical Kinetics. Princeton University Press

77. Hauptmann W, Votsmeier M, Gieshoff J, et al (2009) Inverse hysteresis during the NO oxidation on Pt under lean conditions. Applied Catalysis B: Environmental 93:22–29. https://doi.org/10.1016/j.apcatb.2009.09.008

78. Dubbe H, Eigenberger G, Nieken U (2016) Hysteresis Phenomena on Pt- and Pd-Diesel Oxidation Catalysts: Experimental Observations. Top Catal 59:1054–1058. https://doi.org/10.1007/s11244-016-0589-8

79. Fernandes VR, Bossche MV den, Knudsen J, et al (2016) Reversed Hysteresis during CO Oxidation over $Pd_{75}Ag_{25}$(100). ACS Catal 6:4154–4161. https://doi.org/10.1021/acscatal.6b00658

80. Casapu M, Fischer A, Gänzler AM, et al (2017) Origin of the Normal and Inverse Hysteresis Behavior during CO Oxidation over Pt/Al_2O_3. ACS Catalysis 7:343–355. https://doi.org/10.1021/acscatal.6b02709

81. Abedi A, Hayes R, Votsmeier M, Epling WS (2012) Inverse Hysteresis Phenomena During CO and C_3H_6 Oxidation over a Pt/Al_2O_3 Catalyst. Catal Lett 142:930–935. https://doi.org/10.1007/s10562-012-0861-x

82. Berzins AR, Vong MSWL, Sermon PA, Wurie AT (1984) Isothermal Chemisorption upon Oxide-Supported Platinum. Adsorption Science & Technology 1:51–76. https://doi.org/10.1177/026361748400100104

83. Schalow T, Brandt B, Laurin M, et al (2006) CO oxidation on partially oxidized Pd nanoparticles. Journal of Catalysis 242:58–70. https://doi.org/10.1016/j.jcat.2006.05.021

84. Mars P, van Krevelen DW (1954) Oxidations carried out by means of vanadium oxide catalysts. Chemical Engineering Science 3:41–59. https://doi.org/10.1016/S0009-2509(54)80005-4

85. L'vov BV, Galwey AK (2013) Catalytic oxidation of CO on platinum. J Therm Anal Calorim 111:145–154. https://doi.org/10.1007/s10973-012-2241-6

86. Ertl G (2008) Reactions at Surfaces: From Atoms to Complexity (Nobel Lecture). Angewandte Chemie International Edition 47:3524–3535. https://doi.org/10.1002/anie.200800480

87. Norton PR, Davies JA, Jackman TE (1982) Absolute coverages of CO and O on Pt(111); comparison of saturation CO coverages on Pt(100), (110) and (111) surfaces. Surface Science Letters 122:L593–L600. https://doi.org/10.1016/0167-2584(82)90130-X

88. Gao F, Cai Y, Gath KK, et al (2009) CO Oxidation on Pt-Group Metals from Ultrahigh Vacuum to Near Atmospheric Pressures. 1. Rhodium. J Phys Chem C 113:182–192. https://doi.org/10.1021/jp8077979

89. Gao F, Wang Y, Cai Y, Goodman DW (2009) CO Oxidation on Pt-Group Metals from Ultrahigh Vacuum to Near Atmospheric Pressures. 2. Palladium and Platinum. J Phys Chem C 113:174–181. https://doi.org/10.1021/jp8077985

90. Weaver JF, Kan HH, Shumbera RB (2008) Growth and properties of high-concentration phases of atomic oxygen on platinum single-crystal surfaces. J Phys: Condens Matter 20:184015. https://doi.org/10.1088/0953-8984/20/18/184015

91. Ackermann MD (2007) Operando SXRD: a new view on catalysis. Doctoral dissertation, Leiden University

92. Farkas A, Zalewska-Wierzbicka K, Bachmann C, et al (2013) High Pressure Carbon Monoxide Oxidation over Platinum (111). J Phys Chem C 117:9932–9942. https://doi.org/10.1021/jp401867g

93. Spronsen MA van, M. Frenken JW, N. Groot IM (2017) Surface science under reaction conditions: CO oxidation on Pt and Pd model catalysts. Chemical Society Reviews 46:4347–4374. https://doi.org/10.1039/C7CS00045F

94. Bobaru ŞC (2006) High-pressure STM studies of oxidation catalysis. Leiden University

95. McCrea K, Parker JS, Chen P, Somorjai G (2001) Surface structure sensitivity of high-pressure CO dissociation on Pt(557), Pt(100) and Pt(111) using sum frequency generation surface vibrational spectroscopy. Surface Science 494:238–250. https://doi.org/10.1016/S0039-6028(01)01469-8

96. Alayon EMC, Singh J, Nachtegaal M, et al (2009) On highly active partially oxidized platinum in carbon monoxide oxidation over supported platinum catalysts. Journal of Catalysis 263:228–238. https://doi.org/10.1016/j.jcat.2009.02.010

97. Rijn R van, Balmes O, Resta A, et al (2011) Surface structure and reactivity of Pd(100) during CO oxidation near ambient pressures. Phys Chem Chem Phys 13:13167–13171. https://doi.org/10.1039/C1CP20989B

98. Shipilin M, Gustafson J, Zhang C, et al (2015) Transient Structures of PdO during CO Oxidation over Pd(100). J Phys Chem C 119:15469–15476. https://doi.org/10.1021/acs.jpcc.5b04400

99. Hendriksen BLM, Bobaru SC, Frenken JWM (2004) Oscillatory CO oxidation on Pd(100) studied with in situ scanning tunneling microscopy. Surface Science 552:229–242. https://doi.org/10.1016/j.susc.2004.01.025

100. Blomberg S, Hoffmann MJ, Gustafson J, et al (2013) In Situ X-Ray Photoelectron Spectroscopy of Model Catalysts: At the Edge of the Gap. Phys Rev Lett 110:117601. https://doi.org/10.1103/PhysRevLett.110.117601

101. Chen M, Wang XV, Zhang L, et al (2010) Active Surfaces for CO Oxidation on Palladium in the Hyperactive State. Langmuir 26:18113–18118. https://doi.org/10.1021/la103140w

102. Hendriksen BLM, Bobaru SC, Frenken JWM (2005) Looking at Heterogeneous Catalysis at Atmospheric Pressure Using Tunnel Vision. Top Catal 36:43–54. https://doi.org/10.1007/s11244-005-7861-7

103. Hendriksen BLM, Ackermann MD, van Rijn R, et al (2010) The role of steps in surface catalysis and reaction oscillations. Nature Chem 2:730–734. https://doi.org/10.1038/nchem.728

104. Toyoshima R, Yoshida M, Monya Y, et al (2012) In Situ Ambient Pressure XPS Study of CO Oxidation Reaction on Pd(111) Surfaces. J Phys Chem C 116:18691–18697. https://doi.org/10.1021/jp301636u

105. Berlowitz PJ, Peden CHF, Goodman DW (1988) Kinetics of carbon monoxide oxidation on single-crystal palladium, platinum, and iridium. J Phys Chem 92:5213–5221. https://doi.org/10.1021/j100329a030

106. Chen MS, Cai Y, Yan Z, et al (2007) Highly active surfaces for CO oxidation on Rh, Pd, and Pt. Surface Science 601:5326–5331. https://doi.org/10.1016/j.susc.2007.08.019

107. Toyoshima R, Yoshida M, Monya Y, et al (2013) In Situ Photoemission Observation of Catalytic CO Oxidation Reaction on Pd(110) under Near-Ambient Pressure Conditions: Evidence for the Langmuir–Hinshelwood Mechanism. J Phys Chem C 117:20617–20624. https://doi.org/10.1021/jp4054132

108. Zhang F, Pan L, Li T, et al (2014) CO Oxidation on PdO(101) during Temperature-Programmed Reaction Spectroscopy: Role of Oxygen Vacancies. J Phys Chem C 118:28647–28661. https://doi.org/10.1021/jp509383v

109. Graham GW, König D, Poindexter BD, et al (1999) Ellipsometric study of a palladium catalyst during the oxidation of carbon monoxide and methane. Topics in Catalysis 8:35–43. https://doi.org/10.1023/A:1019128203919

110. Ledesma C, Yang J, Chen D, Holmen A (2014) Recent Approaches in Mechanistic and Kinetic Studies of Catalytic Reactions Using SSITKA Technique. ACS Catal 4:4527–4547. https://doi.org/10.1021/cs501264f

111. Efstathiou AM, Gleaves JT, Yablonsky GS (2012) Transient Techniques: Temporal Analysis of Products and Steady State Isotopic Transient Kinetic Analysis. Wiley-VCH

112. Happel J (1978) Transient tracing. Chemical Engineering Science 33:1567. https://doi.org/10.1016/0009-2509(78)85214-2

113. Bennett CO (1982) Understanding Heterogeneous Catalysis Through the Transient Method. In: Catalysis Under Transient Conditions. American Chemical Society, pp 1–32

114. Biloen P (1983) Transient kinetic methods. Journal of Molecular Catalysis 21:17–24. https://doi.org/10.1016/0304-5102(93)80108-7

115. Burch R, Shestov AA, Sullivan JA (1999) A Steady-State Isotopic Transient Kinetic Analysis of the $NO/O_2/H_2$ Reaction over Pt/SiO_2 Catalysts. Journal of Catalysis 188:69–82. https://doi.org/10.1006/jcat.1999.2653

116. Balakos MW, Chuang SSC, Srinivas G (1993) Transient infrared study of methanation and ethylene hydroformylation over Rh/SiO_2 catalysts. Journal of Catalysis; (United States) 140:1: https://doi.org/10.1006/jcat.1993.1083

117. Kalamaras CM, Panagiotopoulou P, Kondarides DI, Efstathiou AM (2009) Kinetic and mechanistic studies of the water–gas shift reaction on Pt/TiO_2 catalyst. Journal of Catalysis 264:117–129. https://doi.org/10.1016/j.jcat.2009.03.002

118. Srinivas G, Chuang SSC, Balakos MW (1993) An in situ IR study coupled with transient kinetic analysis of hydroformylation. AIChE Journal 39:530–532. https://doi.org/10.1002/aic.690390318

119. Shannon SL, Goodwin JG (1995) Characterization of Catalytic Surfaces by Isotopic-Transient Kinetics during Steady-State Reaction. Chem Rev 95:677–695. https://doi.org/10.1021/cr00035a011

120. Bennett CO (1999) Experiments and Processes in the Transient Regime for Heterogeneous Catalysis. In: Haag WO, Gates BC, Knözinger H (eds) Advances in Catalysis. Academic Press, pp 329–416

121. Efstathiou AM, Verykios XE (1997) Transient methods in heterogeneous catalysis: Experimental features and application to study mechanistic aspects of the CH_4/O_2 (OCM), NH_3/O_2 and NO/He reactions. Applied Catalysis A: General 151:109–166. https://doi.org/10.1016/S0926-860X(96)00262-1

122. Tamaru K (1965) Adsorption Measurements during Surface Catalysis. In: Eley DD, Pines H, Weisz PB (eds) Advances in Catalysis. Academic Press, pp 65–90

123. Mirodatos C (1991) Use of isotopic transient kinetics in heterogeneous catalysis. Catalysis Today 9:83–95. https://doi.org/10.1016/0920-5861(91)85011-V

124. Spivey JJ, Roberts GW, Jr JGG, et al (2004) Turnover frequencies in metal catalysis: Meanings, functionalities and relationships. In: Catalysis. pp 320–348

125. Boudart M, Djega-Mariadassou G (2014) Kinetics of Heterogeneous Catalytic Reactions. Princeton University Press

126. Happel J (2012) Isotopic Assessment of Heterogeneous Catalysis. Elsevier

127. Kao J-Y, Piet-Lahanier H, Walter E, Happel J (1992) Reversible reactions over non-metallic catalysts: A transient isotopic tracing of the isobutane-isobutene-hydrogen system over chromia. Journal of Catalysis 133:383–396. https://doi.org/10.1016/0021-9517(92)90248-G

128. Mirodatos C (1986) Benzene hydrogenation: an isotopic transient study. J Phys Chem 90:481–487. https://doi.org/10.1021/j100275a026

129. Ali SH, Goodwin JG (1997) Impact of Readsorption Effects and Their Removal from Surface Reaction Parameters Obtained by Isotopic Transient Kinetic Analysis: Methanol Synthesis on Pd/SiO_2. Journal of Catalysis 171:339–344. https://doi.org/10.1006/jcat.1997.1778

130. Calla JT, Bore MT, Datye AK, Davis RJ (2006) Effect of alumina and titania on the oxidation of CO over Au nanoparticles evaluated by ^{13}C isotopic transient analysis. Journal of Catalysis 238:458–467. https://doi.org/10.1016/j.jcat.2006.01.009

131. Basallote MG, Bernal S, Gatica JM, Pozo M (2002) Steady-state isotopic transient kinetic analysis of the H_2/D_2 exchange reaction as a tool for characterising the metal phase in supported platinum catalysts. Applied Catalysis A: General 232:39–50. https://doi.org/10.1016/S0926-860X(02)00077-7

132. Hargreaves JSJ, Jackson SD, Webb G (2006) Isotopes In Heterogeneous Catalysis. World Scientific

133. Peil KP, Marcelin G, Goodwin JG (1992) The Role of Lattice Oxygen in the Oxidative Coupling of Methane. In: Wolf EE (ed) Methane Conversion by Oxidative Processes: Fundamental and Engineering Aspects. Springer Netherlands, Dordrecht, pp 138–167

134. Meunier FC (2010) The power of quantitative kinetic studies of adsorbate reactivity by operando FTIR spectroscopy carried out at chemical potential steady-state. Catalysis Today 155:164–171. https://doi.org/10.1016/j.cattod.2009.11.017

135. Dalziel K, O'Brien JRP (1957) Spectrokinetic studies of the reaction of hydrogen peroxide with haemoglobin in dithionite solutions. Biochem J 67:124–136

136. Ueno A, Onishi T, Tamaru K (1970) Dynamic technique to elucidate the reaction intermediate in surface catalysis. Water-gas shift reaction. Trans Faraday Soc 66:756–763. https://doi.org/10.1039/TF9706600756

137. Chuang SSC, Pien SI (1992) Infrared study of the CO insertion reaction on reduced, oxidized, and sulfided Rh/SiO_2 catalysts. Journal of Catalysis 135:618–634. https://doi.org/10.1016/0021-9517(92)90058-P

138. Goguet A, Meunier FC, Tibiletti D, et al (2004) Spectrokinetic Investigation of Reverse Water-Gas-Shift Reaction Intermediates over a Pt/CeO_2 Catalyst. J Phys Chem B 108:20240–20246. https://doi.org/10.1021/jp047242w

139. Meunier FC, Tibiletti D, Goguet A, et al (2005) On the reactivity of carbonate species on a Pt/CeO_2 catalyst under various reaction atmospheres: Application of the isotopic exchange technique. Applied Catalysis A: General 289:104–112. https://doi.org/10.1016/j.apcata.2005.04.018

140. Tibiletti D, Meunier FC, Goguet A, et al (2006) An investigation of possible mechanisms for the water–gas shift reaction over a ZrO_2-supported Pt catalyst. Journal of Catalysis 244:183–191. https://doi.org/10.1016/j.jcat.2006.09.004

141. Tibiletti D, Goguet A, Reid D, et al (2006) On the need to use steady-state or operando techniques to investigate reaction mechanisms: An in situ DRIFTS and SSITKA-based study example. Catalysis Today 113:94–101. https://doi.org/10.1016/j.cattod.2005.11.013

142. Meunier FC, Tibiletti D, Goguet A, et al (2007) On the complexity of the water-gas shift reaction mechanism over a Pt/CeO_2 catalyst: Effect of the temperature on the reactivity of formate surface species studied by operando DRIFT during isotopic transient at chemical steady-state. Catalysis Today 126:143–147. https://doi.org/10.1016/j.cattod.2006.10.003

143. Meunier FC, Reid D, Goguet A, et al (2007) Quantitative analysis of the reactivity of formate species seen by DRIFTS over a $Au/Ce(La)O_2$ water–gas shift catalyst: First unambiguous evidence of the minority role of formates as reaction intermediates. Journal of Catalysis 247:277–287. https://doi.org/10.1016/j.jcat.2007.02.013

144. Meunier FC, Goguet A, Hardacre C, et al (2007) Quantitative DRIFTS investigation of possible reaction mechanisms for the water–gas shift reaction on high-activity Pt- and Au-based catalysts. Journal of Catalysis 252:18–22. https://doi.org/10.1016/j.jcat.2007.09.003

145. Olympiou GG, Kalamaras CM, Zeinalipour-Yazdi CD, Efstathiou AM (2007) Mechanistic aspects of the water–gas shift reaction on alumina-supported noble metal catalysts: In situ DRIFTS and SSITKA-mass spectrometry studies. Catalysis Today 127:304–318. https://doi.org/10.1016/j.cattod.2007.05.002

146. Jacobs G, Davis BH (2007) Low temperature water–gas shift: Applications of a modified SSITKA–DRIFTS method under conditions of H_2 co-feeding over metal/ceria and related oxides. Applied Catalysis A: General 333:192–201. https://doi.org/10.1016/j.apcata.2007.07.029

147. Daly H, Ni J, Thompsett D, Meunier FC (2008) On the usefulness of carbon isotopic exchange for the operando analysis of metal–carbonyl bands by IR over ceria-containing catalysts. Journal of Catalysis 254:238–243. https://doi.org/10.1016/j.jcat.2007.12.013

148. Kalamaras CM, Olympiou GG, Efstathiou AM (2008) The water-gas shift reaction on Pt/γ-Al_2O_3 catalyst: Operando SSITKA-DRIFTS-mass spectroscopy studies. Catalysis Today 138:228–234. https://doi.org/10.1016/j.cattod.2008.06.010

149. Kalamaras CM, Americanou S, Efstathiou AM (2011) "Redox" vs "associative formate with –OH group regeneration" WGS reaction mechanism on Pt/CeO_2: Effect of platinum particle size. Journal of Catalysis 279:287–300. https://doi.org/10.1016/j.jcat.2011.01.024

150. Kalamaras CM, Dionysiou DD, Efstathiou AM (2012) Mechanistic Studies of the Water–Gas Shift Reaction over Pt/$Ce_xZr_{1-x}O_2$ Catalysts: The Effect of Pt Particle Size and Zr Dopant. ACS Catal 2:2729–2742. https://doi.org/10.1021/cs3006204

151. Wang J, Kispersky VF, Nicholas Delgass W, Ribeiro FH (2012) Determination of the Au active site and surface active species via operando transmission FTIR and isotopic transient experiments on 2.3wt.% Au/TiO_2 for the WGS reaction. Journal of Catalysis 289:171–178. https://doi.org/10.1016/j.jcat.2012.02.008

152. Shekhar M, Wang J, Lee W-S, et al (2012) Counting Au catalytic sites for the water–gas shift reaction. Journal of Catalysis 293:94–102. https://doi.org/10.1016/j.jcat.2012.06.008

153. Kalamaras CM, Petallidou KC, Efstathiou AM (2013) The effect of La^{3+}-doping of CeO_2 support on the water-gas shift reaction mechanism and kinetics over Pt/$Ce_{1-x}La_xO_{2-\delta}$. Applied Catalysis B: Environmental 136–137:225–238. https://doi.org/10.1016/j.apcatb.2013.02.003

154. Petallidou KC, Kalamaras CM, Efstathiou AM (2014) The effect of La^{3+}, Ti^{4+} and Zr^{4+} dopants on the mechanism of WGS on ceria-doped supported Pt catalysts. Catalysis Today 228:183–193. https://doi.org/10.1016/j.cattod.2013.10.081

155. Cámara AL, Chansai S, Hardacre C, Martínez-Arias A (2014) The water–gas shift reaction over CeO_2/CuO: Operando SSITKA–DRIFTS–mass spectrometry study of low temperature mechanism. International Journal of Hydrogen Energy 39:4095–4101. https://doi.org/10.1016/j.ijhydene.2013.05.087

156. Petallidou KC, Boghosian S, Efstathiou AM (2015) Low-temperature water–gas shift on $Pt/Ce_{0.5}La_{0.5}O_2{-}\delta$: Effect of support synthesis method. Catalysis Today 242:153–167. https://doi.org/10.1016/j.cattod.2014.06.042

157. Lohitharn N, Goodwin JG (2008) Effect of K promotion of Fe and FeMn Fischer–Tropsch synthesis catalysts: Analysis at the site level using SSITKA. Journal of Catalysis 260:7–16. https://doi.org/10.1016/j.jcat.2008.08.011

158. Yang J, Tveten EZ, Chen D, Holmen A (2010) Understanding the Effect of Cobalt Particle Size on Fischer−Tropsch Synthesis: Surface Species and Mechanistic Studies by SSITKA and Kinetic Isotope Effect. Langmuir 26:16558–16567. https://doi.org/10.1021/la101555u

159. Carvalho A, Ordomsky VV, Luo Y, et al (2016) Elucidation of deactivation phenomena in cobalt catalyst for Fischer-Tropsch synthesis using SSITKA. Journal of Catalysis 344:669–679. https://doi.org/10.1016/j.jcat.2016.11.001

160. Vasiliades MA, Kalamaras CM, Govender NS, et al (2019) The effect of preparation route of commercial $Co/\gamma\text{-}Al_2O_3$ catalyst on important Fischer-Tropsch kinetic parameters studied by SSITKA and CO-DRIFTS transient hydrogenation techniques. Journal of Catalysis 379:60–77. https://doi.org/10.1016/j.jcat.2019.09.008

161. Öcal M, Oukaci R, Marcelin G, et al (2000) Steady-state isotopic transient kinetic analysis on Pd-supported hexaaluminates used for methane combustion in the presence and absence of NO. Catalysis Today 59:205–217. https://doi.org/10.1016/S0920-5861(00)00284-4

162. Machocki A, Rotko M, Gac W (2009) Steady State Isotopic Transient Kinetic Analysis of Flameless Methane Combustion over Pd/Al_2O_3 and Pt/Al_2O_3 Catalysts. Top Catal 52:1085–1097. https://doi.org/10.1007/s11244-009-9253-x

163. Machocki A, Rotko M, Stasinska B (2008) SSITKA studies of the catalytic flameless combustion of methane. Catalysis Today 137:312–317. https://doi.org/10.1016/j.cattod.2007.11.027

164. Rotko M, Machocki A, Słowik G (2014) The mechanism of the CH_4/O_2 reaction on the $Pd–Pt/\gamma\text{-}Al_2O_3$ catalyst: A SSITKA study. Applied Catalysis B: Environmental 160–161:298–306. https://doi.org/10.1016/j.apcatb.2014.05.037

165. Sadovskaya EM, Suknev AP, Pinaeva LG, et al (2004) Mechanism and kinetics of the selective NO reduction over Co-ZSM-5 studied by the SSITKA technique: 2. Reactivity of NOx-adsorbed species with methane. Journal of Catalysis 225:179–189. https://doi.org/10.1016/j.jcat.2004.03.032

166. Sadovskaya EM, Suknev AP, Pinaeva LG, et al (2001) Mechanism and Kinetics of the Selective NO Reduction over Co-ZSM-5 Studied by the SSITKA Technique: Part 1: NOx Adsorbed Species Formation. Journal of Catalysis 201:159–168. https://doi.org/10.1006/jcat.2001.3256

167. Sadovskaya EM, Suknev AP, Goncharov VB, et al (2004) Reaction Kinetics and Mechanism of Selective NO Reduction on a Co-ZSM-5 Catalyst as Studied by SSITKA.

Kinetics and Catalysis 45:436–445. https://doi.org/10.1023/B:KICA.0000032181.81830.fd

168. Schuurman Y, van Veen AC, Chupin C, Mirodatos C (2006) Can isotopic transient and formal steady-state kinetics lead to a converging surface chemistry analysis? Case study on the selective reduction of NO by CH_4 over Co-ZSM-5 catalysts. Top Catal 39:45–52. https://doi.org/10.1007/s11244-006-0036-3

169. Sullivan JA, Burch R, Shestov AA (2000) Transient Techniques in the Study of Lean-NOx Reduction Over Supported Pt Catalysts. Chemical Engineering Research and Design 78:947–953. https://doi.org/10.1205/026387600528201

170. Oukaci R, Blackmond DG, Goodwin JGJr, Gallaher GR (1992) Steady-State Isotopic Transient Kinetic Analysis Investigation of CO-O_2 and CO-NO Reactions over a Commercial Automotive Catalyst. In: Catalytic Control of Air Pollution. American Chemical Society, pp 61–72

171. Calla JT, Davis RJ (2005) Investigation of Alumina-Supported Au Catalyst for CO Oxidation by Isotopic Transient Analysis and X-ray Absorption Spectroscopy. J Phys Chem B 109:2307–2314. https://doi.org/10.1021/jp0488719

172. Calla JT, Davis RJ (2006) Oxygen-exchange reactions during CO oxidation over titania- and alumina-supported Au nanoparticles. Journal of Catalysis 241:407–416. https://doi.org/10.1016/j.jcat.2006.05.017

173. Pansare SS, Sirijaruphan A, Goodwin JG (2005) Au-catalyzed selective oxidation of CO: a steady-state isotopic transient kinetic study. Journal of Catalysis 234:151–160. https://doi.org/10.1016/j.jcat.2005.06.012

174. Clark JC, Dai S, Overbury SH (2007) Operando studies of desorption, reaction and carbonate formation during CO oxidation by Au/TiO_2 catalysts. Catalysis Today 1–2:135–142. https://doi.org/10.1016/j.cattod.2006.10.008

175. Polychronopoulou K, AlKhoori AA, Efstathiou AM, et al (2021) Design Aspects of Doped CeO_2 for Low-Temperature Catalytic CO Oxidation: Transient Kinetics and DFT Approach. ACS Appl Mater Interfaces 13:22391–22415. https://doi.org/10.1021/acsami.1c02934

176. Sirijaruphan A, Goodwin JG, Rice RW (2004) Investigation of the initial rapid deactivation of platinum catalysts during the selective oxidation of carbon monoxide. Journal of Catalysis 221:288–293. https://doi.org/10.1016/S0021-9517(03)00247-1

Chapter II- Material and Methods

1- Catalyst Synthesis

1.1- Incipient wetness impregnation (IWI)

1.1.1- Theory

Incipient wetness impregnation or dry impregnation is the most commonly employed technique for the synthesis of heterogeneous catalysts [1]. This method is highly favored due to its simplicity, cost-effectiveness, and minimal waste generation. It consists on saturating a support material with a solution containing a precursor of the active component in catalyst synthesis [2]. The active metal precursor is dissolved in either an aqueous or organic solution, which is then added to the catalyst support with a volume equal to the pore volume. Through capillary action, the solution diffuses into the pores of the support material and the concentration profile of the impregnated compound is influenced by the mass transfer conditions within the pores during impregnation and drying processes. Furthermore, it can be influenced by the interaction between the precursor and the surface. It is also possible to introduce additional ions to adjust reactivity.

1.1.2- Preparation of Pt/Al_2O_3

The preparation of 1wt% of Pt/Al_2O_3 is made with Platinum (II) acetylacetonate precursor [$Pt(acac)_2$, Fluka]. The precursor (0.066 g) is firstly dissolved in a solution of acetone (2.52 mL, VWR Chemicals) with a volume equal to the pore volume of the support based on the incipient wetness impregnation theory. After dissolution, the support γ-Al_2O_3 (2.97 g, supplied by the Centre de Recherches de Solaize Total Energies) is impregnated with the solution containing the active component. The sample was dried overnight at 85 °C, and calcined under air flow (250 mL/min) at 500 °C for 4 hours (ramp 5°C/min) in a quartz tube reactor to desorb the solvent and decompose the precursor residues (Figure II-1). After calcination, the sample is reduced under pure H_2 flow (220 mL/min) at 400 °C for 2.5 hours (ramp 5°C/min) to reduce oxidic platinum species into metallic platinum particles (Figure II-1).

1.2- Wet impregnation

1.2.1- Theory

Wet impregnation is another type of preparation method for the synthesis of heterogeneous catalyst. It consists to saturate the support material with a solution containing the active

component precursor, using an excess volume of solvent. This approach enables effective dispersion of the precursor of the active component throughout the catalyst and plays a crucial role in facilitating the impregnation process and promoting optimal contact between the support material and the active species. In this case, the mechanism of solution transport is altered from a capillary action process to a slower diffusion process.

1.2.2- Preparation of Pd/Al_2O_3

The preparation of 1wt% of Pd/Al_2O_3 is made with Palladium (II) acetylacetonate [$Pd(acac)_2$, Fluka]. The precursor (0.143 g) is firstly dissolved in an excess solution of acetone (VWR Chemicals). After dissolution, the support γ-Al_2O_3 (4.96 g, supplied by the Centre de Recherches de Solaize Total Energies) is impregnated with the solution containing the active component under stirring. The sample was then dried overnight at 85 °C, calcined at 500 °C and finally reduced at 400 °C following the same procedure than for Pt catalyst (Figure II-1).

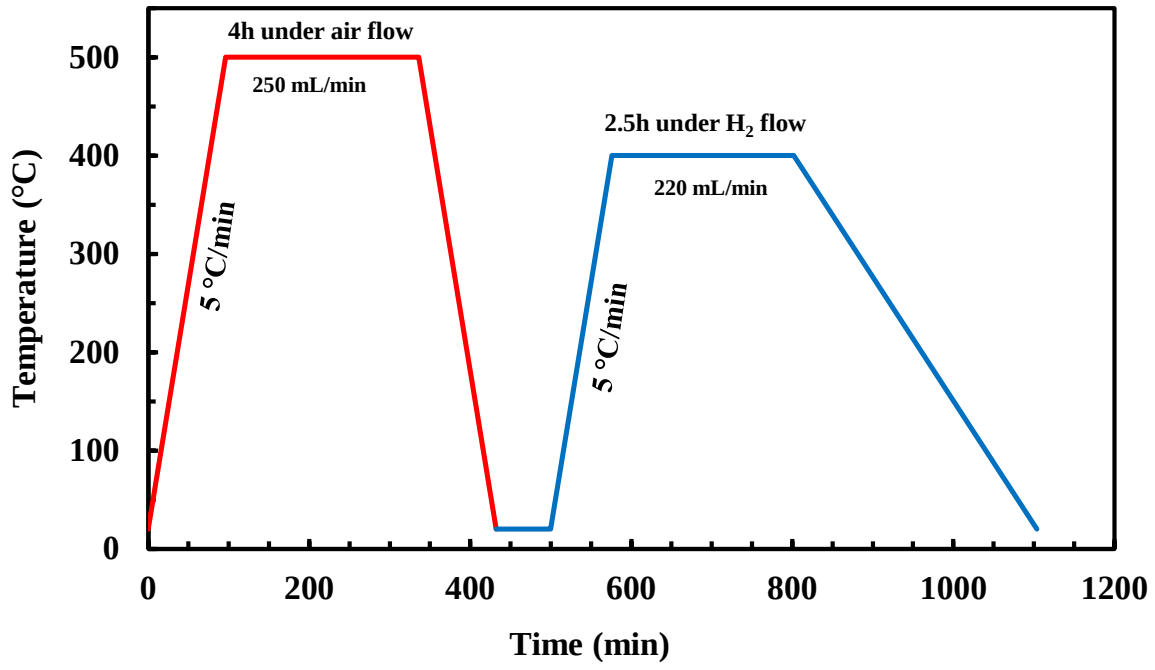

Figure II-1- Sequence for the calcination and reduction for Pt/Al_2O_3 and Pd/Al_2O_3 thermal treatments.

2- Catalyst Characterizations

2.1- Inductively coupled plasma-optical emission spectrometry (ICP-OES)

2.1.1- Theory

Inductively coupled plasma-optical emission spectrometry is an analytical technique used to identify and quantify the elements present in a sample. This technique operates on the principle that atoms and ions can absorb energy, causing electrons to transition from their ground state to an excited state. During analysis, the source of that energy is heat from an argon plasma that is used to generate excited atoms and ions of the elements contained in the sample [3]. As the electron returns from a higher to a lower energy level, it emits characteristic radiation at specific wavelengths that is detected by an optical spectrometer. By analyzing the emitted radiation, the presence and concentration of the elements in the sample can be determined.

2.1.2- Experimental Method

ICP analysis was performed in the "Spectrométrie par torche à plasma" platform of the Research Federation Michel-Eugène Chevreul hosted by the LASIRE laboratory using ICP-OES 5110 (Agilent Technologies). 50 mg of sample were dissolved into aqua regia and then heated to 110 °C. After that, the sample was diluted with ultra-pure water and pumped into a nebulizer before to be introduced to the plasma flame. Intensity of the characteristic's wavelengths emitted by the Pt and Pd elements were measured by a photomultiplier and their concentrations were determined by comparing the intensities with that of reference samples as standards.

2.2- Nitrogen Physisorption

2.2.1- Theory

Textural properties of catalytic materials are tested by nitrogen physisorption measurements at liquid nitrogen temperature. Before analysis, the samples undergo a vacuum degassing process to eliminate any impurities. Pore size distribution, which is a commonly used method to detect the surface properties of the target materials, is a crucial parameter for characterizing their porosity. According to the definition of International Union of Pure and Applied Chemistry (IUPAC) porous solid materials can be categorized into three types based on the pore diameter (d): microporous materials ($d < 2$ nm), mesoporous materials ($2 \text{ nm} < d < 50$ nm), and

macroporous materials (d > 50 nm). The determination of pore size/volume distribution was calculated according to Barrett-Joyner-Halenda theory (BJH) [4] from the adsorption and desorption curves. The specific surface area can be estimated using the Brunauer-Emmett-Teller (BET) model [5] that predicts the quantity of molecules required to form a monolayer from the nitrogen adsorption isotherm at 77 K.

2.2.2- Experimental Method

Nitrogen physisorption measurements were performed on a Micromeritics TriStar II instrument (UCCS-Lille). The experiments were conducted using 0.2 g of powder sample, previously outgazed at 150 °C under vacuum for 2 h to eliminate any impurities that may alter the experiment. After that, the tube is immersed in a Dewar filled with liquid nitrogen where the adsorption process occurs. The desorption occurs when the sample is returned to room temperature. The same procedure was realized to both catalyst Pt/Al_2O_3 and Pd/Al_2O_3.

2.3- Hydrogen Chemisorption

2.3.1- Theory

Hydrogen chemisorption is a characterization technique that involves determining the amount of hydrogen chemisorbed to the surface of metal sites by dissociation of the H_2 molecule. It enables to deduce the number of hydrogen atoms chemisorbed per metal site (H/M), but also to estimate the dispersion and particle size of the metal sites. Prior the adsorption, reduction pretreatment was carried out to reduce all the material's active metal sites and ensure dissociative adsorption of hydrogen. The chemisorption temperature was adapted to the nature of metal (Pt or Pd). The protocols are detailed in the next section.

The mean particle size of metal (d) is calculated using the formula:

$$d = \alpha \frac{M}{\rho N_A} \frac{1}{D a_m}$$

where α is a geometrical parameter chosen equal to 6 supposing particles to be spherical, M is the atomic mass of the metal, ρ is the mass density (21.45 g/cm^3 for Pt and 12.02 g/cm^3 for Pd), N_A is the Avogadro's number (6.022×10^{23} mol^{-1}), D is the dispersion of Pt and Pd assuming

that H/M =1 and a_m is the surface area occupied by an atom of hydrogen on polycrystalline surface (8.07 $Å^2$) [6].

2.3.2- Experimental Method

H_2 chemisorption measurement was carried in a Micromeritics Autochem II instrument using a pulse technique (UCCS-Lille). In case of Pt/Al_2O_3, the catalyst (50 mg) was preheated in pure H_2 at 400 °C and outgassed in flowing Argon at 400 °C before the adsorption. Then the temperature of the catalytic bed was reduced to 30 °C in order to perform the measurement in which H_2 pulses (5 vol% H_2 in Ar) were injected until saturation.

For Pd/Al_2O_3, another protocol was applied because palladium reacts with H_2 at ambient temperature to form palladium hydrides (PdH_x) which decompose around 90 °C. Prior to the adsorption, the catalyst (50 mg) was pretreated under 5 vol% H_2/Ar at 400 °C for 5 h. The temperature of the catalyst sample was then reduced to 0 °C under Ar gas atmosphere in order to perform the chemisorption measurements during which H_2 pulses (5 vol% H_2 in Ar) were injected until saturation.

3- Catalytic Activity Measurements

3.1- Experimental Setup

The study of CO oxidation mechanism on Pt and Pd catalysts is carried out by coupling the SSITKA technique followed by mass spectrometry with transmission Fourier transform infrared (see Figure II-2). This technique is defined by an isotopic perturbation (transient regime) in a stationary medium, enabling crucial kinetic information (concentration, lifetime and coverage rate of intermediate species) to be obtained for understanding mechanistic steps, while simultaneously observing and discriminating active and spectator species adsorbed to the material surface. The equipment is controlled by an automated interface enabling rapid changes in gas flow, temperature control and repeatability of isotopic experiments. In addition, a specific cell reactor, optimized and modeled within the team, was used because it is capable of providing optimized times response for reliable quantification in time resolved experiments.

3.1.1. Gas distribution

The gas distribution system is fully automated by a Beckhoff® controller. The automate also controls 3 pneumatic valves which select the flows that can enter the reactor (Figure II-2).

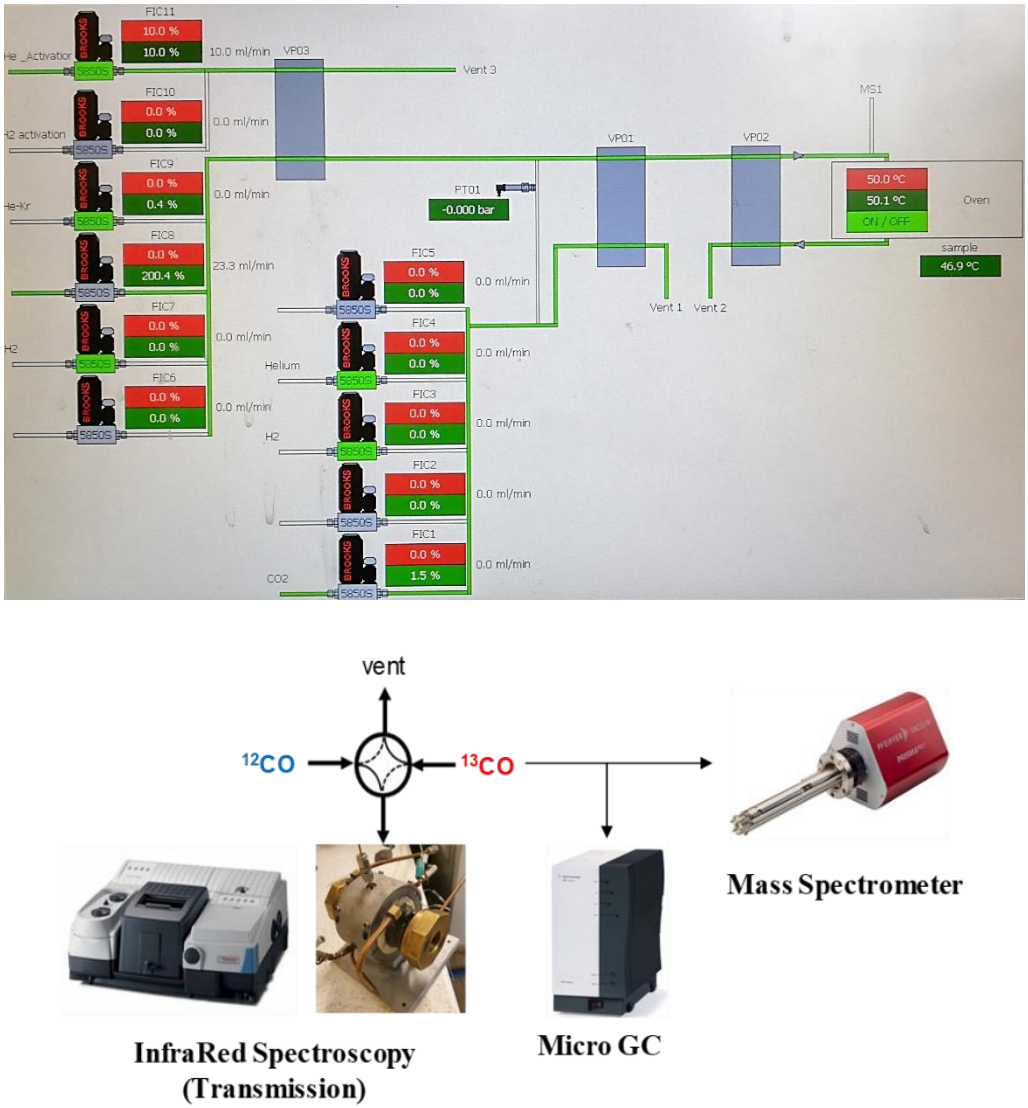

Figure II-2- Scheme of gas distribution and of overall setup (with analyzers).

The set-up contains 3 separate gas line (channels), each one with a specific use. The channel 3 used to do the pretreatment of the catalyst before reaction under He or 5% H_2/He (30 mL min^{-1} at 300 °C or 400 °C). The two other channels (1 and 2) are used to send the reaction mixture to the reactor cell containing the catalyst. In the first channel, a reaction mixture containing unlabeled carbon monoxide ^{12}CO, oxygen and helium was set. In the second channel, the reaction mixture containing the labeled carbon monoxide ^{13}CO, oxygen, krypton and methane

diluted l in He was used. Gas concentrations, flows and bottle compositions are summarized in the Table II-1.

Table II-1- Gas concentrations, flow and bottle compositions in channels 1 and 2.

Channel 1

Gas	In the reaction mixture		Bottle composition
	Concentration	Flow (mL min^{-1})	
^{12}CO	2000 ppm	0.48	5% ^{12}CO in He
O_2	10%	1.2	100% O_2
He	-	10.32	100% He

Channel 2

Gas	In the reaction mixture		Bottle composition
	Concentration	Flow (mL min^{-1})	
^{13}CO	2000 ppm	0.024	99% ^{13}CO
O_2	10%	1.2	100% O_2
CH_4	7960 ppm	4.776	2% CH_4 in He
Kr	5000 ppm	6	1% Kr in He

It is worth to note that the total flow mixture is kept constant in both channels at 12 mL min^{-1} as well as the concentrations of gas reactants (2000 ppm of CO and 10% O_2) to ensure isobaric conditions during SSITKA experiment. A pressure sensor is present between channels 1 and 2 to control the differential pressure. The gas flows of ^{12}CO and ^{13}CO are delivered by 2 Bronkhorst® *EL-FLOW prestige* mass flow controllers (0.014-0.7 mL min^{-1} flow range) using the Bronkhorst® *Flow Plot* program installed on PC. For other gases, the gas flows are controlled by Brooks® mass flow controllers thanks to the automate. All mass flow controllers were calibrated before catalytic test. A statistical study has been done in order to verify the reproducibility of the SSITKA method. The result is presented in Annex, Figure SII-1.

3.1.2. Reactor cell design

The reactor cell used for catalytic test is a homemade transmission IR cell with an internal low dead volume inferior to 0.5 cm^3 (Figure II-3).

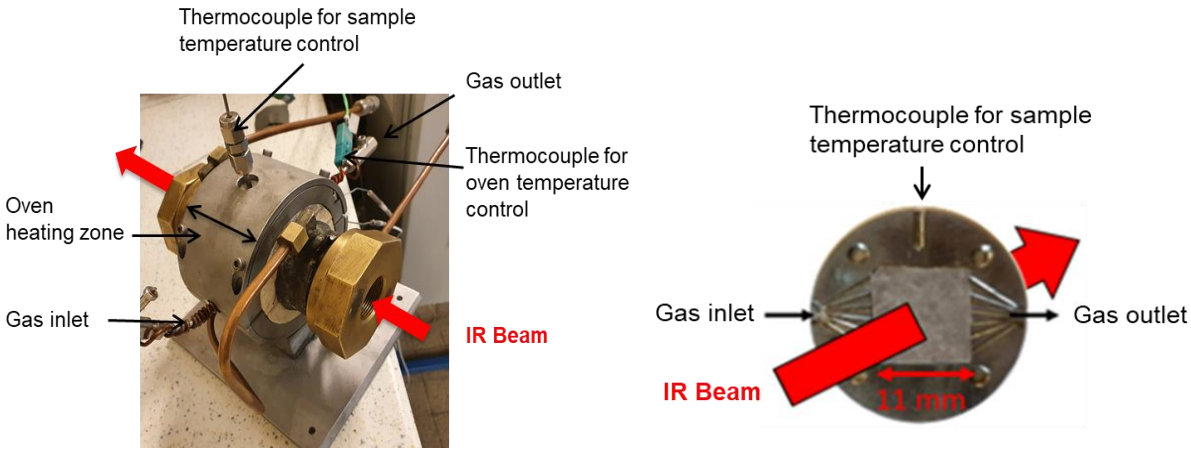

Figure II-3- Picture of IR transmission reactor cell (left) and of the sample holder (right) for the catalyst in square pellet form.

The transmission IR cell (so-called sandwich cell) consists of a series of 6 KBr windows and a sample holder placed in the center of the reactor. The reactor cell is loaded with the catalyst in a square pellet form. To do this, the sample is finely crushed and pressed into a disk (<1000 kg/cm^2). The circular pellet is cut into a square of 11mm*11 mm. The square pellet is placed in the sample holder. The wafer is only pressed on the border (less than half mm) by the two stainless steel plates of the sample holder (Figure II-3). In our conditions we assume that the complete surface of the square pellet is in contact with the gas mixture. The wafer thickness is approximately 100 µm taking into account density of sample, weight and surface of the wafer. It should be mentioned that the sample holder is rather thin (total thickness of approx. 2 mm) leading to dead volume around the wafer of 1.1*1.1*0.2=0.242 mL.

The oven covers a large part of the tube (approx. 6 cm) and both the temperature of the oven and of the sample are controlled and monitored using the Beckhoff® automate. Different programs of heating can be created with different ramp temperature. The oven can heat the catalyst up to 550 °C for thermal treatments as well as in situ/operando experiments. For that, a thermocouple is plugged directly in the sample holder (very close to the wafer). The KBr windows, with thermal conductivity slightly lower than stainless steel, are also heated by the oven. For these reasons we assume isothermal conditions in all directions. The calculation of concentration gradient between the feed and the external surface of particles shows that the gradient is negligible (below 1%). The cell was connected upstream to the system of gas delivery and downstream to the µ-gas chromatography and mass spectrometer analyzers.

3.1.3. Infrared Spectroscopy

The advantage of IR spectroscopy technique is that it allows for non-destructive and fast analysis of the sample.

The evolution of the adsorbed species on the catalytic material was analyzed by a Thermo Scientific Nicolet 6700 FTIR spectrometer equipped with a MCT detector. The IR spectra is collected in rapid-scan mode using 1 scan per spectra with a spectral resolution of 2 cm^{-1}. The optical velocity is set to 6.329 cm/s with an aperture of 69. A background spectrum is collected before and after the pretreatment of the catalyst. During reaction, series of spectra is recorded during 30 min to follow the evolution of adsorbed species during the reactant isotopic switch ($^{12}CO \rightarrow {}^{13}CO$). The spectrum of the empty cell with KBr windows is used as background to reprocess single beam spectra.

3.1.4. Micro Gas Chromatography

Micro Gas Chromatography (µ-GC) is a common type of chromatography used in analytical chemistry to detect and quantify gases in a mixture. The gas mixtures are introduced through the µ-injector and transferred into the capillary column (stationary phase) carried along by a continuous flow of inert carrier gas, which is the mobile phase. The column, where the chromatographic separation takes place, is typically enclosed within a temperature-controlled oven. When the separated components of the sample exit the column, they enter a micro–Thermal Conductivity Detector (µ-TCD), which detects and provides electronic signal proportional to the amount of the component present in the mixture.

The gas flow composition from IR cell inlet/outlet was analyzed by a µ-GC Varian 490 equipped with 2 columns and pure He as carrier gas. The calibrations were performed for all gases before the catalytic test.

3.1.5. Mass Spectrometer

Mass spectrometry is a valuable analytical tool used for determining the mass-to-charge ratio (m/z) of one or more molecules in a given sample. Generally, mass spectrometers serve a variety of purposes, including identifying unknown compounds through molecular weight determination, quantifying known compounds, and revealing the structural and chemical characteristics of

molecules. This apparatus is composed of three essential components: an ionization source, a mass analyzer, and ion detection system.

The process involves converting molecules into gas-phase ions, enabling them to be manipulated through external electric fields. Following ionization, these ions are meticulously sorted and separated based on their mass-to-charge ratios. The isolated ions are subsequently quantified and relayed to a data system, where their m/z ratios are recorded alongside their respective abundances.

The composition analysis of the gas entering and leaving the IR cell was performed using a quadrupole mass spectrometer (Pfeiffer QMS 200, 70 eV electronic impact, detection = electron multiplier). The mass-to-charge ratios of the different gases used in the catalytic tests were recorded every 20 ms on the *Quadstar* software. Each gas can be detected using different m/z ratios with different relative intensities. Mainly, the m/z with the highest intensity was chosen except for methane for which the m/z = 16 conflicts with ^{16}O intensity. The m/z of each gas with their relative intensities are given in the Table II-2 (values in bold have been recorded).

Table II-2- m/z of the gas used during the SSITKA experiment with their relative intensities: values recorded are in bold (from the library of Quadstar software).

Gas	m/z ratios	Relative i
He	**4**	100 %
CH_4	12	2.4 %
	13	7.7 %
	14	15.6 %
	15	85.8 %
	16	100 %
	17	1.2 %
^{12}CO	12	4.5 %
	14	6000 ppm
	16	9000 ppm
	28	100 %
	29	1.1 %
^{13}CO	13	4.5 %
	16	9000 ppm
	29	100 %
O_2	16	11.4 %
	32	100 %
	33	1000 ppm
	34	4000 ppm
$^{12}CO_2$	12	6 %
	13	1000 ppm
	16	8.5 %
	22	1.2 %
	28	11.4 %
	29	1000 ppm
	44	100 %
	45	1.3 %
	46	4000 ppm
$^{13}CO_2$	13	6 %
	16	8.5 %
	29	11.4 %
	45	100 %
	46	1000 ppm
	47	4000 ppm
Kr	42	10 %
	82	20.32 %
	83	20.3 %
	84	100 %
	86	30.53 %

3.2- Catalytic test

3.2.1- CO oxidation reaction in absence of CO_2

Around 2000 ppm CO/10% O_2/He gas flow mixture was sent to Pt/Al_2O_3 at a total flow rate of 12 mL min^{-1} (122 L h^{-1} g^{-1}). The temperature was increased from 50 °C up to 131 °C (1 °C/min) corresponding to a CO conversion of 11%. After 30 min of isotherm equilibration, the SSITKA-IR experiment was performed by switching the reactant from ^{12}CO to its labelled counterpart ^{13}CO at the same concentration, pressure and temperature. This $^{12}CO \rightarrow {}^{13}CO$ gas switch step was repeated three times to record the concentration evolution of reversibly adsorbed CO and C_x intermediates but also to check reproducibility (true steady-state achieved). 5000 ppm of Kr and 7900 ppm of CH_4 were used as inert gas for kinetic analysis. The SSITKA gas switching procedure can be summarized as:

$$2000\ ppm {}^{12}CO/10\%O_2/He \rightarrow 2000\ ppm {}^{13}CO/10\%O_2/5000\ ppm Kr/7900\ ppm CH_4/He$$

Finally, the catalyst was heated up to 300 °C (1 °C/min) and during cooling down, the SSITKA-IR experiment was subsequently repeated at the same CO conversion (11% − 136 °C).

The same procedure was realized for the Pd/Al_2O_3 catalyst. The SSITKA-IR experiment was realized at 116 °C with a conversion level around 8%. Then, the catalyst was heated up to 400 °C (1° C/min). During the cooling down, the SSITKA-IR experiment was repeated at both the same CO conversion (8% − 124 °C) and at the same temperature (116 °C − 5%).

3.2.2- CO oxidation reaction in presence of CO_2

Similar experiment procedure has been applied in presence of $^{12}CO_2$ for both catalysts. The initial pretreatment was conserved for both catalysts. Around 2000 ppm CO_2 was added to the gas flow mixture and sent to the catalyst at a total flow rate of 12 mL min^{-1}. The temperature was increased from 50 °C up to the temperature corresponding to the same CO conversion level obtained in the experiment without CO_2, i.e. 136 °C for Pt/Al_2O_3 and 116 °C for Pd/Al_2O_3. After 30 min of isotherm equilibration, the SSITKA-IR experiment was performed by switching the reactant from ^{12}CO to its labelled counterpart ^{13}CO at the same concentration, pressure and temperature. The new SSITKA gas switching procedure is:

$$2000\ ppm {}^{12}CO/10\%O_2/2000\ ppm {}^{12}CO_2/He$$

$$\rightarrow 2000\ ppm {}^{13}CO/10\%O_2/2000\ ppm {}^{12}CO_2/Kr/CH_4/He$$

Finally, the catalyst was heated up to 300 °C (1 °C/min). During cooling down, the SSITKA-IR experiment was repeated at the same CO conversion.

3.2.3- CO_2 exchange on alumina support

The γ-Al_2O_3 support was finely crushed and pressed into square pellet before to be loaded in the reactor IR cell. Prior to the $^{12}CO_2/^{13}CO_2$ exchange, the support was activated at 400 °C/5 h under 5% H_2/He (30 mL min^{-1}). Around 2000 ppm of $^{12}CO_2$/10% O_2/He gas flow mixture was sent to the support pellet at a flow of 12 mL min^{-1}. The temperature was increased from 50 °C to 116 °C then to 131 °C in order to realize the SSITKA-IR experiments. After 30 min of isotherm equilibration, the $^{12}CO_2$ was switched to its labeled counterpart $^{13}CO_2$ at the same concentration, pressure and temperature. This $^{12}CO_2$ → $^{13}CO_2$ gas switch step was repeated three times to check reproducibility. The SSITKA gas switching procedure is as follows:

2000 ppm$^{12}CO_2$/10%O_2/He → 2000 ppm$^{13}CO_2$/10%O_2/5000 ppmKr/7900 ppmCH_4/He

3.2.4- Pulses test

For this test, the catalyst was heated to a temperature corresponding to a determined CO conversion under $^{12}CO/O_2$ mixture. After 30 min of isotherm equilibration, a hydrogen pulse (1s) has been sent to the catalyst before performing the isotopic exchange step ^{12}CO →^{13}CO following the sequence below (Figure II-4). This sequence has been repeated several times to study the effect of H_2 pulses on CO conversion.

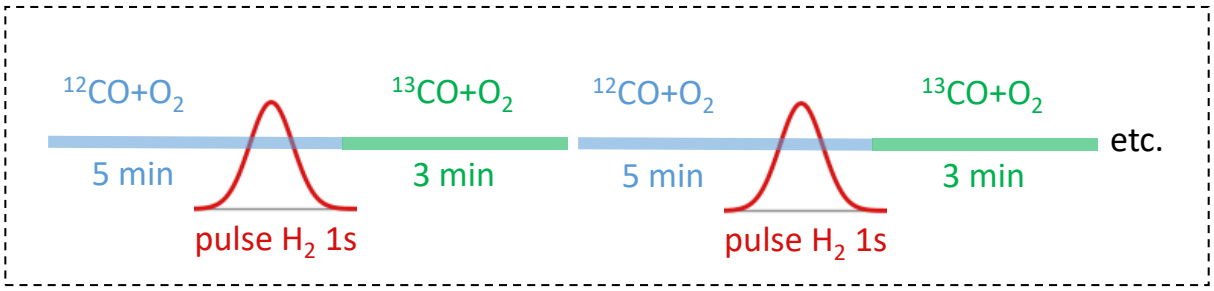

Figure II-4- Gas sequence used for pulses test.

The tests were followed using µ-GC analysis, to record the evolution of CO concentration, and IR spectroscopy analysis to observe the formation and evolution of adsorbed species.

References

1. Sietsma JRA, Jos van Dillen A, de Jongh PE, de Jong KP (2006) Application of ordered mesoporous materials as model supports to study catalyst preparation by impregnation and drying. In: Gaigneaux EM, Devillers M, De Vos DE, et al (eds) Studies in Surface Science and Catalysis. Elsevier, pp 95–102

2. Regalbuto J (2016) Catalyst Preparation: Science and Engineering. CRC Press

3. ICP-OES principle, ICP-OES Analysis, ICP-OES FAQ's | Agilent. https://www.agilent.com/en/support/atomic-spectroscopy/inductively-coupled-plasma-optical-emission-spectroscopy-icp-oes/icp-oes-faq. Accessed 19 Jun 2023

4. Barrett EP, Joyner LG, Halenda PP (1951) The Determination of Pore Volume and Area Distributions in Porous Substances. I. Computations from Nitrogen Isotherms. J Am Chem Soc 73:373–380. https://doi.org/10.1021/ja01145a126

5. Brunauer S, Emmett PH, Teller E (1938) Adsorption of Gases in Multimolecular Layers. J Am Chem Soc 60:309–319. https://doi.org/10.1021/ja01269a023

6. Bergeret G, Gallezot P (2008) Particle Size and Dispersion Measurements. In: Handbook of Heretogeneous Catalysis. Wiley-VCH, pp 738–765

7. What is FTIR Spectroscopy? https://www.sigmaaldrich.com/FR/fr/technical-documents/technical-article/analytical-chemistry/photometry-and-reflectometry/ftir-spectroscopy. Accessed 20 Jun 2023

Chapter III- Investigating the true role of hydrogen-carbonate species during CO oxidation reaction on PGM/Al_2O_3

1- Introduction

The CO oxidation reaction, one of the main reaction in three-way catalytic converter, is mainly catalyzed by supported Platinum Group Metals (PGMs) [1–4]. Despite the fact that CO oxidation appears to be a simple reaction commonly associated to the Langmuir-Hinshelwood mechanism [5, 6], the fundamental understanding of the process over supported PGM catalysts is still a matter of debate. During the last decade, many efforts have been made to acquire a comprehensive knowledge regarding the CO oxidation on Pd and Pt catalysts. Investigating the nature of active sites and the role of surface adsorbed species formed during the reaction, namely carbonyls, formates, carbonates, and hydrogen-carbonates is critical in order to better understand the mechanism at hand and increase the activity of the catalyst at low temperatures (T < 200 °C) in other hand.

In this thesis work, we focused on the role of carbonates and hydrogen carbonates in the CO oxidation. Indeed, their involvement in the reaction mechanism has not been explicitly demonstrated in the literature. Some authors have suggested that carbonates are active species [7, 8] while others have not provided explicit information regarding their role [9, 10]. In order to settle this debate, we choose in this chapter to perform SSITKA-transmission IR experiments during the oxidation of CO on Pt/Al_2O_3 and Pd/Al_2O_3 at low temperature. The powerful combination of SSITKA and IR has enabled us to identify the nature of surface adsorbed species and determine their kinetic parameters. Additionally, it has allowed for discrimination between active and inactive species in the reaction mechanism by highlighting the phenomenon of product re-adsorption.

2- Initial Catalyst Characterization

As described in the experimental section, the catalysts were prepared using impregnation method and characterized using various techniques after calcination. A summary of the characterization results can be found in Table III-1.

ICP-OES analysis was firstly performed to determine the final mass loading of metal. The loading of Pt supported on Al_2O_3 was estimated to 0.82 wt%, while the Pd/Al_2O_3 catalyst showed a Pd loading of around 0.87 wt%.

Textural properties such as specific surface area (SSA) and pore volume were also determined for both catalysts and the support material. IUPAC type IV isotherms were found for all alumina-based materials as expected in case of mesoporous materials (Figure III-1).

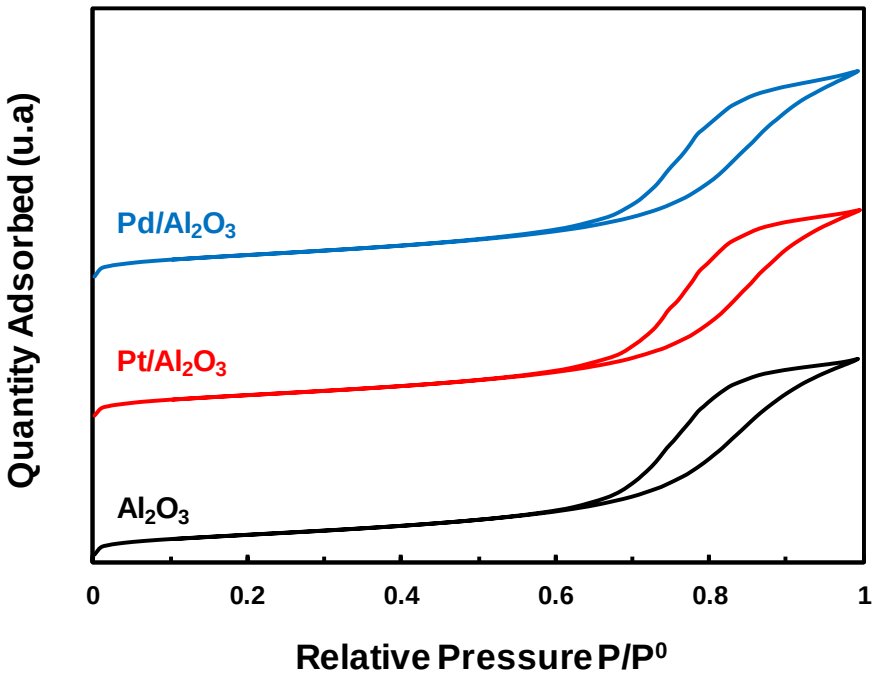

Figure III-1- N_2 isotherms for Al_2O_3, Pt/Al_2O_3 and Pd/Al_2O_3.

The bare support γ-Al_2O_3 has a SSA of around 225 m^2 g^{-1} and a pore volume of 0.76 cm^3 g^{-1}, both values within the expected range for this type of material. A slight increase is observed for metal supported catalysts with SSA and pore volume of 232 m^2 g^{-1} and 0.8 cm^3 g^{-1} for Pt/Al_2O_3, and 235 m^2 g^{-1} and 0.79 cm^3 g^{-1} for Pd/Al_2O_3.

Additionally, H_2 chemisorption pulse experiments were conducted to assess the dispersion level and average particle size of each catalyst. A dispersion of 68 % was found for Pt/Al_2O_3 corresponding to a mean particle size of 1.65 nm. Similarly, Pd/Al_2O_3 shows a dispersion of 71% corresponding to a mean particle size of 1.54 nm.

Table III-1- Textural properties, metal loading, dispersion and particle size determined on γ-Al_2O_3, Pt/Al_2O_3 and Pd/Al_2O_3 materials.

	Metal loading (%)	SSA (m^2 g^{-1})	Pore Volume (cm^3 g^{-1})	Dispersion (%)	Mean Particle Size (nm)
γ-Al_2O_3	-	225	0.76	-	-
Pt/Al_2O_3	0.82	232	0.80	68	1.65
Pd/Al_2O_3	0.87	235	0.79	71	1.54

3- SSITKA-IR studies on CO oxidation reaction

3.1- CO oxidation on Pt/Al_2O_3

For the catalytic test, 5.9 mg of Pt/Al_2O_3 was loaded into the IR reactor cell in the shape of a square wafer and pretreated during 5 h under He at 300 °C. The initial investigation has focused on the typical CO oxidation reaction introducing only CO and O_2 in the reactor. Subsequently, tests were conducted by adding $^{12}CO_2$ into the reaction mixture in order to check product re-adsorption effect.

3.1.1- CO oxidation without CO_2 in the reaction mixture

Firstly, a SSITKA-IR experiment during the CO oxidation on Pt/Al_2O_3 was realized at isobar and isotherm conditions following the sequence below:

$$2000\ ppm\,^{12}CO/10\%O_2/He \rightarrow 2000\ ppm\,^{13}CO/10\%O_2/Kr/CH_4/He$$

The normalized MS signals of ^{12}CO, ^{13}CO, $^{12}CO_2$, $^{13}CO_2$ and CH_4 are presented in Figure III-2 as a function of time after applying the reactant isotopic switching from ^{12}CO to ^{13}CO at low conversion (χ_{CO} = 11% at 131 °C) to maintain the chemical regime of the reaction. It should also be mentioned that the CO conversion is equal to the CO_2 yield, suggesting the absence of significant coke formation.

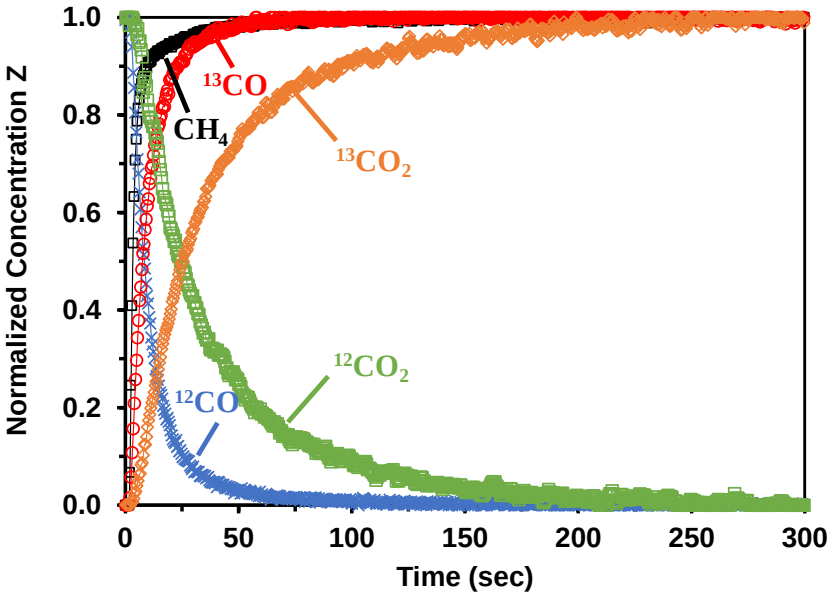

Figure III-2- Normalized concentration (Z) transient response curves of CH_4, ^{12}CO, ^{13}CO, $^{12}CO_2$ and $^{13}CO_2$ obtained during the SSITKA transient ($^{12}CO/O_2/He \rightarrow {}^{13}CO/O_2/Kr/CH_4/He$) on Pt/Al_2O_3 at 131 °C (χCO = 11%).

As required by the SSITKA theory [11], the sum of ^{12}CO and ^{13}CO normalized concentrations as well as $^{12}CO_2$ and $^{13}CO_2$ concentrations is equal to 1 throughout experimental time. Figure III-2 shows that both the transient response curves of ^{12}CO, ^{13}CO and $^{12}CO_2$, $^{13}CO_2$ cross each other at 0.5. We should mention here that the two curves of normalized concentrations of Kr and CH_4 overlap perfectly validating the use of CH_4 as a tracer in the current SSITKA test as illustrated in Figure III-3. It is worthy to note also that CH_4 doesn't react on Pt/Al_2O_3 at the investigated temperature (131 °C) while allowing for a time correlation (exact time of the reactant switch) with IR experiment. Indeed, the advantage of using CH_4 is that it vibrates under IR excitation showing a relatively intense IR band at 3017 cm^{-1} while of course, Kr is IR invisible.

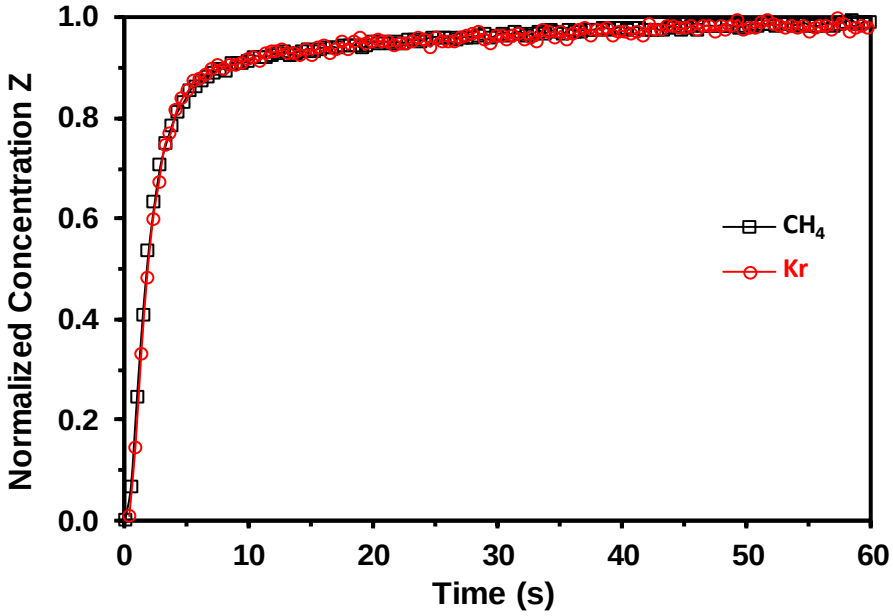

Figure III-3- Comparison between the normalized concentrations of CH_4 and Kr obtained during the SSITKA transient experiment ($^{12}CO/O_2/He \rightarrow {}^{13}CO/O_2/Kr/CH_4/He$) on Pt/Al_2O_3 at 131 °C.

As seen in Figure III-2, the ^{13}CO transient response curve lags behind that of the tracer (CH_4) due to the formation of reversibly adsorbed CO during oxidation reaction. Similarly, the $^{13}CO_2$ transient response curve lags behind that of ^{13}CO indicating that, in theory, the formation of $^{13}CO_2$ passes through one or more adsorbed reaction intermediates after ^{13}CO adsorption. Based on the SSITKA theory (eqs. I-5 and I-6, Chapter I section 3.2), the time integrations of observed delays between the response curves of CH_4 and ^{13}CO, then ^{13}CO and $^{13}CO_2$ provide the mean surface residence times τ of reversibly adsorbed CO (τ_{CO} = 5.2 s) and intermediates (τ_C = 29.9 s), respectively. The latter values allow calculating the surface concentrations and coverages of each species. A concentration of 13.4 µmol g^{-1} of CO surface-adsorbed species (N_{CO}) per gram of catalyst is reached corresponding to a Pt surface coverage of about 47% based on Pt amount

and dispersion (θ_{CO} = 0.47). This value can be compared to the expected CO surface coverage based on a heat of CO adsorption of 110 kJ mol^{-1} reported by Bourane et al. [12]. The theoretical CO surface coverage was estimated to be ~ 80% at 131 °C on Pt/Al_2O_3 catalyst. The lower value of θ_{CO} found here could be most likely explained by the competitive adsorption of oxygen, introduced in large amount, on the Pt surface sites.

In addition, a concentration of 9.8 µmol g^{-1} of C_x-adsorbed intermediate is determined. These values are summarized later in Table III-3.

The nature of the adsorbed species during the transient CO oxidation experiment on Pt/Al_2O_3 was simultaneously followed by *operando* transmission IR spectroscopy. Two spectra are presented in Figure III-4 corresponding to the $^{12}CO+O_2$ and $^{13}CO+O_2$ stages at the steady state (1 min after isotopic reactant switching in case of ^{13}CO) and 131 °C. These spectra were obtained after background treatment and subtraction of empty cell spectra.

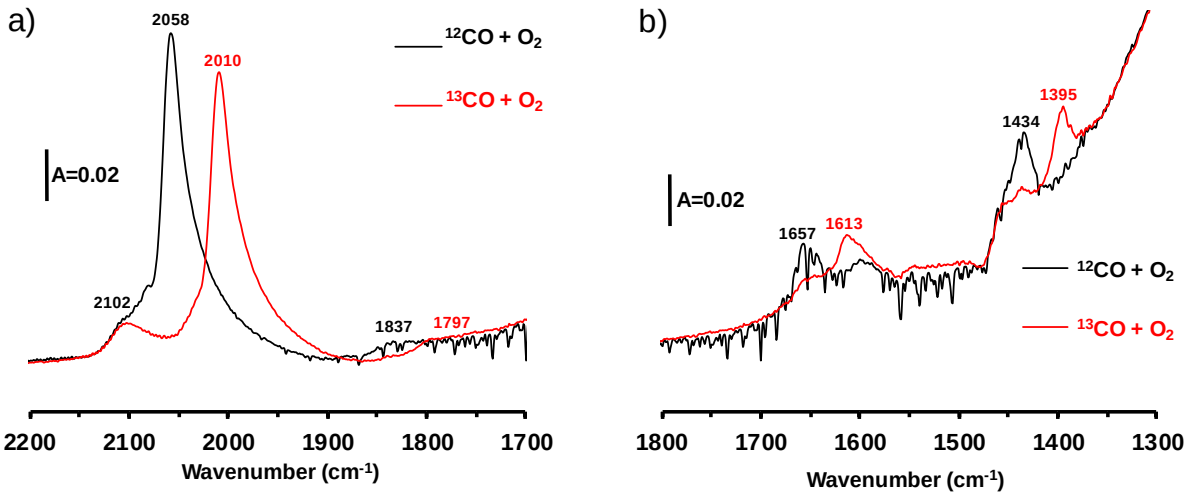

Figure III-4- IR spectra recorded on Pt/Al_2O_3 during CO oxidation at 131 °C in the presence of $^{12}CO/O_2/He$ (black) and $^{13}CO/O_2/Kr/CH_4$ /He (red) reaction mixtures: (a) carbonyl region and (b) carbonate region.

The black line in Figure III-4a, corresponding to the spectrum recorded in presence of ^{12}CO and O_2 in the carbonyl wavenumber region ($2200 - 1700\ cm^{-1}$), shows a strong IR band at 2058 cm^{-1}. This band corresponds to the stretching C ≡ O vibration of the ^{12}CO species linearly adsorbed on metallic Pt atom [12, 13]. A red shift of this band upon ^{13}CO exchange is observed, giving rise to a band at 2010 cm^{-1} (red line) corresponding to the ^{13} C-labelled linear carbonyls adsorbed on Pt^0. Carbonyls adsorbed on oxidized $Pt^{\delta+}$ are also observed on both spectra in Figure III-4a as a smaller IR bands around 2102 cm^{-1} [14]. No isotopic shift was observed in

that case. The presence of bridged ^{12}CO carbonyl species adsorbed on two metallic platina was also observed at 1837 cm^{-1} along with an isotopic ^{13}CO shift after the transient reactant exchange towards a wavenumber at 1797 cm^{-1}.

The carbonate region represented in Figure III-4b (1800 − 1300 cm^{-1}) can be decomposed with the bands at 1434 and 1657 cm^{-1} corresponding to the hydrogen-carbonate species ν(OCO) symmetric and ν(OCO) asymmetric stretching vibrations, respectively [15]. A band near 1215 cm^{-1} corresponding to the bending δ(OH) vibrations as well as the stretching ν(OH) band at higher wavenumber would be expected for hydrogen-carbonates species. However, due to the low energy in these ranges, we were not able to distinguish them (Figure SIII-1). As for linear carbonyl species, a red isotopic shift is clearly spotted over the hydrogen-carbonates O = C = O bands. Upon exchange with ^{13}CO, the bands at 1434 and 1657 cm^{-1} shift towards the bands at 1395 and 1613 cm^{-1}, respectively. Band assignments are summarized in Table III-2. A correlation is observed between experimental (i_{exp} = $\nu^{12}CO/\nu^{13}CO$) and theoretical (i_{theo} = $\sqrt{\mu 13CO/\mu 12CO}$ = 1.022) calculation of isotopic ratios.

Table III-2- Assignment of observed IR band during SSITKA $^{12}CO/^{13}CO$ oxidation experiment on Pt/Al_2O_3 and isotopic ratios.

Species	Vibration	Wavenumber (cm^{-1}) ^{12}CO	Wavenumber (cm^{-1}) ^{13}CO	$i_{exp} = \nu^{12}CO/\nu^{13}CO$
Linear carbonyls on Pt^0	Stretching ν(CO)	2058	2010	1.024
Linear carbonyls on $Pt^{\delta+}$	Stretching ν(CO)	2102	x	x
Bridged carbonyls on Pt^0	Stretching ν(CO)	1837	1797	1.022
Hydrogen-carbonates on alumina	Stretching ν(OCO) symmetric	1434	1395	1.028
	Stretching ν(OCO) asymmetric	1657	1613	1.027
	Bending δ(OH)	1215	x	x

The comparison of infrared spectroscopic data and kinetic measurements can grant us the ability to link a particular surface intermediate to a given reaction product [16]. The normalized concentration of CH_4, ^{13}CO, $^{13}CO_2$ obtained from MS and the IR band intensity evolution of asymmetric hydrogen carbonate at 1613 cm^{-1} are presented in Figure III-5 as a function of time. Please note that the IR signal at 1613 cm^{-1} was normalized taking into account the experimental

percentage of exchange at 300 s (area ratio between ^{12}C and ^{13}C bands from spectra in, i.e. 93%).

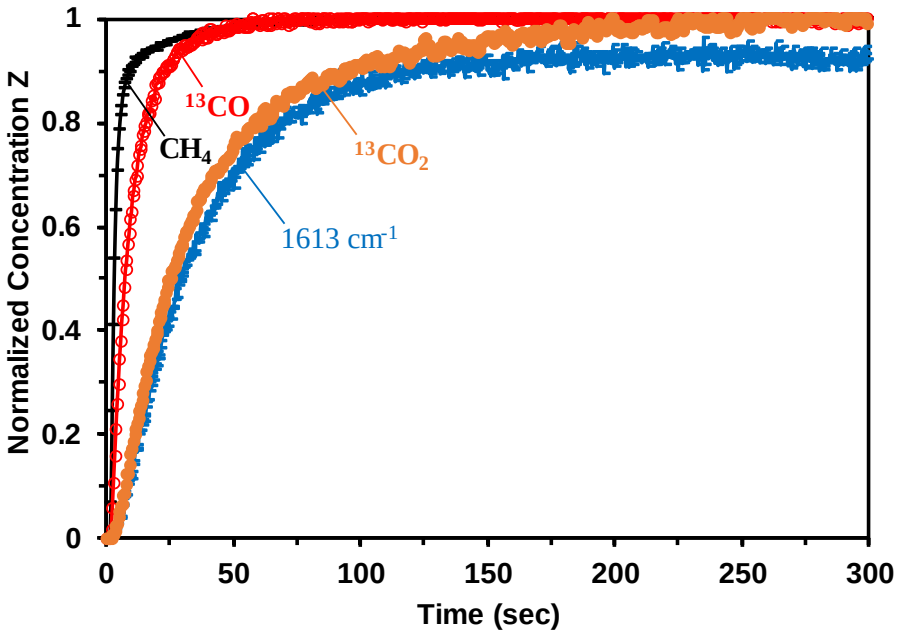

Figure III-5- Comparison of the relative rates of exchange between MS signals (^{13}CO, $^{13}CO_2$) and the IR band intensity evolution of hydrogen-carbonate (1613 cm^{-1}) species during SSITKA exchange on Pt/Al_2O_3 at 131 °C. The CH_4, inert gas, was used to match the zero time of both MS and IR signals.

The result indicates that the hydrogen carbonate exhibits a similar behavior, i.e., comparable formation rates, to that of $^{13}CO_2$ product. This suggests that hydrogen carbonates could be active intermediates in the formation of CO_2. However, a slight lag of the hydrogen carbonate band intensity curve behind the $^{13}CO_2$ transient response curve raises a doubt in determining clearly whether the hydrogen-carbonate species are formed simultaneously with CO_2 or after its formation. Further investigation and analysis are required to draw definitive conclusions regarding the role of hydrogen carbonate in CO_2 formation.

Indeed, as indicated in chapter 1, re-adsorption/desorption of product on inactive sites can occur during the reaction. This effect is difficult to avoid or interpret because, in that case, the experimental surface concentration of intermediates, obtained with SSITKA analysis, would be overestimated while the reactivity will be underestimated [11]. Shannon and Goodwin have proposed several experimental solutions to detect this problem of re-adsorption [17]. Among them, the addition of unlabeled product to the reactive feed stream able to block re-adsorption sites and compete with labeled product formed during the reaction. The overestimation of SSITKA C-pool due to CO_2 re-adsorption effect was previously reported by Efstathiou [18] in

the case of the water-gas shift reaction at high temperature and Calla et al. [19] for CO oxidation over Au particles. Further experiments were conducted following this idea.

3.1.2- CO oxidation in presence of CO_2 in the gas mixture

The same experiment of CO oxidation with O_2 on Pt/Al_2O_3 catalyst has been repeated by adding, in that case a significant amount of $^{12}CO_2$ in both SSITKA feeds resulting in the sequence below:

$$^{12}CO/O_2/\mathbf{2000\ ppm\ ^{12}CO_2}/He \rightarrow {}^{13}CO/O_2/\mathbf{2000\ ppm\ ^{12}CO_2}/Kr/CH_4/He$$

The normalized IR signals of ^{13}CO, $^{13}CO_2$ and CH_4 are represented as a function of time in Figure III-6 after applying the reactant isotopic switch at low conversion (χ_{CO} = 11% at 136 °C). It is important to mention here that the increase of temperature from 131 °C to 136 °C (to achieve the iso-conversion) will influence the calculated kinetic parameters, as the rate constant also rises. This apparent inhibitory effect of CO_2, in addition to potential experimental errors, is intriguing and may be linked to a slight decrease in the proportion of carbonyl species present at the Pt surface. This change could possibly be attributed to hysteresis-like phenomena [20].

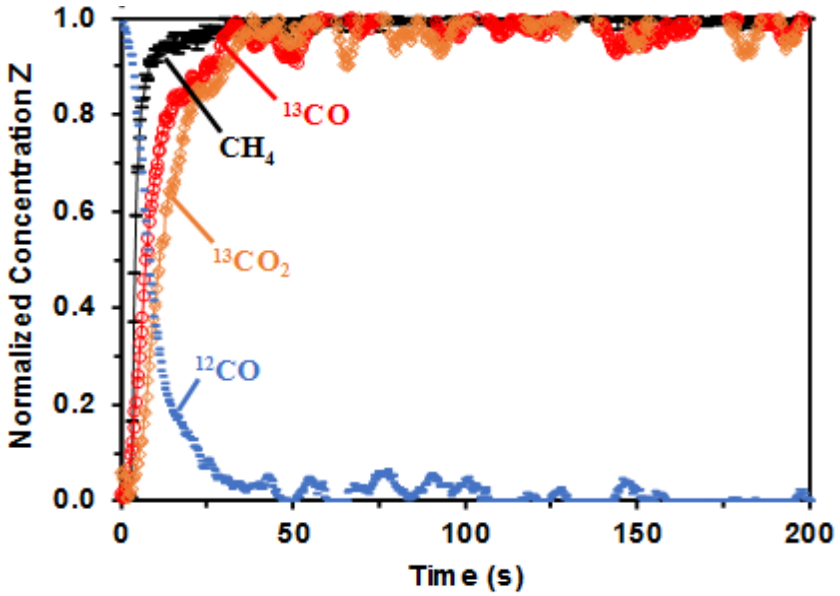

Figure III-6- Normalized concentrations of CH_4, ^{12}CO, ^{13}CO and $^{13}CO_2$ obtained after the SSITKA transient in the presence of CO_2 in the feed ($^{12}CO/O_2/^{12}CO_2/He \rightarrow {}^{13}CO/O_2/^{12}CO_2/Kr/CH_4/He$) on Pt/Al_2O_3 at 136 °C (χCO = 11%).

In the presence of CO_2, the mean surface residence times of reversibly adsorbed CO (τ_{CO}) and active intermediates (τ_C) appear to be equal to 5.2 s and 3.6 s, respectively. While no significant effect of CO_2 is observed on τ_{CO}, the area between the ^{13}CO and $^{13}CO_2$ curves vanished quasi-

completely leading to a drastic decrease of the τ_C value (Table III-3). Consequently, new calculations of the surface concentration and coverage of CO on catalytic surface from MS signals appear to be quite similar to the value determined without the presence of CO_2, i.e. N_{CO} = 12.8 µmol g^{-1} and θ_{CO} = 0.45, unlike those obtained for C_x-adsorbed intermediate with N_C dropping from 9.8 µmol g^{-1} to 1.4 µmol g^{-1} in the presence of CO_2. However, it is worth remembering that the total number of adsorbed species at the surface doesn't change, with the exception of any variations due to the temperature change. It is likely that the pool of C-containing intermediates was simultaneously filled by the $^{12}CO_2$ co-feeding, part that is not taken into account in this case.

Table III-3- Mean residence time τ, concentration N, surface coverage θ, and TOF_{ITK} of adsorbed CO and intermediates during SSITKA CO oxidation experiments on Pt/Al_2O_3 with and without the presence of CO_2 in the gas feed.

	T (°C)	τ_{CO} (s)	N_{CO} (µmol g^{-1})	θ_{CO} (on Pt)	τ_C (s)	N_C (µmol g^{-1})	TOF_{ITK} ($\times 10^{-2}$ s^{-1})
Without CO_2	131	5.2	13.4	0.47	29.9	9.8	1.4
With CO_2	136	5.2	12.8	0.45	3.6	1.4	2.7

The TOF_{ITK} were also calculated based on the concentration of all the active species that truly participate in the formation of the reaction product (N_{CO}+N_C). The value increases from 0.014 to 0.027 s^{-1} in the presence of CO_2. It is worth noting that this calculation takes into account the active sites defined by SSITKA measurements concentration and not the amount of Pt exposed surface sites determined by H_2-chemisorption as conventionally adopted for TOF_{chem} determination [21]. For comparison the TOF_{chem} was evaluated to 0.01 s^{-1} in both cases, giving us an underestimated value of the true site activity.

IR spectra analysis has also been performed to observe the evolution of adsorbed species on the catalytic surface after reactant exchange to ^{13}CO in the presence of CO_2.

Figure III-7 shows the IR spectra recorded during the $^{12}CO+O_2+^{12}CO_2$ and $^{13}CO+O_2+^{12}CO_2$ flow stages at the steady state (1 min after isotopic reactant switching in case of ^{13}CO) at 136 °C in both carbonyl (2200-1700 cm^{-1}) and carbonate region (1800-1300 cm^{-1}). These spectra were obtained after background treatment and subtraction of water and empty cell spectra.

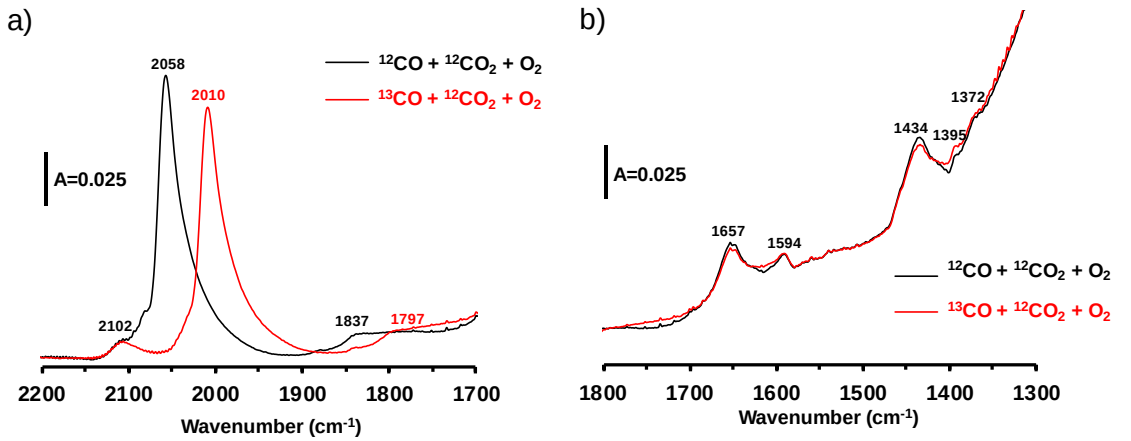

Figure III-7- IR spectra recorded during CO oxidation on Pt/Al_2O_3 at 136 °C in the presence of $^{12}CO/O_2/^{12}CO_2/He$ (black) and $^{13}CO/O_2/^{12}CO_2/Kr/CH_4/He$ (red) reaction mixture: (a) carbonyl region and (b) carbonate region.

As seen previously, a shift of the ^{12}CO linear species adsorbed on metallic Pt band initially at 2058 cm^{-1} towards the band of its labelled counterpart ^{13}CO adsorbed linear species at 2010 cm^{-1} was observed. Once again, CO-$Pt^{\delta+}$ carbonyls are observed at 2102 cm^{-1} in both feeds without any isotopic effect while bridged carbonyls (Pt_2CO) are shifted from 1837 cm^{-1} to 1797 cm^{-1} regarding to $^{12}CO \rightarrow {}^{13}CO$ reactant switch. Interestingly, in the presence of CO_2, the bands at 1434 cm^{-1} and 1657 cm^{-1} observed in the carbonate region and attributed to O = C = O symmetric and asymmetric stretching vibrations of hydrogen-carbonate species respectively, are not shifted after reactant exchange to ^{13}CO. Other low-intensity non-shifted bands appear at 1594 cm^{-1}, 1395 cm^{-1} and 1372 cm^{-1} which can be assigned to OCO asymmetric stretching, C–H bending and OCO symmetric stretching vibrations of formate species formed on alumina surface, respectively [22, 23].

The experiments were repeated in both the presence and absence of CO_2 to validate the reproducibility of our findings using a different wafer of Pt/Al_2O_3 (m= 7.3 mg). An increase of the surface residence time values (τ_{CO} and τ_c) is to note compared to the previous results (Figures SIII-2 and SIII-3). These variations can be attributed to the different experimental conditions in terms of mass and temperature between the two experiments. However, the results are consistent with our earlier observations that the presence of CO_2 has no significant effect on τ_{co} and leads to a large decrease in the area between ^{13}CO and $^{13}CO_2$ (see table SIII-1). Likewise, similar observations were made for the IR spectra in both the presence and absence of CO_2 (Figures SIII-4 and SIII-5). The linear and bridged carbonyls exhibited a shift toward

lower wavenumbers during the $^{12}CO \rightarrow ^{13}CO$ exchange in both conditions, while the hydrogen-carbonate species did not show any significant shift in the presence of CO_2.

3.1.3- Discussion on Pt/Al_2O_3

The CO adsorption on Pt/Al_2O_3 mainly forms linear carbonyl type species adsorbed on metallic Pt^0 as observed at 2058 cm^{-1} (^{12}CO) and 2010 cm^{-1} (^{13}CO) with *operando* IR spectroscopy and, in lower extent, bridged carbonyl species on metallic Pt^0 at 1837 cm^{-1} (^{12}CO) and 1797 cm^{-1} (^{13}CO) (Figure III-4). Moreover, after 1 min of the isotopic exchange, a complete vanish of the bands at 2058 cm^{-1} and 1837 cm^{-1} is observed which can be related to a high exchange rate and so high reactivity of CO adsorbed on Pt^0 during the experiment. This result is furthermore coherent with the gas phase evolution of ^{13}CO observed by mass spectrometry (Figure III-2) that reaches its maximum at around 60 s. In the meantime, no isotopic exchange during the $^{12}CO \rightarrow ^{13}CO$ SSITKA experiment was observed for carbonyls adsorbed on $Pt^{\delta+}$ suggesting a low reactivity and so their spectator nature in CO oxidation reaction at low temperature.

An important lag was observed initially between the normalized ^{13}CO and $^{13}CO_2$ concentration curves indicating in theory the formation and participation of C-adsorbed intermediates in the CO_2 production. According to the IR results (Figure III-4) hydrogen-carbonate species seems to be the most serious contender to play the role of active intermediates in the CO oxidation reaction due to a high $^{12}C \rightarrow ^{13}C$ exchange rate at 131 °C comparable to the rate of CO_2 product formation (Figure III-5). The SSITKA-IR experiment in the presence of CO_2 in the feed was performed to obtain additional information concerning the re-adsorption effect and the role of hydrogen-carbonate during CO oxidation. As a matter of fact, the simultaneous saturation of the catalyst surface with adsorbed $^{12}CO_2$ reduces drastically the amount of C-containing intermediate species (N_C) at the same CO conversion and reaction temperature. This result proves that the lag firstly observed between ^{13}CO and $^{13}CO_2$ MS curves during the SSITKA experiment without CO_2 is due in reality to the re-adsorption of the CO_2, produced by the CO oxidation, on the surface of the catalyst support rather than to intermediate formation or reactivity to form CO_2. IR spectra recorded in the presence of $^{12}CO_2$ in the reactant feed also confirm this trend in which IR bands of hydrogen-carbonate species don't show any $^{12}C \rightarrow ^{13}C$ isotopic shift anymore. This observation clearly indicates that their formation is induced in that case by the adsorption of $^{12}CO_2$ already present in the gas feed rather than the conjugation of the reactants $^{13}CO+O_2$ with surface hydroxyls from alumina.

3.2- CO oxidation on Pd/Al_2O_3

Similarly to Pt/Al_2O_3, the catalytic reaction of CO oxidation over Pd/Al_2O_3 was performed. A wafer of 7.5 mg of Pd/Al_2O_3 was loaded into the IR reactor cell and reduced at 400 °C for 5 h under 5% H_2/He prior to the reaction test. The reaction was initially investigated in absence of CO_2 in the reaction mixture, then CO_2 was co-feeded to highlight the re-adsorption effect.

3.2.1- CO oxidation in absence of CO_2 in gas mixture

In a first approach, the SSITKA CO oxidation reaction was performed without the presence of CO_2 in the gas mixture. The following isotopic switch was performed at 116 °C in steady state conditions:

$$2000\ ppm\ ^{12}CO/10\%O_2/He \rightarrow 2000\ ppm\ ^{13}CO/10\%O_2/Kr/CH_4/He$$

Figure III-8 shows the isotopic transient response curves of ^{12}CO, ^{13}CO, $^{12}CO_2$, $^{13}CO_2$ and CH_4 right after the isotopic switch. As expected, isotopic peers cross each other at the normalized value of 0.5 ensuring the right condition of the exchange. The CO conversion is here limited to 8.5% to maintain the chemical regime of the reaction, and it should be noted that no coke formation was detected.

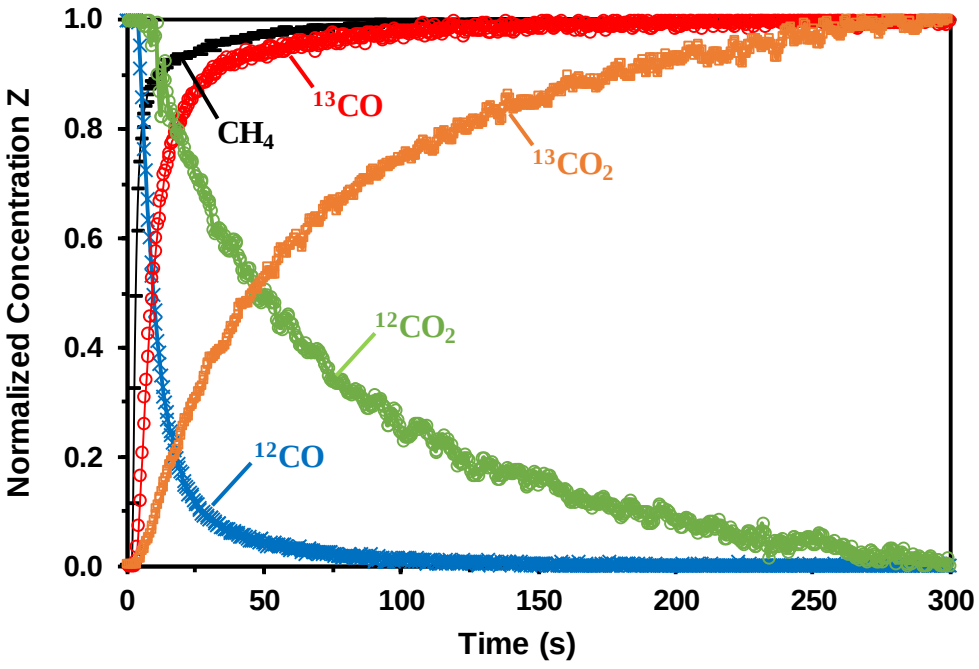

Figure III-8- Normalized concentration (Z) transient response curves of CH_4, ^{12}CO, ^{13}CO, $^{12}CO_2$ and $^{13}CO_2$ obtained during the SSITKA transient ($^{12}CO/O_2/He \rightarrow {}^{13}CO/O_2/Kr/CH_4/He$) on Pd/Al_2O_3 at 116 °C (χCO = 8.5%).

The ^{13}CO transient response curve lags behind that of CH_4 due to a detectable concentration of reversibly adsorbed carbonyls on Pd during the reaction. In the same manner, the transient response curve of $^{13}CO_2$ lags behind the ^{13}CO response curve and this is attributed to the formation of one or several intermediates from the reactants, before they lead to the formation of the product of the reaction, CO_2.

The area integrations between the response of CH_4 tracer and ^{13}CO, and that between the ^{13}CO and $^{13}CO_2$ lead to the mean surface residence time τ of reversibly adsorbed CO (τ_{CO} = 8.6 s) and C-containing intermediates (τ_C = 55.5 s). The surface concentrations and surface coverages of these adsorbed species are reported in Table III-5**.** A concentration N_{CO} of adsorbed carbonyls of around 17.4 µmol per gram of catalyst was obtained, corresponding to a surface coverage θ_{CO} on Pd (based on Pd amount and dispersion) of ~30%. This value can be compared to the expected CO surface coverage based on a heat of CO adsorption of 29 kcal/mol reported by Szanyi et *al.* [24]. The theoretical CO surface coverage was estimated to be ~ 95% at 116 °C on a bare Pd (100) surface. The lower value of θ_{CO} found here could be partly explained by the competitive adsorption of oxygen, introduced in large amount, on the Pd surface sites. In addition, the concentration of C-containing intermediates, N_C was estimated to 10.4 µmol per gram of catalyst.

IR transmission spectra were recorded before and after the reactant gas switch to determine the chemical nature of adsorbed species during the CO oxidation reaction on Pd/Al_2O_3. Figure III-9 presents two spectra showing the composition of adsorbed phase on the surface of Pd/Al_2O_3 at 116 °C under the reaction mixtures of $^{12}CO + O_2$ (in black) and $^{13}CO + O_2$ (in red) at the steady state reaction conditions. These spectra were obtained after background treatment and subtraction of empty cell spectra.

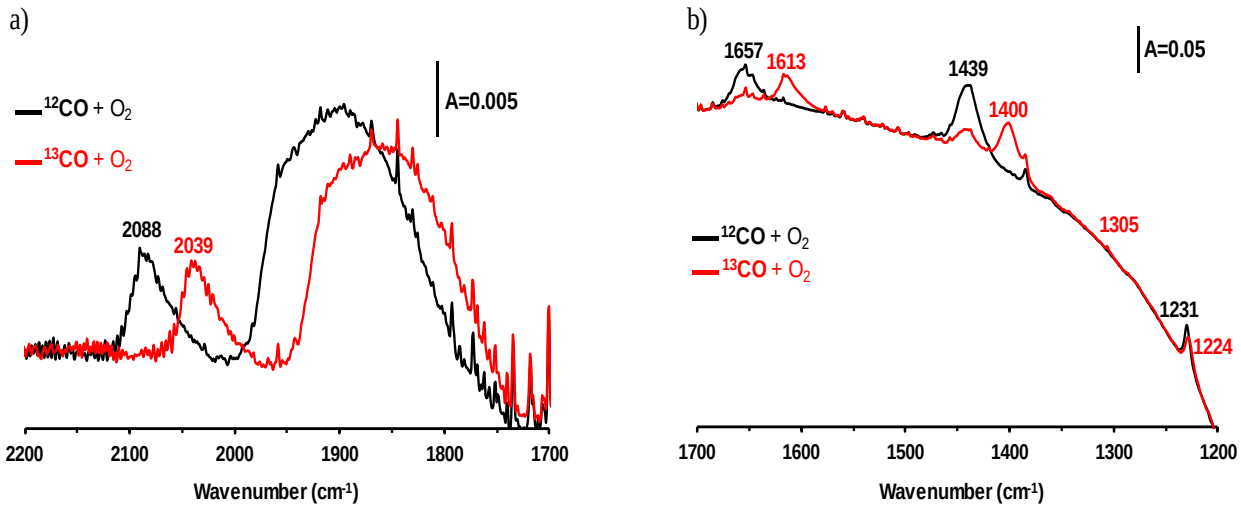

Figure III-9- IR spectra recorded on Pd/Al_2O_3 during CO oxidation at 116 °C in the presence of $^{12}CO/O_2/He$ (black) and $^{13}CO/O_2/Kr/CH_4/He$ (red) reaction mixture: (a) carbonyl region and (b) carbonate region.

In the carbonyl region (2200-1700 cm^{-1}) shown in Figure III-9a, the IR band observed at 2088 cm^{-1} (black signal) before the isotopic switch is attributed to linear ^{12}CO adsorbed on Pd. According to the literature, linear CO are more likely to be adsorbed on metallic Pd^0 particle corner sites or (111) facets [25, 26]. The larger IR signal observed between 2000 and 1800 cm^{-1} can be decomposed into several overlapping infrared bands corresponding to bridged and multi-bonded ^{12}CO adsorbed on palladium [27, 28]. After applying the isotopic exchange (Figure III-9a, red curve), a complete red shift of the linear and bridged/multi-bonded CO bands adsorbed on Pd was observed, giving rise to new ^{13}CO IR bands at 2039 and 1950-1750 cm^{-1}, respectively.

The formation of hydrogen-carbonate species on the alumina support was detected in the carbonate region (1700-1200 cm^{-1}) shown in Figure III-9b. The IR bands at 1657 cm^{-1} and 1439 cm^{-1} appearing under ^{12}CO conditions were attributed to the asymmetric and symmetric stretching $\nu(O^{12}CO)$ vibrations of hydrogen-carbonate species, respectively [15, 29, 30]. The latter are accompanied by a small band near 1231 cm^{-1} corresponding to the bending $\delta(OH)$ vibration. Unfortunately, due to the low extinction coefficient in the stretching OH region, the expected $\nu(OH)$ band of these species was not clearly observed, as well as the negative OH band due to the consumption of a surface hydroxyl group present on the γ-alumina surface. Upon exchange with ^{13}CO, the hydrogen-carbonate bands recorded at 1231, 1439 and 1657 cm^{-1} are, in large part (≈75 %), red-shifted providing new IR bands centered at 1224, 1400 and 1613 cm^{-1}, respectively. Another IR band was detected at 1384 cm^{-1} in both spectra as shown in Figure III-9b, which does not appear to be impacted by the isotopic $^{12}CO \rightarrow {}^{13}CO$ exchange, evidencing its spectator nature. In addition, gaseous methane was also detected after the

transient exchange with ^{13}CO (red spectrum) by the appearance of an extremely weak absorbance at 1305 cm^{-1}. Band assignments are summarized in Table III-4. A correlation is clearly observed between experimental (i_{exp} = $\nu^{12}CO/\nu^{13}CO$) and theoretical (i_{theo} = 1.022) calculation of isotopic ratios.

Table III-4- Assignment of observed IR band during SSITKA $^{12}CO/^{13}CO$ oxidation experiment on Pd/Al_2O_3 and isotopic ratios.

Species	**Vibration**	**Wavenumber (cm^{-1}) ^{12}CO**	**Wavenumber (cm^{-1}) ^{13}CO**	**i_{exp} = $\nu^{12}CO/\nu^{13}CO$**
Linear carbonyls on Pd	Stretching ν(CO)	2088	2039	1.024
Bridged carbonyls on Pd^0	Stretching ν(CO)	2000-1800	1950-1750	x
Hydrogen carbonates on Alumina	Stretching ν(OCO) asymmetric	1657	1613	1.027
	Stretching ν(OCO) symmetric	1439	1400	1.027
	Bending δ(OH)	1231	1224	1.005

The normalized concentration of CH_4, ^{13}CO, $^{13}CO_2$ obtained from MS and the IR band intensity evolution of linear ^{13}CO (2039 cm^{-1}) and hydrogen carbonate (1613 cm^{-1}) are presented in Figure III-10 as a function of time. Please note that the IR signal at 1613 cm^{-1} was normalized taking into account the real percentage of exchange at 300 s (area ratio between ^{12}C and ^{13}C bands from spectra in Figure III-9b, i.e. 75 %).

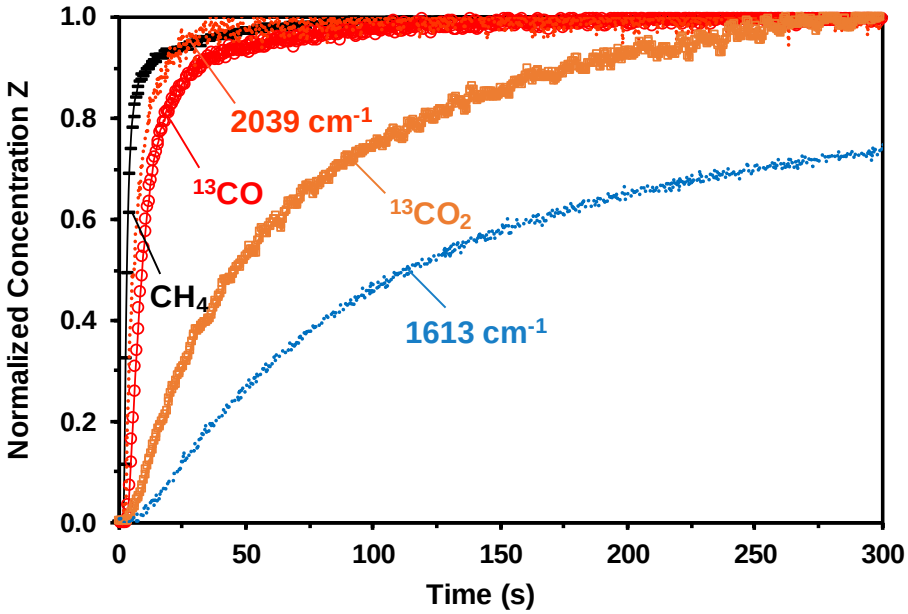

Figure III-10- Comparison of the relative rates of exchange between MS signals (^{13}CO, $^{13}CO_2$) and the IR band intensity evolutions of linear ^{13}CO (2039 cm^{-1}) and hydrogen-carbonate (1613 cm^{-1}) species during SSITKA exchange on Pd/Al_2O_3 at 116 °C. The CH_4, inert gas, was used to match the zero time of both MS and IR signals.

The comparison of signals reveals that the linear ^{13}CO adsorbed IR band at 2039 cm^{-1} follows the same pathway as the response of ^{13}CO in MS. This clearly supports the idea that linear carbonyls adsorbed on metallic Pd play the role of active species in CO oxidation reaction. In contrary, the IR band at 1613 cm^{-1} corresponding to asymmetric ν(OCO) vibration of hydrogen-carbonate species do not follow the same pathway than the normalized concentration evolution of the product $^{13}CO_2$. This latter band is lagged after the $^{13}CO_2$ transient response curve. That behavior tends to confirm the spectator role of hydrogen-carbonate species in reaction mechanism. In order to confirm this latter result, the experiment was repeated introducing unlabeled product to the reactive feed stream and thus demonstrate the re-adsorption process.

3.2.2- CO oxidation in presence of CO_2 in the gas mixture

After adding 2000 ppm of $^{12}CO_2$ in both reaction feeds, the following SSITKA switch was performed on Pd/Al_2O_3:

$$^{12}CO/O_2/\mathbf{2000\ ppm\ ^{12}CO_2}/He \rightarrow {}^{13}CO/O_2/\mathbf{2000\ ppm\ ^{12}CO_2}/Kr/CH_4/He$$

The normalized transient response curves of CH_4, ^{13}CO and $^{13}CO_2$ following the reactant isotopic switch are plotted as a function of time in Figure III-11.

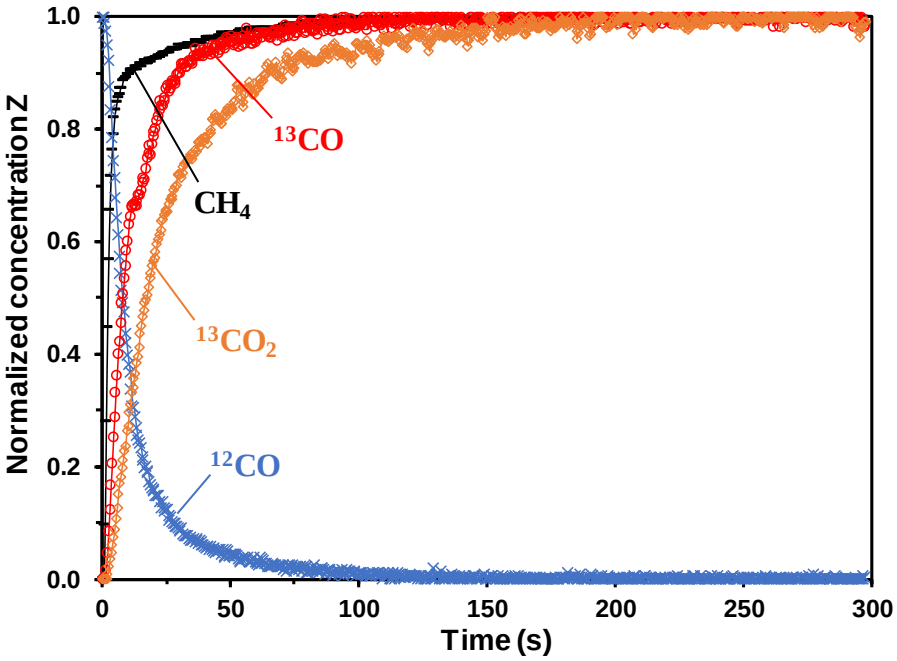

Figure III-11- Normalized concentration evolution response curves of CH_4, ^{12}CO, ^{13}CO and $^{13}CO_2$ obtained following the SSITKA switch in the presence of $^{12}CO_2$ in the feed ($^{12}CO/O_2/^{12}CO_2/He \rightarrow {}^{13}CO/O_2/^{12}CO_2/Kr/CH_4/He$) on Pd/Al_2O_3 at 131 °C (χ_{CO} = 8.8%).

A similar CO conversion as in the previous experiment was maintained (χ_{CO} = 8.8%) by increasing the temperature to 131 °C. Once again, this increase in temperature and apparent inhibitor effect of CO_2 might be related to a change in the proportion of carbonyl species at the Pd surface leading to hysteresis-like phenomena [20].

As a direct effect of adding CO_2 in the feed gas stream, the area between the two ^{13}CO and $^{13}CO_2$ response curves decreased significantly, corresponding to a mean residence time (τ_C) of 18.6 s, three times lower than the value obtained without CO_2 co-addition in the reaction feed gas mixture. The concentration of ^{13}C-containing intermediates (N_C) has decreased to the same extent, ca. 3.7 µmol per gram of catalyst. The different kinetic parameters obtained in the presence and absence of CO_2 are summarized in Table III-5.

Table III-5- Mean residence time τ, concentration N, surface coverage θ and TOF_{ITK} of adsorbed CO and C-containing intermediates calculated from the SSITKA CO oxidation experiments on Pd/Al_2O_3 with and without the presence of CO_2 in the gas feed.

	T (°C)	τ_{CO} (s)	N_{CO} (µmol g^{-1})	θ_{CO} (on Pd)	τ_C (s)	N_C (µmol g^{-1})	TOF_{ITK} ($\times 10^{-3}$ s^{-1})
Without CO_2	116	8.6	17.4	0.30	55.5	10.4	6.7
With CO_2	131	8.2	16.5	0.28	18.6	3.7	9.7

On the contrary, the presence of CO_2 did not have a significant impact on the mean surface residence time and the concentration of reversibly adsorbed carbonyls. Only a small decrease of τ_{CO}= 8.2 s and N_{CO}= 16.5 µmol g^{-1} was observed in the presence of CO_2 due to the slight increase in temperature (change in reaction rate constant, k) and CO conversion (mainly effect of partial pressure of CO). The TOF_{ITK} were also calculated based on the concentration of all the active species that truly participate in the formation of CO_2 (N_{CO}+N_C). The value increases from 0.0067 to 0.0097 s^{-1} with CO_2 co-feeding. For comparison the TOF_{chem}, calculated from Pd amount and dispersion, was evaluated to 0.003 s^{-1} in both cases. Once again, TOF_{chem} seems to underestimate the actual activity of Pd sites (TOF_{ITK}) since the value takes into account non-active Pd sites.

The evolution of adsorbed species on the catalytic surface has been followed by transmission IR spectroscopy during the isotopic exchange in order to observe the effect of the presence of CO_2 in the reactant mixture. The IR spectra recorded at 131 °C in both $^{12}CO+O_2+^{12}CO_2$ and $^{13}CO+O_2+^{12}CO_2$ steady states are presented in Figure III-12. These spectra were obtained after background treatment and subtraction of the background treatment and subtraction of water and empty cell spectra.

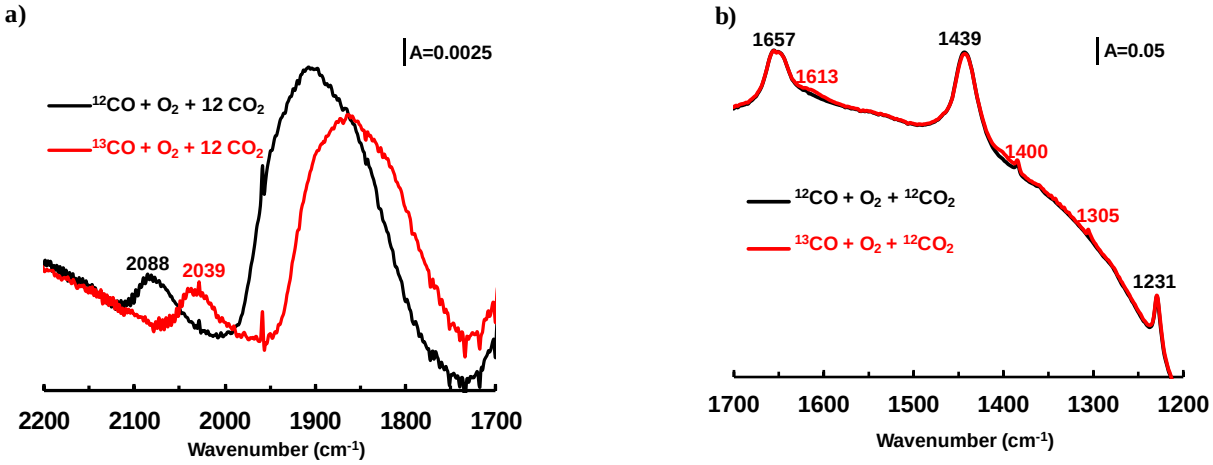

Figure III-12- IR spectra recorded on Pd/Al_2O_3 during CO oxidation at 131 °C in the presence of $^{12}CO/O_2/^{12}CO_2/He$ (black) and $^{13}CO/O_2/^{12}CO_2/Kr/CH_4/He$ (red) reaction mixture: (a) carbonyl region and (b) carbonate region.

Figure III-12a shows the red isotopic shift of the IR bands corresponding to linear, bridged and multi-bonded carbonyls on Pd from 2088 cm^{-1} and 2000-1800 cm^{-1} to 2039 cm^{-1} and 1950-1750 cm^{-1} range, respectively. In contrast, IR bands at 1657, 1439 and 1231 cm^{-1} in the carbonate region (Figure III-12) previously assigned to hydrogen-carbonates species, were only ^{12}C →

^{13}C shifted to a very small extent (< 1.5 %) in the presence of CO_2 in the feed. Again, no shift was observed for the small IR band appeared at 1384 cm^{-1}.

3.2.3- Discussion on Pd/Al_2O_3

Mainly linear, bridged, and multi-bonded carbonyl-type species were formed during the CO adsorption on metallic Pd^0 at low temperature. The corresponding $\nu(^{12}C{\equiv}O)$ IR bands observed at 2088 cm^{-1} and in the 2000-1800 cm^{-1} range (Figure III-9a) under ^{12}CO reactant feed disappeared completely ~2 min after the isotopic transient switch towards ^{13}CO, giving rise to the formation of new $\nu(^{13}C{\equiv}O)$ bands at 2039 cm^{-1} and 1950-1750 cm^{-1}. This trend is consistent with the gas phase evolution of ^{13}CO observed by mass spectrometry (Figure III-8), where it reached its maximum concentration after 150 s. The fast $^{12}C \rightarrow {}^{13}C$ isotopic exchange of carbonyls observed in SSITKA-IR demonstrates the high exchange of molecularly adsorbed ^{12}CO with gaseous ^{13}CO and their reactivity towards subsequent reaction intermediates formed in the mechanism of CO oxidation on Pd/Al_2O_3.

Initially, the normalized concentration of ^{13}CO and $^{13}CO_2$ response curves showed a significant time lag (Figure III-8), indicating that in theory the formation of CO_2 product passes through various active intermediates after CO adsorption on Pd. The *operando* IR results (Figure III-9b) reveal that hydrogen-carbonate species are formed on the alumina surface and follow a $^{12}C \rightarrow {}^{13}C$ isotopic red-shift exchange during the experiment. Other weak absorption bands were also observed by IR on the catalyst surface in the carbonate region, but these were clearly identified as *spectator* species in the CO oxidation at low temperatures due to their inability to follow the isotopic exchange. It is worth to note that the $^{12}C \rightarrow {}^{13}C$ exchange of the hydrogen-carbonate species observed by IR on alumina is very slow compared to surface carbonyl exchange, and even incomplete after 5 min of reaction (Figure III-10– 1613 cm^{-1} curve). Moreover, this trend is not consistent with the transient response curve recorded for $^{13}CO_2$ product formation by mass spectrometry.

The addition of 2000 ppm of CO_2 in the feed gas stream proved unequivocally against the previous SSITKA-IR conclusion about the active role of hydrogen-carbonate species in CO oxidation reaction on Pd/Al_2O_3. Indeed, the presence of CO_2 has led to a drastic reduction (three times) of the amount of ^{13}C-containing intermediate species (N_C) compared to the experiment performed without CO_2 at similar CO conversion. Also, the IR spectra recorded in the presence

of CO_2 in the carbonate region (Figure III-12b) show negligible $^{12}C \rightarrow {}^{13}C$ isotopic shift of the IR bands attributed to hydrogen-carbonates. This result confirms clearly that the hydrogen-carbonate species formed during CO oxidation reaction is only a spectator species and *does not* participate in the reaction mechanism of CO_2 formation. This conclusion is also supported by the lag observed in between the relative rate of exchange of $^{13}CO_2$-MS signal and the 1613 cm^{-1} IR band intensity evolution curve of hydrogen-carbonate species (Figure III-10). Therefore, most of the significant time lag firstly observed between ^{13}CO-MS and $^{13}CO_2$-MS signals during the SSITKA experiment without CO_2 in the feed could be attributed to the re-adsorption of CO_2, produced by the CO oxidation, on the surface of the alumina support rather than to the formation of some active intermediate species towards CO_2 formation.

3.3- CO_2 exchange on Al_2O_3 support

As suggested by SSITKA-IR experiment on CO oxidation in presence of CO_2, the hydrogen-carbonate formation will be more likely due to the re-adsorption of the CO_2 product on alumina by combination with a surface hydroxyl group. In order to confirm this hypothesis, a $^{12}CO_2/^{13}CO_2$ SSITKA-IR exchange was performed directly on the bare alumina support, after reduction under H_2 at 400°C, applying the following step-gas switch at 116 and 131 °C:

2000 ppm $^{12}CO_2$/10% O_2/He → 2000 ppm $^{13}CO_2$/10% O_2/Kr/ CH_4/He

The objective of this experience is to confirm the formation route of hydrogen-carbonate species on the support without contribution of the metal. The transient normalized concentration response curves of CH_4 and $^{13}CO_2$ obtained on the alumina following the $^{12}CO_2 \rightarrow {}^{13}CO_2$ switch at 116 and 131 °C are presented in Figure III-13.

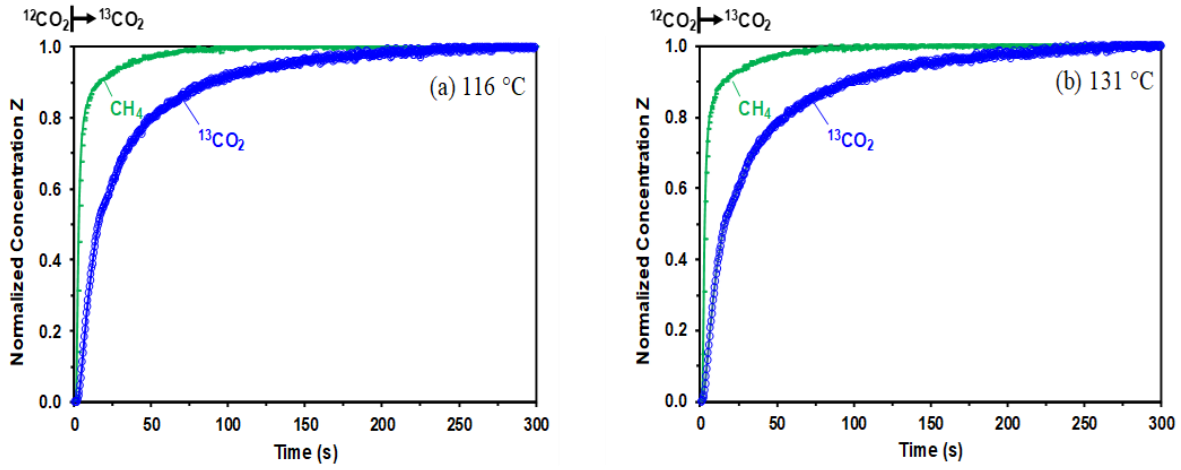

Figure III-13- Normalized concentration transient response curves of CH_4 (green) and $^{13}CO_2$ (blue) obtained after the $^{12}CO_2/O_2/He \rightarrow {}^{13}CO_2/O_2/Kr/CH_4/He$ SSITKA switch on Al_2O_3 (a) at 116 °C and (b) at 131 °C.

The surface residence time (τ_{CO2}) corresponding to the area between the transient curves of CH_4 and $^{13}CO_2$ is estimated about 26.3 s at 116 °C and 28.8 s at 131 °C. A surface concentration of CO_2 (N_{CO2}) adsorbed on the bare support were also estimated to 58 µmol/g at 116 °C and 63 µmol/g at 131 °C.

131 °C. These values were compared with previous results of the CO oxidation on Pd/Al_2O_3 in the presence of CO_2 (Figure III-11) as shown in Figure III-14.

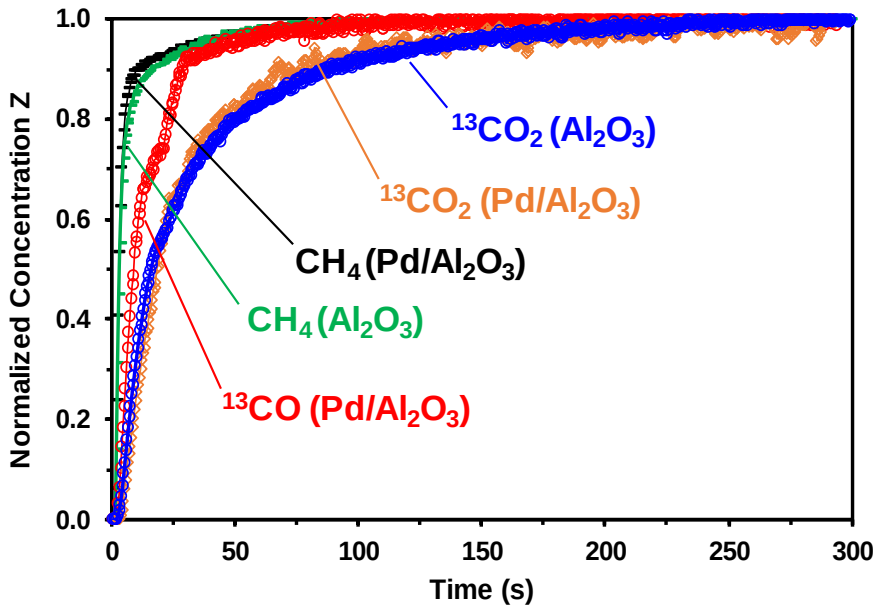

Figure III-14- Comparison of normalized concentration evolution response curves of CH_4 (black), ^{13}CO (red) and $^{13}CO_2$ (orange) obtained after the $^{12}CO/O_2/^{12}CO_2/He \rightarrow {}^{13}CO/O_2/^{12}CO_2/Kr/CH_4/He$ SSITKA switch on Pd/Al_2O_3 at 131 °C and CH_4 (green) and $^{13}CO_2$ (blue) obtained after the $^{12}CO_2/O_2/He \rightarrow {}^{13}CO_2/O_2/Kr/CH_4/He$ SSITKA switch on bare Al_2O_3 at 131 °C.

A clear match between both $^{13}CO_2$ profiles (blue and orange curves) was observed, concomitant with the overlapping methane profiles (black and green curves). Similar surface residence times between CH_4 and $^{13}CO_2$ were estimated in both cases: τ_{CO2} = 28.8 s on Al_2O_3 and τ_{CO2} = 26.7 s on Pd/Al_2O_3. This result confirms the idea that CO_2 curve lag on Pd/Al_2O_3 is only due to CO_2 re-adsorption on the support after its formation in the oxidation process. Regarding the Pt/Al_2O_3, it is important to note that the results are not directly comparable, primarily due to differences in temperature and pretreatment conditions (τ_{CO2} = 8.8 s on Pt/Al_2O_3).

The evolution of surface adsorbed species has also been followed on bare Al_2O_3 by transmission IR spectroscopy during the $^{12}CO_2/^{13}CO_2$ isotopic exchange. The IR spectra recorded in the 1700-1200 cm^{-1} range in both $^{12}CO_2/O_2$ and $^{13}CO_2/O_2$ steady states at 116 and 131 °C are presented in Figure III-15. These spectra were obtained after background treatment and subtraction of the background collected during pretreatment at 200 °C. ^{12}C-containing hydrogen-carbonate species formation was detected around 1655, 1442 and 1233 cm^{-1} (black spectra), bands attributed to the $\nu(OCO)_{asym}$, $\nu(OCO)_{sym}$ and $\delta(OH)$ vibrations respectively. Hydrogen-carbonates ($HCO_{3(ads)}$) are formed following the equation (III-1) where an OH surface group on the alumina surface interacts with CO_2 [29].

$$CO_{2(g)} + OH_{(surf)} \leftrightarrow HCO_{3(ads)} \qquad \text{(III-1)}$$

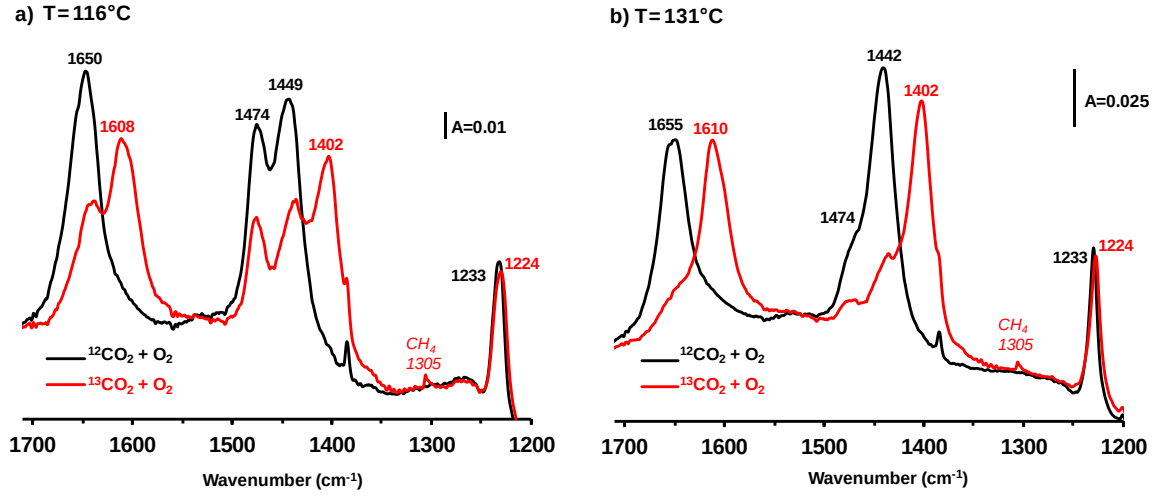

Figure III-15- IR spectra recorded on bare Al_2O_3 in the carbonate region during $^{12}CO_2/^{13}CO_2$ switch in the presence of $^{12}CO_2/O_2$/He (black) and $^{13}CO_2/O_2$/Kr/CH_4/He (red) feeds at (a) 116 °C and (b) 131 °C.

Upon exchange with $^{13}CO_2$, the latter bands were red-shifted towards the bands at around 1610, 1402 and 1224 cm^{-1} (red spectra), respectively, corresponding to ^{13}C-containing hydrogen-carbonate species. Difference spectrum was produced at 116 and 131 °C and shown in Figure

III-16, which clearly showed the partial disappearance of ^{12}C-containing hydrogen-carbonate vibrations (negative bands) towards the appearance of their ^{13}C counterpart. Another IR band appearing at 1474 cm^{-1} in both spectra was attributed to unidentate carbonate species. Its intensity decreases after the $^{13}CO_2$ switch but this band doesn't seem to be isotopically shifted toward lower wavenumbers (Figure III-15). According to experimental isotopic ratio observed in this experiment (i≈1.028), a new band would be expected at 1434 cm^{-1} in that case.

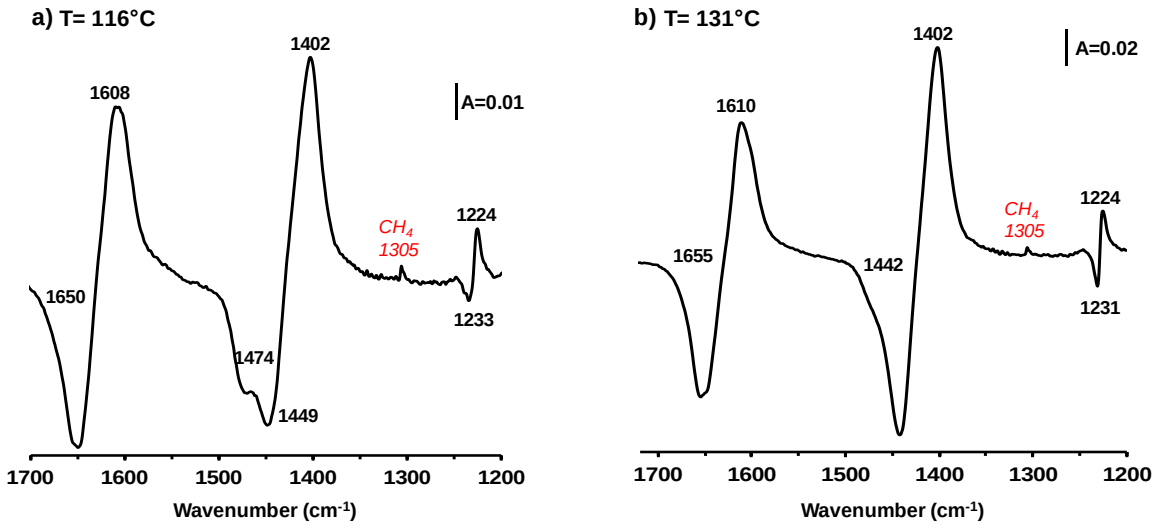

Figure III-16- Difference between $^{13}CO_2$ and $^{12}CO_2$ IR spectra on Al_2O_3 in the carbonate 1700-1200 cm^{-1} range at (a) 116 °C and (b) 131 °C.

This experiment has confirmed the formation pathway of hydrogen carbonate species on the alumina support. It has been demonstrated that these hydrogen carbonate species originate from the reaction of the CO_2 product with surface hydroxyl groups (OH) on the alumina support, independent of the presence of the metal.

4- Conclusion and perspective

A full understanding of CO oxidation mechanism on PGM supported catalysts at low temperature (< 200 °C) is of great importance in order to improve catalyst efficiency and decrease atmospheric pollution levels. The interest for SSITKA-IR methodology is illustrated in this chapter for the discrimination of active and spectator species in a catalytic reaction. This combines both the observation of adsorbed species and the kinetic measurements during CO oxidation reaction at low conversion level (i.e. in chemical regime). In this chapter, the SSITKA technique was successfully coupled to transmission IR spectroscopy in order to elucidate the role of adsorbed species formed on Pt/Al_2O_3 and Pd/Al_2O_3 during the CO oxidation reaction.

The measurement of kinetic parameters, such as the mean residence times and concentrations of surface adsorbed species on Pt/Al_2O_3 and Pd/Al_2O_3 have been combined with the determination of their nature.

Linear carbonyls were predominant on the Pt surface in contrast to Pd, where bridged carbonyls were mainly observed. The dynamic exchange between $^{12}CO + O_2$ and $^{13}CO + O_2$ in the presence and absence of CO_2 in the reaction gas mixture revealed a fast isotopic shift of the IR band signals related to various types of carbonyl species adsorbed on metallic Pt and Pd (linear and bridged carbonyls), suggesting their active contribution to the CO oxidation reaction mechanism.

Contrastingly, hydrogen carbonate species were observed to act as spectator species, as negligible isotopic exchange of the corresponding IR absorption bands was noticed in the presence of CO_2 in the feed gas stream. The lag observed between ^{13}CO and $^{13}CO_2$ on SSITKA normalized concentration curves (without CO_2 added in the feed) was attributed to the re-adsorption of CO_2 product on the bare alumina support, interacting with a surface hydroxyl group. The direct $^{12}CO_2/^{13}CO_2$ exchange observed on alumina provided strong evidence to support this conclusion, indicating that the metal particles are not involved in the formation of hydrogen carbonate species. Interestingly, the behavior of hydrogen-carbonate species was similar on both Pt/Al_2O_3 and Pd/Al_2O_3 catalysts, suggesting that CO_2 re-adsorption occurs primarily on the alumina support rather than being a direct spillover from the metal particles.

It is also important to note that the value of N_C calculated on both Pt and Pd supported on Al_2O_3 did not drop to 0 with the pre-saturation of the surface by CO_2 (N_C = 1.4 and 3.7 µmol g^{-1} on Pt and Pd catalysts, respectively). This observation means either a partial saturation of alumina with carbonate species by the use of 2000 ppm of $^{12}CO_2$ which would be complemented by the formation and re-adsorption of $^{13}CO_2$ during the experiment, or that other C-containing intermediate species could be involved in the CO oxidation mechanism. In the second case, N_C must then be carefully described as consisting of two pools, namely: (i) spectator hydrogen-carbonates, and (ii) active C-containing intermediate species. The latter may be either hydrogen carbonates in a spatial environment close to the metal particle or species of a different nature [31]. A way of invalidating this hypothesis would be to use a support unlikely to form hydrogen carbonates such as SiO_2. However, achieving good PGM dispersion on this support could be challenging. Figure III-17 presents a schematic illustration of this chapter conclusion.

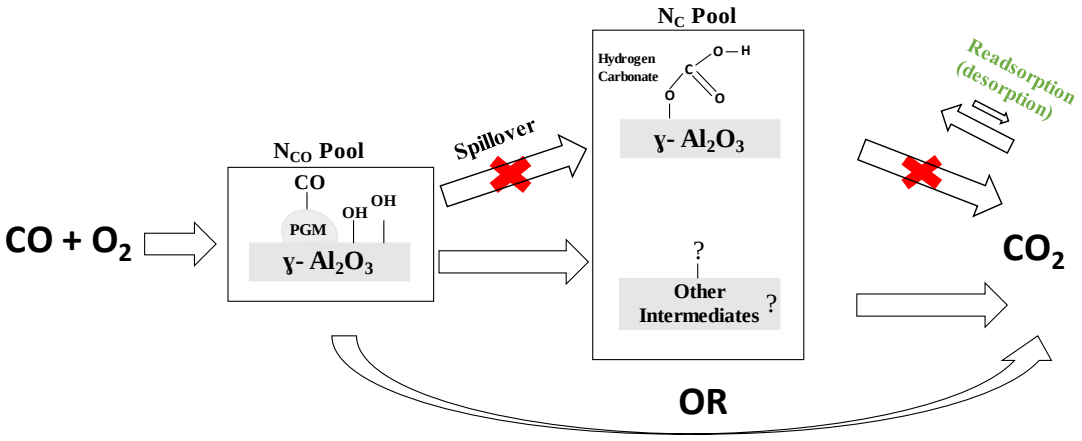

Figure III-17- Contribution of different species in the formation of CO_2 product in CO oxidation over PGM/Al_2O_3 catalysts.

Based on our findings, we can conclude that in the CO oxidation reaction over PGM/Al_2O_3, carbonyls are likely the main active reaction intermediates identified through SSITKA-IR analysis. Our work has identified various types of carbonyls, including linear and bridged carbonyls. Even if all species follow a similar $^{12}CO/^{13}CO$ isotopic exchange, they are not necessarily actively involved in the reaction pathway. Indeed, one of them can be a spectator with a fast conversion into the reactive species. This work paves the way for further analysis to discriminate the individual roles of each carbonyl species according to their adsorption sites during the CO oxidation reaction. This will be the primary focus of the next chapter, as we seek to gain a deeper understanding of the specific contributions of these carbonyl species to the overall reaction mechanism.

References

1. Carlsson P-A, Skoglundh M (2011) Low-temperature oxidation of carbon monoxide and methane over alumina and ceria supported platinum catalysts. Applied Catalysis B: Environmental 101:669–675. https://doi.org/10.1016/j.apcatb.2010.11.008

2. Bourane A, Bianchi D (2002) Oxidation of CO on a Pt/Al_2O_3 Catalyst: From the surface elementary steps to Lighting-Off tests: III. Experimental and kinetic model for Lights-Off tests in excess CO. Journal of Catalysis 209:126–134. https://doi.org/10.1006/jcat.2002.3606

3. Satsuma A, Osaki K, Yanagihara M, et al (2013) Activity controlling factors for low-temperature oxidation of CO over supported Pd catalysts. Applied Catalysis B: Environmental 132–133:511–518. https://doi.org/10.1016/j.apcatb.2012.12.025

4. Phan DQ, Kureti S (2017) CO Oxidation on Pd/Al_2O_3 catalysts under stoichiometric conditions. Top Catal 60:260–265. https://doi.org/10.1007/s11244-016-0608-9

5. Baxter RJ, Hu P (2002) Insight into why the Langmuir–Hinshelwood mechanism is generally preferred. The Journal of Chemical Physics 116:4379–4381. https://doi.org/10.1063/1.1458938

6. Toyoshima R, Yoshida M, Monya Y, et al (2013) In Situ Photoemission Observation of Catalytic CO Oxidation Reaction on Pd(110) under Near-Ambient Pressure Conditions: Evidence for the Langmuir–Hinshelwood Mechanism. J Phys Chem C 117:20617–20624. https://doi.org/10.1021/jp4054132

7. Newton MA (2017) Time Resolved Operando X-ray Techniques in Catalysis, a Case Study: CO Oxidation by O_2 over Pt Surfaces and Alumina Supported Pt Catalysts. Catalysts 7:58. https://doi.org/10.3390/catal7020058

8. Moses-DeBusk M, Yoon M, Allard LF, et al (2013) CO Oxidation on Supported Single Pt Atoms: Experimental and ab Initio Density Functional Studies of CO Interaction with Pt Atom on θ-Al_2O_3(010) Surface. J Am Chem Soc 135:12634–12645. https://doi.org/10.1021/ja401847c

9. Ding K, Gulec A, Johnson AM, et al (2015) Identification of active sites in CO oxidation and water-gas shift over supported Pt catalysts. Science 350:189–192. https://doi.org/10.1126/science.aac6368

10. Newton MA, Ferri D, Smolentsev G, et al (2015) Room-temperature carbon monoxide oxidation by oxygen over Pt/Al_2O_3 mediated by reactive platinum carbonates. Nat Commun 6:8675. https://doi.org/10.1038/ncomms9675

11. Efstathiou AM, Gleaves JT, Yablonsky GS (2012) Transient Techniques: Temporal Analysis of Products and Steady State Isotopic Transient Kinetic Analysis. Wiley-VCH

12. Bourane A, Dulaurent O, Chandes K, Bianchi D (2001) Heats of adsorption of the linear CO species on a Pt/Al_2O_3 catalyst using FTIR spectroscopy: Comparison between TPD and adsorption equilibrium procedures. Applied Catalysis A: General 214:193–202. https://doi.org/10.1016/S0926-860X(01)00483-5

13. Bourane A, Bianchi D (2003) Oxidation of CO on a Pt/Al_2O_3 catalyst: from the surface elementary steps to light-off tests: IV. Kinetic study of the reduction by CO of strongly adsorbed oxygen species. Journal of Catalysis 220:3–12. https://doi.org/10.1016/S0021-9517(03)00267-7

14. Bourane A, Derrouiche S, Bianchi D (2004) Impact of Pt dispersion on the elementary steps of CO oxidation by O_2 over Pt/Al_2O_3 catalysts. Journal of Catalysis 228:288–297. https://doi.org/10.1016/j.jcat.2004.08.020

15. Ojala S, Bion N, Rijo Gomes S, et al (2010) Isotopic Oxygen Exchange over Pd/Al_2O_3 Catalyst: Study on $C^{18}O_2$ and $^{18}O_2$ Exchange. ChemCatChem 2:527–533. https://doi.org/10.1002/cctc.201000033

16. Meunier FC (2010) The power of quantitative kinetic studies of adsorbate reactivity by operando FTIR spectroscopy carried out at chemical potential steady-state. Catalysis Today 155:164–171. https://doi.org/10.1016/j.cattod.2009.11.017

17. Shannon SL, Goodwin JG (1995) Characterization of Catalytic Surfaces by Isotopic-Transient Kinetics during Steady-State Reaction. Chem Rev 95:677–695. https://doi.org/10.1021/cr00035a011

18. Efstathiou AM (2016) Elucidation of mechanistic and kinetic aspects of water-gas shift reaction on supported Pt and au catalysts via transient isotopic techniques. Catalysis 28:175–236

19. Calla JT, Bore MT, Datye AK, Davis RJ (2006) Effect of alumina and titania on the oxidation of CO over Au nanoparticles evaluated by ^{13}C isotopic transient analysis. Journal of Catalysis 238:458–467. https://doi.org/10.1016/j.jcat.2006.01.009

20. Al Soubaihi R, Saoud K, Dutta J (2018) Critical Review of Low-Temperature CO Oxidation and Hysteresis Phenomenon on Heterogeneous Catalysts. Catalysts 8:660. https://doi.org/10.3390/catal8120660

21. Vasiliades MA, Kalamaras CM, Govender NS, et al (2019) The effect of preparation route of commercial $Co/\gamma\text{-}Al_2O_3$ catalyst on important Fischer-Tropsch kinetic parameters studied by SSITKA and CO-DRIFTS transient hydrogenation techniques. Journal of Catalysis 379:60–77. https://doi.org/10.1016/j.jcat.2019.09.008

22. Lorito D, Paredes-Nunez A, Mirodatos C, et al (2016) Determination of formate decomposition rates and relation to product formation during CO hydrogenation over supported cobalt. Catalysis Today 259:192–196. https://doi.org/10.1016/j.cattod.2015.06.027

23. McInroy AR, Lundie DT, Winfield JM, et al (2005) The Application of Diffuse Reflectance Infrared Spectroscopy and Temperature-Programmed Desorption To Investigate the Interaction of Methanol on η-Alumina. Langmuir 21:11092–11098. https://doi.org/10.1021/la051429c

24. Szanyi J, Goodman DW (1994) CO Oxidation on Palladium. 1. A Combined Kinetic-Infrared Reflection Absorption Spectroscopic Study of Pd(100). J Phys Chem 98:2972–2977. https://doi.org/10.1021/j100062a038

25. Xu J, Ouyang L, Mao W, et al (2012) Operando and Kinetic Study of Low-Temperature, Lean-Burn Methane Combustion over a Pd/γ-Al_2O_3 Catalyst. ACS Catal 2:261–269. https://doi.org/10.1021/cs200694k

26. Szanyi J, Kwak JH (2014) Dissecting the steps of CO_2 reduction: 1. The interaction of CO and CO_2 with γ-Al_2O_3: an in situ FTIR study. Phys Chem Chem Phys 16:15117–15125. https://doi.org/10.1039/C4CP00616J

27. Ebbesen SD, Mojet BL, Lefferts L (2009) The influence of water and pH on adsorption and oxidation of CO on Pd/Al_2O_3-an investigation by attenuated total reflection infrared spectroscopy. Phys Chem Chem Phys 11:641–649. https://doi.org/10.1039/B814605E

28. Murata K, Eleeda E, Ohyama J, et al (2019) Identification of active sites in CO oxidation over a Pd/Al_2O_3 catalyst. Phys Chem Chem Phys 21:18128–18137. https://doi.org/10.1039/C9CP03943K

29. Föttinger K, Emhofer W, Lennon D, Rupprechter G (2017) Adsorption and Reaction of CO on (Pd–)Al_2O_3 and (Pd–)ZrO_2: Vibrational Spectroscopy of Carbonate Formation. Top Catal 60:1722–1734. https://doi.org/10.1007/s11244-017-0852-7

30. Busca G, Finocchio E, Escribano VS (2012) Infrared studies of CO oxidation by oxygen and by water over Pt/Al_2O_3 and Pd/Al_2O_3 catalysts. Applied Catalysis B: Environmental 113–114:172–179. https://doi.org/10.1016/j.apcatb.2011.11.035

31. Rousseau S, Marie O, Bazin P, et al (2010) Investigation of Methanol Oxidation over Au/Catalysts Using Operando IR Spectroscopy: Determination of the Active Sites, Intermediate/Spectator Species, and Reaction Mechanism. J Am Chem Soc 132:10832–10841. https://doi.org/10.1021/ja1028809

Chapter IV- Linear and bridged carbonyls in CO oxidation reaction: Reactivity and kinetic study

1- Introduction

Pt and Pd-based systems have been extensively used as highly effective catalysts in CO oxidation reactions leading research to focus on the interaction of CO with platinum and palladium surfaces considering numerous techniques [1–7]. In the previous chapter, we have utilized the SSITKA coupled with IR spectroscopy to investigate the CO oxidation reaction on Pt/Al_2O_3 and Pd/Al_2O_3 in order to understand the true role of species formed during the reaction. It was revealed that hydrogen-carbonate species primarily act as spectator species while carbonyls are mainly the active species for this reaction. Several types of linear and bridged carbonyls have been detected on Pt and Pd surfaces (in Figure IV-1) in presence of ^{12}CO and O_2 in different proportions. In the case of Pt: linear CO species were notably dominant, characterized by a strong IR band at 2058 cm^{-1} [8, 9] while a very small intensity is observed at 1837 cm^{-1} for bridged carbonyls adsorbed on two metallic platinum sites. In addition, a small IR band was observed at 2102 cm^{-1} corresponding to carbonyls adsorbed on oxidized $Pt^{\delta+}$ [10]. As for Pd, the larger IR signal observed between 2000 and 1800 cm^{-1} can be decomposed into several overlapping infrared bands corresponding to bridged and multi-bonded ^{12}CO adsorbed on palladium [11, 12]. The smaller IR band observed at 2088 cm^{-1} is attributed to linear ^{12}CO adsorbed on Pd. According to the literature [13, 14], linear CO are more likely to be adsorbed on metallic Pd^0 particle corner sites or (111) facets.

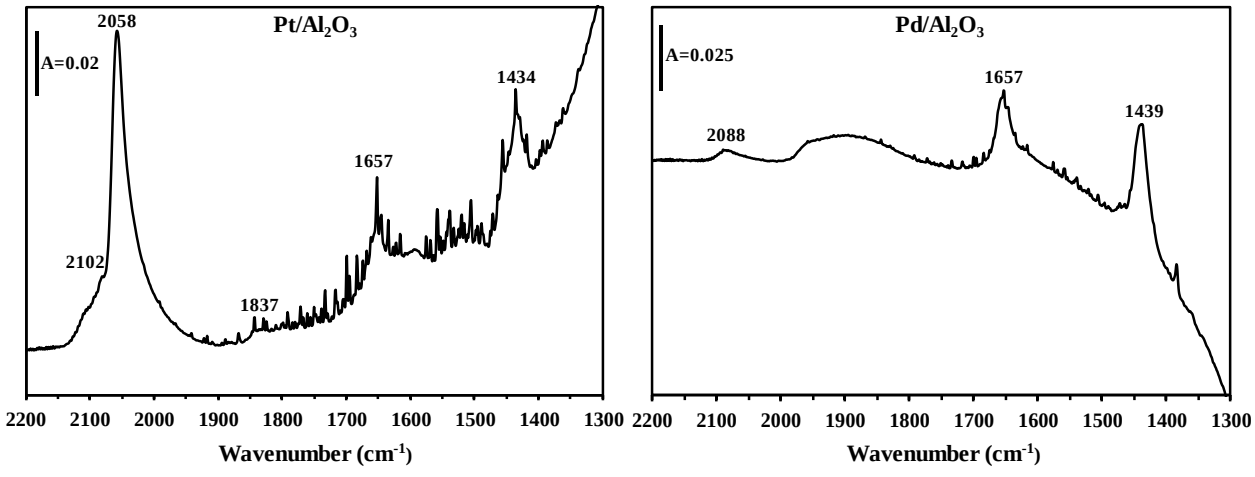

Figure IV-1- IR spectra recorded on Pt/Al_2O_3 (131 °C) and Pd/Al_2O_3 (116 °C) during CO oxidation ($^{12}CO/O_2$/He).

Even if carbonyls appeared to be the main pool of reactive species, the question of individual reactivity of these species remains. As a result, our attention in this chapter will be directed towards husking the reactivity of each linear and bridged carbonyls in relation to the CO

oxidation reaction mechanism. To achieve this, we will investigate the kinetic of isotopic exchange based on deconvolution method of infrared carbonyl bands, along with their overlapping regions, during the SSITKA process.

2- Fitting methodology

The kinetic analysis of the isotopic exchange rate constant of each individual bands of linear and bridged carbonyls was attempted based on the deconvoluted IR spectra recorded during isotopic exchange at different instants t. Each IR band was fitted using a sum of Gaussian model fit equation:

$$f(x) = \sum_{i=1}^{n} A_i \; e^{\frac{-(x-x_i)^2}{(2{s_i}^2)}} \qquad \text{(IV-1)}$$

where A_i, x_i and s_i are coefficients corresponding to the height (maximum), the position and the full width at half maximum (FWHM) of the band, respectively.

The fitting procedure was realized using the free version of *Igor pro 9.02* software and involved several steps:

- **<u>1st STEP</u>: Fit of IR signals under ^{12}CO at 0 s**

The number n of bands to fit was chosen according to the literature review such as n=5 for CO adsorbed on Pt and Pd particles. Initial guessed A, x_i and s_i coefficients were provided to the software in order to fit the IR signal curve under ^{12}CO conditions at 0 s between 2200 and 1900 cm^{-1} or 2200 and 1700 cm^{-1} for Pt or Pd, respectively. A linear baseline (y = Ba*x+Bb) was imposed on the system between the two wavenumber limits. The Igor calculator was then left free to optimize the fit giving us the new calculated positions (x_i), heights (A_i) and FWHM (s_i) of the different bands at t=0s (Annexes SIV-1 and SIV-2). It worth to note that at t=0 s, no ^{13}C-containing IR band is observed while ^{12}CO signals are at their maximum height.

- **<u>2nd STEP</u>: Fit of IR signals under ^{13}CO at 60 s** (after SSITKA switch)

The same process was repeated for the IR signal ^{13}CO adsorbed on Pt and Pd at 60 s (i.e. 1 min after the ^{12}CO→^{13}CO SSITKA switch). Here, the first guesses on the band positions were calculated manually, when a band shifting was observed, by considering an isotopic exchange difference Δi of 48 cm^{-1} (position of the band at 60 s = position of the band at 0 seconds - Δi). The FWHM determined for ^{12}CO bands were also chosen as first guessed for ^{13}CO. Once again, after applying a linear baseline, Igor software was left free to optimize the fit giving us the new calculated positions (x_i), heights (A_i) and FWHM (s_i) of the different bands at t=60 s (Annexes

SIV-1 and SIV-2). We admitted that at t=60 s, the ^{12}C bands vanish completely (A_i=0, except for CO adsorbed on oxidized Pt), while the ^{13}C bands have reached their maximum height.

- **<u>3rd STEP</u>: Fit of IR signals during the $^{12}CO \rightarrow {}^{13}CO$ isotopic exchange**

For other time intervals between 0 and 60 seconds, we assumed that both the ^{12}CO and ^{13}CO adsorbed bands coexist, following the hypothesis that the intensity of the ^{12}CO bands should only decrease while the intensity of the ^{13}CO bands should increase over time. In these cases, we applied several constraints to our IR signal fitting:

(i) The band wavenumber (positions x_i) and FWHM (s_i) values obtained at 0 and 60 s are considered unchanged overall time. We used the sum of 9 Gaussian fits in total for CO adsorbed on Pt/Al_2O_3 (4 bands switching from ^{12}CO to ^{13}CO + ^{12}CO on $Pt^{\delta+}$) and 10 Gaussian fits on Pd/Al_2O_3 (5 bands switching from ^{12}CO to ^{13}CO).

(ii) Beside applying a height maximum limit based on the respective maximum height for each band determined at 0 and 60 s, band's height coefficients were left free for further calculation and optimization of the fits by the Igor application. In certain instances, the software may yield a negative value for the band height. In such cases, we assume that the bands have completely vanished ($A_i = 0$) and we fix the height at 0 for all subsequent time intervals.

(iii) As previously a linear baseline was set for each IR spectra.

3- Results and discussions

3.1- Reactivity of carbonyls on Pt/Al_2O_3

The evolution of linear and bridged carbonyl bands recorded at different instant t during $^{12}CO \rightarrow {}^{13}CO$ isotopic exchange on Pt/Al_2O_3 at 131 °C (χ_{CO} = 11%, θ_{CO} = 0.47) is presented in Figure IV-2.

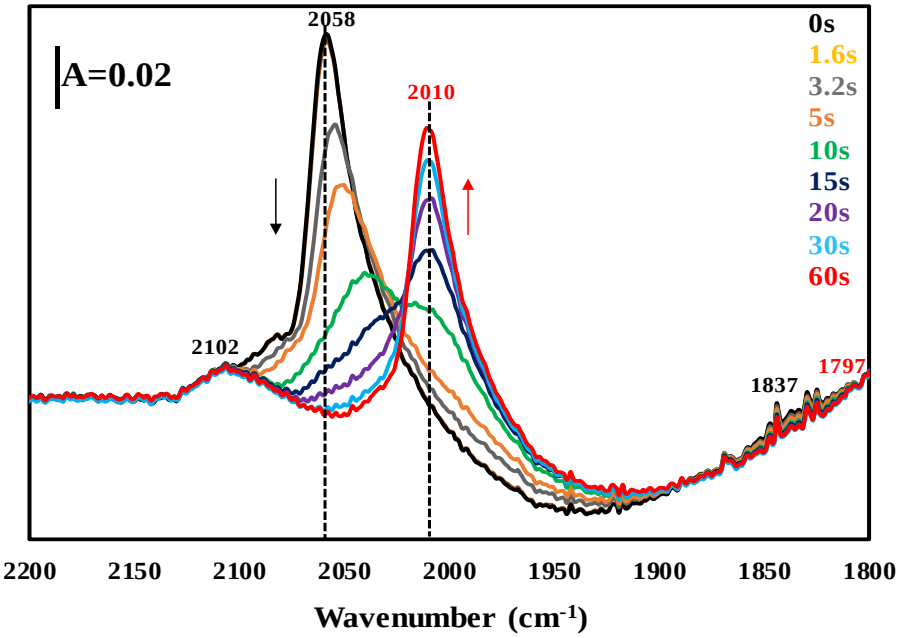

Figure IV-2- Evolution of linear and bridged carbonyl bands during $^{12}CO \rightarrow ^{13}CO$ isotopic exchange on Pt/Al_2O_3 (131 °C, χ_{CO} = 11%, θ_{CO} = 0.47), at different instant t.

The intensity of the band centered at 2058 cm^{-1}, attributed to linear carbonyls adsorbed on Pt, gradually decreases during the isotopic switch, transitioning to a lower band at 2010 cm^{-1}. This latter is increasing progressively, reaching its maximum after 60 seconds. The same observation can be made for the low band corresponding to bridged carbonyls which follow an isotopic shift from 1837 cm^{-1} to 1797 cm^{-1} upon exchange. On the contrary, the band at 2102 cm^{-1} corresponding to carbonyl species adsorbed on oxidized Pt, do not exhibit a shift during the isotopic exchange. We suppose that the wavenumber of each carbonyl band in isothermal conditions is independent of surface carbonyl coverage, especially during the isotopic exchange.

Looking at the isotopic exchange of carbonyls, we can observe that no single isosbestic point was formed around 2030 cm^{-1}, clearly meaning that several bands, and so type of carbonyls, are present under the carbonyl IR signal with different exchange kinetics. According to the literature, the band assigned to linear carbonyls can be decomposed into four bands at 2090, 2065, 2050 and 2020 cm^{-1} [15]. Prior works identified 2020 cm^{-1} band as linear carbonyls adsorption on Pt sub-nanometer particles, 2065 cm^{-1} band as linear carbonyls adsorption on Pt steps and 2090 cm^{-1} as linear adsorption of carbonyls on Pt terraces [16]. The band at 2050 cm^{-1} was not clearly identified in the literature. A tentative is made in this thesis to assign it to CO adsorbed on Pt particles of intermediate size (few nano to sub-nano limit). These previous results were used as first guesses in our IR signal fitting process as described in previous section

(2. Fitting method). It is worth to note that due to the low intensity of the bridged carbonyl band, no deconvolution analysis was attempted.

The fitting was realized only on linear carbonyl bands representing the main IR signal. The results obtained at 0 and 60 s are presented in Figure IV-3a and b respectively. These figures illustrate the original non-smoothed IR spectra (in red), the global fitting function curve (in black), and the 5 adsorbed linear ^{12}CO or ^{13}CO on Pt bands fitted after deconvolution. As previously mentioned, the band at 2098 cm^{-1}, corresponding to carbonyl adsorbed on oxidized Pt, was kept constant during the fitting process (no isotopic shift). The fitting results for all spectra at various time points are provided in the annex SIV-1.

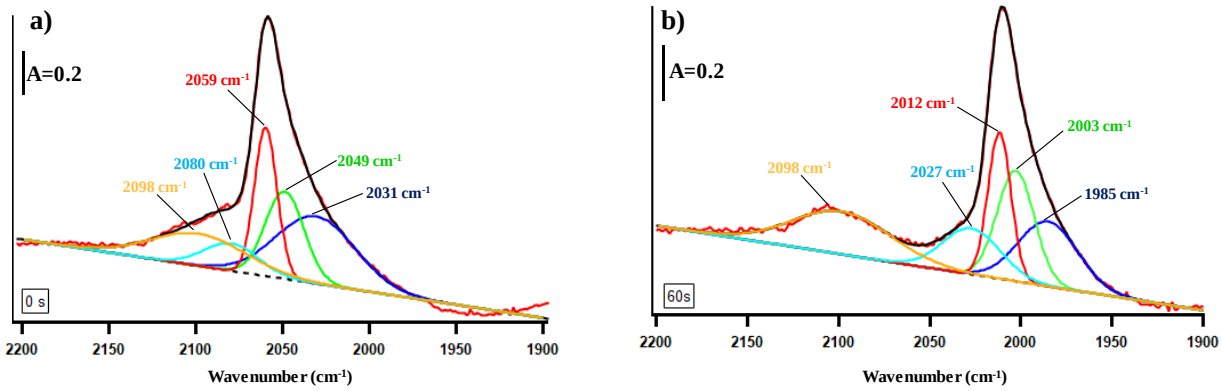

Figure IV-3- Individual adsorption bands of the 5 adsorbed CO species obtained after the deconvolution of the recorded spectrum on Pt/Al_2O_3: a) at 0s and b) 60s. The non-smoothed raw IR signal is represented in red, the result of deconvolution (5 Gaussian sum) by the black line and the baseline by the dashed black line.

Parameters resulting from deconvolution at 0 and 60 s, including the band positions and FWHM are summarized in Table IV-1. These values were then used as constants to fit all the further spectra. The assignment and the name given (L1 to L4) to each band are also reported in Table IV-1.

Table IV-1- Adsorbed CO on Pt band positions and FWHM resulted from spectra deconvolution at 0 and 60 s. These coefficients were then used as constants for further fittings.

		^{12}CO bands *from spectrum at 0 s*		^{13}CO bands *from spectrum at 60 s*	
Assignment [15, 16]		**Position (cm^{-1})**	**FWHM (cm^{-1})**	**Position (cm^{-1})**	**FWHM (cm^{-1})**
CO on $Pt^{\delta+}$	-	2098	27.2	2098 (^{12}CO)	27.2
CO on Pt terraces	L1	2080	15.7	2027	15.7
CO on Pt steps	L2	2059	6.5	2012	6.3
(CO on Pt particles of intermediate size)	L3	2049	11.1	2003	10.2
CO on Pt sub-nanometer particles	L4	2031	22.9	1985	16.3

The evolution in the heights of these 8 bands (hence, not considering CO on $Pt^{\delta+}$) have been summarized in the Table IV-2 below.

Table IV-2- Evolution of band heights for ^{12}CO and ^{13}CO linear species at different times of the isotopic exchange.

	^{12}CO bands				^{13}CO bands			
Bands *(cm^{-1})* / **Time**	**2080** L1	**2059** L2	**2049** L3	**2031** L4	**2027** L1	**2012** L2	**2003** L3	**1985** L4
0 s	0.0140	0.0762	0.0447	0.0344	0	0	0	0
1.6 s	0.0135	0.0729	0.0459	0.0344	0	0	0.0003	0
3.2 s	0.008	0.0343	0.05	0.037	0	0	0.0003	0.005
5 s	0.0034	0	0.0467	0.0365	0.01	0	0.0015	0.0116
10 s	0.0002	0	0.0156	0.035	0.0121	0.0012	0.0146	0.0164
15 s	0	0	0.0034	0.0213	0.0198	0.0152	0.0267	0.0205
20 s	0	0	0	0.0109	0.0205	0.032	0.0351	0.0226
30 s	0	0	0	0.0034	0.0201	0.0459	0.0399	0.0239
60 s	0	0	0	0	0.0178	0.0564	0.0427	0.0249

Kinetic analysis of the band's evolution was then performed. The area under each 4 bands was integrated, using Igor's *areaXY* function, at the different time intervals. Area's evolutions were normalized between 0 and 1 and plotted as $^{12}CO/^{13}CO$ pairs for comparison (colored dotted/solid lines respectively), as a function of time of isotopic exchange in Figure IV-4.

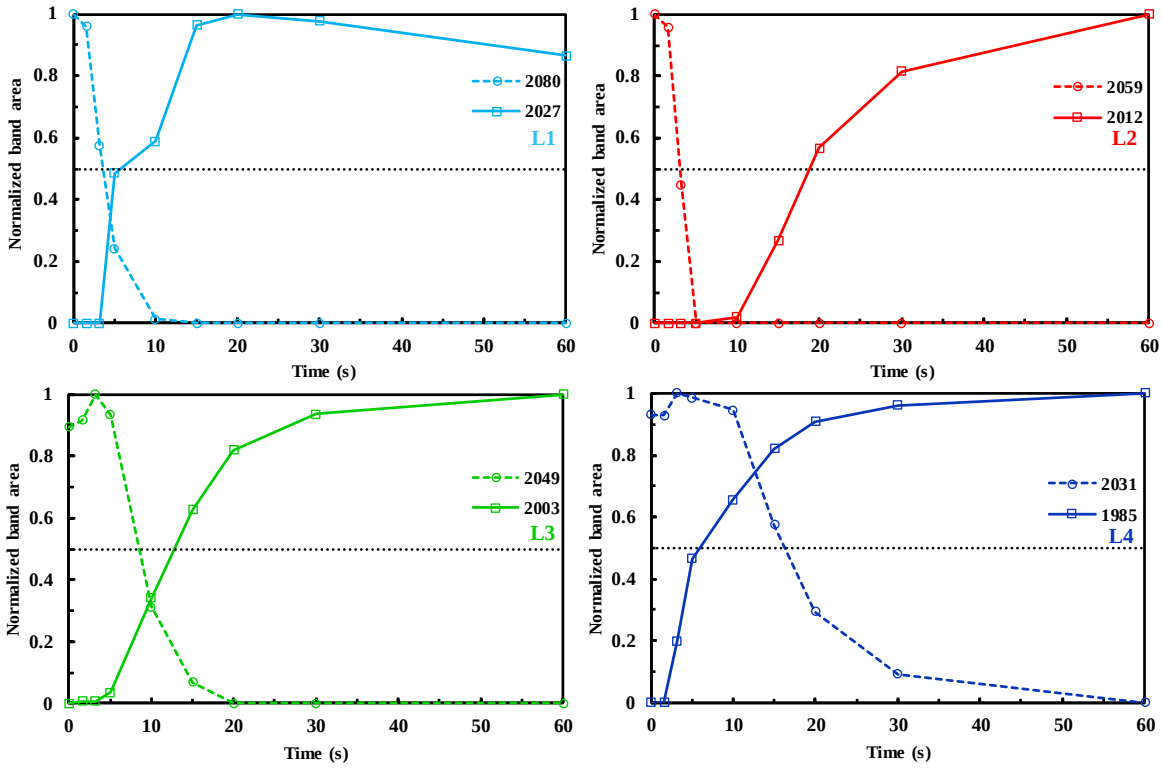

Figure IV-4- Evolution of normalized area for adsorbed ^{12}CO and corresponding adsorbed ^{13}CO: L1 (cyan), L2 (red), L3 (green) and L4 (blue) bands during isotopic exchange.

Figure IV-4 illustrates the asymmetric exchange of all adsorbed ^{12}CO species with their corresponding ^{13}CO counterparts during the isotopic exchange. Indeed, it is obvious that the ^{12}CO and ^{13}CO band area evolutions do not intersect each other at the normalized value of 0.5. In the SSITKA theory, the simultaneous exchange of ^{12}C carbonyl species by ^{13}C carbonyl species leads to a symmetric evolution of normalized concentration curves. Both normalized concentration curves should cross at 0.5 in this case. On the other hand, the superimposition of a slower exchange of ^{13}CO than for ^{12}CO and a faster consumption of ^{12}C carbonyl species for CO_2 product compared to the one of ^{13}CO can lead to a temporary change of the sum of normalized band areas. It is then expected that both normalized concentration curves should not cross at 0.5 during the isotopic exchange.

Different behaviors are observed for the decrease of ^{12}CO species band areas: The bands L1 and L2, i.e. at 2080 and 2059 cm^{-1}, experience a significant decrease in areas right from the outset of the isotopic exchange, reaching values close to 0 in just 10 and 5 seconds, respectively. In contrast, the 2049 cm^{-1} band area (L3) remains relatively stable for 5 seconds before to

gradually decrease to 0 after 20 s of exchange. Similarly, the area of L4 species band centered at 2031 cm^{-1} remains relatively constant for the first 10 s and then starts to decrease progressively to reach 0 at the end of the exchange (~60 s). Concerning the appearance of adsorbed ^{13}CO species, on one hand, the areas of bands L2 and L3 at 2012 and 2003 cm^{-1} display an upward trend after 5 seconds, gradually increasing to their maximum values at 60 s. On the other hand, the area of the L4 bands at 1985 cm^{-1} initiates its ascent sooner (1.6 s) reaching almost its maximum after 30 s of exchange. In contrast, the band L1 centered at 2027 cm^{-1} shows a different pattern, while its area starts to rise after 3 seconds, it exhibits the faster increase to its maximum reached around 15 s approximately.

In conclusion, it becomes clear that each species exhibits a unique behavior in terms of its isotopic exchange rate. The transient kinetic exchange rate constants (k') for each ^{12}CO bands were determined using a kinetic model, as described in the literature [17], according to the provided equation:

$$\ln \alpha = - k't \quad ; \text{with } \alpha = \frac{A_i(t)}{A_0(t=0s)} \tag{IV-2}$$

In equation IV-2, α corresponds to the ratio of the IR band area for each individual deconvoluted linear-type adsorbed CO species on Pt at a given time, t, to the IR band area obtained at t=0 s for each respective band. Figure IV-5 presents linear plots of ln α versus time for the 4 linear adsorbed ^{12}CO species. Based on equation IV-2, the absolute slope value provides the apparent exchange rate constant (k'^{12}CO) of each carbonyls species. The values are summarized in Table IV-3.

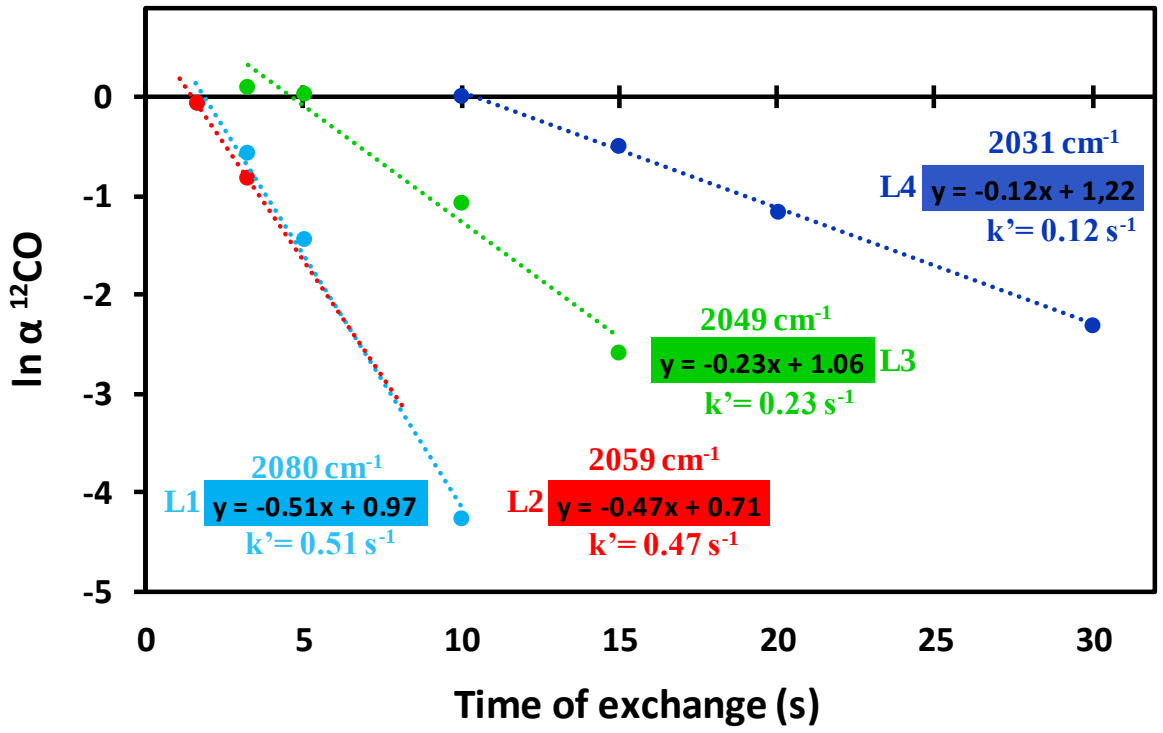

Figure IV-5- Plot of ln α vs. time (s) for the 4 linear CO species (L1 to L4) adsorbed on Pt during $^{12}CO \rightarrow {}^{13}CO$ SSITKA experiment at 131 °C.

The results suggest distinct reactivity patterns towards CO oxidation among these four carbonyl species. The bands L1 and L2 at 2080 and 2059 cm^{-1} display nearly identical k' values (k'_{L1}=0.51 s^{-1} and k'_{L2}=0.47 s^{-1}) and so reactivity. It is worth to note that the error on k'_{L2} might be important as only 2 data points can be exploited. Nevertheless, the latter species undergo isotopic exchange at a notably faster rate than L3 and L4 species at 2049 and 2031 cm^{-1} showing k'_{L3}=0.23 s^{-1} and k'_{L4}=0.12 s^{-1}. For comparison, the exchange rate constant corresponding to the bridged carbonyls adsorbed on Pt at 1837 cm^{-1} (not shown in Figure IV-5) was also estimated to 0.32 s^{-1}.

As shown in Figure IV-4, the $^{12}C/^{13}C$ exchange of CO adsorbed species is not symmetric. Similarly, the rate constants for the appearance of ^{13}CO species on the Pt surface were evaluated using the following equation IV-3.

$$\ln \alpha = k't \quad ; \text{with } \alpha = \frac{A_i(t)}{A_{60}(t=60s)} \qquad \text{(IV-3)}$$

In that case, α corresponds to the ratio of the IR band area for each individual deconvoluted linear-type adsorbed CO species on Pt at a given time, t, to the IR band area obtained at t=60 s for each respective band. The calculated apparent exchange rate constant ($k'^{13}CO$) of each carbonyls species are given in Table IV-3.

Table IV-3- Exchange kinetic rate constant for the four linear adsorbed CO disappearing (k'^{12}CO) and appearing (k'^{13}CO) on Pt during ^{12}CO→^{13}CO SSITKA experiment at 131 °C.

131 °C	**L1**	**L2**	**L3**	**L4**
k' (^{12}CO) *s^{-1}*	0.51	0.47	0.23	0.12
k' (^{13}CO) *s^{-1}*	0.05	0.33	0.48	0.15

The table shows that the exchange kinetic rate constant (k'^{13}CO = 0.15 s^{-1}) of L4 band is similar to the exchange kinetic rate of its disappearance (k'^{12}CO = 0.12 s^{-1}). In contrast, L2 and L3 exhibit different values for k'^{13}CO compared to k'^{12}CO; higher (x2) for L3 and lower (-30%) for L2. However, there's a notable disparity in the k' values of L1 due certainly to the rapid evolution in area, increasing abruptly from 0 to 50% (Figure IV-4), that makes it challenging to accurately assess the k'^{13}CO value, which then appears lower than expected (k'^{13}CO (L1) = 0.05 s^{-1}). Overall, it's difficult to draw any direct conclusions based on the comparison of the ^{12}CO and ^{13}CO kinetic values, especially as a time lag (3-5 s) is observed, particularly for L1, L2 and L3 bands before the appearance of ^{13}CO species on Pt surface.

However, the separate evolution analysis of band areas led us to think that L1 and L2 species, corresponding to CO adsorbed on Pt terraces and steps, might be the main active intermediates in the CO oxidation reaction on Pt/Al_2O_3. In order to get a better idea on the overall surface coverage of the catalyst during the ^{12}CO→^{13}CO SSITKA process we decided to plot the sum of the ^{12}CO and ^{13}CO band areas as a function of time.

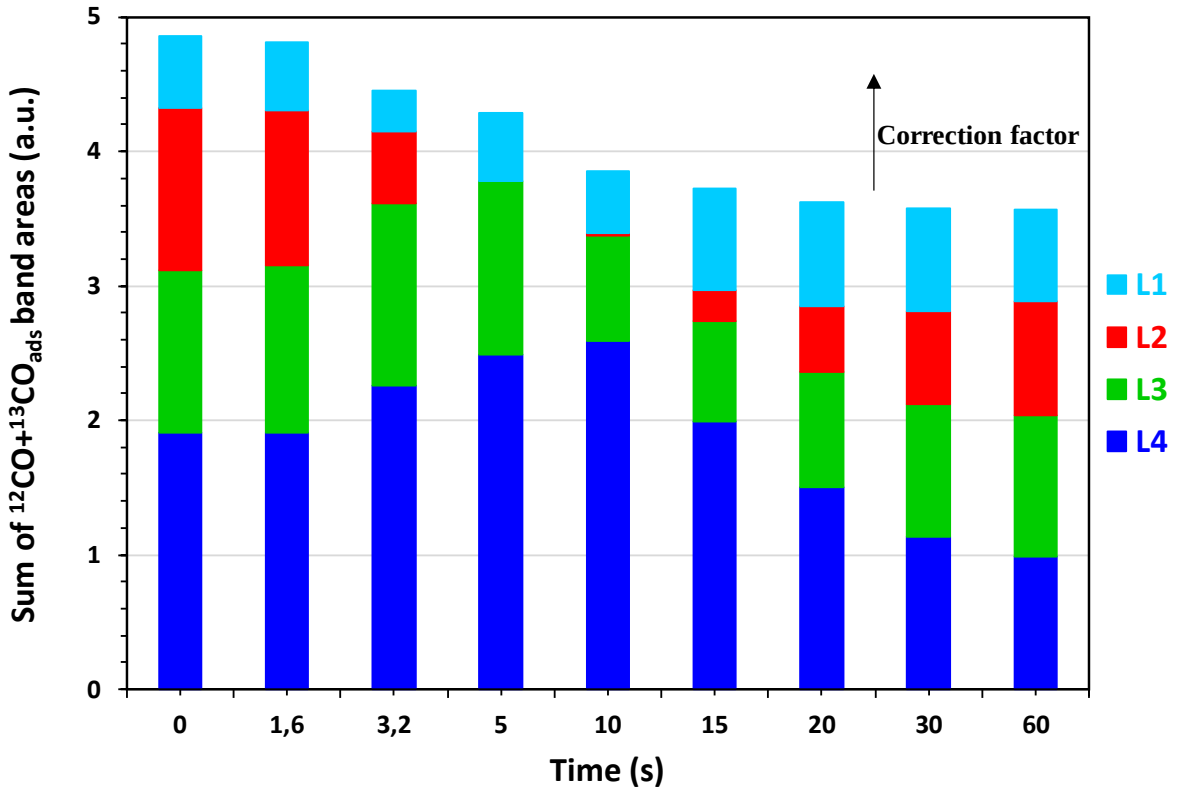

Figure IV-6- Evolution of sum of the areas of ^{12}CO and ^{13}CO bands during $^{12}CO \rightarrow ^{13}CO$ isotopic exchange on Pt/Al_2O_3.

The result, as presented in Figure IV-6, illustrates the behaviors of the different bands, namely L1, L2, L3, and L4, in term of Pt surface coverage evolution during the isotopic exchange. However, as observed at t = 0 s and 60 s, the areas of the ^{12}CO and ^{13}CO bands do not align at their respective maximum values. To address this, correction factors have been applied on the values of ^{13}CO band areas. Our assumption here is that the surface coverage at the beginning (t=0 s) and the end (t=60 s) of the exchange should be exactly the same as steady-state conditions are kept during the overall SSITKA process. A correction factor f was determined for each species (L1 to L4) using the Equation IV-4, calculating the area ratios between the ^{12}CO bands at 0 second and the ^{13}CO bands at 60 seconds. The values are given in Table IV-4. Subsequently, the ^{13}CO bands areas (of all time intervals) will be adjusted by dividing them by the corresponding correction factor (Equation IV-5).

$$f = A_0(^{12}CO)/A_{60}(^{13}CO) \quad \text{(IV-4)}$$

$$A^*_t(^{13}CO) = A_t(^{13}CO) \times f \quad \text{(IV-5)}$$

Table IV-4- Calculated correction factors for each CO adsorbed IR bands on Pt.

	L1	L2	L3	L4
f	1.27	0.71	0.87	0.51

The new sums of the band areas were then plotted as a function of time in Figure IV-7 using the corrected values for ^{13}CO bands (A^*_t).

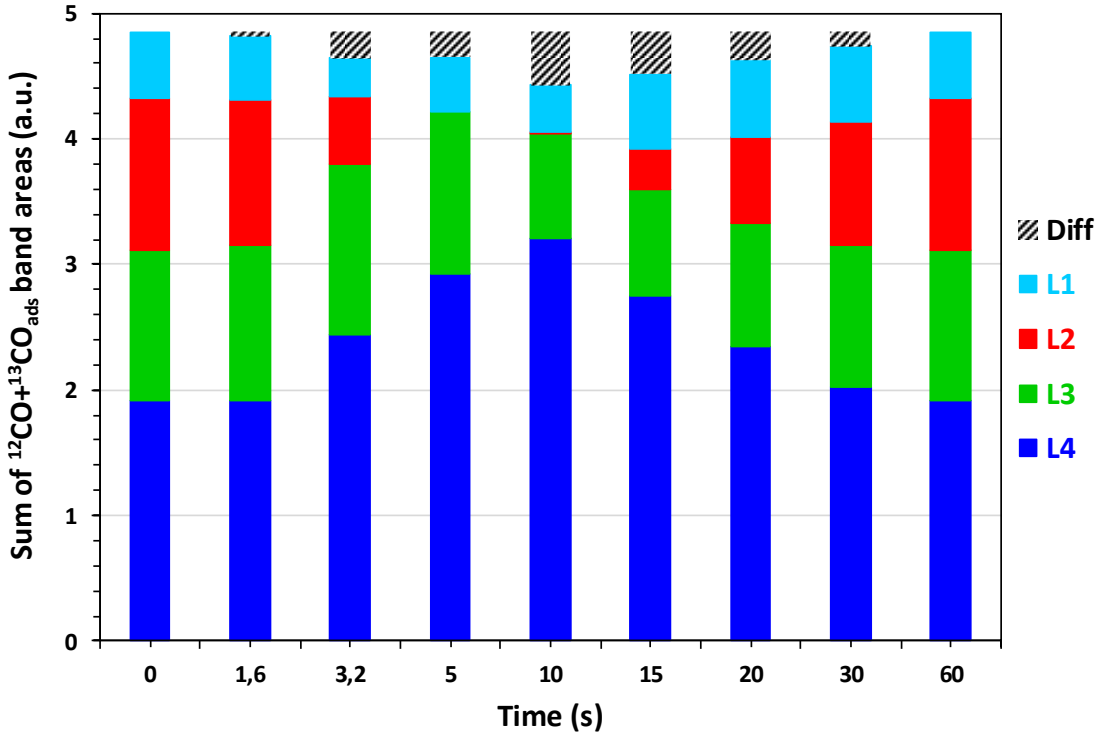

Figure IV-7- Evolution of the sum of adsorbed L1 to L4 ^{12}CO and corrected ^{13}CO band areas during isotopic exchange on Pt/Al_2O_3.

The cumulated $^{12}CO+^{13}CO$ L1 band, associated with carbonyls adsorbed on Pt terraces, exhibits initially a fast decrease in intensity (-43% at 3.2 s) before returning to its initial value after 15 seconds. In contrast, the evolution of L3 band sum displays an initial increase (+13% at 3.2 s) followed by a significant decrease (-31%) after 10 seconds. Remarkably, the sum of L2 bands, corresponding to carbonyls adsorbed on Pt steps, remains stable at the first instant of the exchange to vanish rapidly and completely at 5 seconds, before beginning a progressive gradual increase to its maximum value (60 s). The opposite is clearly observed for the sum of L4 band areas which seems to compensate for the decreases observed in other bands, especially L2. As evident, L4 sum increases progressively, reaching its maximum value (+67% at 10 s) when other sums are minimal before decreasing to its initial value as the isotopic exchange progresses.

The increase in L4 area sums illustrates an accumulation of adsorbed ^{12}CO and ^{13}CO on the associated Pt surface site, which would be consistent with a non-active behavior. Similar conclusion can be drawn for L3 species for which cumulative effect is also observed at the beginning of the exchange (to a lesser extent). These results are in line with their lower kinetic rate constants. On the contrary, the reactivity of L2 species appears to be much faster than the isotopic exchange process on Pt step sites since the L2 bands are no longer observable for a short period. This result tends to seriously designate the L2 species as the main intermediate in the CO_2 formation while L1 species could have a more minor role to play in the reaction despite its higher $k'^{12}CO$ value calculated previously. Indeed, only a small decrease in the quantity of CO adsorbed on Pt terrace is observed in the first 10 seconds of the exchange. It is worth to note also that the sums of all bands slightly deviate from the maximum value (~4.9) during the SSITKA switch. The missing part is highlighted using black stripes, named *diff*, in Figure IV-7. This difference is maximum at 10 seconds, representing almost 9% of the initial/final sum of IR areas. Several possible hypotheses could explain this phenomenon, such as a higher CO_2 production (higher conversion) leading to a decrease in CO surface coverage. However, the respect of steady-state conditions during SSITKA tends to invalidate this idea. As mentioned in chapter 3, a competition exists for the coverage of the Pt surface between O and CO during the reaction. In consequence, a different sharing of surface adsorption sites or the presence of a greater number of vacant sites could be responsible for the decrease in total CO coverage.

In conclusion, this work has enabled the differentiation of L2 from the rest of the linear bands, suggesting its involvement in product formation and identifying it as the main active species in the CO oxidation reaction on Pt/Al_2O_3. The next challenge will be to repeat this analysis on Pd surface and discriminate the carbonyls adsorbed reactive species in the CO oxidation reaction.

3.2- Reactivity of carbonyls on Pd/Al_2O_3

In the case of Pd/Al_2O_3 catalyst, it has been previously noted that during CO oxidation, the IR spectra primarily exhibit intense bridged carbonyl signal between 2000 and 1750 cm^{-1} versus linear carbonyl intensity (2100-2000 cm^{-1}). The evolution of all carbonyl bands recorded at different instant of the $^{12}CO \rightarrow {}^{13}CO$ isotopic exchange on Pd/Al_2O_3 at 116 °C (χ_{CO} = 8.5%, θ_{CO} = 0.30) is presented in Figure IV-8.

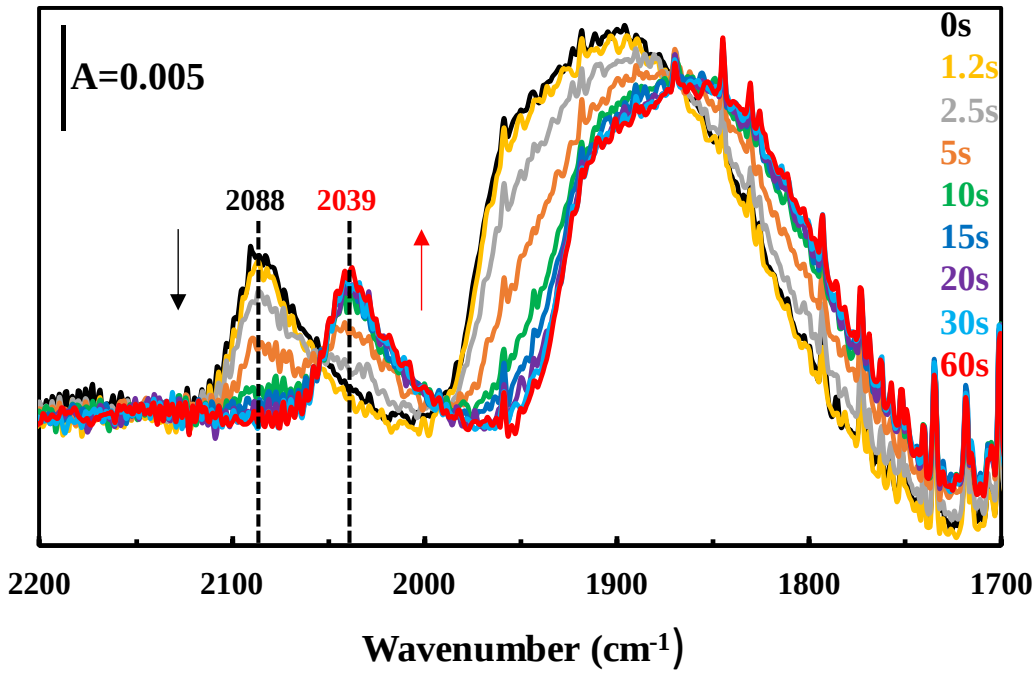

Figure IV-8- Evolution of linear and bridged carbonyl bands during isotopic exchange at different instant t.

Figure IV-8 illustrates the gradual decrease of the linear carbonyl band at 2088 cm^{-1} during the isotopic exchange, vanishing entirely after 10 seconds. This disappearance give rise to the emergence of the corresponding ^{13}C linear carbonyl counterpart at 2039 cm^{-1} increasing progressively and reaching its maximum after 60 seconds. A broad band was observed for the bridged carbonyl between 2000 and 1750 cm^{-1} with a higher intensity than carbonyls. This signal display distinct complexity, consisting of multiple overlapping bands that shift to lower wavenumbers ($\Delta i \approx 48$ cm^{-1}) after isotopic exchange.

According to the literature, the linear carbonyl band observed on Pd can be decomposed into 2 overlapped bands at 2088 cm^{-1} and 2059 cm^{-1} [18]. The first is assigned to linearly adsorbed CO on terrace sites [19] while the band at 2059 cm^{-1} accounts for linearly adsorbed CO on low-coordinated adsorption sites (corners or edges) [20]. In that case, an isosbestic point is observed at 2060 cm^{-1} during the exchange of linear carbonyls, probably indicating a similar exchange kinetics for the two types of species. Concerning the bridged carbonyl, prior studies show that the signal can be decomposed into three types of overlapped bands at 1957, 1908 and 1848 cm^{-1}. The band at 1957 cm^{-1} is attributed to bridged carbonyl on Pd(100) [21], 1908 cm^{-1} to bridge-bound CO on Pd(100) [22] and the band at 1848 cm^{-1} to adsorbed CO on 3-fold hollow sites [23]. In the case of bridged carbonyls exchange on Pd, an intersection of the IR signals is observed around 1860 cm^{-1} but a clear isosbestic point is difficult to identify. The different carbonyls species adsorbed on Pd are illustrated in Figure SIV-3 (Annex).

The literature assignments were firstly chosen as guessed to perform the IR signal Gaussian deconvolution using the fitting model previously applied to Pt/Al_2O_3.

Figure IV-9 illustrates the original non smoothed IR spectra curve (in red), the global fitting function curve (in black), and the 2 linear CO and 3 bridged CO bands fitted after deconvolution for the spectra at 0 s (^{12}CO - Figure V-9a) and 60 s (^{13}CO - Figure V-9b). The fitted signals of spectra obtained at various time points of the exchange process are provided in the annex SIV-2.

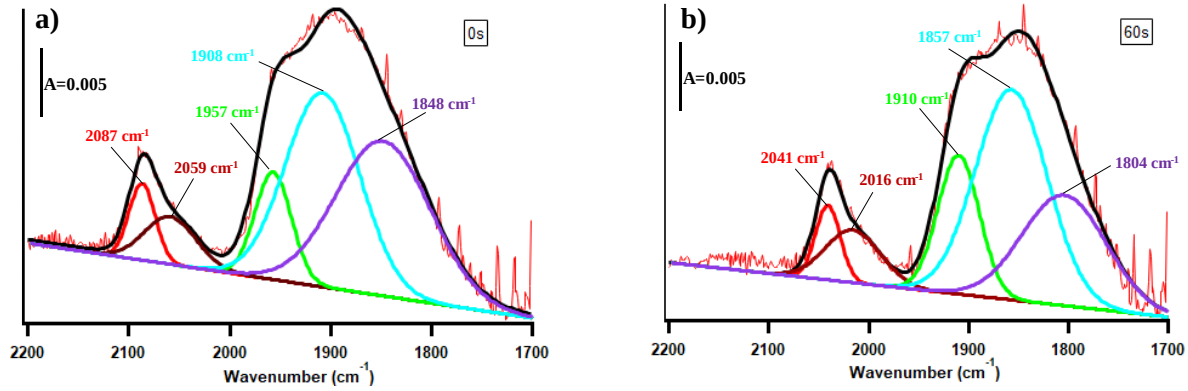

Figure IV-9- Individual adsorption bands of the 5 adsorbed CO species obtained after the deconvolution of the recorded spectrum on Pd/Al_2O_3: a) at 0s and b) 60s. The non-smoothed raw IR signal is represented in red and the result of deconvolution (5 Gaussian sum) by the black line.

The optimized fitting parameters (band positions and FWHM) given by the *Igor* software for ^{12}CO bands (0s) and their corresponding counterparts ^{13}CO bands after isotopic exchange (60s) are listed in the Table IV-5 below.

Table IV-5- Adsorbed CO on Pd band positions and FWHM resulted from spectra deconvolution at 0 and 60 s. These coefficients were then used as constants for further fittings.

		^{12}CO bands *from spectrum at 0 s*		^{13}CO bands *from spectrum at 60 s*	
Assignment [19–23]		**Position (cm^{-1})**	**FWHM (cm^{-1})**	**Position (cm^{-1})**	**FWHM (cm^{-1})**
Linearly adsorbed CO on terraces sites	**L1**	2087	12.9	2041	12.3
Linearly adsorbed CO on low-coordinated adsorption sites (corners or edges)	**L2**	2059	25.4	2016	27.5
Bridged carbonyl on Pd(100)	**L3**	1957	18.1	1910	20.7
Bridge-bound CO on Pd(100)	**L4**	1908	36.9	1857	36
Adsorbed CO on 3-fold Hollow sites	**L5**	1848	46.9	1804	42.1

These positions and FWHM were then set as constants to fit the other spectra. A label (L1 to L5) was also given to each band in for further reference along with their corresponding assignment. The evolution in the heights of these 10 bands have been summarized in the Table IV-6.

Table IV-6- Evolution of band heights for ^{12}CO and ^{13}CO linear and bridged species on Pd at different times of the isotopic exchange.

	^{12}CO bands					^{13}CO bands				
Bands (cm^{-1}) / Time	**2087 L1**	**2059 L2**	**1957 L3**	**1908 L4**	**1848 L5**	**2041 L1**	**2016 L2**	**1910 L3**	**1857 L4**	**1804 L5**
0s	0.006	0.004	0.008	0.014	0.011	0	0	0	0	0
1.2s	0.005	0.003	0.008	0.013	0.011	0	0	0.0009	0.0007	0.00001
2.5s	0.0041	0.0031	0.0054	0.0119	0.0108	0.0008	0.0006	0.0009	0.0009	0.0009
5s	0.002	0.001	0.001	0.008	0.0097	0.0028	0.0006	0.0019	0.0028	0.0009
10s	0.0008	0	0	0.0034	0.0091	0.0042	0.0016	0.0048	0.0043	0.0015
15s	0.0002	0	0	0.0008	0.0091	0.0044	0.0017	0.0069	0.0059	0.002
20s	0.0002	0	0	0.0007	0.0044	0.0045	0.0028	0.0078	0.0099	0.0046
30s	0.0002	0	0	0	0.0025	0.0048	0.0028	0.0078	0.0113	0.0048
60s	0	0	0	0	0	0.0049	0.0035	0.0091	0.0138	0.0072

Likewise, the areas of individual ^{12}CO and ^{13}CO bands were computed and plotted after normalization as a function of time of isotopic exchange in Figure IV-10 and Figure IV-11. Normalized evolutions of ^{12}CO and ^{13}CO conjugate band areas are represented by colored dotted and solid lines, respectively.

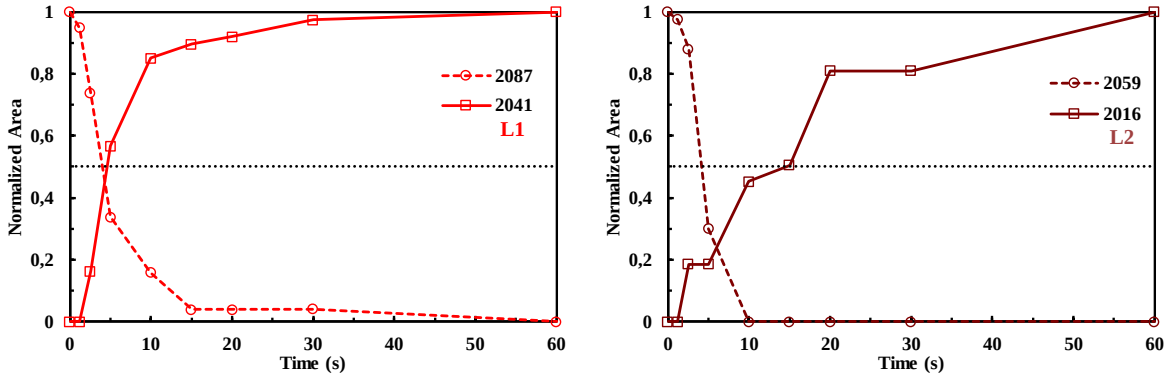

Figure IV-10- Evolution of normalized area for adsorbed linear ^{12}CO and corresponding linear ^{13}CO L1 (red) and L2 (dark brown) bands during isotopic exchange.

Figure IV-10 illustrates the evolution of normalized areas of both CO linearly adsorbed species (L1 and L2) on Pd. It's worth noting that these two bands do not exhibit identical behavior throughout the isotopic shift. The band L1(^{12}CO) at 2087 cm^{-1} exchanges symmetrically with the band L1(^{13}CO) at 2041 cm^{-1}, intersecting at ~0.5 at 5 seconds. In that case around 90% of $^{12}CO \rightarrow {}^{13}CO$ exchange is observed at the Pd surface in the first 15 seconds. Otherwise, the behavior of the L2 (^{13}CO) bands at 2016 cm^{-1} does not mirror the pattern of its homologue ^{12}CO band at 2059 cm^{-1}, since a slower increase in area is observed as a function of time. Indeed, the band at 2059 cm^{-1} vanishes completely after 10 seconds when only 45% of its ^{13}CO counterpart (2016 cm^{-1}) has reappeared on the Pd surface. The latter ^{13}CO band increases gradually until 60 seconds but does not reach a clear asymptote.

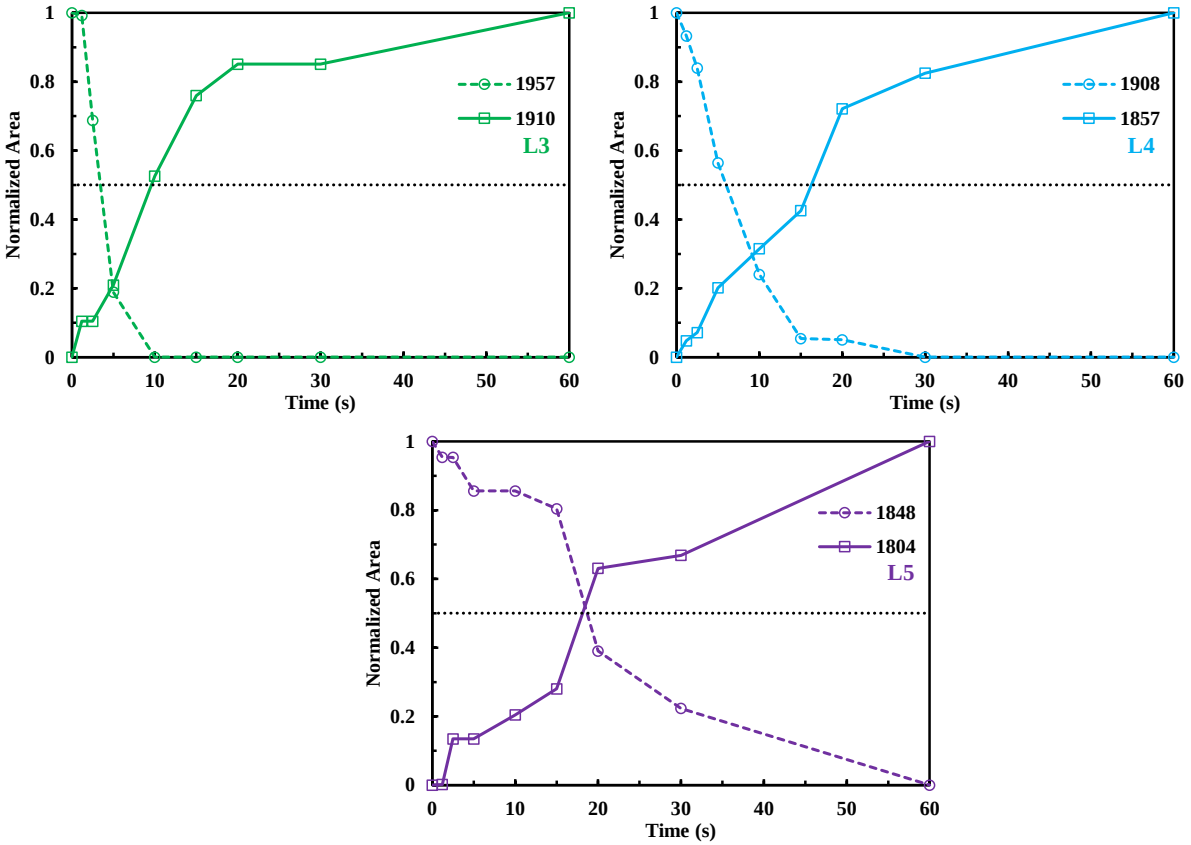

Figure IV-11- Evolution of normalized area for adsorbed bridged ^{12}CO and corresponding bridged ^{13}CO L3 (green), L4 (blue) and L5 (purple) bands during isotopic exchange.

Figure IV-11 depicts the evolution of normalized areas of the 3 types of bridged carbonyl (L3, L4 and L5) adsorbed on Pd during isotopic exchange. Once again, these bands exhibit diverse behaviors. Firstly, the L5(^{12}CO) band at 1848 cm^{-1} exchanges symmetrically with its corresponding L5(^{13}CO) band at 1804 cm^{-1}. However, their exchange process is relatively long since the two curves are crossing each other at ~0.5 just before 20 seconds. On the contrary, the other two types of bridged carbonyls do not show mirror pattern. The band L3(^{12}CO) at 1957 cm^{-1} experiences a significant decrease initially, disappearing after 10 seconds while its counterpart L3(^{13}CO) band at 1910 cm^{-1} gradually increases, reaching only 50% of its maximum area at 10 seconds. The band L4(^{12}CO) at 1908 cm^{-1} steadily decreases, disappearing at 30 seconds, while its homologue L4(^{13}CO) band at 1857 cm^{-1} increases progressively until 60 seconds. It is worth to note that in the case of CO isotopic exchange on Pd almost no time lag was observed, ^{13}CO species appearing quasi-immediately on the surface after the reactant switch.

As in the case of Pt, each carbonyl adsorbed on Pd exhibit a unique behavior during the $^{12}CO \rightarrow {}^{13}CO$ isotopic exchange. In order to continue our analysis, the transient kinetic exchange rate constants (k') for each ^{12}CO bands were estimated using the previously described kinetic model (Equation IV-2). Figure IV-12 displays linear plots of ln α as a function of time of exchange for the five linearly and bridged adsorbed ^{12}CO species bands. According to Equation IV-2, the absolute slope value yields the apparent exchange rate constant (k'^{12}CO) of each species. The k' values are given in Table IV-7.

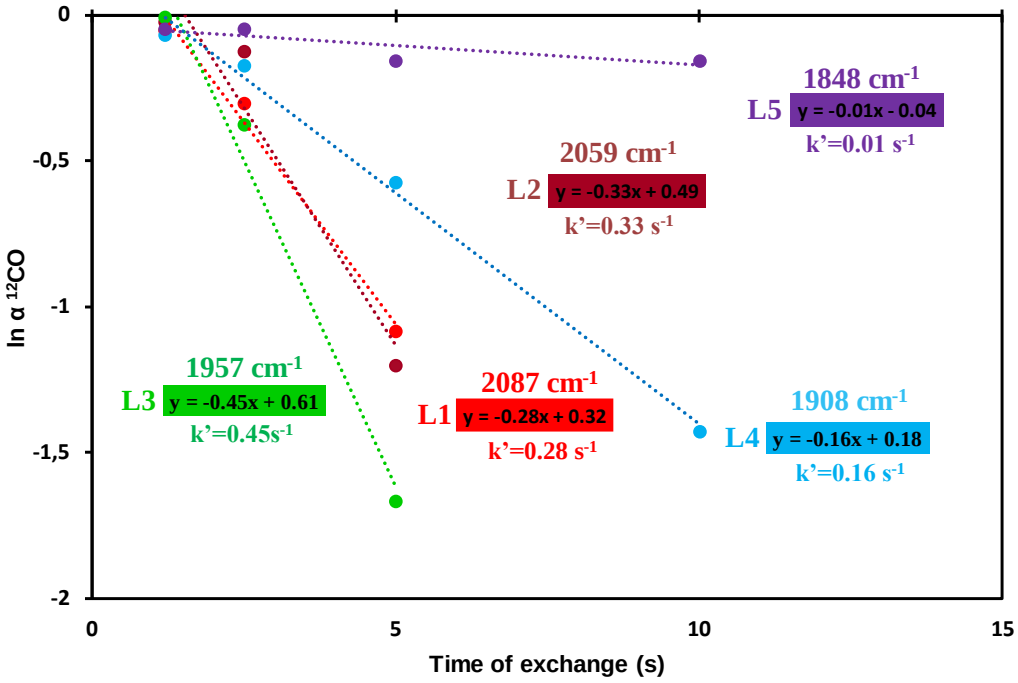

Figure IV-12- Plot of ln α vs. time (s) for the 5 types of adsorbed CO species (L1 to L5) adsorbed on Pd during the $^{12}CO \rightarrow {}^{13}CO$ SSITKA experiment at 116 °C.

The results in Figure IV-12 illustrate through the determination of the exchange rate, the varying reactivity toward CO oxidation of each adsorbed carbonyl species. The bands L1 and L2, corresponding to linear carbonyls at 2087 and 2059 cm^{-1} respectively, display similar reactivity as evidenced by close k' values (k'_{L1}=0.28 s^{-1} and k'_{L2}=0.33 s^{-1}). This result is consistent with the observation of an isosbestic point on Figure IV-8 during the isotopic exchange of linear carbonyls. Otherwise, the bridged carbonyls exhibit different reactivity. The faster kinetic rate constant k'_{L3}=0.45 s^{-1}, even higher than that of linear carbonyls, is observed for the band L3 at 1957 cm^{-1} attributed to bridged carbonyl adsorbed on Pd(100). Conversely the L4 and L5 bands, centered at 1908 cm^{-1} and 1848 cm^{-1} respectively, show much lower kinetic rate constants, i.e. k'_{L4}=0.16 s^{-1} and k'_{L5}=0.01 s^{-1}.

For the sake of comparison, the rate constants corresponding to the formation of 13-carbonyls species (k'^{13}CO) on the Pd surface were also calculated according to Equation IV-3 and the values are given in Table IV-7 below.

Table IV-7- Exchange kinetic rate constant for the five linear and bridged adsorbed CO disappearing (k'^{12}CO) and appearing (k'^{13}CO) on Pd during ^{12}CO→^{13}CO SSITKA experiment at 116 °C.

116 °C	**L1**	**L2**	**L3**	**L4**	**L5**
k' (^{12}CO) *s^{-1}*	0.28	0.33	0.45	0.16	0.01
k' (^{13}CO) *s^{-1}*	0.20	0.18	0.21	0.21	0.06

The table shows that the exchange kinetic rate constant (k'^{13}CO) of all 5 bands band are quite different in comparison to the exchange kinetic rate of its disappearance (k'^{12}CO). For example, L1, L2, L3 exhibit a higher kinetic rate constant k'^{12}CO compared to k'^{13}CO; higher (x1.5) for L1 and higher (x2) for L2 and L3 respectively. In contrast, L4 and L5 present a lower kinetic rate constant k'^{12}CO compared to k'^{13}CO; lower (-25%) for L4 and lower (x6) for L5. Overall, it's difficult to draw any direct conclusions based on the comparison of the ^{12}CO and ^{13}CO kinetic values, especially as a time lag (2 s) is observed, particularly for L1, L2 and L5 bands before the appearance of ^{13}CO species on Pd surface.

In a first attempt, the analysis of the separate area's evolution brings us to the conclusion that linear carbonyls (L1 and L2) and bridged carbonyls adsorbed on Pd (100) (L3 species) could be the best candidates to play an active role in the CO oxidation reaction while L4 and L5 would play a minor role. In order to verify this idea, the total surface coverage evolution of Pd during the ^{12}CO→^{13}CO SSITKA process was examined by plotting the sum of the ^{12}CO and ^{13}CO band areas as a function of time in Figure IV-13.

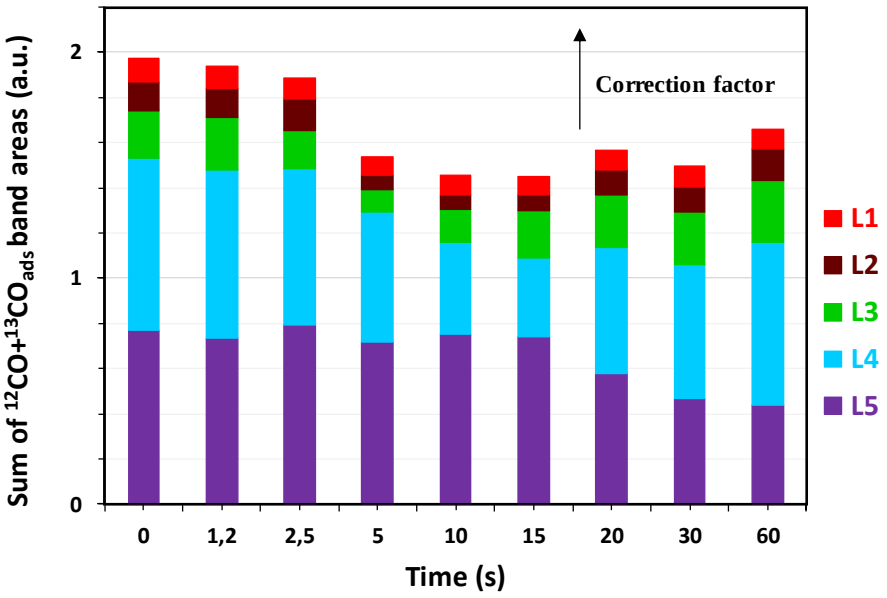

Figure IV-13- Evolution of sum of the areas of ^{12}CO and ^{13}CO bands during isotopic exchange on Pd/Al_2O_3.

Just like in the case of Pt, the maximum area values of the ^{12}CO and ^{13}CO bands at 0 and 60 s, respectively, do not correspond to each other due to the difference of extinction coefficient values for ^{12}C and ^{13}C carbonyls. Therefore, correction factors have also been utilized here to correct each individual L1 to L5 ^{13}CO areas and normalize their combinations according to the approach described previously in Equations IV-4 and IV-5. The values of the 5 correction factors are given in Table IV-8 and the new combinations of band areas are plotted as a function of time in Figure IV-14.

Table IV-8- Calculated correction factors for each CO adsorbed IR bands on Pd.

	L1	L2	L3	L4	L5
f	0.83	1.07	1.33	0.95	0.57

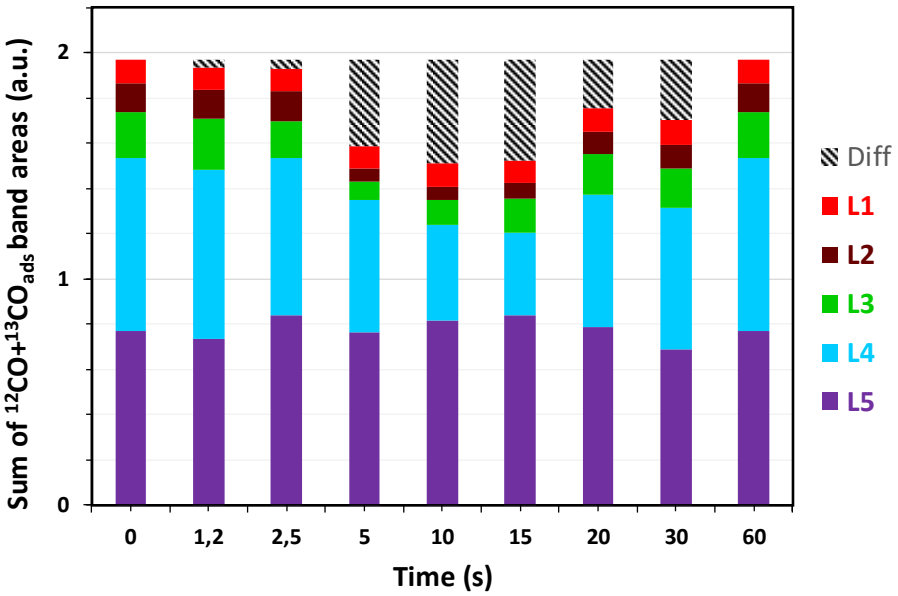

Figure IV-14- Evolution of the sum of adsorbed L1 to L5 ^{12}CO and corrected ^{13}CO band areas during isotopic exchange on Pd/Al_2O_3.

Figure IV-14 illustrates that the area of cumulated L1 bands, representing the linear carbonyl species adsorbed on Pd terraces, remains relatively stable during the isotopic exchange. Similarly, the L5 bands do not show any area trend, only experiencing random variations (0.76 ± 0.08). Conversely, the sum of $^{12}CO+^{13}CO$ L2 band areas, corresponding to the linear carbonyls adsorbed on low coordinated sites, initially maintains a stable value before decreasing significantly at 5 seconds (-51%), then returning to its initial surface after 20 seconds. As the latter, the L3 bands experiences a sharp decline in area starting at 2.5 seconds (-60% at 5 s) followed by a gradual increase from 10 seconds up to its maximum value. Finally the L4 bands, assigned to bridge-bound CO on Pd(100) and contributing initially for almost 40% of the surface coverage, undergo a slow decrease up to 15 seconds (-52%), then increase to return progressively to their initial level. As previously, we can observe that the sums of all bands deviate from the maximum value (~2) during the isotopic exchange process. The difference (*diff*), highlighted by black stripes in Figure IV-14, represents more than 20% of missing CO adsorbed at 10 seconds compared to the initial coverage. Once again, this effect could certainly be attributed to the competitive adsorption of CO and O existing on Pd surface during the oxidation reaction. It should be noted that a much higher *diff* percentage is obtained for Pd compared with Pt catalyst (~9%) perhaps because of the greater affinity of Pd particles for oxidation [24].The results provide better insight into the contribution of each species in CO oxidation. Notably, the bridge-bound carbonyls (L3 bands), which showed previously the higher kinetic rate constant (k'^{12}CO), definitely play a substantial role in driving CO_2

production. Both L2 and L4 species, despite their varying reactivity (with L2 exchanging more rapidly than L4), also seem to contribute to the formation of CO_2. Conversely, it clearly appears that the last two carbonyl species, L1 and L5, would have a minor role or would not even participate in the CO_2 formation. Especially, the adsorbed CO on 3-fold hollow sites (L5), which has a very slow kinetic rate constant ($k'^{12}CO = 0.01\ s^{-1}$) and fluctuating band areas, illustrates a spectator behavior.

In conclusion, the kinetic study realized on Pd/Al_2O_3 do not allow a clear discrimination of a unique active species as for the case of Pt. However, the crucial role L3 bridged carbonyls in CO_2 formation was identified while a CO adsorbed on a 3-fold hollow site seems useless. Moreover, it is interesting to see that a relatively high kinetic rate constant, such as the case of L1 species (CO on Pd terrace; $k'^{12}CO = 0.28\ s^{-1}$), is not synonymous with major involvement in product formation.

4- Conclusion

This chapter has illuminated the reactivity of linear and bridged carbonyl bands on both Pt and Pd supported on Al_2O_3. In the context of Pt/Al_2O_3, the prevalence of linear bands was evident, with four distinct types of these bands identified through deconvolution based on existing literature. Each peak exhibited distinct adsorption site characteristics and kinetic rate constants for exchange. The rapid exchange rates were attributed to bands linked to carbonyl adsorption on terrace sites (2080 cm^{-1}) and carbonyl adsorption on subnanometer particles (2059 cm^{-1}), both demonstrating the highest kinetic rate constants. The analysis of the overall surface coverage area of the catalyst during isotopic exchange has confirmed the non-active behavior of L3 and L4 species, consistent with their lower kinetic rate constant. Furthermore, this investigation has identified that the linear CO adsorbed on Pt steps specie is the main intermediate in the CO_2 formation while the linear CO adsorbed on Pt terraces specie might play a minor role in product formation despite having a higher kinetic rate constant.

Similarly, in the case of Pd/Al_2O_3, a predominance of linear and bridged carbonyl bands was observed. These were further deconvoluted into five distinct types of bands and subjected to fitting to explore their reactivity and role in CO_2 formation. Just as like in the Pt/Al_2O_3 case, each peak exhibited its own unique kinetic rate constant. The most rapid exchange occurred in the band at 1957 cm^{-1}, associated with bridged carbonyl adsorbed on Pd(100), as well as the

band at 2059 cm^{-1}, linked to linear carbonyl adsorbed on low-coordinated sites. The analysis of the overall surface coverage area has provided insights into the roles of each species in the CO oxidation reaction. It reveals that the bridge-bound carbonyls (L3 bands) play a major role in CO_2 production, while L2 and L4 play a minor role. In contrast, the adsorbed CO on 3-fold hollow sites (L5) appears to be an inactive species in the CO oxidation reaction, consistent with its lower kinetic exchange. Another important conclusion from this study is that a band with a high kinetic rate constant might exchange rapidly to its counterpart without significantly affecting product formation as the case of L1 band in the case of Pd/Al_2O_3. This study's significance is highlighted by its revelation that the linear and bridged carbonyls, previously assumed to be active species, are actually composed of multiples bands, not all of which participate in the reaction mechanism. This newfound understanding will provide a profound insight into the distinct roles played by each species formed. Consequently, it will facilitate a more comprehensive grasp of which specific bands contribute to the catalytic activity's high performance.

References

1. Shigeishi RA, King DA (1976) Chemisorption of carbon monoxide on platinum {111}: Reflection-absorption infrared spectroscopy. Surf Sci 58:379–396. https://doi.org/10.1016/0039-6028(76)90477-5

2. Ertl G, Neumann M, Streit KM (1977) Chemisorption of CO on the Pt(111) surface. Surf Sci 64:393–410. https://doi.org/10.1016/0039-6028(77)90052-8

3. Steininger H, Lehwald S, Ibach H (1982) On the adsorption of CO on Pt(111). Surf Sci 123:264–282. https://doi.org/10.1016/0039-6028(82)90328-4

4. Heyden BE, Bradshaw AM (1983) The adsorption of CO on Pt(111) studied by infrared reflection—Absortion spectroscopy. Surf Sci 125:787–802. https://doi.org/10.1016/S0039-6028(83)80060-0

5. Satsuma A, Osaki K, Yanagihara M, et al (2013) Activity controlling factors for low-temperature oxidation of CO over supported Pd catalysts. Appl Catal B Environ 132–133:511–518. https://doi.org/10.1016/j.apcatb.2012.12.025

6. Peterson EJ, DeLaRiva AT, Lin S, et al (2014) Low-temperature carbon monoxide oxidation catalysed by regenerable atomically dispersed palladium on alumina. Nat Commun 5:4885. https://doi.org/10.1038/ncomms5885

7. Ivanova AS, Slavinskaya EM, Gulyaev RV, et al (2010) Metal–support interactions in Pt/Al_2O_3 and Pd/Al_2O_3 catalysts for CO oxidation. Appl Catal B Environ 97:57–71. https://doi.org/10.1016/j.apcatb.2010.03.024

8. Bourane A, Bianchi D (2003) Oxidation of CO on a Pt/Al_2O_3 catalyst: from the surface elementary steps to light-off tests: IV. Kinetic study of the reduction by CO of strongly adsorbed oxygen species. J Catal 220:3–12. https://doi.org/10.1016/S0021-9517(03)00267-7

9. Bourane A, Dulaurent O, Chandes K, Bianchi D (2001) Heats of adsorption of the linear CO species on a Pt/Al_2O_3 catalyst using FTIR spectroscopy: Comparison between TPD and adsorption equilibrium procedures. Appl Catal Gen 214:193–202. https://doi.org/10.1016/S0926-860X(01)00483-5

10. Bourane A, Derrouiche S, Bianchi D (2004) Impact of Pt dispersion on the elementary steps of CO oxidation by O_2 over Pt/Al_2O_3 catalysts. J Catal 228:288–297. https://doi.org/10.1016/j.jcat.2004.08.020

11. Ebbesen SD, Mojet BL, Lefferts L (2009) The influence of water and pH on adsorption and oxidation of CO on Pd/Al_2O_3 —an investigation by attenuated total reflection infrared spectroscopy. Phys Chem Chem Phys 11:641–649. https://doi.org/10.1039/B814605E

12. Murata K, Eleeda E, Ohyama J, et al (2019) Identification of active sites in CO oxidation over a Pd/Al_2O_3 catalyst. Phys Chem Chem Phys 21:18128–18137. https://doi.org/10.1039/C9CP03943K

13. Szanyi J, Kwak JH (2014) Dissecting the steps of CO_2 reduction: 1. The interaction of CO and CO_2 with γ-Al_2O_3: an in situ FTIR study. Phys Chem Chem Phys 16:15117–15125. https://doi.org/10.1039/C4CP00616J

14. Xu J, Ouyang L, Mao W, et al (2012) Operando and Kinetic Study of Low-Temperature, Lean-Burn Methane Combustion over a Pd/γ-Al_2O_3 Catalyst. ACS Catal 2:261–269. https://doi.org/10.1021/cs200694k

15. Sangnier A, Genty E, Iachella M, et al (2021) Thermokinetic and Spectroscopic Mapping of Carbon Monoxide Adsorption on Highly Dispersed Pt/γ-Al_2O_3. ACS Catal 11:13280–13293. https://doi.org/10.1021/acscatal.1c04262

16. Barth R, Pitchai R, Anderson RL, Verykios XE (1989) Thermal desorption-infrared study of carbon monoxide adsorption by alumina-supported platinum. J Catal 116:61–70. https://doi.org/10.1016/0021-9517(89)90075-4

17. Vasiliades MA, Kalamaras CM, Govender NS, et al (2019) The effect of preparation route of commercial Co/γ-Al_2O_3 catalyst on important Fischer-Tropsch kinetic parameters studied by SSITKA and CO-DRIFTS transient hydrogenation techniques. J Catal 379:60–77. https://doi.org/10.1016/j.jcat.2019.09.008

18. Gun Oh D, Aleksandrov HA, Kim H, et al (2022) Key Role of a-Top CO on Terrace Sites of Metallic Pd Clusters for CO Oxidation. Chem – Eur J 28:e202200684. https://doi.org/10.1002/chem.202200684

19. Juszczyk W, Karpiński Z, Ratajczykowa I, et al (1989) Characterization of supported palladium catalysts: III. $PdAl_2O_3$. J Catal 120:68–77. https://doi.org/10.1016/0021-9517(89)90251-0

20. Palazov A, Kadinov G, Bonev Ch, Shopov D (1982) Infrared spectroscopic study of the interaction between carbon monoxide and hydrogen on supported palladium. J Catal 74:44–54. https://doi.org/10.1016/0021-9517(82)90007-0

21. Tessier D, Rakai A, Bozon-Verduraz F (1992) Spectroscopic study of the interaction of carbon monoxide with cationic and metallic palladium in palladium–alumina catalysts. J Chem Soc Faraday Trans 88:741–749. https://doi.org/10.1039/FT9928800741

22. Di Gregorio F, Bisson L, Armaroli T, et al (2009) Characterization of well faceted palladium nanoparticles supported on alumina by transmission electron microscopy and FT-IR spectroscopy of CO adsorption. Appl Catal Gen 352:50–60. https://doi.org/10.1016/j.apcata.2008.09.034

23. Yudanov IV, Sahnoun R, Neyman KM, et al (2003) CO Adsorption on Pd Nanoparticles: Density Functional and Vibrational Spectroscopy Studies. J Phys Chem B 107:255–264. https://doi.org/10.1021/jp022052b

24. Spronsen MA van, M. Frenken JW, N. Groot IM (2017) Surface science under reaction conditions: CO oxidation on Pt and Pd model catalysts. Chem Soc Rev 46:4347–4374. https://doi.org/10.1039/C7CS00045F

Chapter V- Hysteresis in CO oxidation reaction: A kinetic study using SSITKA-IR technique.

.

1- Introduction

The catalytic oxidation of CO has gained significant interest within studies on catalytic reaction dynamics. This is primarily attributed to its intricate and dynamic behavior, characterized by phenomena like hysteresis at low temperature [1]. Hysteresis behavior involves the detection of multiple stable states across a diverse array of experimental conditions. Typically, this is evident at lower temperatures, where the catalyst's activity (such as reaction rate or degree of conversion) does not align during light-off and light-out phases [2]. This mismatch is reflected in the conversion vs. temperature plot, resulting in the creation of a hysteresis loop.

The origin of hysteresis remains a topic of ongoing discussion within the literature, giving rise to various explanations. Most of the authors propose that hysteresis arises from the replacement of one steady state with another during gradual temperature shifts. This transition leads to a distinct reaction rate for a consistent temperature, resulting in the observed hysteresis phenomenon [3–5]. But alternative explanations for hysteresis have been put forward, including the concept of a macro-kinetic transition from kinetic to diffusion mode [6], the interaction between diffusion and reaction processes [7, 8], the occurrence of phase transition within catalysts [2] and the possibility of local overheating at active sites [9, 10]. Indeed, understanding the origin behind this phenomenon holds significant promise. Such comprehension can be essential to manipulate catalyst activity and ensuring its sustained high performance at low temperatures. Moreover, it provides valuable insights into instances of reduced activity, aiding in the identification of the root causes behind the decline in catalytic efficiency. This knowledge serves as a foundation for optimizing catalytic processes and designing catalysts that maintain their effectiveness under a wide range of operating conditions.

The use of *in situ* techniques becomes crucial in order to deeply examine the catalyst's surface and identifying the species and intermediates that form during the hysteresis phenomena. The SSITKA-IR technique proves particularly useful for this task. It provides insights into various kinetic parameters, like the concentration of active intermediates and turnover frequencies (TOFs) and allows us to visualize the surface species. The SSITKA-IR technique has already proved its effectiveness in previous chapters enabling us to differentiate between active and inactive species in CO oxidation over PGM/Al_2O_3. Firstly, linear and bridged carbonyls were distinguished from the hydrogen-carbonate species, the latter being inactive in the product formation. In the chapter 4, we delved into the individual reactivity of linear and bridged carbonyls, investigating their behavior during isotopic exchange following the deconvolution of overlapping bands. This exploration unveiled variations in the kinetic rate of each species

during the SSITKA exchange which allowed us to conclude on their true reactivity toward CO oxidation process.

In this chapter, a similar SSITKA-IR approach will be employed comparing the light-off and light-out phases during CO oxidation on Pt/Al_2O_3 and Pd/Al_2O_3 to assess whether the main active carbonyls species exhibit different behaviors. Thus, a better grasp of the hysteresis phenomenon and the observed activity discrepancies is expected. Furthermore, special attention will be given to study the impact of reductive H_2 pulses on the catalytic activity of both catalysts based on our understanding of the hysteresis. The ultimate goal is to gain insights into how these pulses enhance the catalyst's performance and find ways to sustain this heightened level of catalytic activity at low temperature, potentially uncovering strategies for catalyst optimization and stability in CO oxidation reaction.

2- Study of CO oxidation hysteresis

2.1- Hysteresis kinetics investigation on Pt/Al_2O_3

The CO oxidation reaction was performed using a catalyst pellet (5.9 mg) containing 0.82 wt% Pt supported on Al_2O_3 following the pretreatment steps explained in chapter 2. A feed mixture consisting of 2000 ppm of CO and 10% of O_2 in He was introduced into the reactor cell and a full cycle of temperature (increase and decrease) from 50 to 300 °C was applied with a ramp of 1 °C/min. The reaction progress was monitored by gas chromatography (GC) to track the conversion of CO reactant. Figure V-1 shows the CO conversion evolution below 30 % during both the light-off and light-out phases. The full evolution is plotted in Annex Figure SV-1.

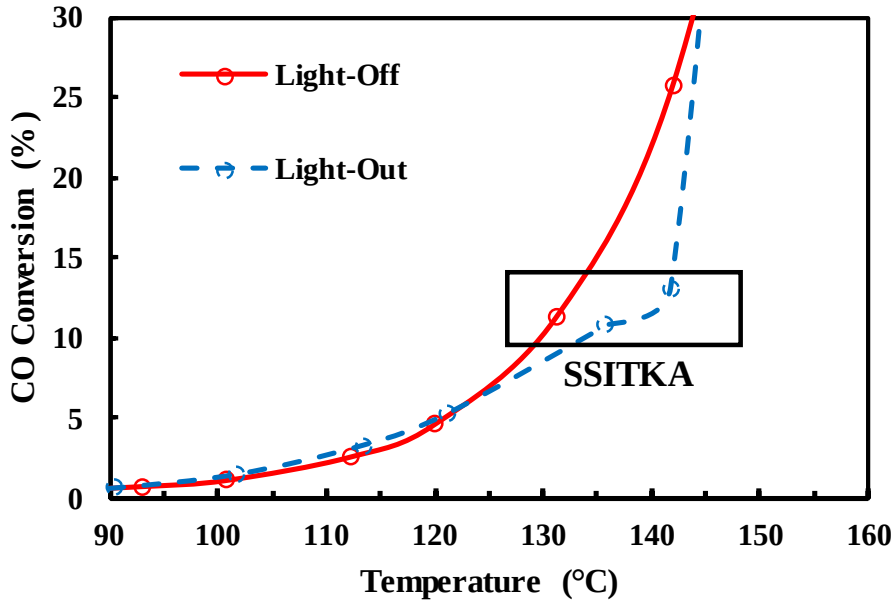

Figure V-1- Evolution of CO conversion below 30% vs. temperature during light-off and light-out of CO oxidation on Pt/Al_2O_3.

It appears clearly that, at low temperature (125-145 °C), the activity of the catalyst during light-off and light-out do not match. The lower activity observed during the light-out step compared to light-off is indicative of an inverse hysteresis phenomenon. The maximum temperature difference for the same conversion level (15%) is approximately 13 °C. It's worth noting that this inverse hysteresis transitions to a normal hysteresis (activity higher in light-out) at higher conversions, with a temperature difference of about 8 °C at 90% of CO conversion level (Figure SV1 in Annex). Activation energies were estimated for both light-off and light-out conditions, revealing a notable distinction. An activation energy of 110 kJ mol^{-1} is obtained during the increase in temperature, i.e. approximately twice as high as that observed during light-out ($E_{a(out)}$ = 68 kJ mol^{-1}).

In order to get more insights about the causes of the hysteresis observed, SSITKA-IR experiments were conducted during both light-off and light-out at the same conversion level (χ_{CO} = 11%) on the Pt catalyst. The latter conversion was reached at 131.0 °C and 135.8 °C during the increase and decrease in temperature, respectively. The normalized MS signals of ^{13}CO, $^{13}CO_2$ and CH_4 (inert) obtained after the isotopic $^{12}CO \rightarrow {}^{13}CO$ switch performed during the light-out phase at 135.8 °C are depicted in Figure V-2**Figure *V-2***. The results obtained for the light-off SSITKA experiment at 131 °C were presented in chapter 3, Figure III-2.

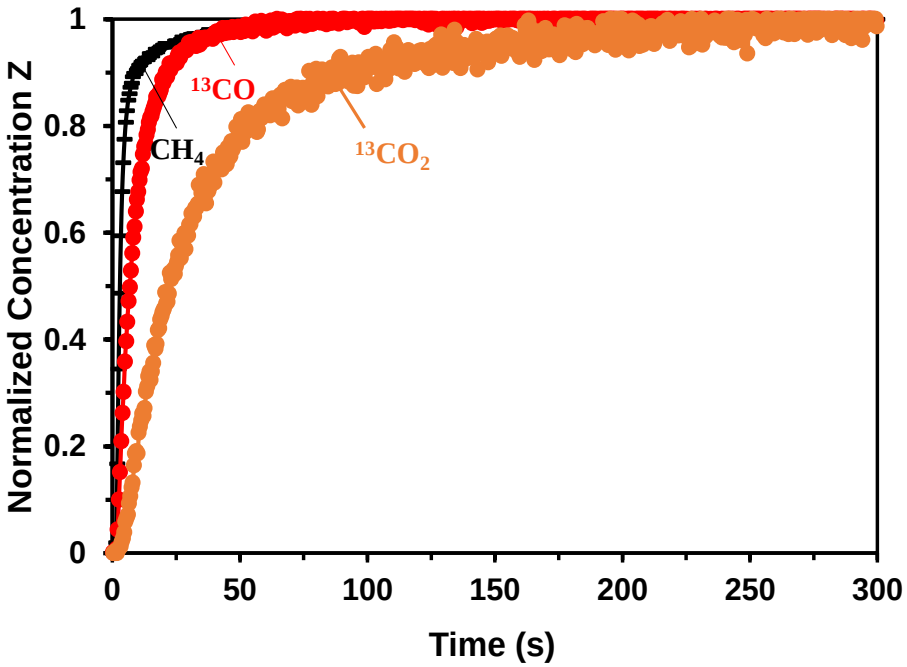

Figure V-2- Normalized concentrations of CH_4, ^{13}CO and $^{13}CO_2$ obtained during the light-out SSITKA experiment ($^{12}CO/O_2/He \rightarrow {}^{13}CO/O_2/Kr/CH_4/He$) on Pt/Al_2O_3 at 135.8 °C (χCO = 11%).

As seen in Figure V-2, the ^{13}CO transient response curve lags behind that of the tracer (CH_4) due to the formation of reversibly adsorbed CO on Pt surface during oxidation reaction. Similarly, the $^{13}CO_2$ transient response curve lags behind that of ^{13}CO indicating that, in theory, the formation of $^{13}CO_2$ product passes through one or more adsorbed reaction intermediates after ^{13}CO adsorption. The mean surface residence times (τ), the concentrations N and surface coverages (θ) of reversibly adsorbed CO and C-contained species were estimated according to SSITKA theory. The results are compared with the values obtained during the light-off SSITKA experiment (Chap 3) in Table V-1.

Table V-1- Mean residence times τ, concentrations N, surface coverages θ of adsorbed CO and C-containing species calculated from the light-off and light-out SSITKA experiments on Pt/Al_2O_3 (χCO = 11%).

	T (°C)	τ_{CO} (s)	N_{CO} (µmol g^{-1})	θ_{CO}	r_{CO} (µmol g^{-1} s^{-1})	τ_C (s)	N_C (µmol g^{-1})
Light-Off	131.0	5.2	13.4	0.47	2.58	29.9	9.8
Light-Out	135.8	4.5	11.8	0.41	2.62	29.5	9.3

The comparison indicates that the quantity of reversibly adsorbed CO during light-off (13.4 µmol g^{-1}) exceeds that during light-out (11.8 µmol g^{-1}) leading also to a decrease of about 13% in Pt surface coverage. However, these results lead to an increase in the rate of CO formation

which is consistent with the increase in temperature according to Arrhenius law. In conclusion, it appears that the comparison of SSITKA kinetic parameters at two different temperature prohibits us from drawing any clear correlation between the quantity of N_{CO} and the catalyst's activity. It is worth to note that the τ_C and N_C are relatively similar in light-off and light-out, decreasing only slightly as a result of the temperature difference. As previously discussed in chapter 3, these values are linked to the re-adsorption of CO_2 product to form hydrogen-carbonate species on the inactive alumina support which certainly explains why they are not affected in the hysteresis process.

Figure V-3 displays a comparison of the spectra recorded at t=0 s (^{12}CO) during both light-off and light-out steps. We focused here on linear carbonyls, which have been proposed to play the main active role in product formation.

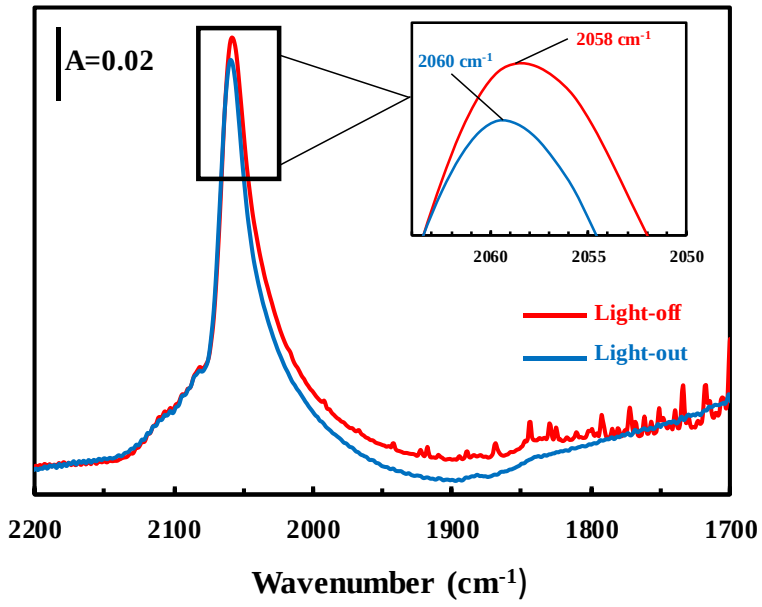

Figure V-3- Comparison of CO linear IR bands at t=0s during light-off (131 °C) and light-out (135.8 °C) SSITKA experiments on Pt/Al_2O_3 (χCO = 11%).

The intensity of the main ^{12}CO linear bands around 2058 cm^{-1} is lower during light-out compared to light-off, accounting for approximately 5% of loss in intensity. This variation could be linked to the decrease of the quantity of reversibly adsorbed CO (-13%), calculated previously between SSITKA experiment. It's also worth noting that a subtle but significant 2 cm^{-1} shift of the adsorbed CO linear band is observed towards higher wavenumbers. However, this blue shift is not consistent with the lower CO surface coverage observed on Pt that should in the contrary increase the possibility of back donation from the metal, due to lesser lateral interactions, and so decrease the wavenumber position of the band (surface coverage ↘ = ν(CO)

↘) [11]. Thus, this shift could be indicative of structural, oxidation or interaction changes occurring at the catalyst's surface during the light-out phase, which may be contributing to the observed differences in catalytic behavior.

In this context, a comprehensive analysis of the overlapped linear carbonyl bands has been conducted using the same kinetic model and methodology as in Chapter 4. The goal was to compare and identify any differences that may exist in terms of species distribution and/or exchange kinetics. The positions of L1 to L4 bands (^{12}CO and ^{13}CO) and their respective FWHM, identified previously in light-off analysis (Table IV-1 in Chap 4), were used as such to fit the IR signal obtained during the light-out SSITKA-IR experiment. The results of the fitting at t=0 s and t=60 s are presented in Figure V-4, respectively.

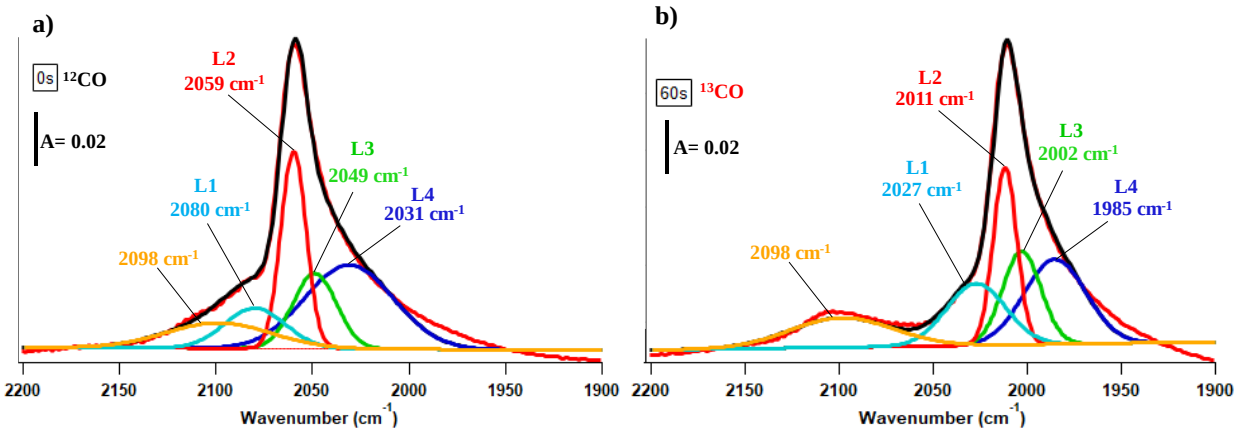

Figure V-4- Individual adsorption bands of the 5 adsorbed CO species obtained after the deconvolution of the recorded spectrum on Pt/Al_2O_3: a) at 0 s and b) 60 s during the light-out SSITKA-IR experiment. The non-smoothed raw IR signal is represented in red and the result of deconvolution (5 Gaussian sum) by the black line.

Figure V-4 presents the original non smoothed IR spectra (in red), the global fitting function curve (in black), and the 5 individuals linearly adsorbed ^{12}CO and ^{13}CO bands fitted after deconvolution of the spectra at 0 s and 60 s obtained during the light-out SSITKA-IR experiment. As mentioned in chapter 4, the band at 2098 cm^{-1}, corresponding to carbonyl adsorbed on oxidized Pt, remained unchanged throughout the fitting process, not showing isotopic shift. The fitting results for all spectra recorded during the light-out SSITKA-IR experiment at various time points are provided in the annex SV-2. The normalized area evolutions of ^{12}CO and ^{13}CO L1 to L4 bands have also been plotted in annex Figure SV-3. As seen previously, the area curves of L2 and L4 exhibited an asymmetric isotopic exchange, not crossing each other at 0.5. In contrast, the area curves of L1 and L3 cross each other at 0.5, indicating a symmetric isotopic exchange, which is distinct from what was observed during light-off.

The kinetic exchange rate constants k' of each individual ^{12}CO carbonyls bands were determined using the same kinetic model used for the light-off experiment. The results of ln α versus time, α corresponding to the area ratio A_t/A_0 for each individual band, are presented in Figure V-5 where the absolute slope value provides k'^{12}CO of each carbonyls species.

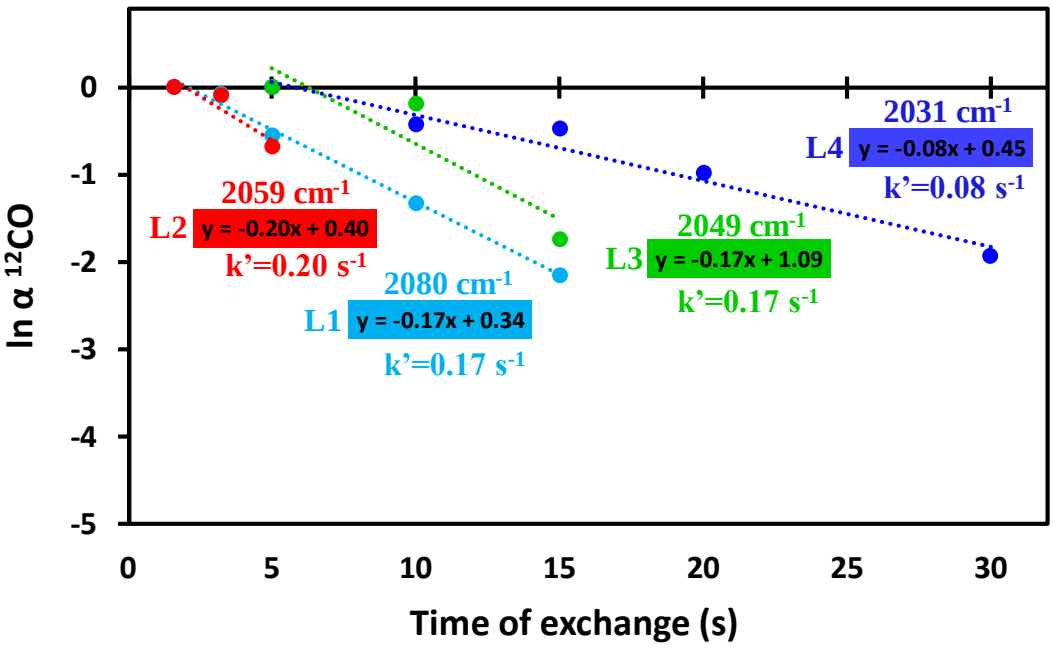

Figure V-5- Plot of ln α vs. time (s) for the 4 linear CO species (L1 to L4) adsorbed on Pt during SSITKA light-out experiment at 135.8 °C.

The graph illustrates that the linear CO species with the bands located at 2080 cm^{-1}, 2059 cm^{-1}, and 2049 cm^{-1} exhibit the highest kinetic exchange rate constants (approximately 0.2 s^{-1}). In contrast, the band L4 at 2031 cm^{-1} is characterized by a notably slower rate constant of around 0.08 s^{-1}. A comparison with k'^{12}CO obtained during light-off SSITKA-IR experiment in chapter 4 is summarized in Table V-2.

Table V-2- Comparison between exchange kinetic rate constants for adsorbed ^{12}CO species on Pt during light-off and light-out SSITKA-IR experiments.

k'^{12}CO (s^{-1})	T (°C)	2080 cm^{-1} L1	2059 cm^{-1} L2	2049 cm^{-1} L3	2031 cm^{-1} L4
Light-Off	131.0	0.51	0.47	0.23	0.12
Light-Out	135.8	0.17	0.20	0.17	0.08

The data clearly show that the L4 band at 2031 cm^{-1} exhibits the lowest kinetic rate constant compared to the other bands, both in light-off and light-out conditions, with an even lower rate in light-out. The bands L1 and L2, centered at 2080 and 2059 cm^{-1}, characterized initially as

the most reactive species (highest k'^{12}CO of the light-off experiment), experience a significant decrease (~60%) in their exchange rate constants during light-out. Similarly, the kinetic rate constant of L3 ^{12}CO species obtained during light-out decreases of about 25% compared to its initial light-off value. These results suggest that the reactivity of carbonyl species decreased overall after a high temperature cycle while maintaining the relative order of reactivity between each species. However, once again, because we are not operating SSITKA-IR experiments at the same temperature during light-off and light-out, a correlation between the variation of kinetic rate constants with hysteresis activity phenomenon would be precipitous.

As deduced using SSITKA analysis, the overall concentration of reversibly adsorbed CO (N_{CO}) on Pt was lower during the light-out phase. In order to get a more details on the species distribution at the Pt surface during the light-out SSITKA process and examine whether there are any changes compared to the light-off results, we decided to plot the sum of the ^{12}CO and ^{13}CO band areas as a function of time.

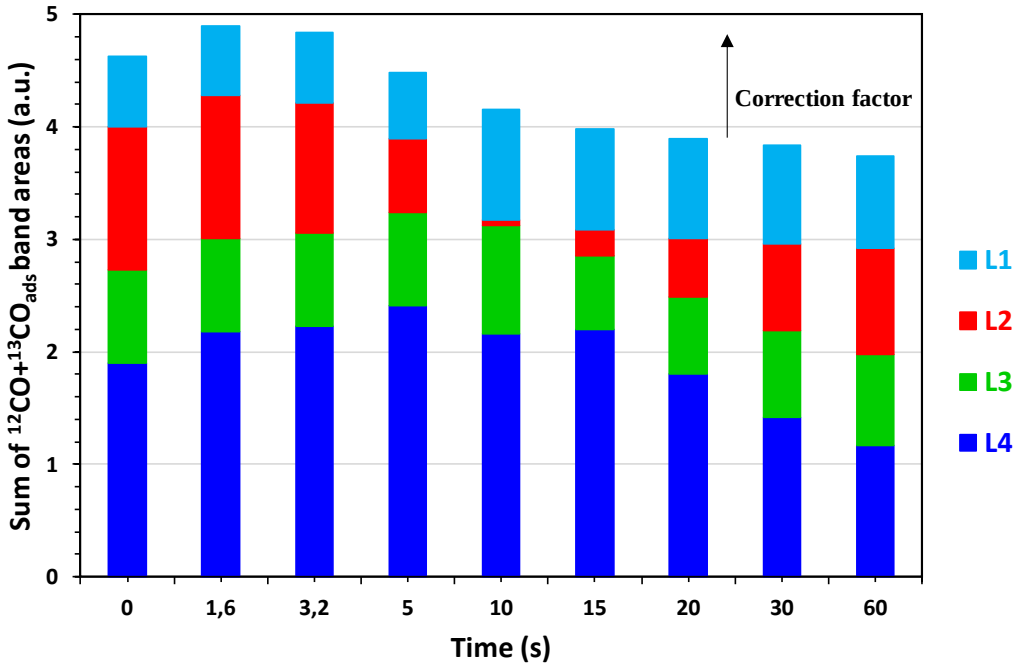

Figure V-6- Evolution of sum of the areas of adsorbed L1 to L4 ^{12}CO + ^{13}CO bands during ^{12}CO→^{13}CO light-out isotopic exchange on Pt/Al_2O_3 at 135.8 °C.

The result, presented in Figure V-6, illustrates the behaviors of the different bands, namely L1, L2, L3, and L4, in term of Pt surface coverage evolution during the light-out isotopic exchange. Correction factors, reported in annex Table SV-1, have been applied on the values of ^{13}CO band areas to align the area maximum values at t = 0 s and 60 s (method detailed in chapter 4). After

correction, the new areas sums were compared in Figure V-7 to the corrected sums obtained during the light-off process (Figure IV-7) for chosen time.

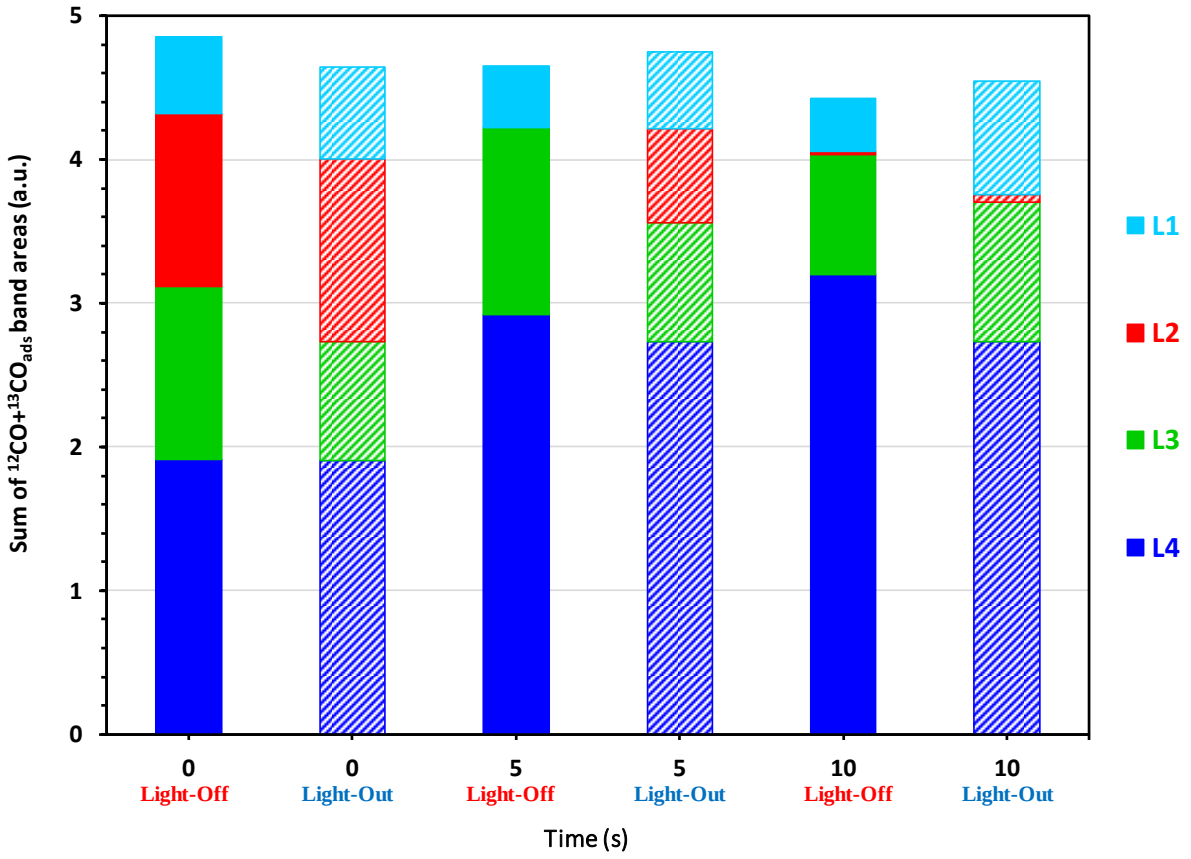

Figure V-7- Comparison of the corrected sum of adsorbed L1 to L4 ^{12}CO + ^{13}CO band areas during light-off and light-out SSITKA-IR experiment on Pt/Al_2O_3 at 0, 5 and 10 s.

Figure V-7 shows that initially (t=0 s), L3 species is more abundant on the Pt in the light-off phase while other bands, L1, L2, and L4, exhibit much comparable distribution in both conditions. However, the main difference is observed at 5 seconds where the L2 species, which we recognized as the main active intermediate in product formation during the light-off activity, has completely disappear from the surface in contrast with the light-out L2 area decreasing more slowly to its minimum level at 10 seconds (-96%). This discrepancy is consistent with the reduced rate constant k'^{12}CO observed for L2 species during the light-out phase. At 10 seconds, while L1 and L3 species concentrations have slightly decreased during the light-off, accumulations of L1 (+27%), L3 (+18%) and L4 (+44%) signals were now observed at the Pt surface (light-out). The same behavior was already shown for L3 and L4 species during the

light-off reflecting, in line with low kinetic rate constants, their inactive role in the CO oxidation.

In conclusion, no significant differences are observed in the behavior of the L3 and L4 during isotopic exchange between the light-off and light-out conditions, excepted for the lowest quantity of L3 species initially present on the Pt surface. Concerning L2, assigned to CO adsorbed on Pt step, the much lower exchange kinetic rate constant $k'^{12}CO$ observed during light-out experiment is also reflected into the difference in time required to reach its minimum coverage. Nevertheless, L2 still appears to be the main reactive species in the CO oxidation process while the role of L1 species (CO adsorbed on Pt terrace) seems more limited. However, with a difference of 5 °C between both conditions, any tentative to explain the hysteresis with the kinetic results obtained would be inaccurate. In order to get valuable insights into the underlying factors contributing to the hysteresis phenomenon, an investigation at iso-temperature (but different conversion) should be performed. Unfortunately, the latter was not conducted in this thesis work for Pt catalyst.

2.2- Hysteresis kinetics investigation on Pd/Al_2O_3

The CO oxidation reaction has been carried out on the pre-treated 0.87 wt% Pd/Al_2O_3 catalyst (7.5 mg). A feed mixture consisting of 2000 ppm of CO and 10% of O_2 in He was introduced into the IR reactor cell. The experimental procedure involved a full cycle of temperature (increase and decrease 1 °C/min) up to 400 °C. The reaction progress was monitored by gas chromatography (GC) to track the conversion of reactants. Figure V-9 shows the evolution of CO conversion below 30 % during both the light-off and light-out phases. The full evolution is plotted in Annex SV-4.

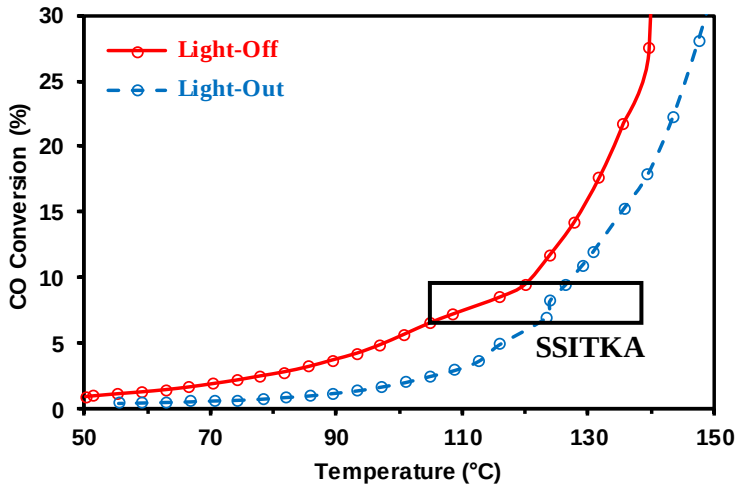

Figure V-8- Evolution of CO conversion below 30% vs temperature during light-off and light-out of CO oxidation on Pd/Al_2O_3.

Figure V-8 illustrates a notable difference between the activity observed during temperature cycle on Pd/Al_2O_3 reflecting an inverse hysteresis behavior, wherein the catalyst's activity during light-off exceeds that of the light-out phase. A constant ~10 °C hysteresis was observed here at low temperatures and a larger inverse hysteresis is still observed at higher temperature ($\Delta T_{90\%}$ = 20 °C, Figure SV-4). Activation energies were determined for both the light-off and light-out conditions. The results revealed a notable difference, with an activation energy during light-off of 42 kJ mol^{-1}, being only half the value of that calculated for light-out (79 kJ mol^{-1}).

Aiming to elucidate the underlying cause of the observed activity difference, SSITKA-IR was conducted during the light-off CO oxidation phase on Pd/Al_2O_3 at a temperature of 116 °C with a CO conversion level of 8%. Subsequently, during the light-out phase, isotopic exchange was performed at the same conversion level (8%) but at a slightly higher temperature of 124 °C (inverse hysteresis). Additionally, another isotopic exchange was conducted during light-out, maintaining the same temperature as during light-off (116°C), but with a reduced conversion level of around 5%. The results of transient normalized MS responses curves of CH_4, ^{13}CO and $^{13}CO_2$ obtained after the isotopic $^{12}CO \rightarrow {}^{13}CO$ switch performed during the light-out phase at 8% (124 °C) of CO conversion and at the 116 °C (χ_{CO} = 5%) are presented in Figure V-9 (The results of light-off have already been presented in chapter 3, Figure III-8).

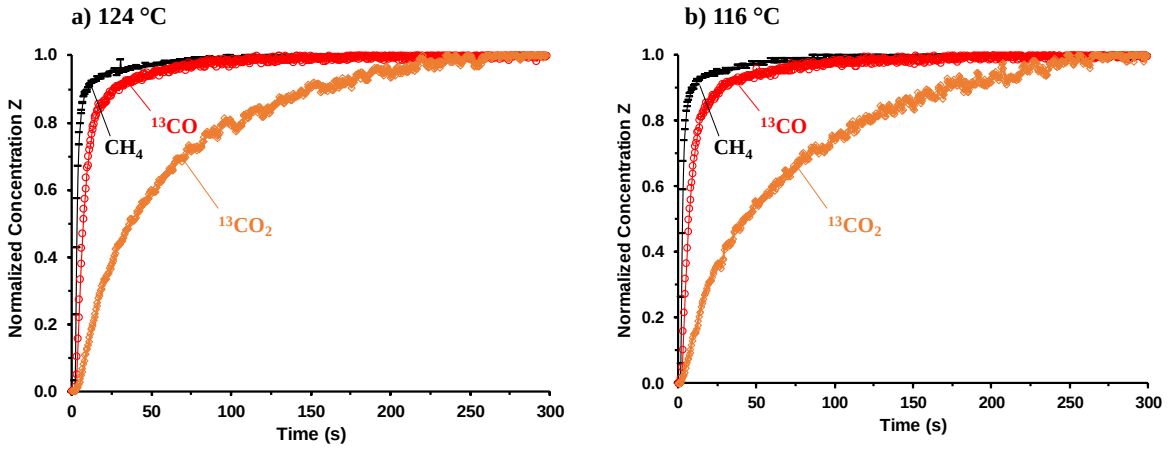

Figure V-9- Normalized concentrations of CH_4, ^{13}CO and $^{13}CO_2$ obtained during the light-out SSITKA transient ($^{12}CO/O_2/He \rightarrow {}^{13}CO/O_2/Kr/CH_4/He$) on Pd/Al_2O_3 (a) at 124 °C ($\chi CO = 8\%$) and (b) at 116 °C ($\chi CO = 5\%$).

The results show that in both cases the ^{13}CO transient response curves lag behind that of CH_4 due to the CO converted but also to a detectable concentration of reversibly adsorbed carbonyls (CO) formed on Pd surface during the reaction. In the same manner, the transient response curves of $^{13}CO_2$ lag behind that of ^{13}CO response curves. But this evolution was mainly attributed in chapter 3 to the phenomenon of CO_2 product re-adsorption, forming hydrogen-carbonate species on Al_2O_3, during the reaction.

According to SSITKA theory, the mean surface residence times (τ), concentration (N) and surface coverage (θ) of reversibly adsorbed carbonyls and other C-containing species have been determined during the light-out phase (at iso-conversion and iso-temperature). The results are presented in Table V-3 and compared with the values obtained during the light-off SSITKA experiment (Chap 3, Table III-5).

Table V-3- Mean residence times τ, concentrations N, surface coverages θ, of adsorbed CO and C-containing species calculated from the light-off and light-out SSITKA experiments on Pd/Al_2O_3.

	T (°C)	χ_{CO} (%)	τ_{CO} (s)	N_{CO} (µmol g^{-1})	θ_{CO}	r_{CO} (µmol $g^{-1}s^{-1}$)	τ_C (s)	N_C (µmol g^{-1})
Light-Off	116	8	8.6	17.4	0.30	2.02	55.5	10.4
Light-Out	124	8	6.8	13.7	0.24	2.01	45.8	8.3
	116	5	8.0	16.7	0.29	2.09	53.5	5.8

The results highlight that during light-off, the surface residence time of reversibly adsorbed carbonyls, along with their concentration, are notably higher when compared to the light-out

phase, in both conditions. Specifically, at isoconversion, the amount N_{CO} decreases by approximately 21% (13.7 µmol g^{-1}), whereas at isotemperature, the decrease was much lower, at around 4% (16.7 µmol g^{-1}) leading to a slight reduction of Pd surface coverage from 30% to 24 and 29%, respectively. Concerning the rate of CO formation calculated from SSITKA formula, it is not impacted by the increase in temperature at 124 °C while its values increase for the light-out isotemperature condition (χ_{CO}=5%, 116 °C). At 116 °C, any temperature effect is excluded and the observed decrease in the amount of reversibly adsorbed carbonyls on Pd can be directly correlated with a reduction in the activity of the catalyst compared to light-off activity.

It is worth to note that in the case of Pd, the values τ_C and N_C have changed significantly between light-off and light-out, decreasing from 10.4 µmol g^{-1} to 8.3 µmol g^{-1} at isoconversion then to 5.8 µmol g^{-1} at 116 °C during light-out. As previously discussed, these values are linked to the re-adsorption of CO_2 product to form hydrogen-carbonate species on the inactive alumina support. Thus, a change in alumina surface during the experiment would ultimately be reflected by a difference in N_C values. This observation leads us to believe that the surface of the Pd/Al_2O_3 catalyst has undergone various modifications during the hysteresis loop.

Figure V-10 displays the spectra of linear and bridged carbonyls recorded before the isotopic switch (t=0 s, under $^{12}CO+O_2$) performed in light-off and light-out conditions.

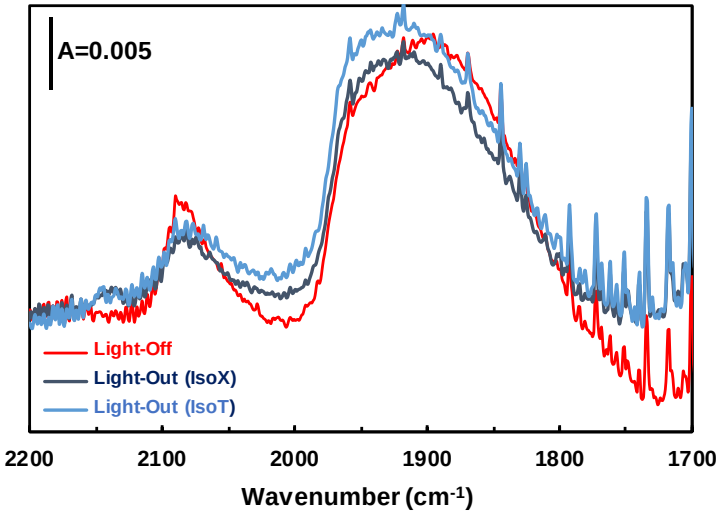

Figure V-10- Comparison of the spectra of linear and bridged carbonyls recorded at t=0 s during light-off (116 °C, red) and light-out at isoconversion (124 °C, light blue) and isotemperature (116 °C, dark blue).

Comparing the spectra obtained during light-off and light-out reveals that the intensity of the CO linear bands at 2088 cm^{-1} is greater during light-off than during light-out. However, when it comes to the bridged bands, conducting a precise comparison becomes more challenging due

to the multiple overlapping bands. A comparison of the evolution of the areas of linear and bridged bands in all conditions has been conducted. The results reveal that, during light-out, the area of the linear bands decreased by approximately 47% at isoconversion and 42% at isothermal conditions. As for the bridged bands, their area decreased by about 25% during light-out at isoconversion and 18% at isothermal conditions. Moreover, in a first raw observation of the spectra, we can see that a significant change occurs in the distribution of bridged carbonyls bands between the light-off (in red) and the light-out experiments (in blue), both latter looking more or less similar in species distribution. These findings underscore the significant changes occurring on the Pd surface.

In this context, an investigation of the kinetic exchange of each linear and bridged band has been performed and their reactivities have been compared during both the light-off and isotemperature light-out phases. At this stage, the isoconversion results have been abandoned to avoid any temperature effect and facilitate further interpretations. The methodology explained in chapter 4 for the light-off experiment was used to fit the different CO adsorbed bands obtained during the light-out SSITKA-IR experiment at 116 °C. The positions of L1 to L5 bands (^{12}CO and ^{13}CO) and their respective FWHM, identified previously (Table IV-5 in Chap 4), were used as such to fit the IR signal. The fitting results at t=0 s and t=60 s after the SSITKA $^{12}CO \rightarrow {}^{13}CO$ switch at 116°C are presented in the Figure V-11a and Figure V-11b, respectively.

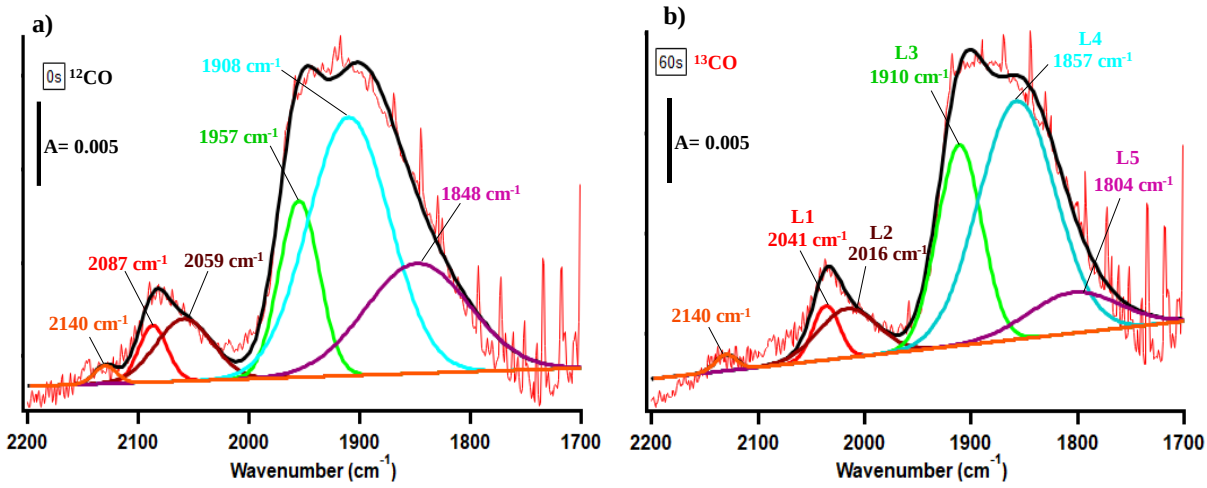

Figure V-11- Individual adsorption bands of the adsorbed CO species obtained after the deconvolution of the recorded IR spectrum on Pd/Al_2O_3: a) at 0 s and b) at 60 s during the isotemperature light-out SSITKA-IR experiment. The non-smoothed raw IR signal is represented in red and the result of deconvolution (6 Gaussian sum) by the black line.

Figure V-11 shows the results of the global fitting in black and the initial non-smoothed IR spectra in red. The individual bands are clearly indicated in the figure by their respective wavenumbers and named (L1 to L5). As mentioned before, the linear CO bands have been deconvoluted into 2 bands, one centered at 2087 cm^{-1} or 2041 cm^{-1} and the other at 2059 cm^{-1} or 2016 cm^{-1} for adsorbed ^{12}CO or ^{13}CO, respectively. Concerning the bridged carbonyls, they will be decomposed into 3 separate bands, located at the beginning (t= 0s) at 1957, 1908 and 1848 cm^{-1} then shifted, under ^{13}CO exchange, at 1910, 1857 and 1804 cm^{-1} respectively. A sixth bands was considered in the fitting at 2140 cm^{-1} attributed to carbonyls adsorbed on oxidized Pd site. However, this small band doesn't shift upon isotopic exchange. The fitting results for all spectra recorded during the isotemperature light-out SSITKA-IR experiment at various time points are provided in the annex SV-5. The normalized area evolutions of ^{12}CO and ^{13}CO L1 to L5 bands have also been plotted in annex figure SV-6. This evolution reflected unique behavior through isotopic exchange for each $^{12}CO/^{13}CO$ band pairs. Only L5 band show almost symmetrical exchange, intersecting at around 0.5 while other bands show asymmetrical $^{12}CO/^{13}CO$ evolution.

Consequently, we determined the kinetic exchange rate constants k' of each individual ^{12}CO carbonyls bands using the model previously detailed for the light-off experiment. The plots of ln α versus time of exchange, with α corresponding to the area ratio A_t/A_0 for each individual band, are given in Figure V-12. The absolute slope values are directly equal to the k'^{12}CO of each carbonyls species.

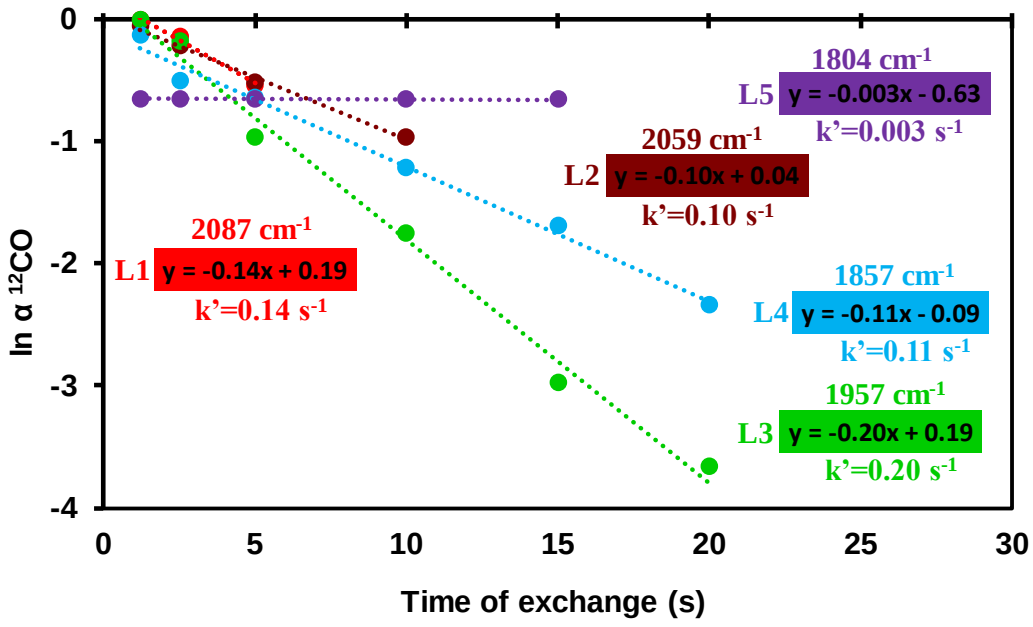

Figure V-12- Plot of ln α vs. time (s) for the 5 types (L1 to L5) of adsorbed CO species on Pd during light-out SSITKA-IR experiment performed at isotemperature (116 °C, χ_{CO}=5%).

Figure V-12 shows that the bridged carbonyls L3 species at 1957 cm^{-1} exhibit the highest kinetic rate constants (k'^{12}CO = 0.20 s^{-1}) while the linear L1 and L2 carbonyls as well as the bridged L4 CO are characterized by slightly lower constants between 0.10 and 0.14 s^{-1}. In contrast, the band L5 at 1804 cm^{-1} presents a very slow rate constant of 0.003 s^{-1}. A comparison with the k'^{12}CO values obtained at the same temperature during light-off SSITKA-IR experiment in chapter 4 is summarized in Table V-4. This comparison provides an efficient means to observe the kinetic changes in linear and bridged carbonyls during exchange.

Table V-4- Comparison between exchange kinetic rate constants for adsorbed ^{12}CO species on Pd during light-off and light-out SSITKA-IR experiments at isotemperature (116 °C).

k'^{12}CO (s^{-1})	χ_{CO} %	2087 cm^{-1} L1	2059 cm^{-1} L2	1957 cm^{-1} L3	1908 cm^{-1} L4	1848 cm^{-1} L5
Light-Off	8	0.22	0.33	0.45	0.16	0.01
Light-Out	5	0.14	0.10	0.20	0.11	0.003

Table V-4 provides clear evidence that the kinetic rate constants during the light-out phase are lower than those during the light-off phase for both linear and bridged carbonyl bands even if the temperature is maintained at the same level. During the light-off phase, the bands L3 and L2, centered at 1957 and 2059 cm^{-1} respectively, exhibited the highest kinetic rate constants,

indicating they are the fastest to undergo exchange. However, during the light-out, these species experience a significant decrease (more than twice) in their rate constant values. As a result, the band L1 at 2087 cm^{-1} demonstrates a higher kinetic rate constant ($k'^{12}CO=0.14\ s^{-1}$) compared to the L2 band at 2059 cm^{-1} ($k'^{12}CO=0.10\ s^{-1}$) during light-out SSITKA experiment, making now the bands L1 and L3 the most reactive species toward isotopic exchange. On another hand, the band L5 at 1848 cm^{-1}, retains its very slow kinetics during both exchange processes. In conclusion, a slight alteration in the reactivity order of the carbonyls species was observed, accompanied by a significant reduction in their exchange kinetic rate constants during light-out.

In order to get more details on the species distribution on Pd surface during the light-out SSITKA experiment at 116 °C and examine whether there are any changes compared to the light-off results, we plotted the sum of the ^{12}CO and ^{13}CO band areas as a function of time in Figure V-13.

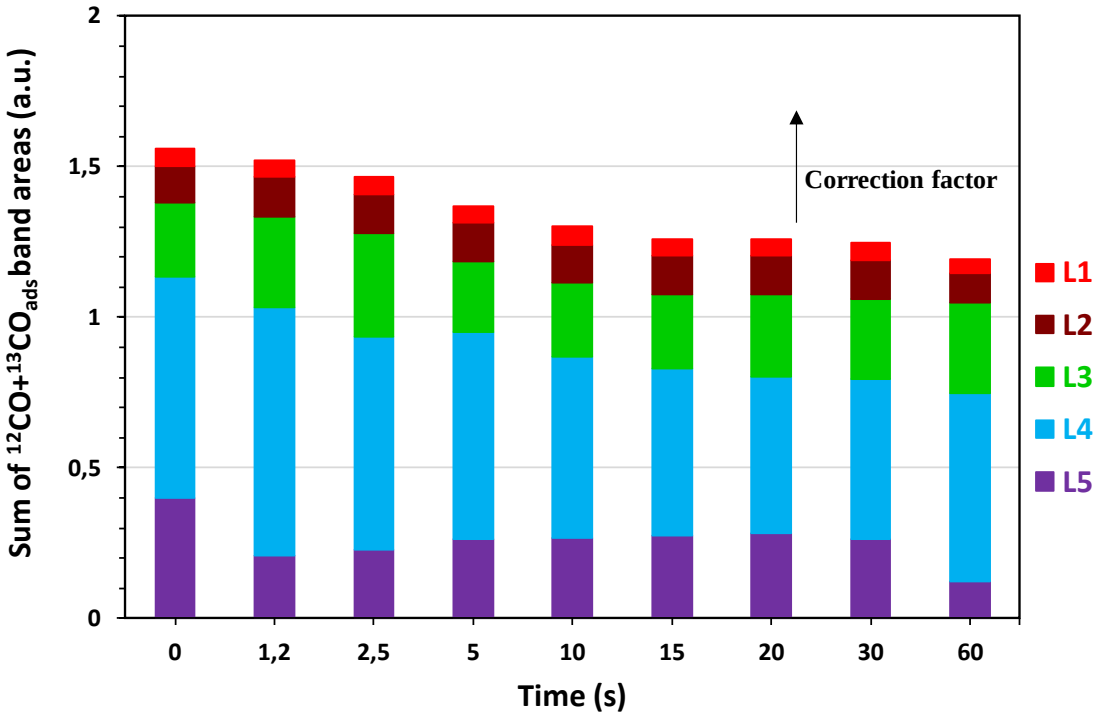

Figure V-13- Evolution of sum of the areas of adsorbed L1 to L5 ^{12}CO + ^{13}CO bands during $^{12}CO \rightarrow {}^{13}CO$ light-out isotopic exchange on Pd/Al_2O_3 at 116 °C.

The results illustrate the behaviors of the different bands, namely L1 to L5, in term of Pd surface coverage evolution during the light-out isotopic exchange. On first sight, it seems that the distribution of the different carbonyl species on the Pd surface stays relatively constant. Before

to perform more analysis, the correction factors, reported in Table SV-2, have been applied on the values of ^{13}CO band areas to align both maximum values at t=0 s and 60 s (method detailed in chapter 4). Then, the new results were compared to the sums obtained during the light-off process (Figure IV-14) for 3 chosen times in Figure V-14.

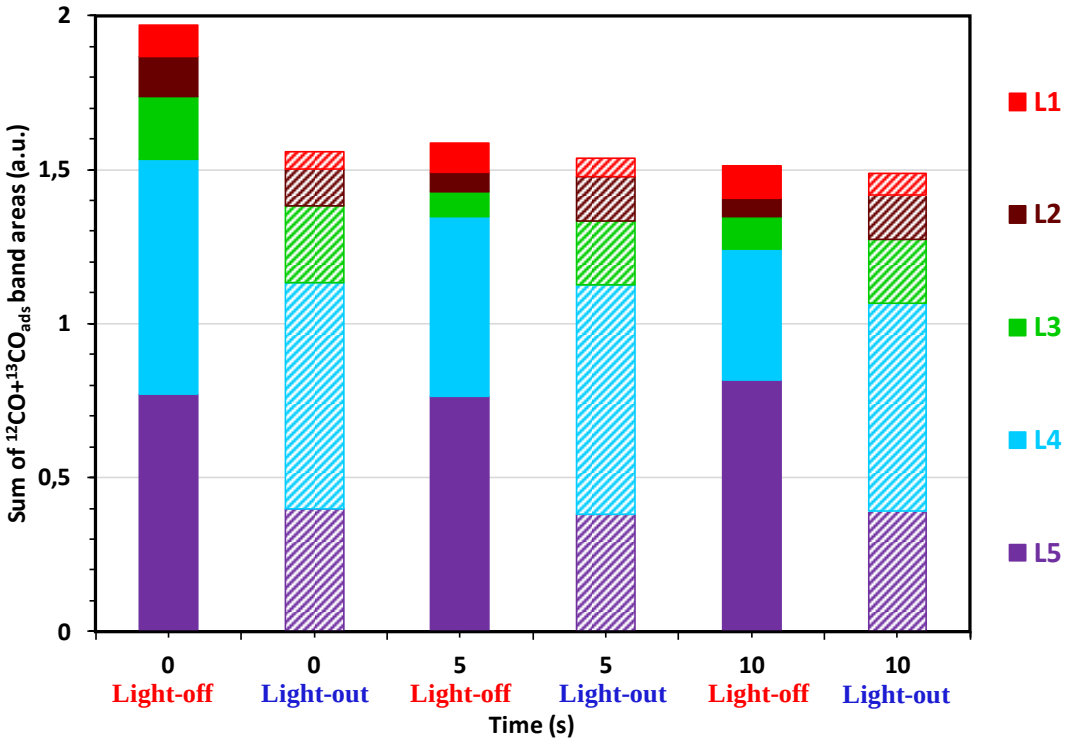

Figure V-14- Comparison of the corrected $^{12}CO+^{13}CO$ sum of adsorbed L1 to L5 band areas during light-off and light-out SSITKA-IR experiment (116 °C) on Pd/Al_2O_3 at 0, 5 and 10 s.

Figure V-14 shows that initially (t=0 s), L1 and L5 species are more abundant on the Pd in the light-off phase than light-out while other bands, L2, L3 and L4 exhibit much comparable distribution on both conditions. However, the main difference is observed at 5 seconds where the L3 species, which we recognized as it plays a crucial role in product formation during the light-off activity, has decreased significantly (-60%) in contrast with the light-out L3 area decreasing in a much lesser extent (-16%) at 5 seconds. This discrepancy is consistent with the reduced rate constant k'^{12}CO observed for L3 species during the light-out phase. At 10 seconds, while L2 and L4 species concentrations have slightly decreased during the light-off, accumulations of L1 (+22%) and L2 (+19%) signals were now observed at the Pd surface (light-out) compared to initially (t=0 s). It is also worth to note that the quantities of L4 and L5 species stay relatively constants during this 10 first seconds of isotopic exchange in light-out.

In conclusion, concerning L3, assigned to bridged carbonyls on Pd (100), the much lower exchange kinetic rate constant k'^{12}CO observed during light-out experiment is also associated

with an important difference in term of proportion of species exchange at their respective minimum level. Nevertheless, L3 still appears to be the main reactive species in the CO oxidation process while the role of L1, L2 and L4 species seems to be more minor. Conversely, it clearly appears that the last carbonyl species, L5, would not even participate in the CO_2 formation, showing also a very low kinetic rate constant.

In summary, the observed difference in activity at the same temperature during both light-off and light-out phases is closely related to a kinetic change. This change is due to not only a decrease in the quantity of reversibly adsorbed CO, as determined by SSITKA, but also to a reduction in the kinetic rate constant of various linear and bridged carbonyl bands during light-out. Furthermore, the behavior of these bands during isotopic exchange differs between the two conditions. Particularly noteworthy is the observation that L3, which has been suggested to play a significant role in CO_2 product formation along with L2 and L4, is not consumed as extensively in light-out than during light-off experiment, resulting in lower activity during light-out.

3- Transient conditions during CO oxidation: a solution for higher catalyst activity?

Further experiments were conducted on Pt/Al_2O_3 and Pd/Al_2O_3 catalyst by sending reductive pulses of H_2 in isotherm conditions to study the impact on the catalytic surface and correlated activity in CO oxidation. For Pt/Al_2O_3, new catalyst pellet of 5.9 mg was firstly preheated (1 °C/min) to 128 °C, resulting in a CO conversion of 17.5%. For Pd/Al_2O_3, new catalyst pellet of 7.5 mg was preheated (1 °C/min) to 131 °C, achieving a CO conversion of around 11%. The reaction was maintained at an isothermal condition for 30 minutes to ensure a stable conversion rate before initiating $^{12}CO \rightarrow {}^{13}CO$ isotopic reactant switch. After 5 min, the ^{12}CO reactant was again admitted in the reactor and a pulse of 5% H_2/He, lasting for 1 second, was introduced into the reaction mixture. After each pulse, an isotopic $^{12}CO \rightarrow {}^{13}CO$ switch was carried out before returning to the ^{12}CO reactant. This sequence was repeated five times.

3.1- Effect of H_2 pulses on Pt/Al_2O_3 activity

A comparison of the kinetic calculations (τ_{CO}, N_{CO}, θ_{CO}, r_{CO}, $TOF_{CO,ITK}$ and $TOF_{CO,chem}$) obtained from SSITKA analysis on Pt/Al_2O_3, before the H_2 pulses and after each five pulses, is presented in the Table V-5 below.

Table V-5- Comparison of SSITKA kinetic parameters (τ_{CO}, N_{CO_0}, θ_{CO}, r_{CO}, TOF_{CO}) obtained before and after H_2 pulses on Pt/Al_2O_3 at 128 °C.

128 °C	τ_{CO} (s^{-1})	N_{CO} ($\mu mol\ g^{-1}$)	θ_{CO}	r_{CO} ($\mu mol\ g^{-1}s^{-1}$)	$TOF_{CO,ITK}$ (s^{-1})	$TOF_{CO,chem}$ (s^{-1})
Before Pulse- X_0=17.5%	9.74	18.0	0.63	1.85	0.103	0.065
Pulse 1- X_1=21.8%	8.03	14.1	0.49	1.76	0.124	0.061
Pulse 2- X_2=22.1%	7.77	13.6	0.48	1.75	0.129	0.061
Pulse 3- X_3=21.9%	7.33	12.8	0.45	1.75	0.136	0.061
Pulse 4- X_4=22.1%	8.18	14.3	0.50	1.75	0.122	0.061
Pulse 5- X_5=22%	8.07	14.1	0.49	1.75	0.124	0.061

Following the first injection of H_2 pulse, the conversion level increases to reach around 22% of CO converted then stabilizes to this value for subsequent pulses. The concentration of reversibly adsorbed CO before H_2 pulse was approximately 18 $\mu mol\ g^{-1}$ corresponding to a surface coverage of Pt around 63%. After H_2 pulses, these parameters decrease and fluctuate around 14 $\mu mol\ g^{-1}$ and 50% for N_{CO} and surface coverage, respectively. This decrease is also accompanied by a slight reduction in the rate of CO formation as calculated by SSITKA formulae $r_{CO} = N_{CO}/\tau_{CO}$. This evolution is surprising as the rate of CO conversion is expected to increase when the conversion increase at the same temperature according to Arrhenius law. In consequence, the TOF_{ITK} estimated by SSITKA also increases (+20%) after the H_2 pulses, in contrast to the TOF_{chem} which slightly decreases after the pulses.

Furthermore, a comparison of IR signals obtained before and right after each H_2 pulse is presented in Figure V-15.

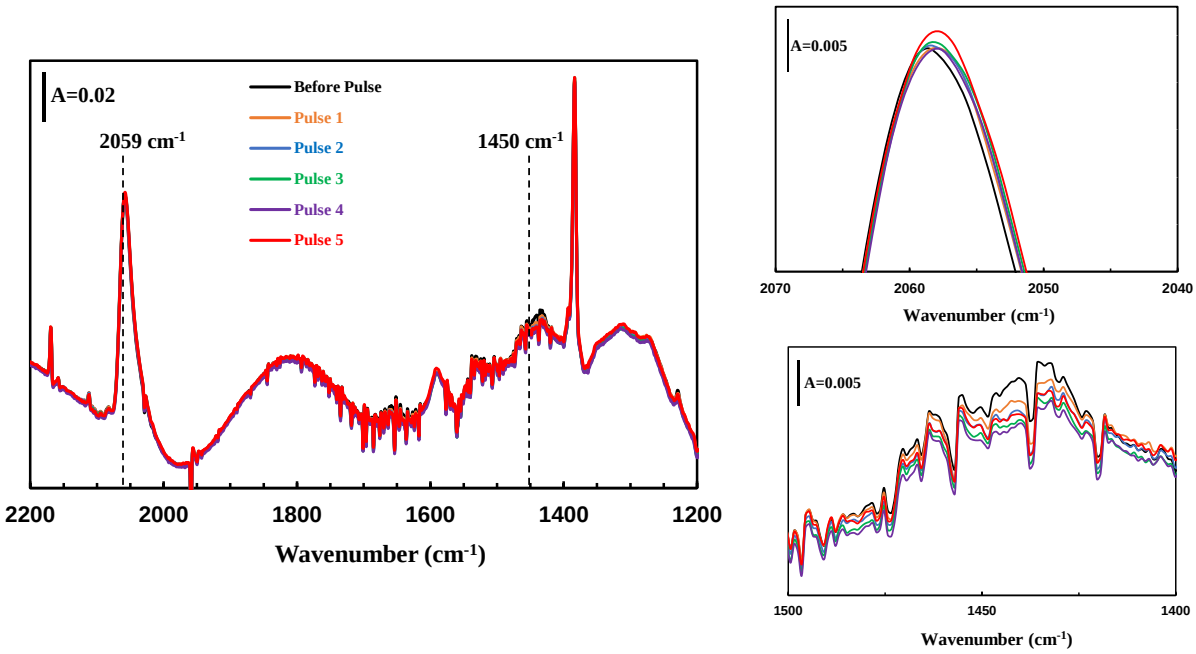

Figure V-15- Comparison of IR signals recorded before and after each pulse H_2 pulse on Pt/Al_2O_3 at 128 °C. Zoom inset on carbonyl and carbonates bands.

Figure V-15 clearly shows that the intensities of both linear and bridged carbonyl bands did not change after H_2 pulse. However, a slight shift toward lower wavenumber is observed for the band at 2059 cm^{-1}, consistent with a lower oxidation state of Pt under H_2. Similarly, no significant change was observed in the carbonate region except a small decrease around 1435 cm^{-1} that could correspond to a reduction of hydrogen-carbonate species. Finally, it appears that the impact of H_2 pulses on catalytic activity is relatively minor, as it only results in a slight increase in CO conversion and no significant changes are detected on catalytic surface.

3.2- Effect of H_2 pulses on Pd/Al_2O_3 activity

Similarly, a comparison of the kinetic calculations (τ_{CO}, N_{CO}, θ_{CO}, r_{CO}, $TOF_{CO,ITK}$ and $TOF_{CO,chem}$) obtained from SSITKA analysis on Pd/Al_2O_3, before the H_2 pulses and after each five pulses, is presented in the Table V-6 below.

Table V-6- Comparison of SSITKA kinetic parameters (τ_{CO}, Nco, θco, Rco, TOFco) obtained before and after H_2 pulses on Pd/Al_2O_3 at 131 °C.

131 °C	τ_{CO} (s^{-1})	N_{CO} (µmol g^{-1})	θ_{CO}	r_{CO} (µmol $g^{-1}s^{-1}$)	$TOF_{CO,ITK}$ (s^{-1})	$TOF_{CO,chem}$ (s^{-1})
Before Pulse- X_0=11.1%	5.4	10.7	0.18	1.96	0.184	0.034
Pulse 1- X_1=25%	6.3	10.3	0.18	1.65	0.160	0.028
Pulse 2- X_2=30%	5.5	8.5	0.15	1.54	0.181	0.027
Pulse 3- X_3=29.9%	5.6	8.6	0.15	1.55	0.180	0.027
Pulse 4- X_4=29.3%	5.5	8.6	0.15	1.56	0.180	0.027
Pulse 5- X_5=29.1%	5.5	8.5	0.15	1.56	0.183	0.027

The initial conversion level of Pd/Al_2O_3 was estimated to be approximately 11% at a temperature of 131 °C before the introduction of H_2 pulses. Following the injection of the first H_2 pulse, the conversion level increases significantly to reach around 25%. Subsequently, the conversion level increases and remains stable around 30%. Table V-6 shows that the concentration of reversibly adsorbed CO (initially estimated about 10.7 µmol g^{-1}) experiences a slight decrease after the first pulse to 10.3 µmol g^{-1}. Its value decreases further after the second pulse, stabilizing at approximately 8.6 µmol g^{-1} for the subsequent pulses. Simultaneously, the surface coverage, initially estimated at 18%, decreases to 15% after the second pulse and remains constant for the subsequent pulses. Concerning the rate of CO formation, a noticeable decrease is observed after the first H_2 pulse accompanied by a decrease in the TOF_{chem} and TOF_{ITK}. While TOF_{chem} remains then constant at 0.027 s^{-1}, the TOF_{ITK} increase back to its initial value at around 0.18 s^{-1}.

As a direct consequence of the H_2 pulses, there is a consistent decrease in all kinetic parameters observed by SSITKA. This decrease is accompanied by a significant increase in the conversion level and catalytic activity. This intriguing observation suggests that the H_2 pulses induce changes in the catalyst's behavior, resulting in enhanced overall catalytic performance. A surface analysis of the catalyst is essential to detect any changes or modifications that may occur following the H_2 pulses. Furthermore, a comparison of the IR signals recorded in the region of carbonyls and carbonates before and after each pulse is presented in the Figure V-16.

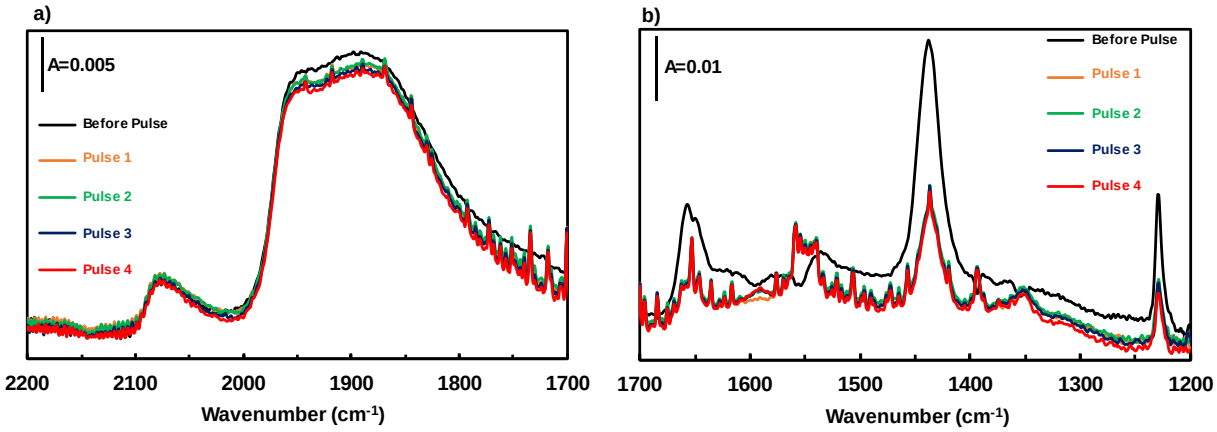

Figure V-16- Comparison of IR signals recorded before and after H_2 pulses on Pd/Al_2O_3 at 131 °C: a) carbonyl region, b) carbonate region.

Figure V-16 reveals that in the carbonyl region, the intensity of linear carbonyl bands did not change after H_2 pulses. However, in contrast, the bridged carbonyl bands exhibit a slight decrease in intensity after the first pulse, that remains constant for the subsequent pulses. Regarding the carbonate region, there is a significant decrease in the intensity of the hydrogen-carbonate bands at 1657 and 1439 cm^{-1} and their corresponding OH vibration band at 1231 cm^{-1} after the first pulse. Intensity level is then maintained constants for the subsequent pulses. These observations suggest that the H_2 pulses may selectively and moderately impact the bridged carbonyl species while significantly affecting the hydrogen-carbonate species on the alumina surface. In contrast, the linear carbonyls appear to remain relatively unaffected by the H_2 pulses.

An additional test has been performed on the Pd/Al_2O_3 catalyst to investigate the impact of a single pulse on its activity. The experiment involves exposing the catalyst's surface to H_2 for varying durations (1 s, 1 min and 5 min) and subsequently introducing the reaction mixture to observe the catalyst's activity over time. The results of this experiment are presented in the Figure V-18 below, providing insights into how the catalyst's performance is affected by different exposure times to H_2. Furthermore, it illustrates how the activity of the catalyst evolves over time after the pulse, shedding light on the dynamics of catalyst behavior in response to these different exposure durations to H_2.

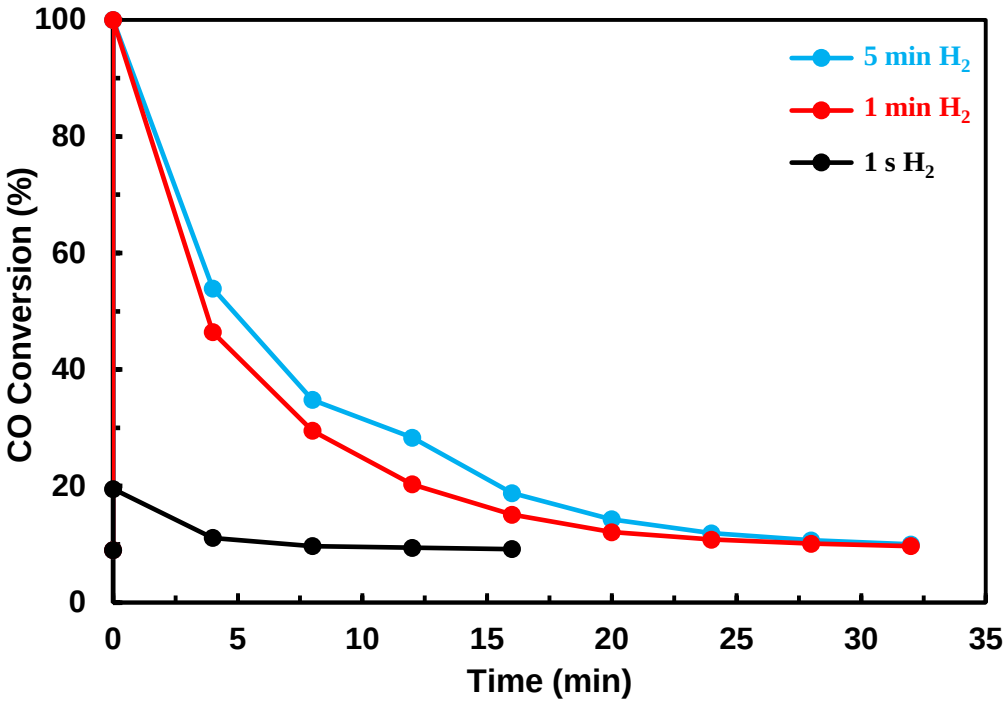

Figure V-17- Evolution of CO conversion as a function of time after different exposure time to H_2.

Figure V-17 illustrates a significant impact of H_2 exposure time on the conversion level, which was initially estimated at around 9% before exposure to H_2 in this experiment. After 5 minutes and 1 minute of exposure to H_2, the conversion level sharply increases to reach 100% directly after this exposure. However, this high conversion level gradually decreases over time, ultimately returning to its initial value after 30 minutes. In contrast, for the 1 second H_2 exposure, the CO conversion increases, but in a much lower extent, reaching around 20%. It then starts to decrease progressively, returning to its initial value very quickly (<10 minutes). These findings suggest that the duration of exposure to H_2 has a significant impact on the catalyst's conversion rate. Interestingly, it seems that a 100% CO conversion is possible on Pd catalyst at low temperature if expose to reductive environment. However further experiment would be needed to determine if CO oxidation to form CO_2 was the only reaction responsible for CO conversion after H_2 pulses. SSITKA-IR experiment could also be performed to look at the kinetics and distribution of intermediate species.

4- Conclusion

The hysteresis phenomenon observed in the low-temperature CO oxidation reaction has been investigated for both Pd/Al_2O_3 and Pt/Al_2O_3 catalysts, with a more significant effect observed

on the Pd catalyst. To understand the underlying causes of this phenomenon, SSITKA-IR techniques were employed.

For Pt/Al_2O_3, a comparison of the kinetic rate constants obtained through the previously described kinetic model reveals a decrease in this value during the light-out phase, which is accompanied by a decrease in catalytic activity. Additionally, a decrease in the intensity of the linear CO bands is observed during the light-out phase in coherence with SSITKA calculations. However, comparing the distribution of carbonyls species present on Pt during both conditions does not provide a satisfactory explanation for the observed difference in catalytic activity. It's important to note that, since we were not operating under isothermal conditions, it was challenging to provide an explanation due to the temperature's effect on the kinetic parameters.

In the case of Pd/Al_2O_3, for which the same temperature was maintained in both conditions, the hysteresis phenomenon can be attributed to differences in the kinetic behavior of the different IR bands during isotopic exchange. Notably, there is a slight alteration in the reactivity order of the species, accompanied by a significant reduction in the kinetic rate constants during the light-out phase and a decrease in the amount of active intermediates determined by SSITKA. Additionally, the behavior of the main intermediate IR band during isotopic exchange differs between the two conditions. Consequently, the hysteresis phenomenon can be reasonably attributed to a substantial change in the kinetic behavior of the intermediate species, likely stemming from a reconstruction phenomenon occurring during the end of light-off phase at high temperature.

The effect of reductive H_2 pulses on the activity of both catalysts is noteworthy, with a significant conversion enhancement observed for Pd/Al_2O_3 and a relatively smaller effect on Pt/Al_2O_3. Specifically, for Pd/Al_2O_3, a decrease in the intensity of bridged carbonyl bands and hydrogen carbonate bands was clearly observed after the H_2 pulses. However, it's essential to note that the enhanced catalytic activity is not maintained overtime. Therefore, it's crucial to introduce H_2 pulses in a transient manner to sustain this heightened activity. Interestingly, a brief pulse of 1 second can be sufficient to achieve a substantial conversion increase. Still, to reach the maximum conversion, a longer exposure to H_2 (1 min) is necessary. This indicates that the duration and timing of H_2 pulses play a critical role in optimizing and maintaining the catalyst's enhanced activity.

References

1. Imbihl R, Ertl G (1995) Oscillatory Kinetics in Heterogeneous Catalysis. Chem Rev 95:697–733. https://doi.org/10.1021/cr00035a012

2. Al Soubaihi R, Saoud K, Dutta J (2018) Critical Review of Low-Temperature CO Oxidation and Hysteresis Phenomenon on Heterogeneous Catalysts. Catalysts 8:660. https://doi.org/10.3390/catal8120660

3. Orlik SN, Koval' GL, Fesenko AV, et al (1979) Kinetics of CO oxidation on a palladium-containing catalyst. Theor Exp Chem 15:59–61. https://doi.org/10.1007/BF00524911

4. Kalinkin AV, Boreskov GK, Savchenko VI, Dadayan KA (1980) Study of CO oxidation on the (111) face of nickel during Ni−NiO phase transition. React Kinet Catal Lett 13:111–114. https://doi.org/10.1007/BF02074180

5. Subbotin AN, Gudkov BS, Yakerson VI (2000) Temperature hysteresis phenomena in heterogeneous catalysis. Russ Chem Bull 49:1373–1379. https://doi.org/10.1007/BF02495080

6. Frank-Kamenetskii DA (2015) Diffusion and Heat Exchange in Chemical Kinetics. In: Diffusion and Heat Exchange in Chemical Kinetics. Princeton University Press

7. Smith TG, Zahradnik J, Carberry JJ (1975) Non-isothermal inter-intraphase effectiveness factors for negative order kinetics—CO oxidation over Pt. Chem Eng Sci 30:763–767. https://doi.org/10.1016/0009-2509(75)85104-9

8. SCHMITZ RA (1975) Multiplicity, Stability, and Sensitivity of States in Chemically Reacting Systems—A Review. In: Chemical Reaction Engineering Reviews. American Chemical Society, pp 156–211

9. Subbotin AN, Subbotina IR, Golosman EZ (2015) Hysteresis phenomena in heterogeneous exothermal catalytic reactions and methods for decreasing the overheating of catalyst nanoclusters. Mendeleev Commun 25:216–218. https://doi.org/10.1016/j.mencom.2015.05.020

10. Yuranov I, Kiwi-Minsker L, Slin'ko M, et al (2000) Oscillatory behavior during CO oxidation over Pd supported on glass fibers: experimental study and mathematical modeling. Chem Eng Sci 55:2827–2833. https://doi.org/10.1016/S0009-2509(99)00557-6

11. Kalhara Gunasooriya GTK, Saeys M (2018) CO Adsorption Site Preference on Platinum: Charge Is the Essence. ACS Catal 8:3770–3774. https://doi.org/10.1021/acscatal.8b00214

General Conclusion

The primary aim of this thesis work was to unravel the mechanism underlying CO oxidation on PGM catalysts at low temperatures, with the ultimate objective of enhancing the catalyst's performance under these challenging conditions. To accomplish this, our focus was directed towards investigating the hysteresis phenomenon observed at low temperature. The origins of this phenomenon have been the subject of ongoing debate in the scientific literature. Our mission was to shed light on this phenomenon, not only to understand it but also to leverage this knowledge to improve the catalyst's efficacy at low temperatures. A multi-step approach was adopted to achieve that goal. Our initial step involved the use of the SSITKA technique coupled with IR spectroscopy in order to characterize the catalyst's surface and distinguish between active and inactive species. The third chapter of this thesis specifically delves into the various species formed on the surfaces of Pt and Pd catalysts supported on alumina during the CO oxidation reaction. The SSITKA-IR technique has identified the presence of adsorbed linear and bridged carbonyls, as well as hydrogen carbonate species in the carbonate region, for both catalysts. According to SSITKA theory, species undergoing rapid isotopic exchange are considered active contributors to the reaction mechanism. In this context, linear and bridged carbonyls emerged as the primary active species, while hydrogen carbonate species were identified as inactive species. The experiment involving the direct $^{12}CO_2/^{13}CO_2$ exchange on the bare alumina support has provided clear evidence that hydrogen carbonate species are formed by the interaction of the CO_2 product with a surface hydroxyl group. This phenomenon accounts for the initial delay observed in the normalized concentration profiles of ^{13}CO and $^{13}CO_2$. Furthermore, the behavior of hydrogen carbonate species exhibited remarkable similarity on both Pt/Al_2O_3 and Pd/Al_2O_3 catalysts. This observation suggests that the re-adsorption of CO_2 primarily occurs on the alumina support itself, rather than being a spillover from the metal particles. The non-zero of N_C values obtained on both Pt and Pd catalysts, even after CO_2 pre-saturation, point to either a partial saturation of the alumina support with carbonates or the presence of other carbon-containing intermediate species in the CO oxidation mechanism. This suggests that the pool of N_C should be divided into two categories: 1/spectator hydrogen carbonates and 2/active carbon-containing intermediate species, which could include hydrogen carbonates near the metal particles or different types of chemical species. Another noteworthy finding is that, even if all species follow a similar $^{12}CO/^{13}CO$ isotopic exchange, not all of them are necessarily actively participating in the reaction pathway. In fact, one of

these species can be a spectator with a fast conversion into the reactive species. After identifying the carbonyls as primary active intermediates in the CO oxidation reaction over Pt and Pd supported on alumina, our focus has shifted towards distinguishing their reactivity during the reaction.

In Chapter four, we employed kinetic modeling to delve into the reactivity of these species. In the case of Pt/Al_2O_3, we identified four distinct types of linear bands, according to the existing literature, which we subsequently deconvoluted to analyze their kinetic behavior. Each band exhibited unique adsorption site characteristics and kinetic rate constants for exchange. The most rapid exchange rates were attributed to the bands associated with carbonyl adsorption on Pt terrace sites (2080 cm^{-1}) and Pt step sites (2059 cm^{-1}). Our investigation into the overall surface coverage area of the catalyst during isotopic exchange confirmed the non-active nature of carbonyls adsorbed on smaller particles (~ 1 nm to subnanometer), aligning with their lower kinetic rate constants. Moreover, our research pinpointed linear CO adsorbed on Pt step sites as the primary intermediate in CO_2 formation, while linear CO adsorbed on Pt terrace sites appeared to play a minor role in product formation, despite its higher kinetic rate constant. Similarly, in the case of Pd/Al_2O_3, we identified different types of linear and bridged carbonyls as documented in the literature, which we deconvoluted to assess their kinetic behavior. Each band exhibited its distinct kinetic rate constant. Analyzing the overall surface coverage area shed light on the roles of each species in the CO oxidation reaction. The most rapid exchange was observed for the band at 1957 cm^{-1}, associated with bridged carbonyl adsorbed on Pd(100), as well as the band at 2059 cm^{-1}, linked to linear carbonyl adsorbed on low-coordinated sites. While the bridged carbonyls were shown to play a major role in CO_2 production, the L1 and L2 bands, corresponding to CO adsorbed linearly on Pd, appear to play only minor roles. Similarly, CO adsorbed on the "bridge-bound" and "3 fold hollow" sites appear to be inactive species in the CO oxidation reaction, in line with their lower isotope exchange kinetic constants. An essential conclusion drawn from this study is that a band with a high kinetic rate constant may exchange rapidly to its counterpart without significantly affecting product formation, as observed in the case of the linear carbonyls adsorbed on Pd/Al_2O_3 system. This study's significance lies in revealing that linear and bridged carbonyls, previously assumed to be active species, are actually composed of multiple bands, not all of which participate in the reaction mechanism. The information obtained in the previous chapters have served as the foundation for analyzing the hysteresis phenomenon in chapter five, seeking a plausible understanding of its origin. In the case of Pt/Al_2O_3, a comparison of the kinetic rate constants reveals a decrease

in these values during the light-out phase, which correlates with a decrease in catalytic activity. Furthermore, a reduction in the intensity of linear CO bands is observed during the light-out phase, in line with SSITKA calculations. However, when we compare the distribution of carbonyl species present on Pt under both conditions, it doesn't offer a satisfactory explanation for the observed difference in catalytic activity. It's worth noting that, given the non-isothermal conditions during the experiments, providing an explanation is challenging due to the temperature's impact on the kinetic parameters. In the case of Pd/Al_2O_3, where the temperature was kept constant in both conditions, the hysteresis phenomenon can be attributed to variations in the kinetic behavior of different IR bands during isotopic exchange. Notably, there is a slight alteration in the reactivity order of the species, coupled with a significant reduction in the kinetic rate constants during the light-out phase, and a decrease in the quantity of active intermediates determined by SSITKA. Additionally, the behavior of the main intermediate IR band during isotopic exchange differs between the two conditions. Consequently, it is reasonable to attribute the hysteresis phenomenon to a substantial change in the kinetic behavior of the intermediate species, likely resulting from a reconstruction phenomenon occurring during the light-off phase at high temperatures.

Another aspect explored in this thesis involves the application of reductive H_2 pulses to investigate their impact on catalytic performance, with the ultimate goal of preserving a high level of catalyst activity through the use of H_2 pulses. The application of these reductive H_2 pulses results in a significant increase in conversion observed for Pd/Al_2O_3, while the effect on Pt/Al_2O_3 is comparatively minor. Specifically, for Pd/Al_2O_3, a clear decrease in the intensity of bridged carbonyl bands and hydrogen carbonate bands is observed after the H_2 pulses. It's important to highlight that the heightened catalytic activity is not sustained over time. Therefore, it is crucial to introduce H_2 pulses in a transient manner to maintain this enhanced activity. Interestingly, even a brief pulse of just one second can be sufficient to achieve a substantial increase in conversion. However, to reach the maximum conversion, a longer exposure to H_2 is required. Finally, this thesis work raises the important challenge of designing a catalyst with a maximum abundance of active sites capable of forming reactive carbonyl species at low temperatures in order to achieve increased activity in CO oxidation.

ANNEXES

Chapter II

A statistical study has been done in order to verify the reproducibility of the SSITKA method. For this, a rise in temperature have been carried out to reach 12% of conversion. After a 3h of steady state at this conversion, a series of 10 SSITKA switches have been performed in order to obtain the evolution of τ_{co} and calculate the standard deviation associated. The results are showed in the figure SII-1.

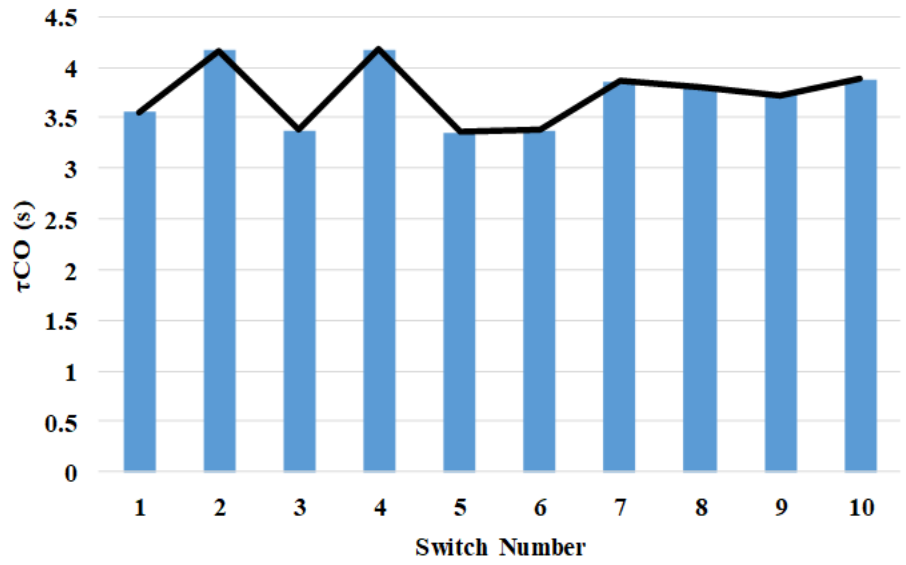

Figure SII-1- Evolution of τ_{co} during several repetitions of the isotopic $^{12}CO/^{13}CO$ switch.

A strong variation of the τ_{co} was observed during the first 5 switches that tends to stabilize for the 5 last switches. The standard deviation calculation for these 10 switches showed a value of 0.304 representing 8.1 % of the mean value while a value of 0.205 representing 5.5 % is obtained if we considered the last 5 switches. These deviations have to be considered for the exploitation of SSITKA results. Increasing the number of switches of the time of steady state stabilization could be suitable to reduce the error and avoid misinterpretation.

Chapter III

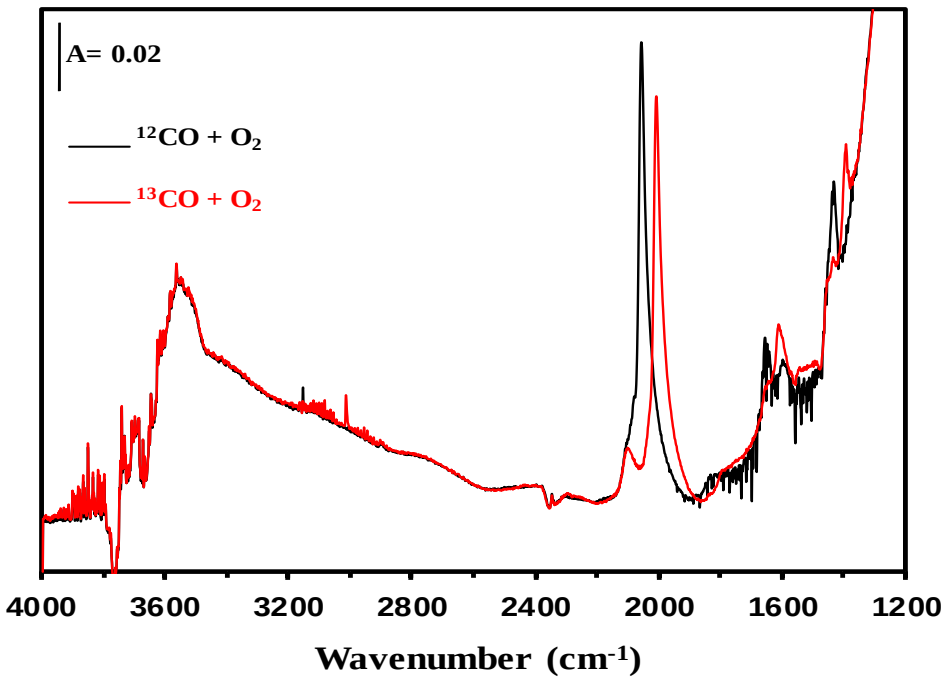

Figure SIII-1- IR spectra recorded on Pt/Al_2O_3 during CO oxidation at 129 °C in the presence of $^{12}CO/O_2/He$ (black) and $^{13}CO/O_2/Kr/CH_4$ /He (red) reaction mixtures in the region 1200 – 4000 cm^{-1}.

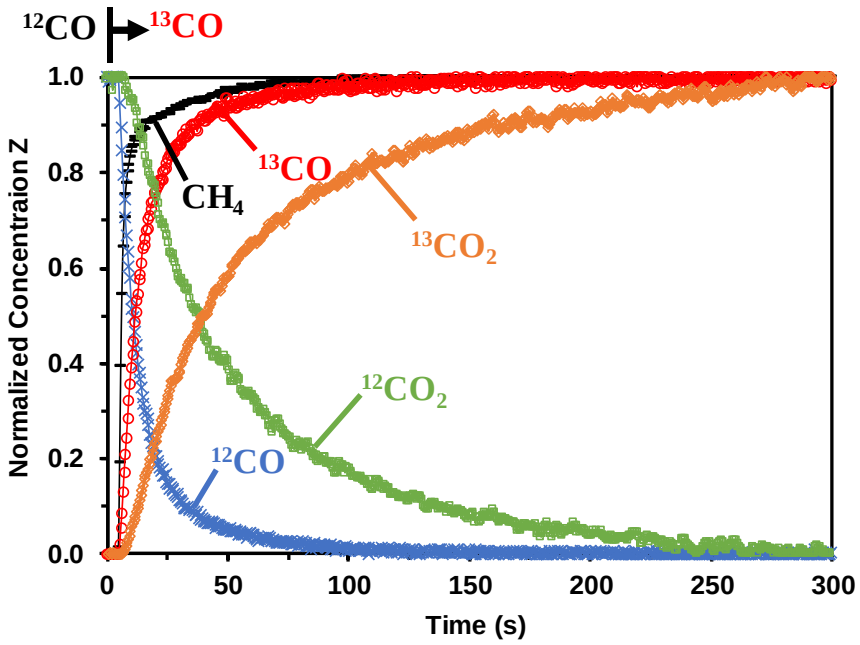

Figure SIII-2- Normalized concentration (Z) transient response curves of CH_4, ^{12}CO, ^{13}CO, $^{12}CO_2$ and $^{13}CO_2$ obtained during the SSITKA transient ($^{12}CO/O_2/He$ → $^{13}CO/O_2/Kr/CH_4/He$) on Pt/Al_2O_3 at 129 °C (χCO = 11%).

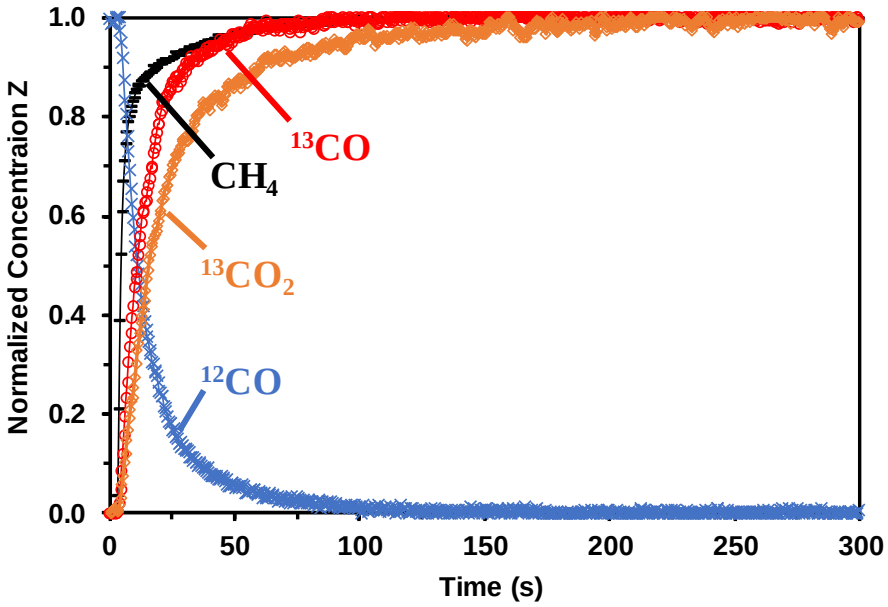

Figure SIII-3- Normalized concentrations of CH_4, ^{12}CO, ^{13}CO and $^{13}CO_2$ obtained after the SSITKA transient in the presence of CO_2 in the feed ($^{12}CO/O_2/^{12}CO_2/He$→$^{13}CO/O_2/^{12}CO_2/Kr/CH_4/He$) on Pt/Al_2O_3 at 122 °C (χCO = 11%).

Table SIII-1- Mean residence time τ, concentration N, surface coverage θ, and TOF_{ITK} of adsorbed CO and intermediates during SSITKA CO oxidation experiments on Pt/Al_2O_3 with and without the presence of CO_2 in the gas feed.

	T (°C)	τ_{CO} (s)	N_{CO} (µmol g^{-1})	θ_{CO} (on Pt)	τ_C (s)	N_C (µmol g^{-1})	TOF_{ITK} (s^{-1})
Without CO_2	129	8.9	18.5	0.65	45.6	11.7	0.008
With CO_2	122	8.9	18.3	0.64	7.9	2.1	0.013

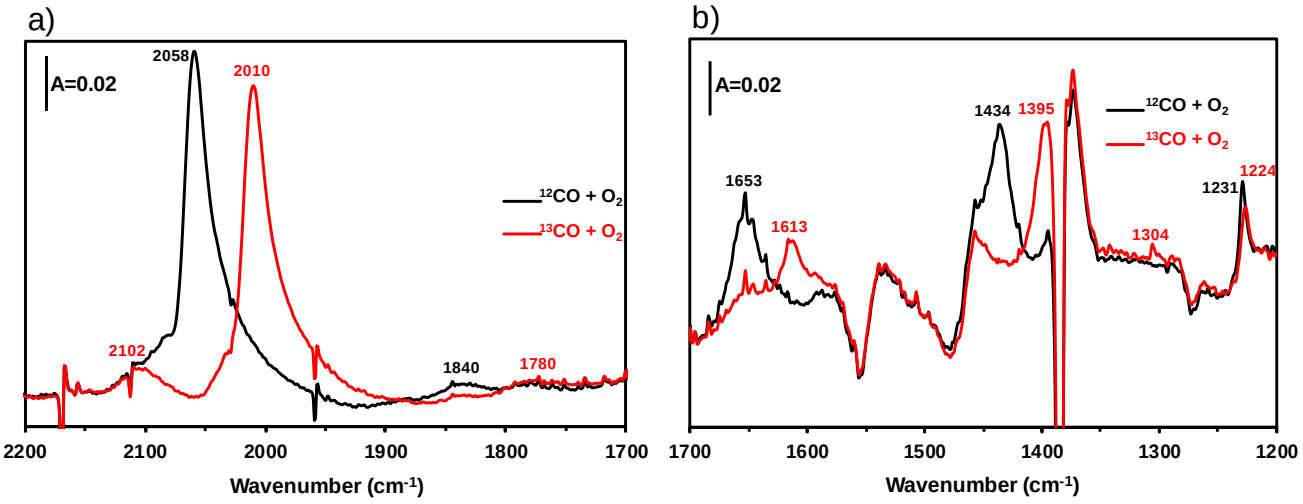

Figure SIII-4- IR spectra recorded on Pt/Al_2O_3 during CO oxidation at 129 °C in the presence of $^{12}CO/O_2$/He (black) and $^{13}CO/O_2/Kr/CH_4$ /He (red) reaction mixtures: (a) carbonyl region and (b) carbonate region.

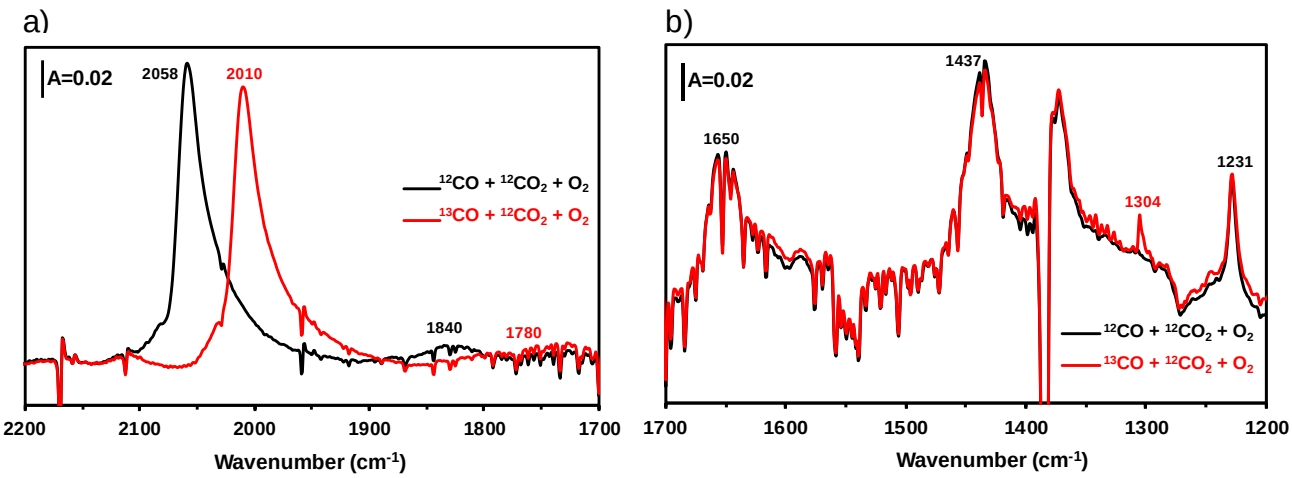

Figure SIII-5- IR spectra recorded during CO oxidation on Pt/Al_2O_3 at 122 °C in the presence of $^{12}CO/O_2/^{12}CO_2/He$ (black) and $^{13}CO/O_2/^{12}CO_2/Kr/CH_4/He$ (red) reaction mixture: (a) carbonyl region and (b) carbonate region.

Chapter IV

SIV-1- CO adsorbed on Pt/Al_2O_3

A_i= Height of the peak
x_i= Peak position
s_i= Full Width at Half Maximum
Ba and Bb= Baseline slope and intercept

Pt/Al_2O_3 t= 0 s

A1	= 0.034418 ± 0.00792
A2	= 0.044705 ± 0.0215
A3	= 0.076184 ± 0.0194
A4	= 0.014024 ± 0.0042
A5	= 0.016505 ± 0
x1	= 2031 ± 8.81
x2	= 2048.8 ± 4.3
x3	= 2059.7 ± 0.18
x4	= 2079.7 ± 2.35
x5	= 2098.5 ± 0
s1	= 22.993 ± 3.53
s2	= 11.149 ± 2.91
s3	= 6.541 ± 0.495
s4	= 15.705 ± 0
s5	= 27.15 ± 0
Ba	= 0.00013413 ± 1.43e-06
Bb	= -1.1477 ± 0.00295

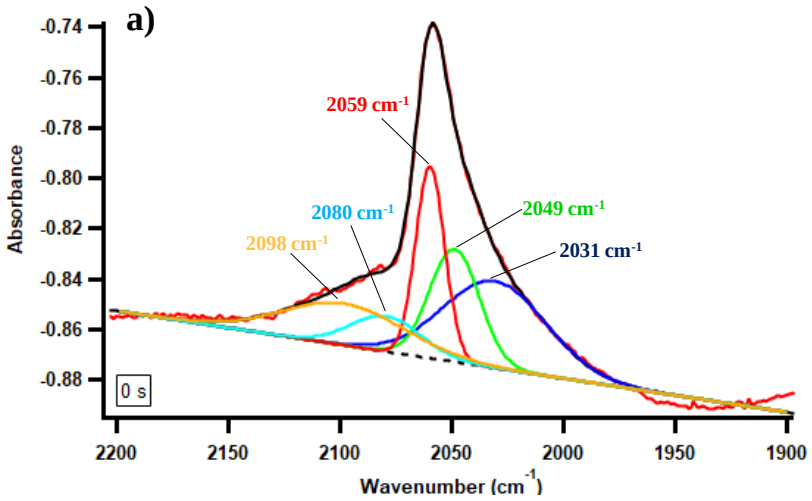

Pt/Al_2O_3 t= 1.6 s

A1	= 0 ± 0
A2	= 0.00031057 ± 0.000617
A3	= 0 ± 0
A4	= 0 ± 0
A5	= 0.034366 ± 0.000586
A6	= 0.04586 ± 0.000882
A7	= 0.072939 ± 0.000841
A8	= 0.013456 ± 0.000451
A9	= 0.016505 ± 0
x1	= 1985.2 ± 0
x2	= 2002.8 ± 0
x3	= 2011.7 ± 0
x4	= 2027 ± 0
x5	= 2031 ± 0
x6	= 2048.8 ± 0
x7	= 2059.7 ± 0
x8	= 2079.7 ± 0
x9	= 2098.5 ± 0
s1	= 16.321 ± 0
s2	= 10.16 ± 0
s3	= 6.2794 ± 0
s4	= 15.705 ± 0
s5	= 22.993 ± 0
s6	= 11.149 ± 0
s7	= 6.541 ± 0
s8	= 15.705 ± 0
s9	= 27.15 ± 0
Ba	= 0.00013401 ± 1.3e-06
Bb	= -1.1473 ± 0.00268

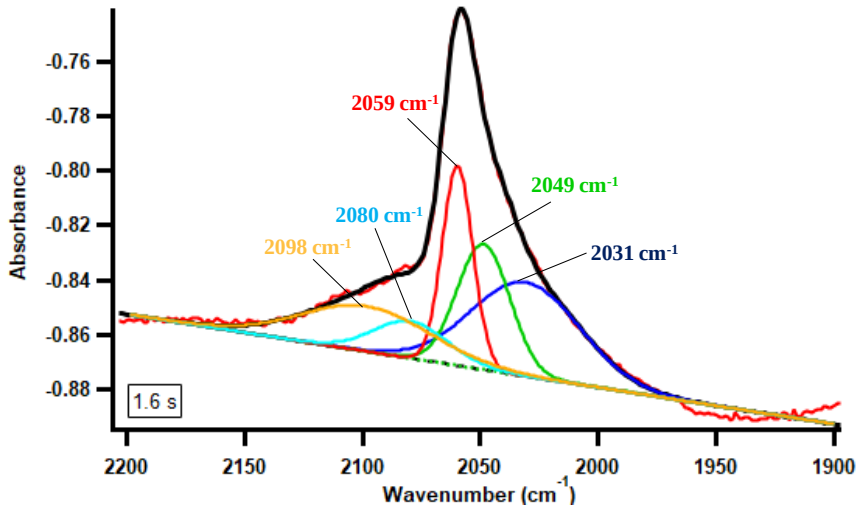

Pt/Al_2O_3 t= 3.2 s

A1	= 0.0050012 ± 0.000541
A2	= 0.00033721 ± 0.000668
A3	= 0 ± 0
A4	= 0 ± 0
A5	= 0.037019 ± 0.000423
A6	= 0.05 ± 0
A7	= 0.034267 ± 0.000689
A8	= 0.0080356 ± 0.00046
A9	= 0.016505 ± 0
x1	= 1985.2 ± 0
x2	= 2002.8 ± 0
x3	= 2011.7 ± 0
x4	= 2027 ± 0
x5	= 2031 ± 0
x6	= 2048.8 ± 0
x7	= 2059.7 ± 0
x8	= 2079.7 ± 0
x9	= 2098.5 ± 0
s1	= 16.321 ± 0
s2	= 10.16 ± 0
s3	= 6.2794 ± 0
s4	= 15.705 ± 0
s5	= 22.993 ± 0
s6	= 11.149 ± 0
s7	= 6.541 ± 0
s8	= 15.705 ± 0
s9	= 27.15 ± 0
Ba	= 0.0001264 ± 1.4e-06
Bb	= -1.1306 ± 0.0029

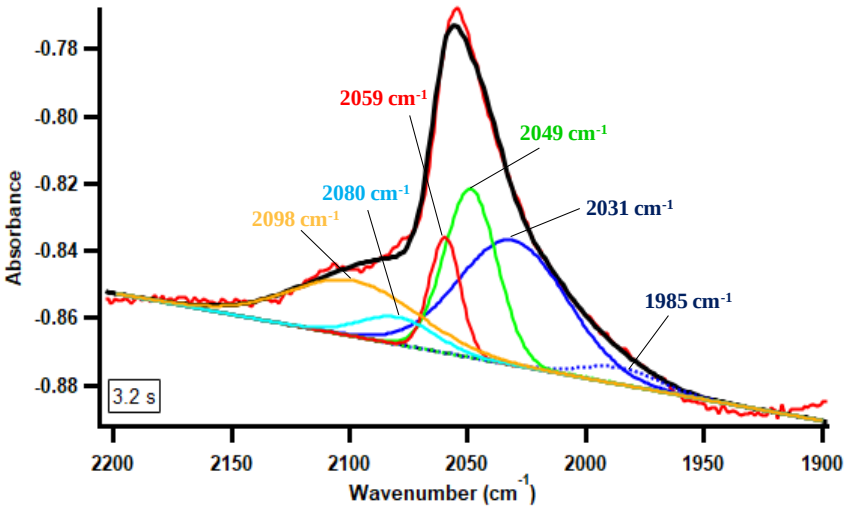

Pt/Al_2O_3 t= 5 s

A1	= 0.011608 ± 0
A2	= 0.0015 ± 0
A3	= 0 ± 0
A4	= 0.01 ± 0
A5	= 0.036525 ± 0.000333
A6	= 0.0467 ± 0.000486
A7	= 0 ± 0
A8	= 0.0033977 ± 0.000301
A9	= 0.016505 ± 0
x1	= 1985.2 ± 0
x2	= 2002.8 ± 0
x3	= 2011.7 ± 0
x4	= 2027 ± 0
x5	= 2031 ± 0
x6	= 2048.8 ± 0
x7	= 2059.7 ± 0
x8	= 2079.7 ± 0
x9	= 2098.5 ± 0
s1	= 16.321 ± 0
s2	= 10.16 ± 0
s3	= 6.2794 ± 0
s4	= 15.705 ± 0
s5	= 22.993 ± 0
s6	= 11.149 ± 0
s7	= 6.541 ± 0
s8	= 15.705 ± 0
s9	= 27.15 ± 0
Ba	= 0.00011909 ± 0
Bb	= -1.1146 ± 0

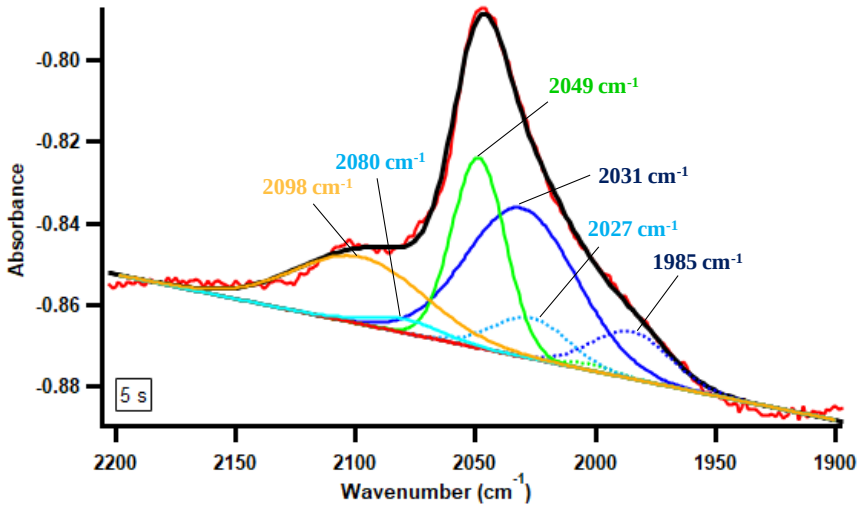

Pt/Al_2O_3 t= 10 s

A1	= 0.016374 ± 0.000344
A2	= 0.014617 ± 0.000531
A3	= 0.0011844 ± 0.000618
A4	= 0.012079 ± 0.000353
A5	= 0.035 ± 0
A6	= 0.015635 ± 0.000354
A7	= 0 ± 0
A8	= 0.00019973 ± 0.000265
A9	= 0.016505 ± 0
x1	= 1985.2 ± 0
x2	= 2002.8 ± 0
x3	= 2011.7 ± 0
x4	= 2027 ± 0
x5	= 2031 ± 0
x6	= 2048.8 ± 0
x7	= 2059.7 ± 0
x8	= 2079.7 ± 0
x9	= 2098.5 ± 0
s1	= 16.321 ± 0
s2	= 10.16 ± 0
s3	= 6.2794 ± 0
s4	= 15.705 ± 0
s5	= 22.993 ± 0
s6	= 11.149 ± 0
s7	= 6.541 ± 0
s8	= 15.705 ± 0
s9	= 27.15 ± 0
Ba	= 0.00011498 ± 8.28e-07
Bb	= -1.1055 ± 0.00172

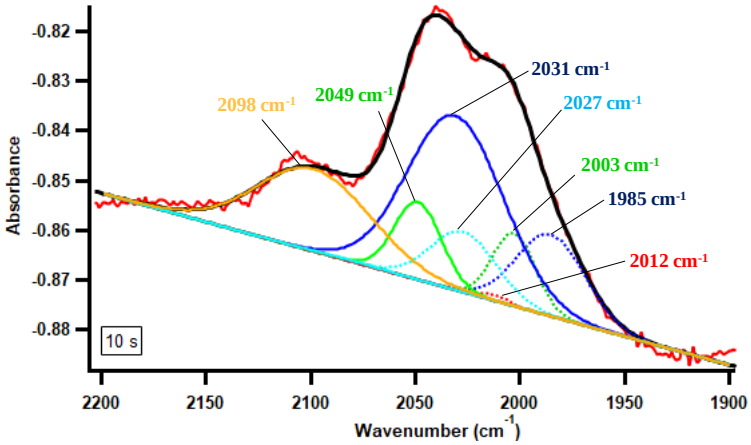

Pt/Al_2O_3 t= 15 s

A1	= 0.020496 ± 0.000338
A2	= 0.026724 ± 0.000602
A3	= 0.015197 ± 0.000594
A4	= 0.0198 ± 0.00168
A5	= 0.021265 ± 0.00189
A6	= 0.0034055 ± 0.00091
A7	= 0 ± 0
A8	= 0 ± 0
A9	= 0.016505 ± 0
x1	= 1985.2 ± 0
x2	= 2002.8 ± 0
x3	= 2011.7 ± 0
x4	= 2027 ± 0
x5	= 2031 ± 0
x6	= 2048.8 ± 0
x7	= 2059.7 ± 0
x8	= 2079.7 ± 0
x9	= 2098.5 ± 0
s1	= 16.321 ± 0
s2	= 10.16 ± 0
s3	= 6.2794 ± 0
s4	= 15.705 ± 0
s5	= 22.993 ± 0
s6	= 11.149 ± 0
s7	= 6.541 ± 0
s8	= 15.705 ± 0
s9	= 27.15 ± 0
Ba	= 0.00011211 ± 7.93e-07
Bb	= -1.0992 ± 0.00164

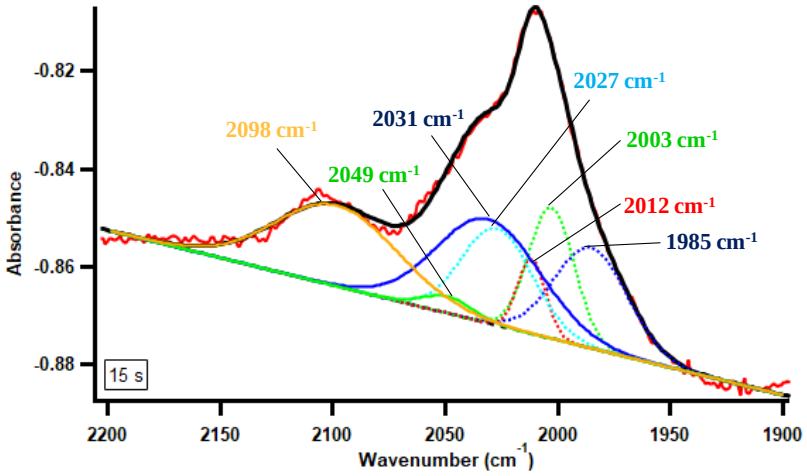

Pt/Al_2O_3 t= 20s

A1	= 0.02264 ± 0.000341
A2	= 0.035072 ± 0.00055
A3	= 0.032019 ± 0.000615
A4	= 0.020539 ± 0.00086
A5	= 0.010921 ± 0.000728
A6	= 0 ± 0
A7	= 0 ± 0
A8	= 0 ± 0
A9	= 0.016505 ± 0
x1	= 1985.2 ± 0
x2	= 2002.8 ± 0
x3	= 2011.7 ± 0
x4	= 2027 ± 0
x5	= 2031 ± 0
x6	= 2048.8 ± 0
x7	= 2059.7 ± 0
x8	= 2079.7 ± 0
x9	= 2098.5 ± 0
s1	= 16.321 ± 0
s2	= 10.16 ± 0
s3	= 6.2794 ± 0
s4	= 15.705 ± 0
s5	= 22.993 ± 0
s6	= 11.149 ± 0
s7	= 6.541 ± 0
s8	= 15.705 ± 0
s9	= 27.15 ± 0
Ba	= 0.00011003 ± 8.32e-07
Bb	= -1.095 ± 0.00172

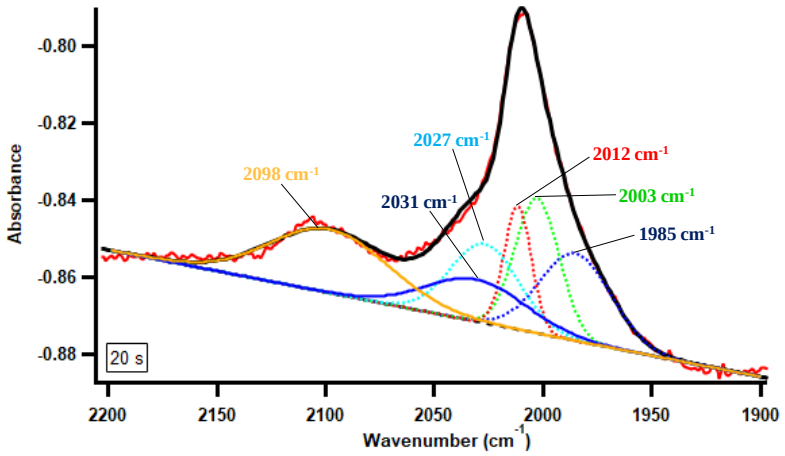

Pt/Al_2O_3 t= 30 s

A1	= 0.023955 ± 0.000297
A2	= 0.039975 ± 0.000479
A3	= 0.045987 ± 0.000536
A4	= 0.020087 ± 0.000749
A5	= 0.0034418 ± 0.000634
A6	= 0 ± 0
A7	= 0 ± 0
A8	= 0 ± 0
A9	= 0.016505 ± 0
x1	= 1985.2 ± 0
x2	= 2002.8 ± 0
x3	= 2011.7 ± 0
x4	= 2027 ± 0
x5	= 2031 ± 0
x6	= 2048.8 ± 0
x7	= 2059.7 ± 0
x8	= 2079.7 ± 0
x9	= 2098.5 ± 0
s1	= 16.321 ± 0
s2	= 10.16 ± 0
s3	= 6.2794 ± 0
s4	= 15.705 ± 0
s5	= 22.993 ± 0
s6	= 11.149 ± 0
s7	= 6.541 ± 0
s8	= 15.705 ± 0
s9	= 27.15 ± 0
Ba	= 0.00010857 ± 7.25e-07
Bb	= -1.0926 ± 0.0015

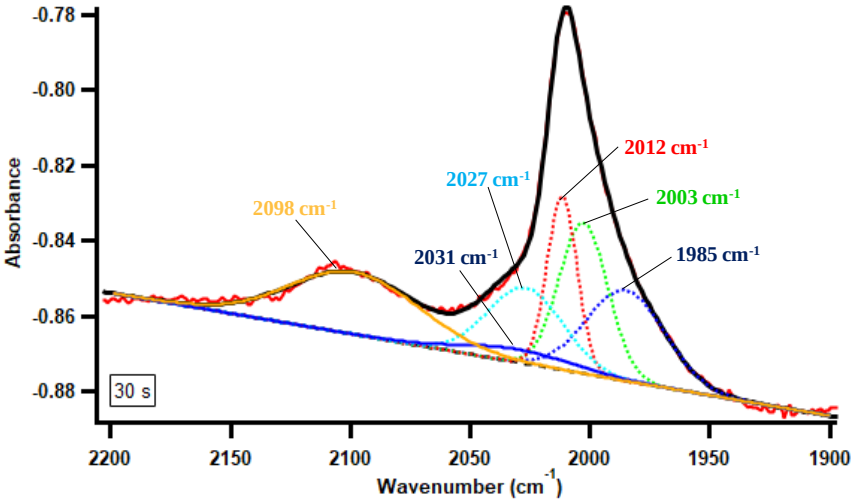

Pt/Al_2O_3 t= 60s

A1	= 0.024936 ± 0.00539
A2	= 0.042735 ± 0.0212
A3	= 0.056402 ± 0.0178
A4	= 0.017773 ± 0.00365
A5	= 0.016505 ± 0.000203
x1	= 1985.2 ± 5.35
x2	= 2002.8 ± 4.01
x3	= 2011.7 ± 0.175
x4	= 2027 ± 5.64
x5	= 2098.5 ± 0
s1	= 16.321 ± 2.05
s2	= 10.16 ± 2.24
s3	= 6.2794 ± 0.473
s4	= 15.705 ± 2.4
s5	= 27.15 ± 0.549
Ba	= 0.00010878 ± 8.53e-07
Bb	= -1.0921 ± 0.00175

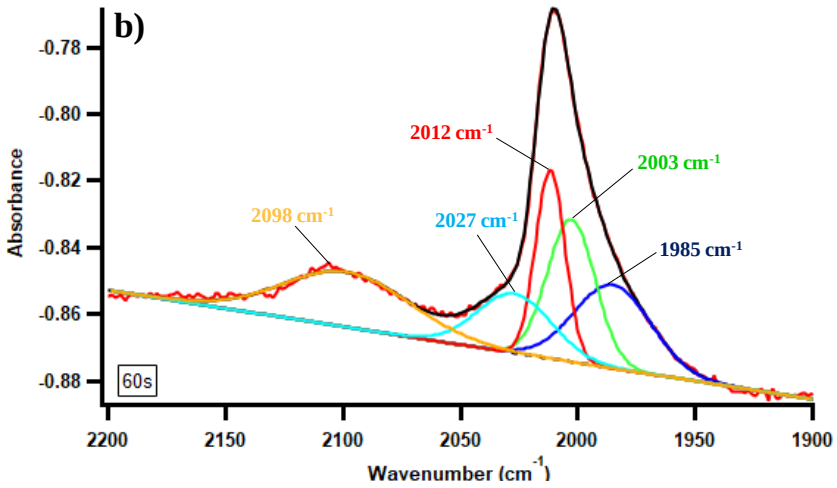

SIV-2-CO adsorbed on Pd/Al_2O_3

Fitting parameters:
A_i= Height of the peak
x_i= Peak position
s_i= Full Width at Half Maximum
Ba and Bb= Baseline slope and intercept

Pd/Al_2O_3 t= 0 s

A1	= 0.0056232 ± 0.000215
A2	= 0.0034815 ± 0.000151
A3	= 0.0078605 ± 0.000477
A4	= 0.014225 ± 0.000154
A5	= 0.011346 ± 0.000388
x1	= 2087 ± 0
x2	= 2059 ± 0
x3	= 1957 ± 0
x4	= 1908 ± 0
x5	= 1848 ± 0
s1	= 12.876 ± 0.546
s2	= 25.366 ± 1.34
s3	= 18.042 ± 0.612
s4	= 36.865 ± 1.42
s5	= 46.952 ± 0.943
Ba	= 1.1098e-05 ± 0
Bb	= 0.23311 ± 0

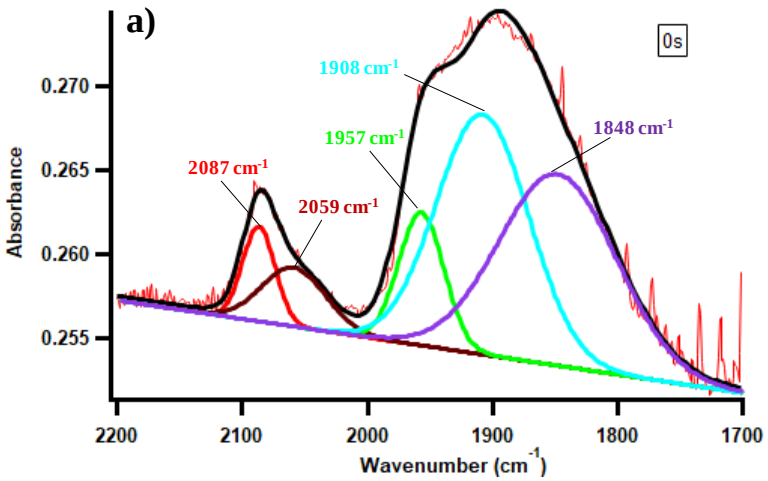

Pd/Al_2O_3 t= 1.2 s

A1	= 0.0053332 ± 0.000147
A2	= 0.0034 ± 0
A3	= 0.0078 ± 0
A4	= 0.013268 ± 0.000342
A5	= 0.010824 ± 0.0018
A6	= 0 ± 0
A7	= 0 ± 0
A8	= 0.00095178 ± 0.000365
A9	= 0.00065707 ± 0.00148
A10	= 1.262e-05 ± 0.000613
x1	= 2087 ± 0
x2	= 2059 ± 0
x3	= 1957 ± 0
x4	= 1908 ± 0
x5	= 1848 ± 0
x6	= 2041 ± 0
x7	= 2016 ± 0
x8	= 1910 ± 0
x9	= 1857 ± 0
x10	= 1804 ± 0
s1	= 12.876 ± 0
s2	= 25.366 ± 0
s3	= 18.042 ± 0
s4	= 36.865 ± 0
s5	= 46.952 ± 0
s6	= 12.261 ± 0
s7	= 27.46 ± 0
s8	= 20.739 ± 0
s9	= 36 ± 0
s10	= 42.096 ± 0
Ba	= 1.0701e-05 ± 0
Bb	= 0.23364 ± 0

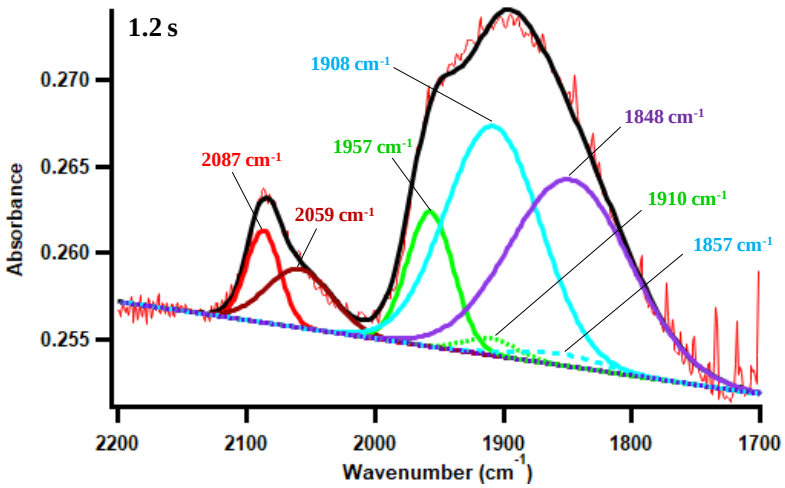

Pd/Al_2O_3 t= 2.5 s

A1	= 0.0041469 ± 0.000227
A2	= 0.0030668 ± 0.000235
A3	= 0.0054076 ± 0.000335
A4	= 0.011941 ± 0.000726
A5	= 0.010824 ± 0.00213
A6	= 0.00080044 ± 0.00029
A7	= 0.00064206 ± 0.000132
A8	= 0.00095178 ± 0.000825
A9	= 0.00098684 ± 0.00192
A10	= 0.00097659 ± 0.000682
x1	= 2087 ± 0
x2	= 2059 ± 0
x3	= 1957 ± 0
x4	= 1908 ± 0
x5	= 1848 ± 0
x6	= 2041 ± 0
x7	= 2016 ± 0
x8	= 1910 ± 0
x9	= 1857 ± 0
x10	= 1804 ± 0
s1	= 12.876 ± 0
s2	= 25.366 ± 0
s3	= 18.042 ± 0
s4	= 36.865 ± 0
s5	= 46.952 ± 0
s6	= 12.261 ± 0
s7	= 27.46 ± 0
s8	= 20.739 ± 0
s9	= 36 ± 0
s10	= 42.096 ± 0
Ba	= 9.6235e-06 ± 0
Bb	= 0.236 ± 0

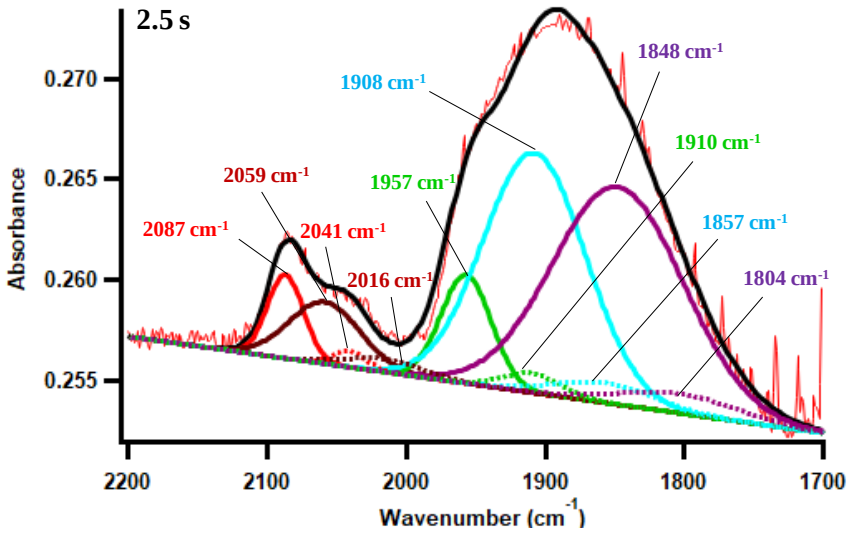

Pd/Al_2O_3 t= 5 s

A1	= 0.0018986 ± 0.000251
A2	= 0.0010457 ± 0.00026
A3	= 0.0014841 ± 0.00037
A4	= 0.0080255 ± 0.000803
A5	= 0.0097122 ± 0.00235
A6	= 0.0027802 ± 0.000321
A7	= 0.00064206 ± 0.000146
A8	= 0.0019104 ± 0.000913
A9	= 0.00278 ± 0.00212
A10	= 0.00097654 ± 0.000754
x1	= 2087 ± 0
x2	= 2059 ± 0
x3	= 1957 ± 0
x4	= 1908 ± 0
x5	= 1848 ± 0
x6	= 2041 ± 0
x7	= 2016 ± 0
x8	= 1910 ± 0
x9	= 1857 ± 0
x10	= 1804 ± 0
s1	= 12.876 ± 0
s2	= 25.366 ± 0
s3	= 18.042 ± 0
s4	= 36.865 ± 0
s5	= 46.952 ± 0
s6	= 12.261 ± 0
s7	= 27.46 ± 0
s8	= 20.739 ± 0
s9	= 36 ± 0
s10	= 42.096 ± 0
Ba	= 7.0233e-06 ± 0
Bb	= 0.24155 ± 0

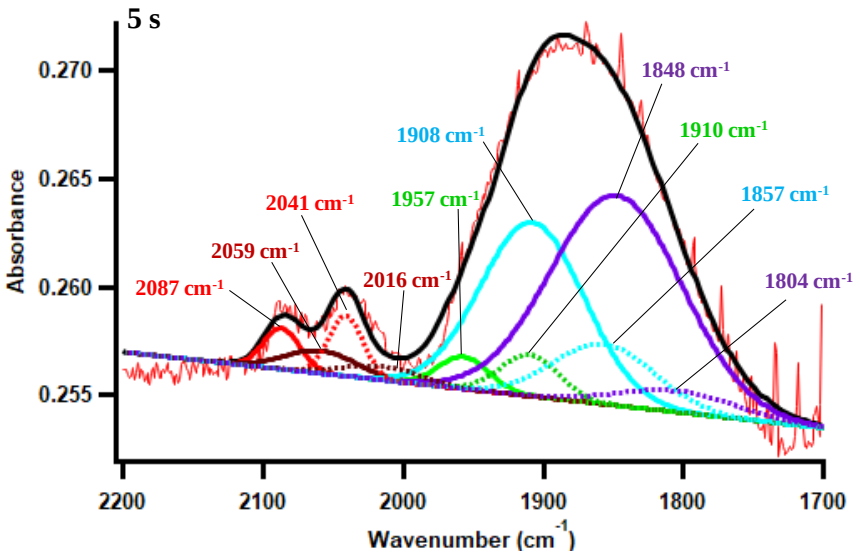

Pd/Al_2O_3 t= 10 s

A1 = 0.00088606 ± 0.000214
A2 = 8.9904e-19 ± 0.000222
A3 = -2.9265e-09 ± 0.000317
A4 = 0.003416 ± 0.000686
A5 = 0.0097123 ± 0.00201
A6 = 0.0041749 ± 0.000274
A7 = 0.0015612 ± 0.000125
A8 = 0.004793 ± 0.000781
A9 = 0.0043491 ± 0.00181
A10 = 0.0014796 ± 0.000645
x1 = 2087 ± 0
x2 = 2059 ± 0
x3 = 1957 ± 0
x4 = 1908 ± 0
x5 = 1848 ± 0
x6 = 2041 ± 0
x7 = 2016 ± 0
x8 = 1910 ± 0
x9 = 1857 ± 0
x10 = 1804 ± 0
s1 = 12.876 ± 0
s2 = 25.366 ± 0
s3 = 18.042 ± 0
s4 = 36.865 ± 0
s5 = 46.952 ± 0
s6 = 12.261 ± 0
s7 = 27.46 ± 0
s8 = 20.739 ± 0
s9 = 36 ± 0
s10 = 42.096 ± 0
Ba = 5.297e-06 ± 0
Bb = 0.24489 ± 0

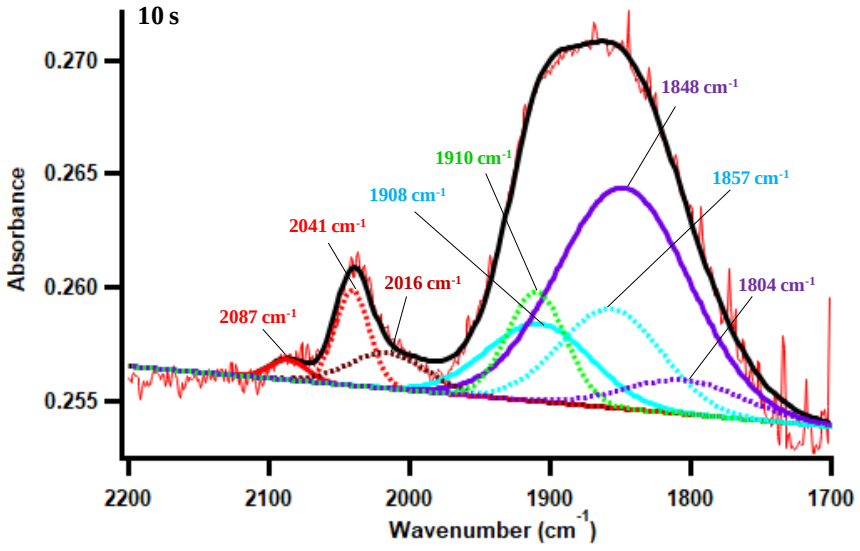

Pd/Al_2O_3 t= 15 s

A1	= 0.00022218 ± 0.000143
A2	= 0 ± 0
A3	= 0 ± 0
A4	= 0.00076906 ± 0.000341
A5	= 0.009122 ± 0.00176
A6	= 0.0043986 ± 0.000187
A7	= 0.0017442 ± 0.000128
A8	= 0.0069216 ± 0.000366
A9	= 0.0058738 ± 0.00145
A10	= 0.0020319 ± 0.000598
x1	= 2087 ± 0
x2	= 2059 ± 0
x3	= 1957 ± 0
x4	= 1908 ± 0
x5	= 1848 ± 0
x6	= 2041 ± 0
x7	= 2016 ± 0
x8	= 1910 ± 0
x9	= 1857 ± 0
x10	= 1804 ± 0
s1	= 12.876 ± 0
s2	= 25.366 ± 0
s3	= 18.042 ± 0
s4	= 36.865 ± 0
s5	= 46.952 ± 0
s6	= 12.261 ± 0
s7	= 27.46 ± 0
s8	= 20.739 ± 0
s9	= 36 ± 0
s10	= 42.096 ± 0
Ba	= 6.2554e-06 ± 0
Bb	= 0.24293 ± 0

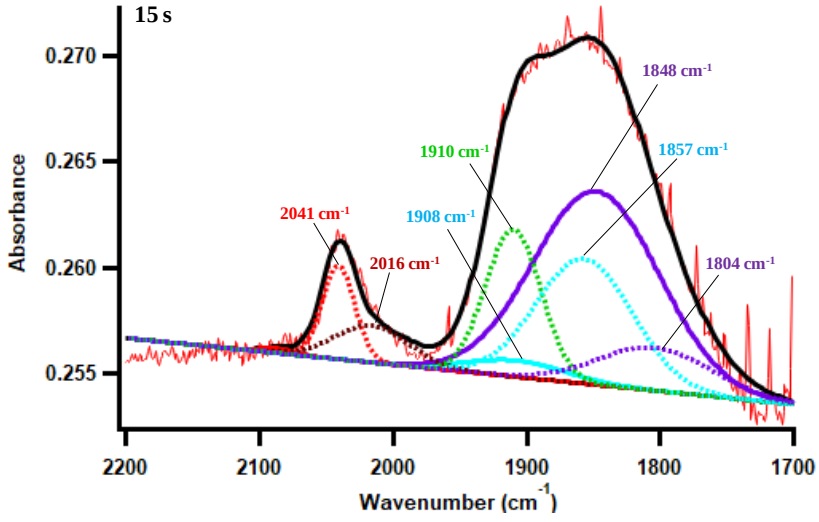

Pd/Al_2O_3 t= 20 s

A1 = 0.00022218 ± 0.000142
A2 = 0 ± 0
A3 = 0 ± 0
A4 = 0.00071768 ± 0.000337
A5 = 0.0044264 ± 0.00174
A6 = 0.0045131 ± 0.000185
A7 = 0.0027961 ± 0.000126
A8 = 0.0077523 ± 0.000361
A9 = 0.0099585 ± 0.00143
A10 = 0.0045719 ± 0.000591
x1 = 2087 ± 0
x2 = 2059 ± 0
x3 = 1957 ± 0
x4 = 1908 ± 0
x5 = 1848 ± 0
x6 = 2041 ± 0
x7 = 2016 ± 0
x8 = 1910 ± 0
x9 = 1857 ± 0
x10 = 1804 ± 0
s1 = 12.876 ± 0
s2 = 25.366 ± 0
s3 = 18.042 ± 0
s4 = 36.865 ± 0
s5 = 46.952 ± 0
s6 = 12.261 ± 0
s7 = 27.46 ± 0
s8 = 20.739 ± 0
s9 = 36 ± 0
s10 = 42.096 ± 0
Ba = 6.4722e-06 ± 0
Bb = 0.2427 ± 0

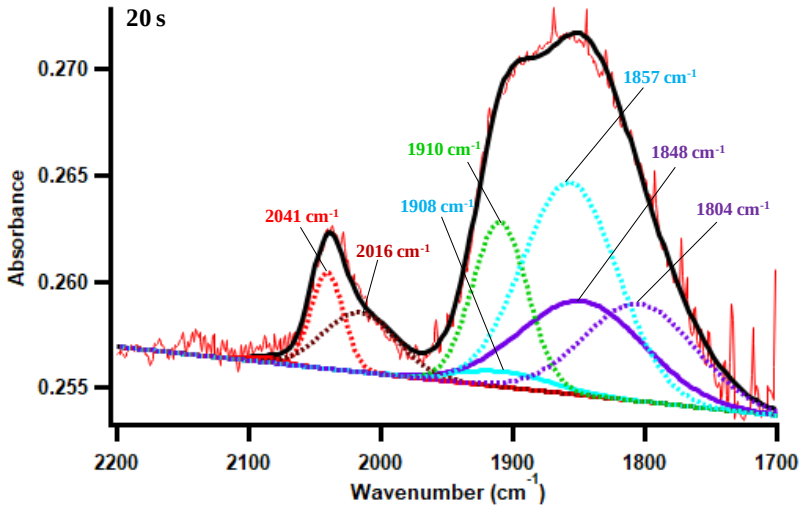

Pd/Al_2O_3 t= 30 s

A1 = 0.00022218 ± 0.000171
A2 = 0 ± 0
A3 = 0 ± 0
A4 = -5.1779e-07 ± 0.000451
A5 = 0.0025336 ± 0.00233
A6 = 0.0047776 ± 0.000248
A7 = 0.0027961 ± 0.000169
A8 = 0.0077521 ± 0.000484
A9 = 0.011389 ± 0.00192
A10 = 0.0048448 ± 0.000792
x1 = 2087 ± 0
x2 = 2059 ± 0
x3 = 1957 ± 0
x4 = 1908 ± 0
x5 = 1848 ± 0
x6 = 2041 ± 0
x7 = 2016 ± 0
x8 = 1910 ± 0
x9 = 1857 ± 0
x10 = 1804 ± 0
s1 = 12.876 ± 0
s2 = 25.366 ± 0
s3 = 18.042 ± 0
s4 = 36.865 ± 0
s5 = 46.952 ± 0
s6 = 12.261 ± 0
s7 = 27.46 ± 0
s8 = 20.739 ± 0
s9 = 36 ± 0
s10 = 42.096 ± 0
Ba = 5.5361e-06 ± 0
Bb = 0.246 ± 0

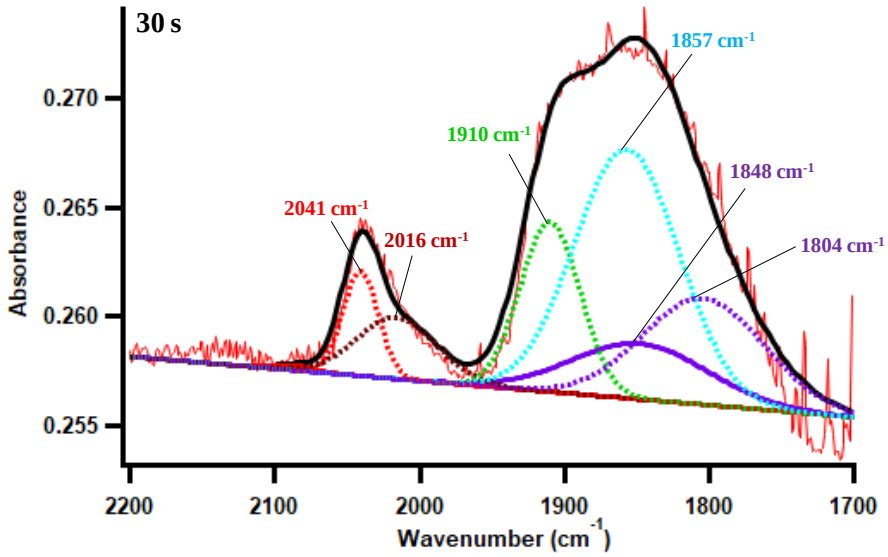

Pd/Al_2O_3 t= 60 s

A1	= 0.0049059 ± 0.000207
A2	= 0.0034504 ± 0.000154
A3	= 0.0091115 ± 0.000147
A4	= 0.013807 ± 0.000155
A5	= 0.007248 ± 0.000119
x1	= 2041 ± 0
x2	= 2016 ± 0
x3	= 1910 ± 0
x4	= 1857 ± 0
x5	= 1804 ± 0
s1	= 12.261 ± 0.62
s2	= 27.46 ± 1.25
s3	= 20.739 ± 0.45
s4	= 36 ± 0
s5	= 42.096 ± 0.823
Ba	= 7.1415e-06 ± 0
Bb	= 0.24103 ± 0

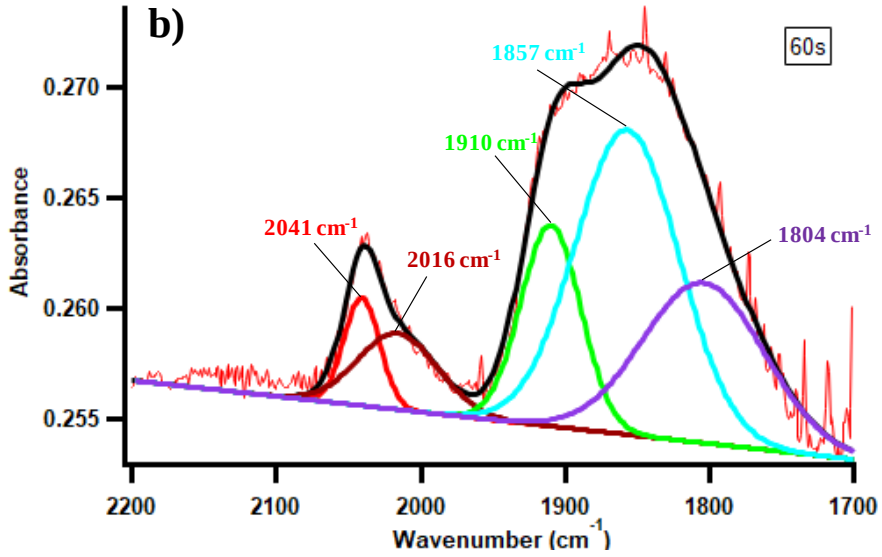

SIV-3- Illustration of different types of linear and bridged palladium carbonyls

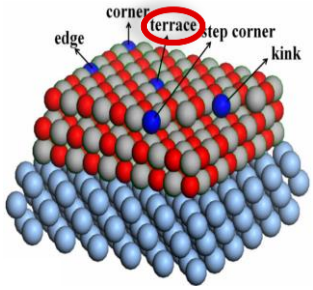

Linear CO on terrace sites

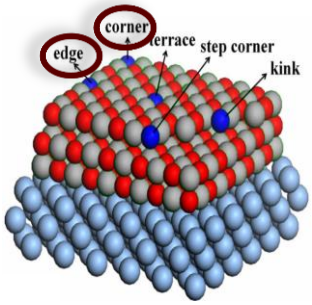

Linear CO on low-coordinated adsorption sites (corners or edges)

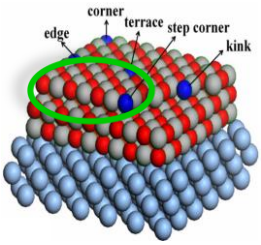

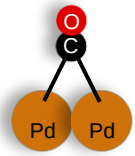

Bridged CO on the step

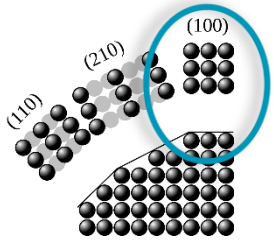

Bridge-bounded CO on Pd (100)

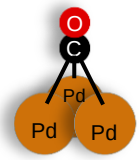

Adsorbed CO on 3-fold hollow sites

Chapter V

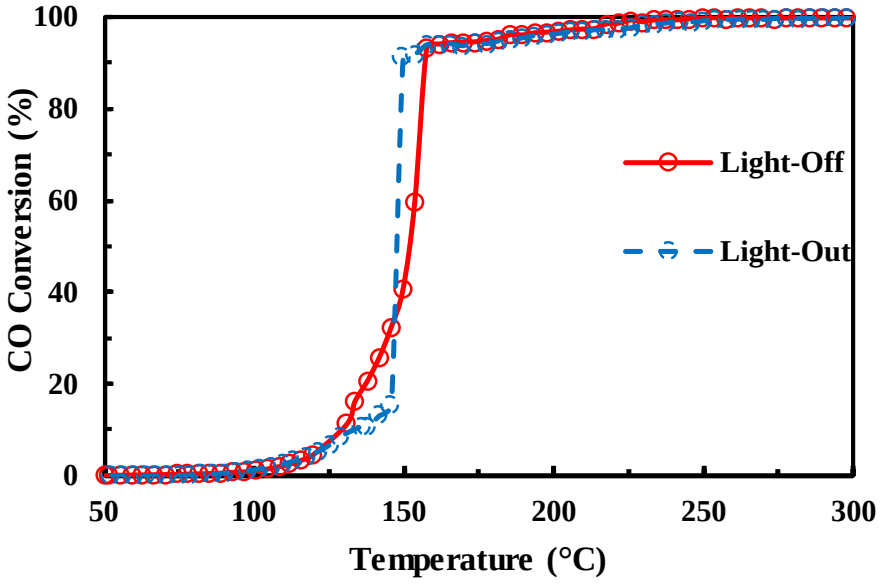

Figure SV-1- Evolution of CO conversion vs. Temperature during light-off and light-out of CO oxidation on Pt/Al_2O_3.

Figures SV-2- CO adsorbed on Pt/Al_2O_3

A_i= Height of the peak
x_i= Peak position
s_i= Full Width at Half Maximum
Ba and Bb= Baseline slope and intercept

Pt/Al_2O_3 t= 0 s

A1	= 0.034227 ± 0.000565
A2	= 0.030811 ± 0.000895
A3	= 0.080383 ± 0.000961
A4	= 0.016431 ± 0.000746
A5	= 0.010341 ± 0.000633
x1	= 2031 ± 0
x2	= 2048.8 ± 0
x3	= 2059.7 ± 0
x4	= 2079.7 ± 0
x5	= 2098.5 ± 0
s1	= 22.993 ± 0
s2	= 11.149 ± 0
s3	= 6.541 ± 0
s4	= 15.705 ± 0
s5	= 27.15 ± 0
Ba	= 3.9676e-06 ± 1.64e-06
Bb	= 0.00092637 ± 0.00333

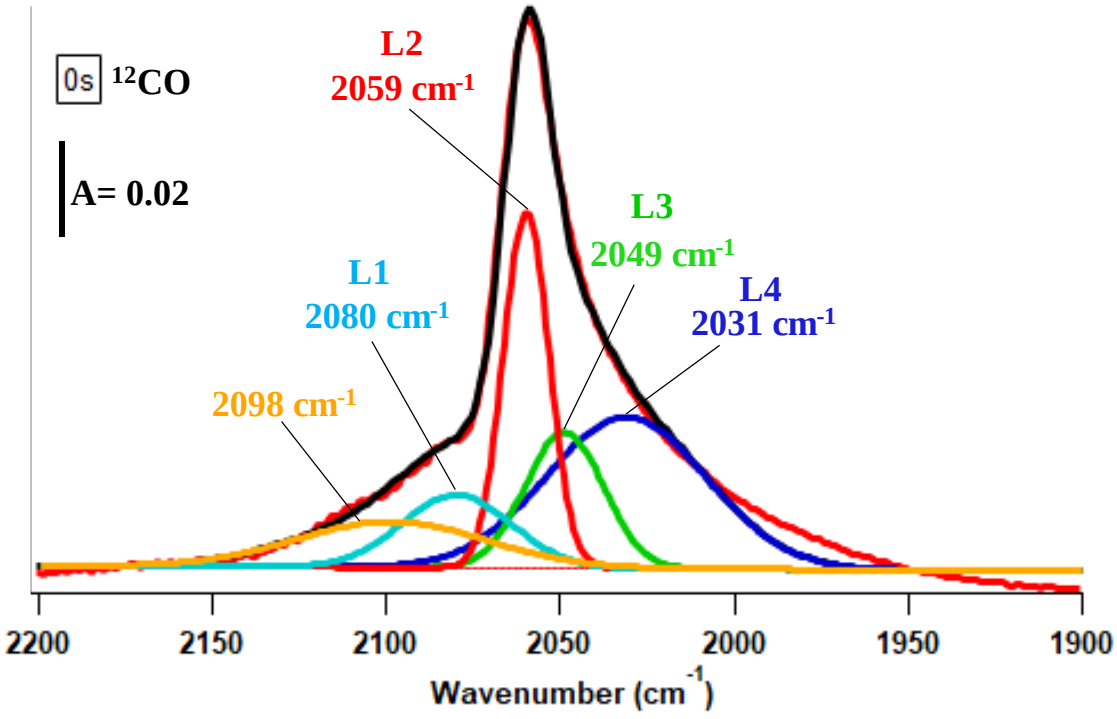

Pt/Al_2O_3 t= 1.2 s

A1	= 0.0069942 ± 0.0003
A2	= 0 ± 0
A3	= 0 ± 0
A4	= 0 ± 0
A5	= 0.034227 ± 0.000341
A6	= 0.030811 ± 0.000557
A7	= 0.080383 ± 0.000579
A8	= 0.016431 ± 0.000315
A9	= 0.010341 ± 0
x1	= 1985.2 ± 0
x2	= 2002.8 ± 0
x3	= 2011.7 ± 0
x4	= 2027 ± 0
x5	= 2031 ± 0
x6	= 2048.8 ± 0
x7	= 2059.7 ± 0
x8	= 2079.7 ± 0
x9	= 2098.5 ± 0
s1	= 16.321 ± 0
s2	= 10.16 ± 0
s3	= 6.2794 ± 0
s4	= 15.705 ± 0
s5	= 22.993 ± 0
s6	= 11.149 ± 0
s7	= 6.541 ± 0
s8	= 15.705 ± 0
s9	= 27.15 ± 0
Ba	= 1.2508e-05 ± 0
Bb	= -0.017408 ± 0.00011

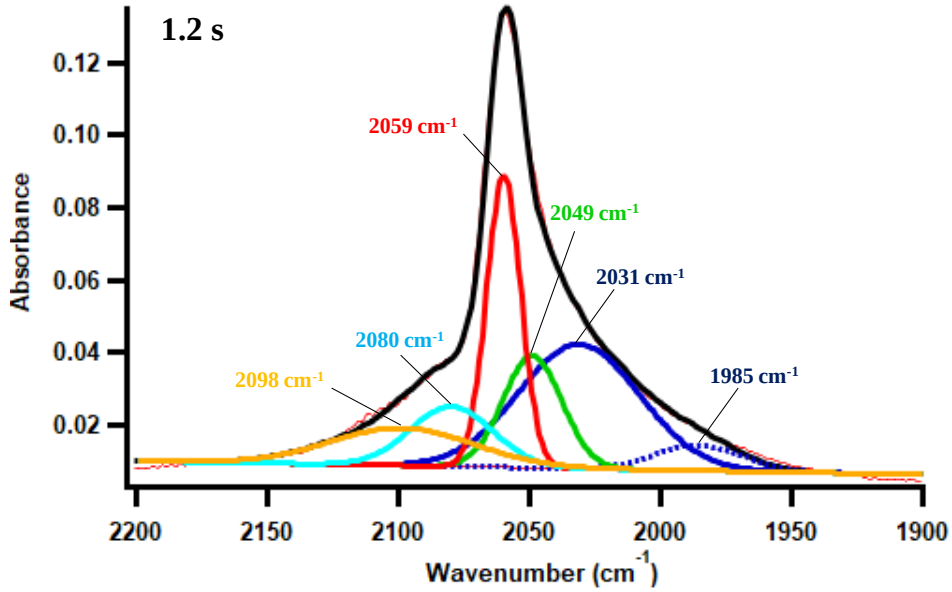

Pt/Al_2O_3 t= 2.5 s

A1	= 0.008156 ± 0.000529
A2	= 0 ± 0
A3	= 0 ± 0
A4	= 0.0012928 ± 0.00288
A5	= 0.034227 ± 0.00288
A6	= 0.030811 ± 0.00102
A7	= 0.073138 ± 0.000782
A8	= 0.015358 ± 0.000438
A9	= 0.010341 ± 0
x1	= 1985.2 ± 0
x2	= 2002.8 ± 0
x3	= 2011.7 ± 0
x4	= 2027 ± 0
x5	= 2031 ± 0
x6	= 2048.8 ± 0
x7	= 2059.7 ± 0
x8	= 2079.7 ± 0
x9	= 2098.5 ± 0
s1	= 16.321 ± 0
s2	= 10.16 ± 0
s3	= 6.2794 ± 0
s4	= 15.705 ± 0
s5	= 22.993 ± 0
s6	= 11.149 ± 0
s7	= 6.541 ± 0
s8	= 15.705 ± 0
s9	= 27.15 ± 0
Ba	= 9.5523e-06 ± 1.09e-06
Bb	= -0.011114 ± 0.00226

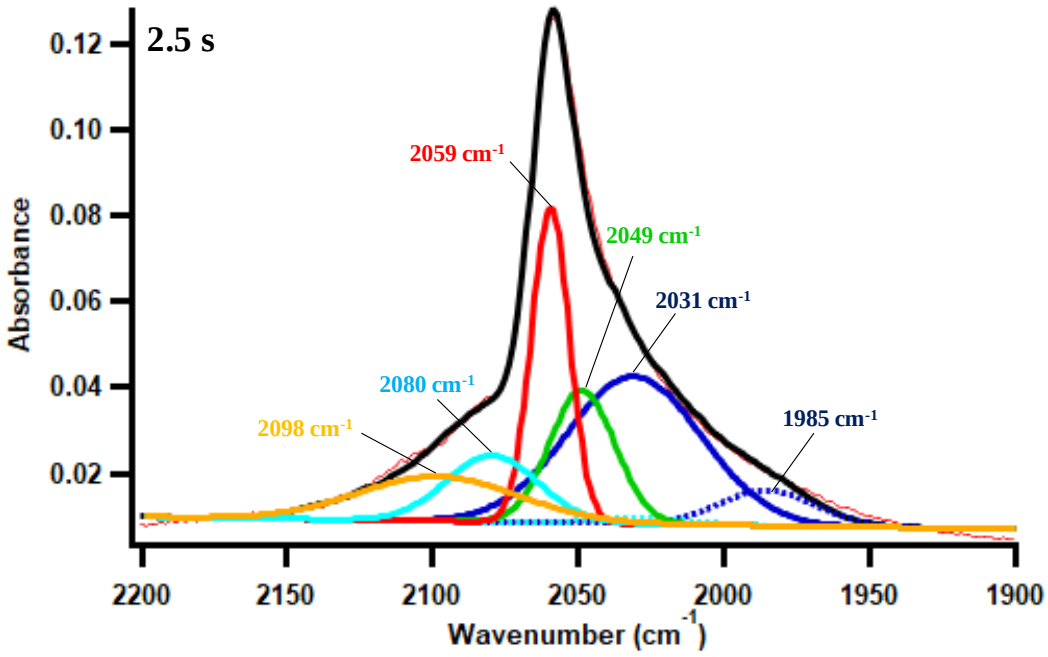

Pt/Al_2O_3 t= 5 s

A1	= 0.012989 ± 0.000992
A2	= 0 ± 0
A3	= 0 ± 0
A4	= 0.0060707 ± 0.00541
A5	= 0.034227 ± 0.00541
A6	= 0.030811 ± 0.00191
A7	= 0.04112 ± 0.00147
A8	= 0.0095613 ± 0.000822
A9	= 0.010341 ± 0
x1	= 1985.2 ± 0
x2	= 2002.8 ± 0
x3	= 2011.7 ± 0
x4	= 2027 ± 0
x5	= 2031 ± 0
x6	= 2048.8 ± 0
x7	= 2059.7 ± 0
x8	= 2079.7 ± 0
x9	= 2098.5 ± 0
s1	= 16.321 ± 0
s2	= 10.16 ± 0
s3	= 6.2794 ± 0
s4	= 15.705 ± 0
s5	= 22.993 ± 0
s6	= 11.149 ± 0
s7	= 6.541 ± 0
s8	= 15.705 ± 0
s9	= 27.15 ± 0
Ba	= 3.2735e-06 ± 2.04e-06
Bb	= 0.0027934 ± 0.00423

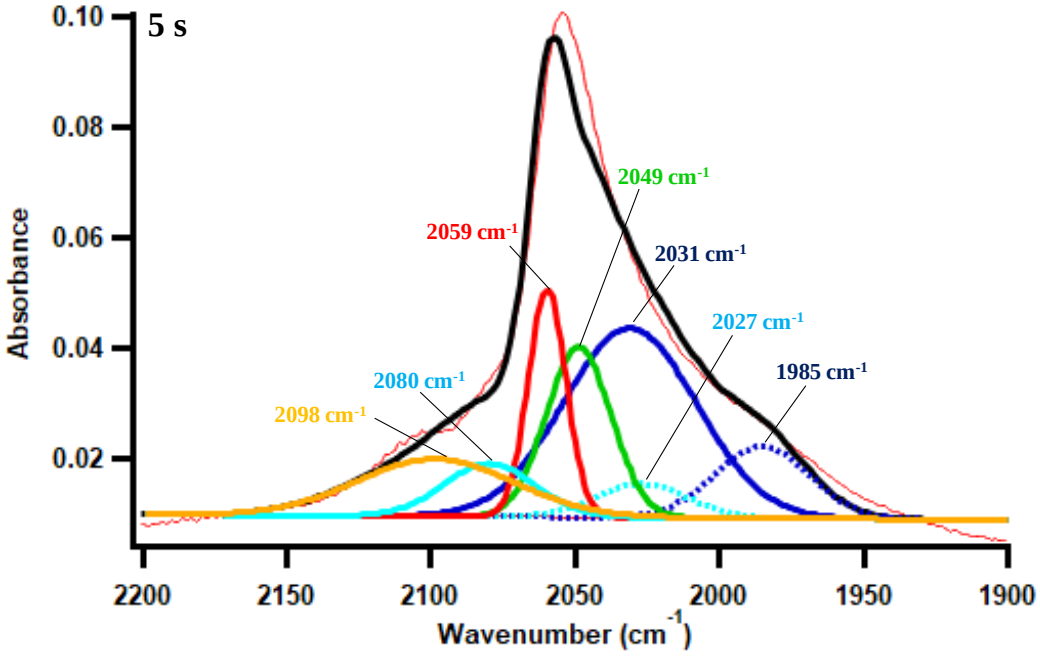

Pt/Al_2O_3 t= 10 s

A1	= 0.023201 ± 0.000716
A2	= 0.011349 ± 0.00149
A3	= 0.0016312 ± 0.000929
A4	= 0.021646 ± 0.00716
A5	= 0.022412 ± 0.00767
A6	= 0.025564 ± 0.00275
A7	= 0.0010678 ± 0.0012
A8	= 0.0043958 ± 0.000809
A9	= 0.010341 ± 0
x1	= 1985.2 ± 0
x2	= 2002.8 ± 0
x3	= 2011.7 ± 0
x4	= 2027 ± 0
x5	= 2031 ± 0
x6	= 2048.8 ± 0
x7	= 2059.7 ± 0
x8	= 2079.7 ± 0
x9	= 2098.5 ± 0
s1	= 16.321 ± 0
s2	= 10.16 ± 0
s3	= 6.2794 ± 0
s4	= 15.705 ± 0
s5	= 22.993 ± 0
s6	= 11.149 ± 0
s7	= 6.541 ± 0
s8	= 15.705 ± 0
s9	= 27.15 ± 0
Ba	= -3.8039e-06 ± 1.27e-06
Bb	= 0.017951 ± 0.00264

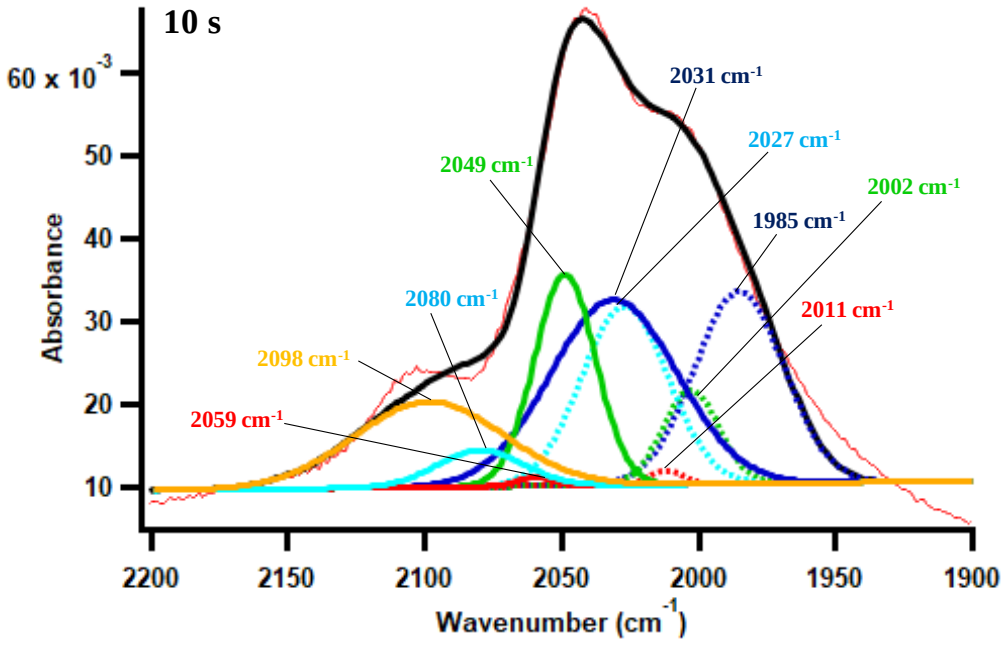

Pt/Al_2O_3 t= 15 s

A1	= 0.027565 ± 0.000587
A2	= 0.027837 ± 0.000909
A3	= 0.033484 ± 0.00106
A4	= 0.021646 ± 0
A5	= 0.01287 ± 0.000689
A6	= -1.5626e-19 ± 0.000981
A7	= 0.001028 ± 0.000872
A8	= 0.0016192 ± 0.00047
A9	= 0.010341 ± 0
x1	= 1985.2 ± 0
x2	= 2002.8 ± 0
x3	= 2011.7 ± 0
x4	= 2027 ± 0
x5	= 2031 ± 0
x6	= 2048.8 ± 0
x7	= 2059.7 ± 0
x8	= 2079.7 ± 0
x9	= 2098.5 ± 0
s1	= 16.321 ± 0
s2	= 10.16 ± 0
s3	= 6.2794 ± 0
s4	= 15.705 ± 0
s5	= 22.993 ± 0
s6	= 11.149 ± 0
s7	= 6.541 ± 0
s8	= 15.705 ± 0
s9	= 27.15 ± 0
Ba	= -9.1581e-06 ± 1.46e-06
Bb	= 0.029485 ± 0.00303

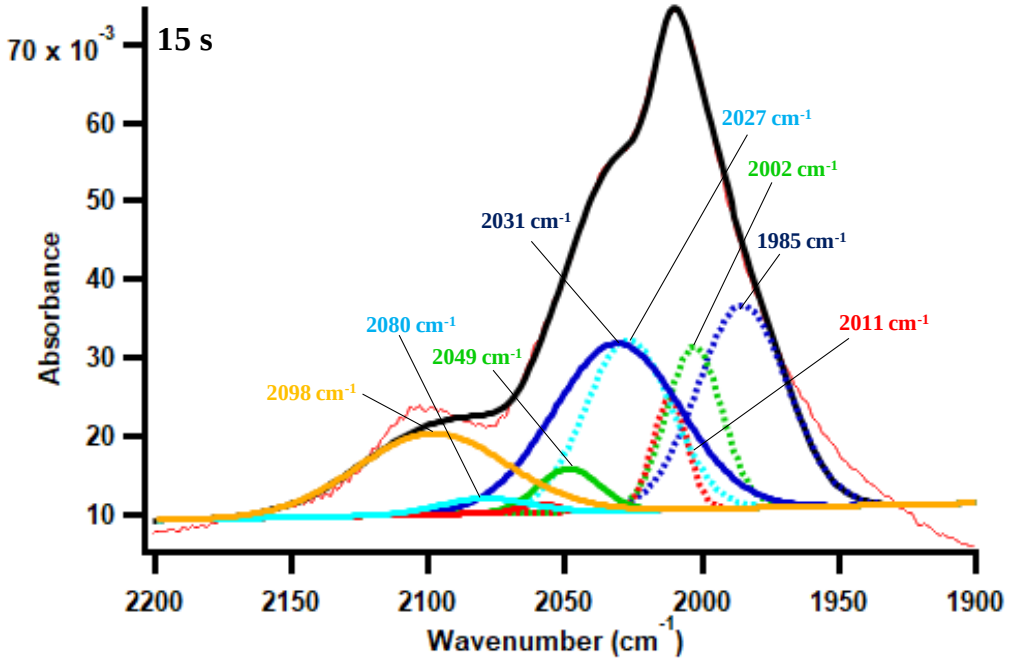

Pt/Al_2O_3 t= 20 s

A1 = 0.027565 ± 0.000583
A2 = 0.027837 ± 0.000903
A3 = 0.033484 ± 0.00098
A4 = 0.021646 ± 0
A5 = 0.01287 ± 0.000444
A6 = 0 ± 0
A7 = 0.001028 ± 0.000698
A8 = 0.0016192 ± 0.000465
A9 = 0.010341 ± 0
x1 = 1985.2 ± 0
x2 = 2002.8 ± 0
x3 = 2011.7 ± 0
x4 = 2027 ± 0
x5 = 2031 ± 0
x6 = 2048.8 ± 0
x7 = 2059.7 ± 0
x8 = 2079.7 ± 0
x9 = 2098.5 ± 0
s1 = 16.321 ± 0
s2 = 10.16 ± 0
s3 = 6.2794 ± 0
s4 = 15.705 ± 0
s5 = 22.993 ± 0
s6 = 11.149 ± 0
s7 = 6.541 ± 0
s8 = 15.705 ± 0
s9 = 27.15 ± 0
Ba = -9.1581e-06 ± 1.46e-06
Bb = 0.029485 ± 0.00303

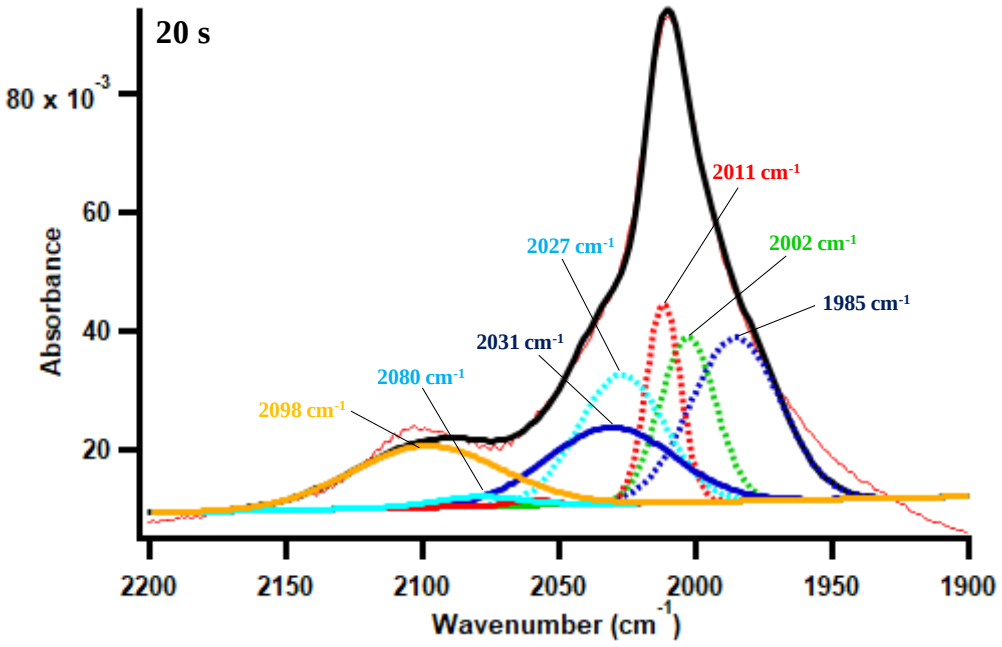

Pt/Al_2O_3 t= 30 s

A1	= 0.029025 ± 0.000584
A2	= 0.031168 ± 0.000904
A3	= 0.050358 ± 0.000981
A4	= 0.021646 ± 0
A5	= 0.0049645 ± 0.000445
A6	= 0 ± 0
A7	= 0.00050535 ± 0.000699
A8	= 0.0016192 ± 0.000465
A9	= 0.010341 ± 0
x1	= 1985.2 ± 0
x2	= 2002.8 ± 0
x3	= 2011.7 ± 0
x4	= 2027 ± 0
x5	= 2031 ± 0
x6	= 2048.8 ± 0
x7	= 2059.7 ± 0
x8	= 2079.7 ± 0
x9	= 2098.5 ± 0
s1	= 16.321 ± 0
s2	= 10.16 ± 0
s3	= 6.2794 ± 0
s4	= 15.705 ± 0
s5	= 22.993 ± 0
s6	= 11.149 ± 0
s7	= 6.541 ± 0
s8	= 15.705 ± 0
s9	= 27.15 ± 0
Ba	= -9.7735e-06 ± 1.46e-06
Bb	= 0.03099 ± 0.00303

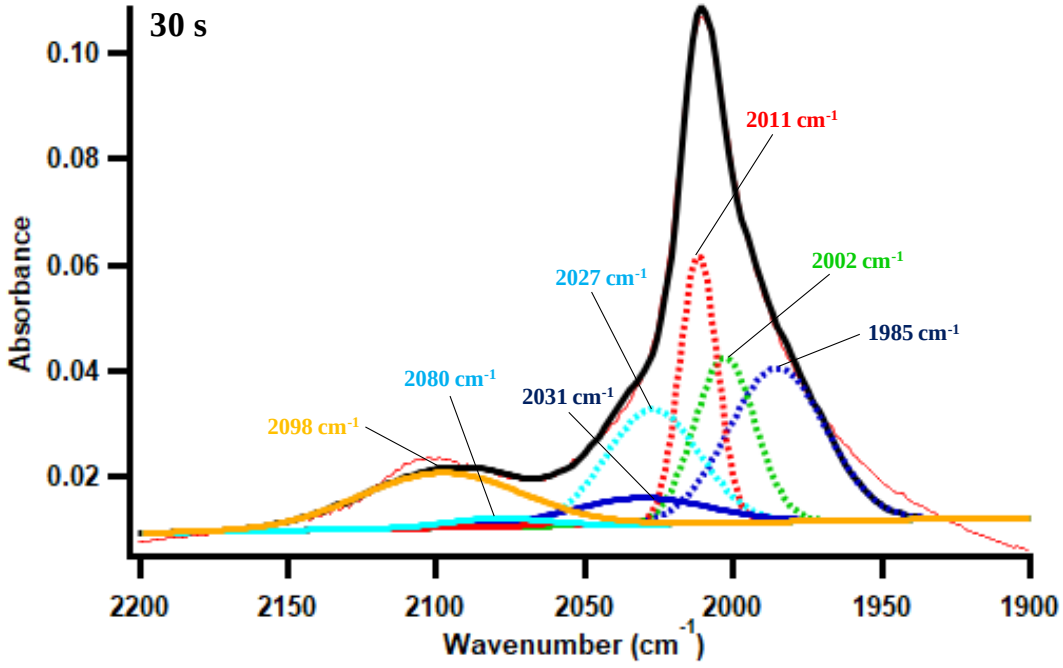

Pt/Al_2O_3 t= 60 s

A1	= 0.029727 ± 0.000586
A2	= 0.032789 ± 0.000911
A3	= 0.062375 ± 0.00102
A4	= 0.021646 ± 0.000502
A5	= 0.010341 ± 0
x1	= 1985.2 ± 0
x2	= 2002.8 ± 0
x3	= 2011.7 ± 0
x4	= 2027 ± 0
x5	= 2098.5 ± 0
s1	= 16.321 ± 0
s2	= 10.16 ± 0
s3	= 6.2794 ± 0
s4	= 15.705 ± 0
s5	= 27.15 ± 0
Ba	= -9.6332e-06 ± 1.48e-06
Bb	= 0.031254 ± 0.00306

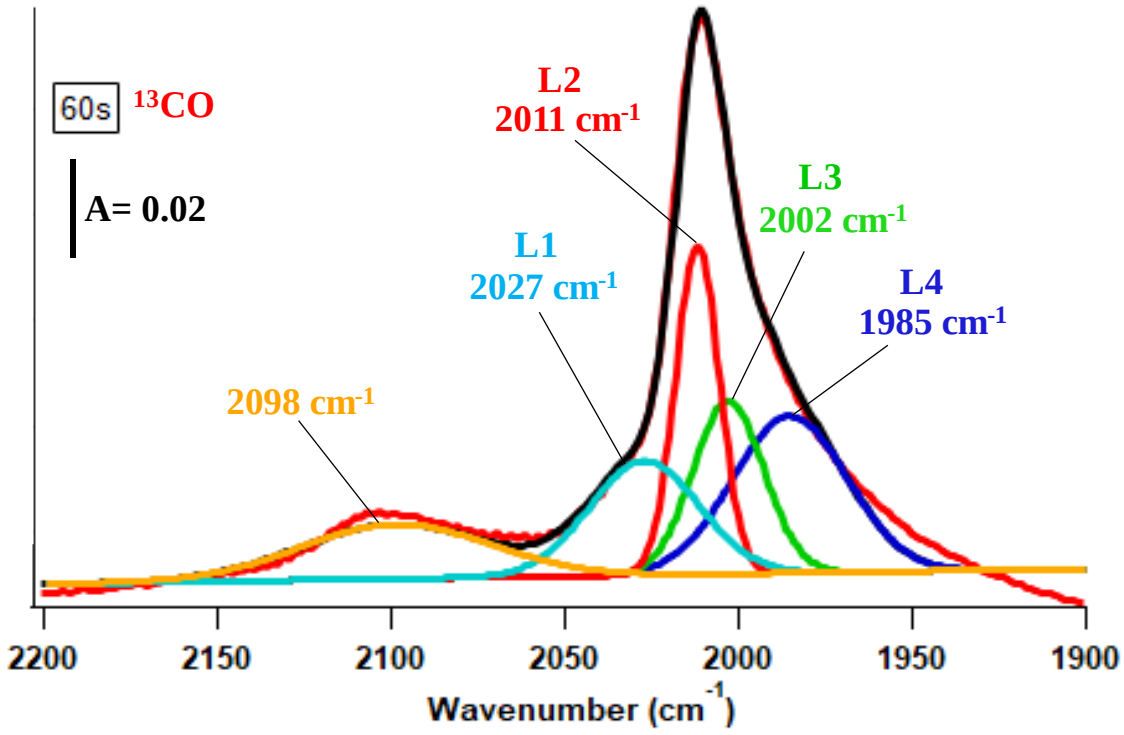

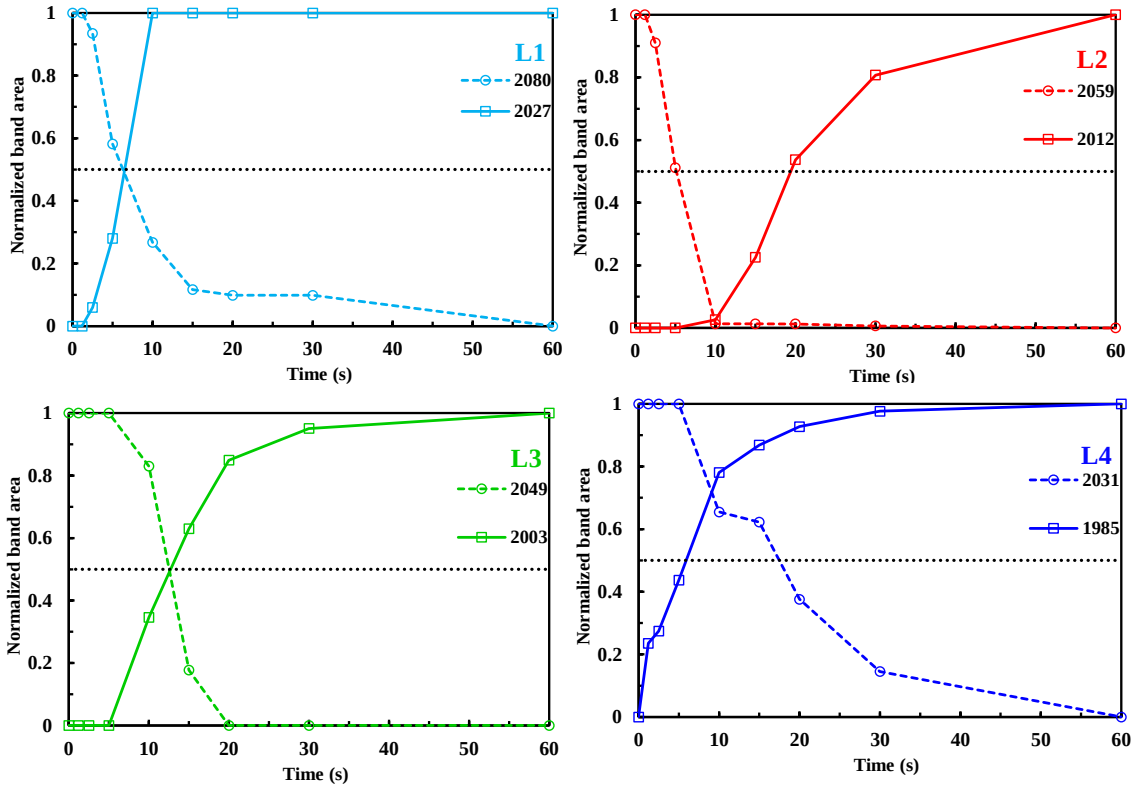

Figure SV-3- Evolution of normalized area for adsorbed ^{12}CO and corresponding adsorbed ^{13}CO: L1 (cyan), L2 (red), L3 (green) and L4 (blue) bands during isotopic exchange during light-out.

Table SV-1- Calculated correction factors for each CO adsorbed IR bands on Pt.

	L1	L2	L3	L4
f	1.32	0.74	0.97	0.62

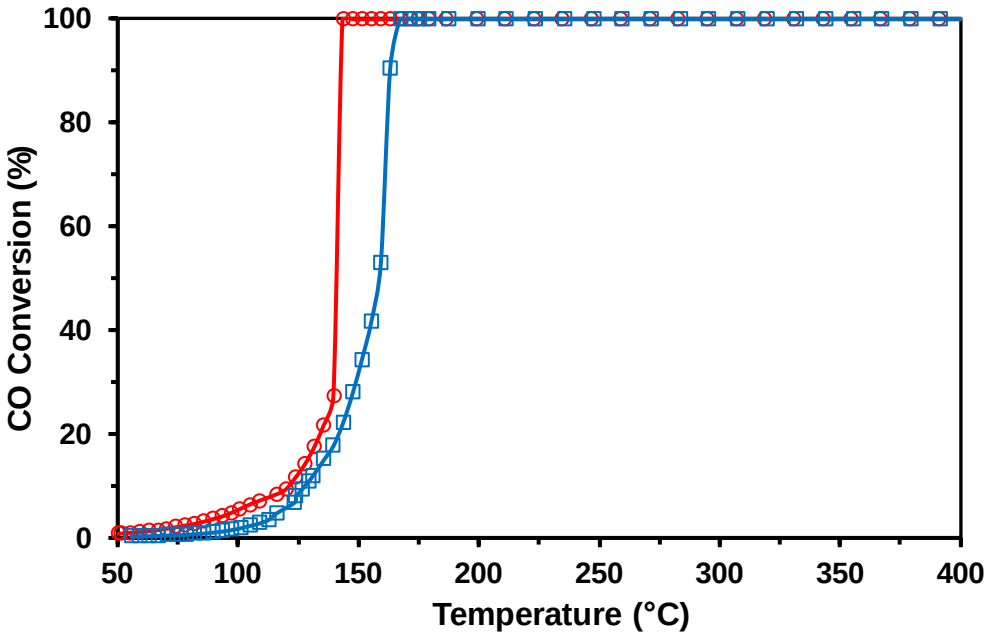

Figure SV-4- Evolution of CO conversion vs. temperature during light-off and light-out of CO oxidation on Pd/Al_2O_3.

Figures SV-5- CO adsorbed on Pd/Al_2O_3

A_i= Height of the peak
x_i= Peak position
s_i= Full Width at Half Maximum
Ba and Bb= Baseline slope and intercept

Pd/Al_2O_3 t= 0 s

A1	= 0.0030022 ± 0.000269
A2	= 0.0033172 ± 0.000217
A3	= 0.0094171 ± 0.00023
A4	= 0.01377 ± 0.000186
A5	= 0.0058576 ± 0.000192
x1	= 2087 ± 0
x2	= 2059 ± 0
x3	= 1957 ± 0
x4	= 1908 ± 0
x5	= 1848 ± 0
s1	= 12.876 ± 0
s2	= 25.366 ± 0
s3	= 18.042 ± 0
s4	= 36.865 ± 0
s5	= 46.952 ± 0
A6	= 0.00096378 ± 0.000291
x6	= 2130.1 ± 3.65
s6	= 10 ± 0
Ba	= -1.9405e-06 ± 4.17e-07
Bb	= 0.27268 ± 0.0008161.2 s

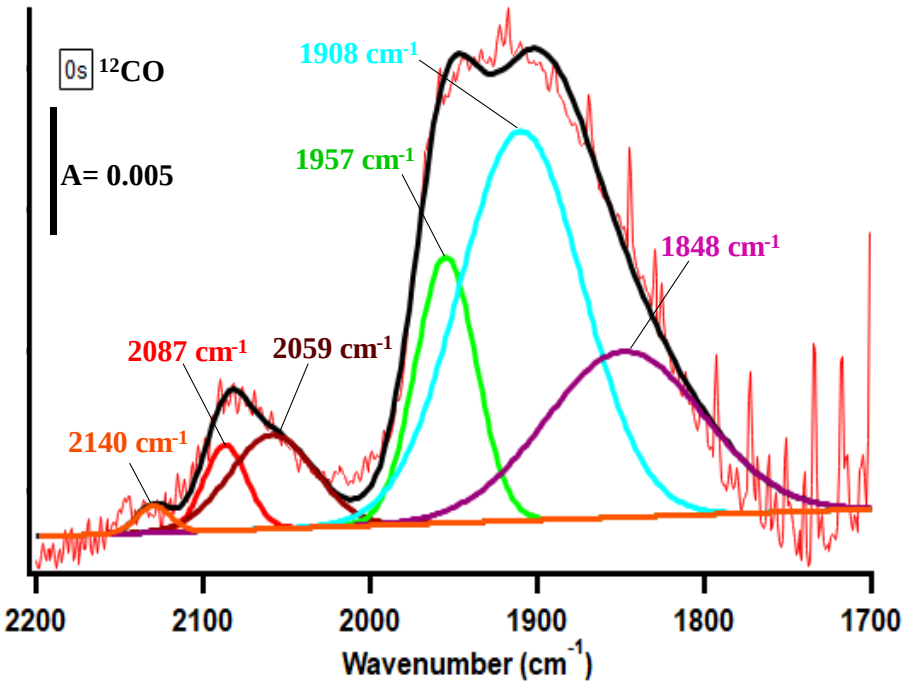

Pd/Al_2O_3 t= 1.2 s

A1	= 0.0030022 ± 0.000281
A2	= 0.003134 ± 0.000227
A3	= 0.0094171 ± 0.000416
A4	= 0.012121 ± 0.00104
A5	= 0.0030688 ± 0.000788
A6	= 0 ± 0
A7	= 0.00044752 ± 0.000203
A8	= 0.0017387 ± 0.00104
A9	= 0.0033852 ± 0.00103
A10	= 0 ± 0
x1	= 2087 ± 0
x2	= 2059 ± 0
x3	= 1957 ± 0
x4	= 1908 ± 0
x5	= 1848 ± 0
x6	= 2036.2 ± 0
x7	= 2016 ± 0
x8	= 1910.9 ± 0
x9	= 1857 ± 0
x10	= 1804 ± 0
s1	= 12.876 ± 0
s2	= 25.366 ± 0
s3	= 18.042 ± 0
s4	= 36.865 ± 0
s5	= 46.952 ± 0
s6	= 12.261 ± 0
s7	= 27.46 ± 0
s8	= 20.799 ± 0
s9	= 36 ± 0
s10	= 42.096 ± 0
A11	= 0.0011236 ± 0.000285
x11	= 2130.1 ± 0
s11	= 10 ± 0
Ba	= -3.162e-06 ± 4.39e-07
Bb	= 0.27521 ± 0.000873

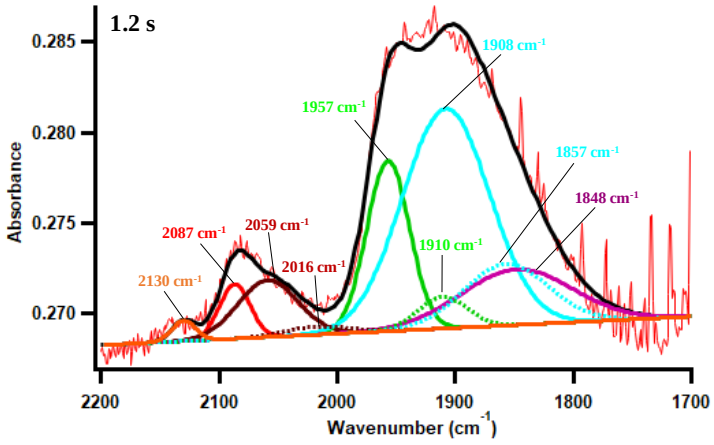

Pd/Al_2O_3 t= 2.5 s

A1	= 0.0026175 ± 0.000314
A2	= 0.002674 ± 0.000287
A3	= 0.0078906 ± 0.000508
A4	= 0.0082849 ± 0.00106
A5	= 0.0030688 ± 0.00427
A6	= 0.00051679 ± 0.000379
A7	= 0.00080843 ± 0.000245
A8	= 0.0045577 ± 0.00126
A9	= 0.0050509 ± 0.00374
A10	= 0.00029395 ± 0.00157
x1	= 2087 ± 0
x2	= 2059 ± 0
x3	= 1957 ± 0
x4	= 1908 ± 0
x5	= 1848 ± 0
x6	= 2036.2 ± 0
x7	= 2016 ± 0
x8	= 1910.9 ± 0
x9	= 1857 ± 0
x10	= 1804 ± 0
s1	= 12.876 ± 0
s2	= 25.366 ± 0
s3	= 18.042 ± 0
s4	= 36.865 ± 0
s5	= 46.952 ± 0
s6	= 12.261 ± 0
s7	= 27.46 ± 0
s8	= 20.799 ± 0
s9	= 36 ± 0
s10	= 42.096 ± 0
A11	= 0.0015394 ± 0.000292
x11	= 2130.1 ± 0
s11	= 10 ± 0
Ba	= -4.0251e-06 ± 5.99e-07
Bb	= 0.27692 ± 0.00124

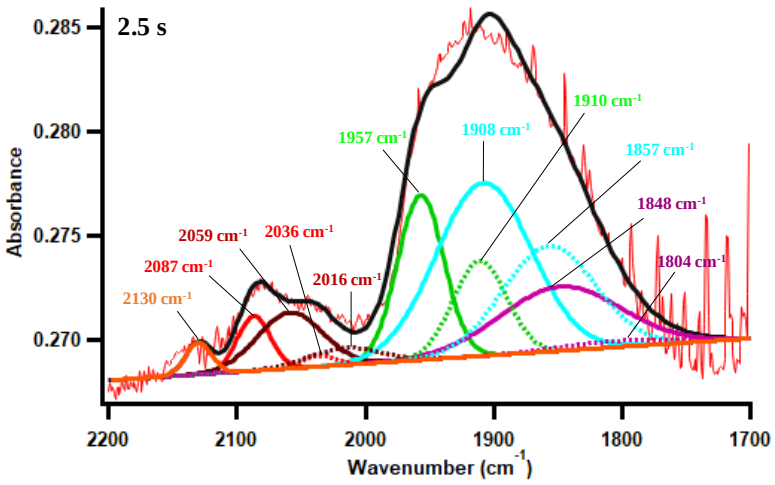

Pd/Al_2O_3 t= 5 s

A1	= 0.0017594 ± 0.000307
A2	= 0.0019753 ± 0.00028
A3	= 0.003569 ± 0.000493
A4	= 0.0072275 ± 0.00103
A5	= 0.0030688 ± 0.00415
A6	= 0.0012793 ± 0.000368
A7	= 0.0014582 ± 0.000239
A8	= 0.0045577 ± 0.00122
A9	= 0.0058221 ± 0.00363
A10	= 0.00088157 ± 0.00153
x1	= 2087 ± 0
x2	= 2059 ± 0
x3	= 1957 ± 0
x4	= 1908 ± 0
x5	= 1848 ± 0
x6	= 2036.2 ± 0
x7	= 2016 ± 0
x8	= 1910.9 ± 0
x9	= 1857 ± 0
x10	= 1804 ± 0
s1	= 12.876 ± 0
s2	= 25.366 ± 0
s3	= 18.042 ± 0
s4	= 36.865 ± 0
s5	= 46.952 ± 0
s6	= 12.261 ± 0
s7	= 27.46 ± 0
s8	= 20.799 ± 0
s9	= 36 ± 0
s10	= 42.096 ± 0
A11	= 0.001606 ± 0.00029
x11	= 2140 ± 0
s11	= 10 ± 0
Ba	= -5.2764e-06 ± 5.88e-07
Bb	= 0.27984 ± 0.00122

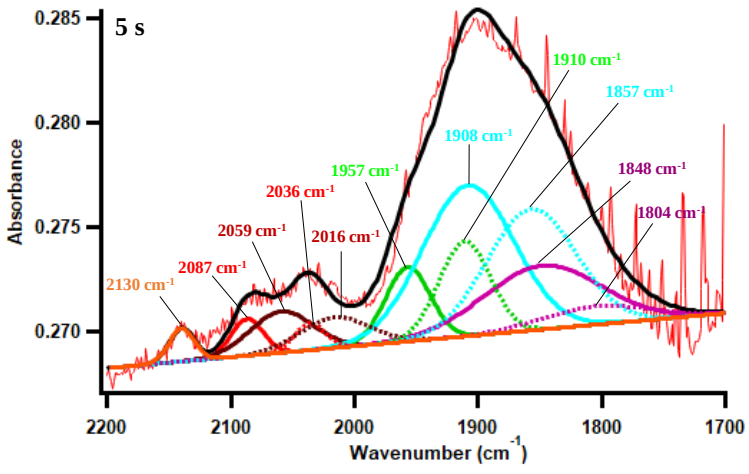

Pd/Al_2O_3 t= 10 s

A1	= 0.0017043 ± 0.000295
A2	= 0.0012586 ± 0.000269
A3	= 0.0016441 ± 0.000475
A4	= 0.0041122 ± 0.000994
A5	= 0.0030688 ± 0.00399
A6	= 0.0017811 ± 0.000354
A7	= 0.0019907 ± 0.000229
A8	= 0.0067455 ± 0.00118
A9	= 0.0073239 ± 0.00349
A10	= 0.00094269 ± 0.00147
x1	= 2087 ± 0
x2	= 2059 ± 0
x3	= 1957 ± 0
x4	= 1908 ± 0
x5	= 1848 ± 0
x6	= 2036.2 ± 0
x7	= 2016 ± 0
x8	= 1910.9 ± 0
x9	= 1857 ± 0
x10	= 1804 ± 0
s1	= 12.876 ± 0
s2	= 25.366 ± 0
s3	= 18.042 ± 0
s4	= 36.865 ± 0
s5	= 46.952 ± 0
s6	= 12.261 ± 0
s7	= 27.46 ± 0
s8	= 20.799 ± 0
s9	= 36 ± 0
s10	= 42.096 ± 0
A11	= 0.0017968 ± 0.000279
x11	= 2140 ± 0
s11	= 10 ± 0
Ba	= -5.8955e-06 ± 5.65e-07
Bb	= 0.28094 ± 0.00117

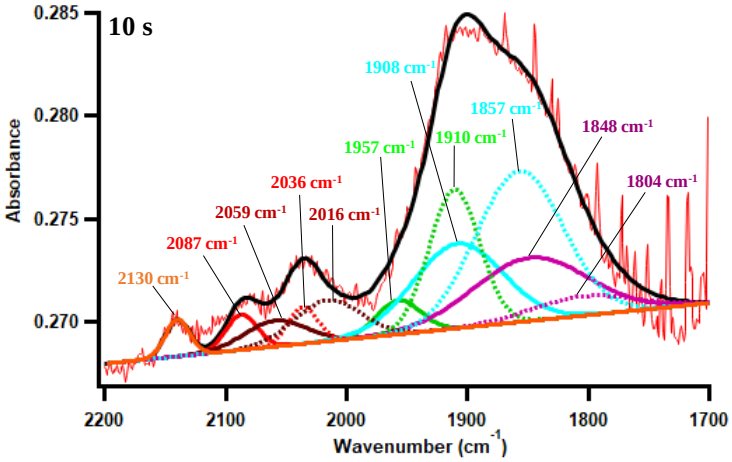

Pd/Al_2O_3 t= 15 s

A1	= 0.0012066 ± 0.000293
A2	= 0.0010002 ± 0.000267
A3	= 0.00047815 ± 0.000472
A4	= 0.0025466 ± 0.000987
A5	= 0.0030688 ± 0.00397
A6	= 0.0017811 ± 0.000352
A7	= 0.0023096 ± 0.000228
A8	= 0.0076875 ± 0.00117
A9	= 0.0080565 ± 0.00347
A10	= 0.0010758 ± 0.00146
x1	= 2087 ± 0
x2	= 2059 ± 0
x3	= 1957 ± 0
x4	= 1908 ± 0
x5	= 1848 ± 0
x6	= 2036.2 ± 0
x7	= 2016 ± 0
x8	= 1910.9 ± 0
x9	= 1857 ± 0
x10	= 1804 ± 0
s1	= 12.876 ± 0
s2	= 25.366 ± 0
s3	= 18.042 ± 0
s4	= 36.865 ± 0
s5	= 46.952 ± 0
s6	= 12.261 ± 0
s7	= 27.46 ± 0
s8	= 20.799 ± 0
s9	= 36 ± 0
s10	= 42.096 ± 0
A11	= 0.0014912 ± 0.000277
x11	= 2140 ± 0
s11	= 10 ± 0
Ba	= -6.3561e-06 ± 5.62e-07
Bb	= 0.28222 ± 0.00116

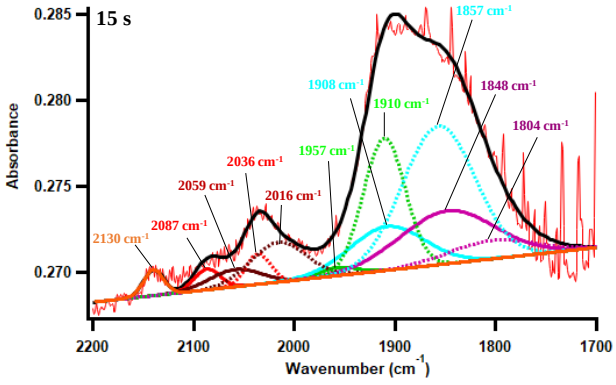

Pd/Al_2O_3 t= 20 s

A1	= 0.0011415 ± 0.000292
A2	= 0.00083722 ± 0.000266
A3	= 0.00024213 ± 0.00047
A4	= 0.0013255 ± 0.000984
A5	= 0.0030688 ± 0.00396
A6	= 0.0019893 ± 0.00035
A7	= 0.0024509 ± 0.000227
A8	= 0.0087998 ± 0.00116
A9	= 0.008616 ± 0.00346
A10	= 0.0012139 ± 0.00145
x1	= 2087 ± 0
x2	= 2059 ± 0
x3	= 1957 ± 0
x4	= 1908 ± 0
x5	= 1848 ± 0
x6	= 2036.2 ± 0
x7	= 2016 ± 0
x8	= 1910.9 ± 0
x9	= 1857 ± 0
x10	= 1804 ± 0
s1	= 12.876 ± 0
s2	= 25.366 ± 0
s3	= 18.042 ± 0
s4	= 36.865 ± 0
s5	= 46.952 ± 0
s6	= 12.261 ± 0
s7	= 27.46 ± 0
s8	= 20.799 ± 0
s9	= 36 ± 0
s10	= 42.096 ± 0
A11	= 0.0014585 ± 0.000276
x11	= 2140 ± 0
s11	= 10 ± 0
Ba	= -6.3212e-06 ± 5.6e-07
Bb	= 0.28163 ± 0.00116

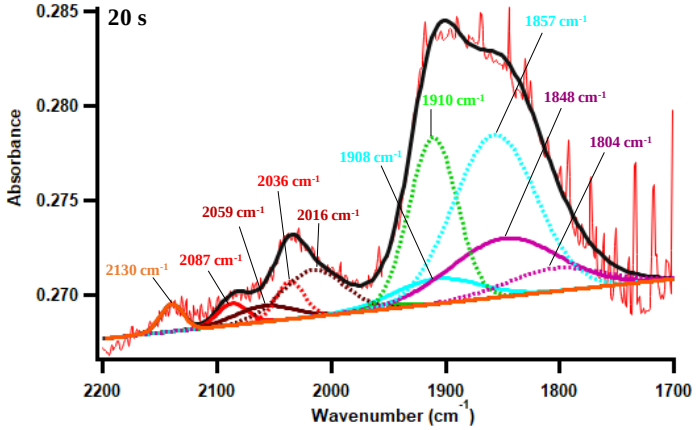

Pd/Al_2O_3 t= 30 s

A1	= 0.0011121 ± 0.000287
A2	= 0.00083722 ± 0.000265
A3	= 0 ± 0
A4	= 0.0011828 ± 0.000633
A5	= 0.0027643 ± 0.00301
A6	= 0.0022253 ± 0.000311
A7	= 0.0024509 ± 0
A8	= 0.0087998 ± 0.000524
A9	= 0.0090075 ± 0.00243
A10	= 0.0012139 ± 0.00116
x1	= 2087 ± 0
x2	= 2059 ± 0
x3	= 1957 ± 0
x4	= 1908 ± 0
x5	= 1848 ± 0
x6	= 2036.2 ± 0
x7	= 2016 ± 0
x8	= 1910.9 ± 0
x9	= 1857 ± 0
x10	= 1804 ± 0
s1	= 12.876 ± 0
s2	= 25.366 ± 0
s3	= 18.042 ± 0
s4	= 36.865 ± 0
s5	= 46.952 ± 0
s6	= 12.261 ± 0
s7	= 27.46 ± 0
s8	= 20.799 ± 0
s9	= 36 ± 0
s10	= 42.096 ± 0
A11	= 0.001687 ± 0.000268
x11	= 2140 ± 0
s11	= 10 ± 0
Ba	= -7.0964e-06 ± 5.38e-07
Bb	= 0.28284 ± 0.0011

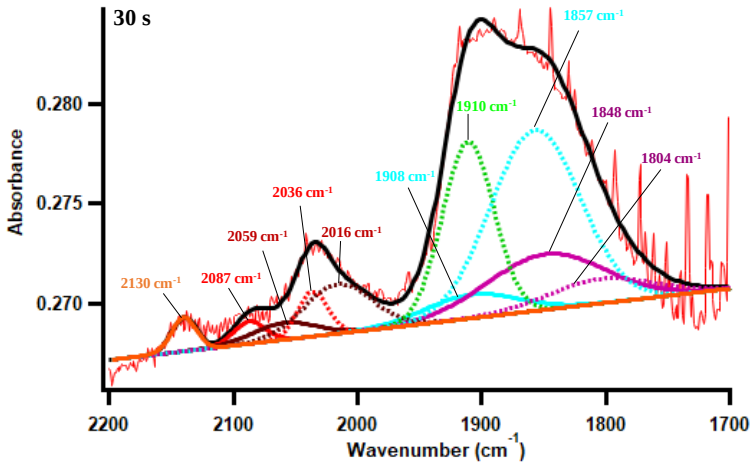

Pd/Al_2O_3 t= 60 s

A1	= 0.0027663 ± 0.000296
A2	= 0.0024427 ± 0.000225
A3	= 0.010103 ± 0.000215
A4	= 0.011924 ± 0.000182
A5	= 0.0021152 ± 0.000227
x1	= 2036.2 ± 0
x2	= 2016 ± 0
x3	= 1910.9 ± 0
x4	= 1857 ± 0
x5	= 1804 ± 0
s1	= 12.261 ± 0
s2	= 27.46 ± 0
s3	= 20.799 ± 0
s4	= 36 ± 0
s5	= 42.096 ± 0
A6	= 0.0013081 ± 0.000259
x6	= 2082.1 ± 2.57
s6	= 10 ± 0
Ba	= -5.7091e-06 ± 4.35e-07
Bb	= 0.28027 ± 0.000885

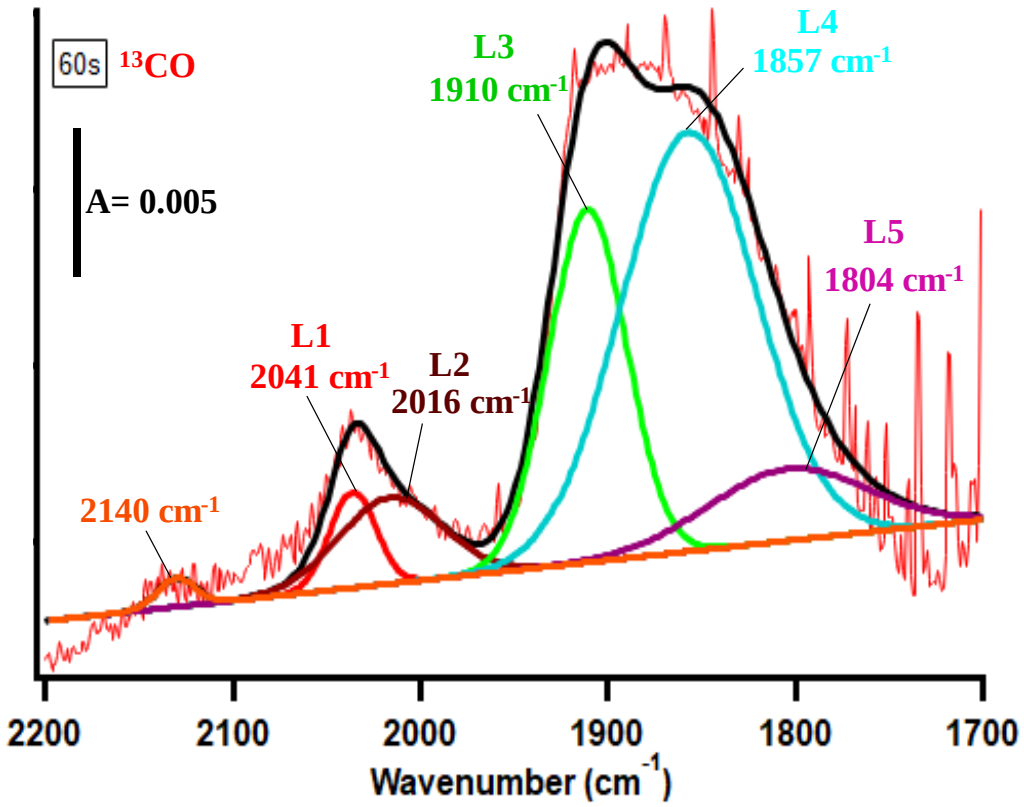

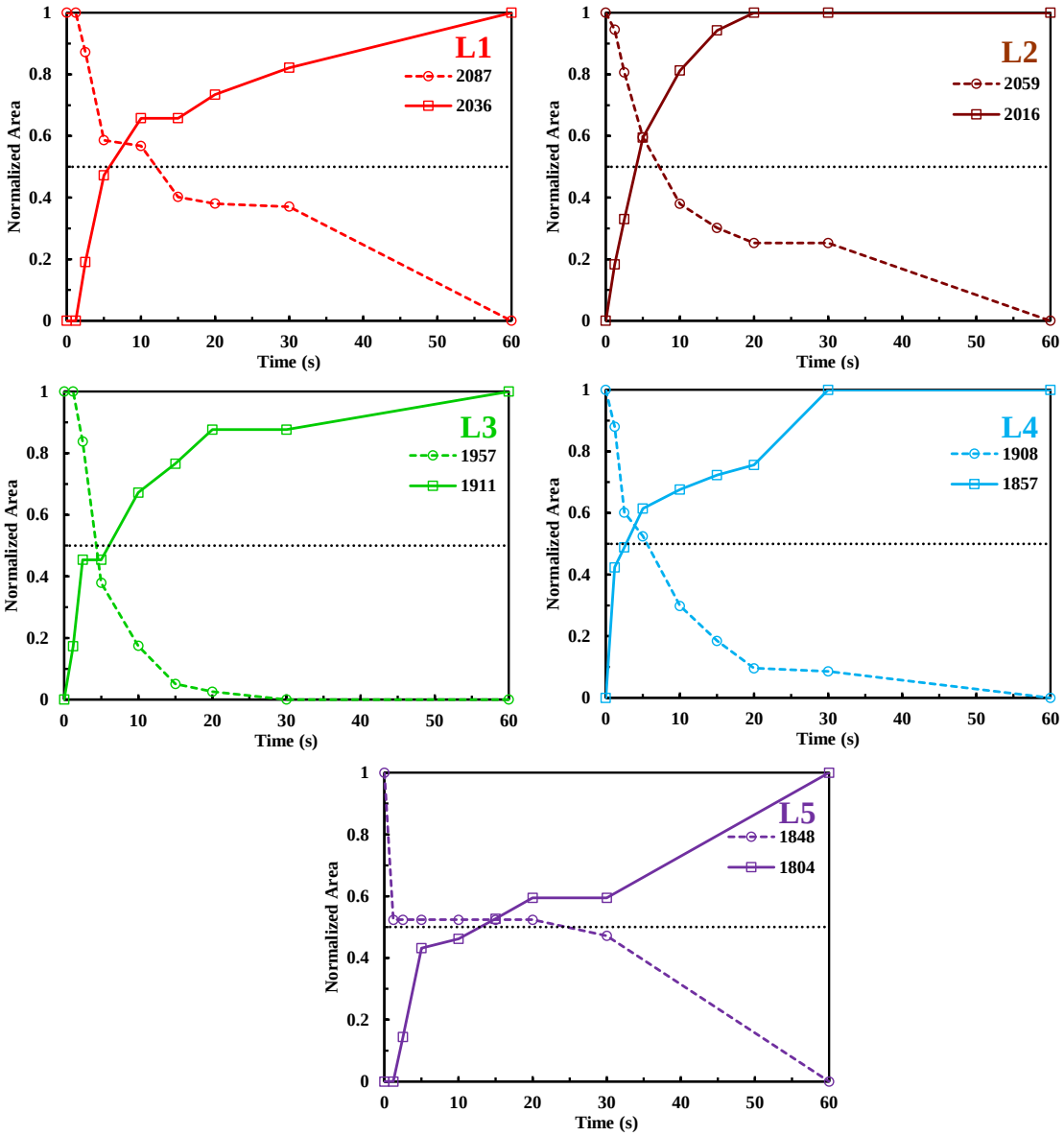

Figure SV-6- Evolution of normalized area for adsorbed linear ^{12}CO and corresponding linear ^{13}CO L1 (red) and L2 (dark brown), L3 (green), L4 (cyan) and L5 (purple) bands during isotopic exchange.

Table SV-2- Calculated correction factors for each CO adsorbed IR bands on Pd.

	L1	L2	L3	L4	L5
f	0.86	0.80	1.23	0.84	0.31

ACKNOWLEDGMENTS

“A person must fight for what he believes in. Half of himself must bleed along the way, he must lose something of himself and leave his desires on the edge of hope.”

With this expression, I end my thesis and write my emotions. Sometimes, the victory at the end of the battle will have less value and taste due to what you experienced during it, but in life, nothing is easy or for free. When I was writing this thesis, I had some personal problems that had a huge impact on me morally, but I got up and carried on alone with my wounds. I'm saying this to tell you that the worst can happen to you on the road to your dreams, but don't let it stop you, keep fighting, even if you're alone, you'll make it, as I did. This little introduction is dedicated to all the people who have lost loved ones and been abandoned on the path to their dreams.

I'd like to start by thanking Christophe and Mélissandre. With them, this work was done successfully despite all the technical difficulties we encountered. You were always there to make sure everything ran smoothly, to guide me and to train me. I've learnt a lot from you, from your experience, your knowledge and your expertise. You set up everything I needed for the thesis, opportunity to teach, training, support, advice and conferences that we attended together (specially the conference at Grindelwald, unforgettable!). Christophe, thank you so much for your advices, for listening to me and helping me, I've learnt a lot from you. Even though you were quite busy with your responsibilities, you were always there for me, answering my questions and intervening in the lab when I needed you. Mélissandre, I'd also like to thank you very much, you were always there, always listening when I had worries and problems. You reassured me a lot when I was afraid and stressed, you gave me advices and you accompanied me well during the writing of the manuscript and I am very grateful. I'd also like to thank Nassim, who was there at the beginning of my PhD, who trained me on the setup and helped me get started. On the other hand, I don't want to thank the SSITKA set-up, he let me down so much during the thesis.

I'd like to thank my office colleagues, Victor, Guillaume (thoughts of our board game evenings), Grèce (the first person I met in the office), Amira (my closest colleague as we work on the same topic), Shilpa, Shuang, Maher (thoughts of our Monday evenings), Ghadir and Valérie who have just started their first year of thesis (Good Luck, you need it). I won't forget Bertha, with whom I began the adventure of the thesis at the same time. I would also like to thank the secretarial team: David, Sandrine, Geoffrey and Barbara for all their help with administrative

formalities. Thanks also to all permanent staff of the lab, Olivier (for all the characterization work), Mélanie and Jean-Charles (we shared the IR lab for a long time), Axel, Jean-François, Carole, Christine, Pascal, Mickael, Elise, Stéphane, Martine and others... I won't forget to thank Mirella, Anne-Sophie and Aurélie with whom I shared 2 years of teaching practical work!

I'd also like to thank all the PhD students, interns and post-docs that I've met over the past 3 years in UCCS, with who I have shared some great moments in the lab, especially at C3, and outside the lab: Massimo, Taha, Abbas, Nicolas, Julien, Teddy (Thoughts on your effort to speak Lebanese), Lei, Mohammad, Sandy, Amaury, Sacha, Theresa (who changed my mood a lot during the writing phase), Nisrine, Sara, Jack (it's not his real first name but he'll get to know himself), Nabil (thought of our outings around the city). Special thanks for my lunch team members where it’s my only moment of the journey that I disconnect from the PhD. Peter, Mariam (the person I bother most), Maria, Céline, Nour, Joey, Odette, Elias, Ali, Iyad, thank you for these unforgettable moments. A big thank you to my second family in Douai with whom I spent a lot of time and BBQs (Adel, Ali, Raafa, Hasan, Ghina, Mohamad, Zeinab, Fatima, Salwa, Ahmad, Doaa and Tamara). A special thought to Kassem, les 2 Husseins, Achraf and Rana (my friends since my arrival in France, with whom I share many memories! I'd also like to thank everyone who passed through, even if they didn't continue the journey with me to the end and left at some point for one reason or another, but we shared memories together one day...

I would like to sincerely thank Dr Frédéric Meunier and Dr Nicolas Bion for agreeing to report on this thesis. I would also like to thank Professor Rose Noelle Vannier and Doctor Claude Mirodatos for serving on my jury as examiners for this work.

I would also like to thank all my colleagues at Hutchinson, who supported me well from the first day of my arrival and helped me to integrate well into this new position and this new adventure, including Bruno (my manager), Huy, Julie, Frédéric, Sébastien, Lionel, Corinne, Enzo, Florence, Vanessa, Thibault, Pauline, Merve, Cyril, Mélina and Raymond…

And finally, this thesis, one of my great victories, I dedicate to my father and mother who have always been there when I've fallen, they've never let me down, always supported me, always given me courage and cheered me up. Thank you, Dad, for your financial support throughout my journey, for listening to me, for your advices and for being my support throughout my life. My mother, my first love, my guardian angel and the secret behind my success, I thank you from the bottom of my heart and I love you so much. Thanks also to my little sisters Sara and Lana, you were also by my side at every moment and offered me every support. I don't tell you

often enough, probably out of modesty, but I love you. Thank you also to all my family in Lebanon and to all my friends with whom I spent a lot of time and grown up. I'd also like to say thank you to Souryana, my favorite little girl, with whom I've talked a lot about my thesis, my work, life and everything else, ¡Muchas gracias querida, eres la mejor chica que he conocido!

And like all stories, there is a beginning and an end, so I finished this manuscript today with all the good and bad memories, hidden between these pages and these words, that I had along the way...

Abstract

The aim of this thesis is to improve our understanding of hysteresis phenomena on noble metals in order to increase catalyst activity at low temperatures. The CO oxidation mechanism was investigated by steady-state isotopic transient kinetic analysis (SSITKA) coupled with Infrared (IR) spectroscopy on Pt- and Pd-based catalysts supported on alumina. This methodology enabled us to discriminate between intermediate and spectator species during the reaction. Firstly, hydrogen carbonates were found to be spectator species, not directly involved in the formation of CO_2 during the reaction. Linear and bridged carbonyl species were therefore identified as potential intermediates. Deconvolution of the different types of carbonyls, followed by kinetic analysis, enabled us to distinguish their reactivity during isotope exchange. In addition, a comparative study of the behavior of adsorbed reactive species during CO oxidation has been carried out to better characterize the hysteresis phenomena on Pt/Al_2O_3 and Pd/Al_2O_3 in order to clarify their origin and better understand their impact on catalytic activity.

Keywords: SSITKA-IR/CO oxidation/Reaction mechanism/Hysteresis

Résumé

L'objectif de cette thèse est d'améliorer la compréhension des phénomènes d'hystérésis sur les métaux nobles afin de pouvoir augmenter l'activité des catalyseurs à basse température. Le mécanisme d'oxydation du CO a été étudié par des analyses cinétiques en régime stationnaire d'un échange isotopique transitoire (SSITKA) couplée à la spectroscopie Infrarouge (IR) sur des catalyseurs à base de Pt et de Pd supportés sur de l'alumine. Cette méthodologie a permis de discriminer les espèces intermédiaires et les espèces spectatrices au cours de la réaction. Tout d'abord, les hydrogénocarbonates se sont révélées être des espèces spectatrices, ne participant pas directement à la formation de CO_2 lors de la réaction. Les espèces carbonyles linéaires et pontées ont donc été identifiées comme des espèces intermédiaires potentielles. Un travail de déconvolution des différents types de carbonyles suivie d'une analyse cinétique ont permis de distinguer leur réactivité lors de l'échange isotopique. De plus, une étude comparative du comportement des espèces réactives adsorbées lors de l'oxydation de CO a été menée lors de la montée et de la descente en température afin de mieux caractériser les phénomènes d'hystérésis sur Pt/Al_2O_3 et Pd/Al_2O_3 pour en préciser l'origine et mieux comprendre l'impact sur l'activité catalytique.

Mots clés : SSITKA-IR/Oxydation de CO/Carbonyles/Hydrogénocarbonates/Hystérésis